Nano- and microstructural transformation processes during diagenesis of biogenic carbonates

vorgelegt von

Laura Antonella Casella

Dissertation zur Erlangung des Grades
DOCTOR RERUM NATURALIUM

Fakultät für Geowissenschaften

Ludwig-Maximilians-Universität München

München, 31.08.2018

Betreuer: Prof. Dr. Wolfgang W. Schmahl

1. Gutachter: Prof. Dr. Wolfgang W. Schmahl
2. Gutachter: Prof. Dr. Anton Eisenhauer

Promotionskomission: Prof. Dr. Wolfgang W. Schmahl
                                   Prof. Dr. Anton Eisenhauer
                                   Prof. Dr. Stuart Gilder
                                   Prof. Dr. Soraya Heuss-Aßbichler
                                   Prof. Dr. Julia Pongratz
                                   Prof. Dr. Claudia Trepmann

Tag der mündlichen Prüfung: 01. März 2019

~ Für Mama ~

„Erfolgreich zu sein, setzt zwei Dinge voraus:

Klare Ziele und den brennenden Wunsch, sie zu erreichen."

— *Johann Wolfgang von Goethe*

Abstract

Biomineralised hard tissues such as shells and skeletons of fossil marine invertebrates constitute the most important physical record of palaeoenvironmental conditions. However, living organisms are not in thermodynamic equilibrium with their environment and create local chemical compartments within their bodies where physiologic processes occur. After death of the organism, physiological conditions, which were present during biomineralisation, are not sustained any further. Thus, the system moves towards equilibrium with the surrounding inorganic physicochemical system. During diagenesis hard tissues may be exposed to elevated temperature and pressure conditions as well as to surrounding fluids over geological time scales. Consequently, the original biogenic structure of aragonitic or calcitic tissue vanishes and is replaced by inorganic structural features often characterised by the occurrence of secondary calcite. Furthermore, degradation of biopolymer matrices, distortion of the initial morphology and microstructural features are commonly caused by diagenetic overprint. The degree of diagenetic alteration of marine skeletal hard tissues may vary significantly and depends on conditions of the particular diagenetic environment. However, the correct assessment of palaeoenvironmental evolution and dynamics based on elemental and isotopic characteristics is only possible when pristine, unaltered hard tissues are analysed. Therefore, the unambiguous distinction between unaltered hard tissues and diagenetically altered parts is of fundamental importance for the reliability of any palaeoenvironmental reconstruction study based on such samples.

In order to improve understanding of diagenetic alteration and to assess the degree of diagenetic overprint of biogenic aragonites and (low-Mg) calcites, modern specimens of selected bivalves (*Arctica islandica*, *Mytilus edulis*), brachiopods (*Terebratalia transversa*), scleractinian corals (*Porites* sp.), and gastropods (*Haliotis ovina*) were subjected to hydrothermal alteration experiments simulating diagenetic alteration. Experiments were conducted between 100 and 175 °C for 1-84 days in solutions simulating either meteoric or burial fluids. Based on the experimental findings the influence of different microstructures on the degree of alteration, and thus, their potential to withstand diagenetic overprint was evaluated. In parallel, diagenetic alteration in selected fossil low-Mg calcite brachiopods such as *Digonella digona*, *Lobothyris punctata*, *Platystrophia laticostata*, and *Quadratirhynchia attenuata* was investigated accordingly. Utilised fossil specimens differed in shell microstructure (punctate/impunctate), lived at different geologic times, and underwent distinct burial depths and conditions.

The qualitative assessment of the degree of alteration was based on images of optical overprint signals on the macro- to the nanometre scale obtained by Field-

Abstract

Emission Scanning Electron Microscopy (FE-SEM), Cathodoluminescence (CL), and Atomic Force Microscopy (AFM). Changes in crystal orientation patterns were determined by high-resolution Electron Backscatter Diffraction (EBSD). This multi-analytical approach was further supported by statistical evaluation of crystal co-orientations and grain size distributions, which allowed to assign qualitative degrees of (simulated) diagenetic alteration to marine calcareous skeletal parts. The results obtained from modern and hydrothermally altered biogenic carbonates allowed for a comparison to naturally altered fossil specimens.

During hydrothermal alteration at 100 °C the initial skeletal morphologies, mineralogies and microstructures were preserved down to the sub-micrometre scale and partial decomposition of biopolymer matrices was observed. In hydrothermal experiments conducted at 175 °C initial biogenic mineralogy was replaced by inorganic calcite due to dissolution-reprecipitation reactions after a dormant time of a few days. However, initially aragonitic skeletons were notably more prone to replacement reactions compared to originally (low-Mg) calcitic or nacreous aragonitic hard tissues resulting in differing degrees of alteration for varying biocarbonate microstructures. With increasing experimental time alteration proceeded and resulted in (1) entire destruction of biopolymers, (2) almost complete replacement of initial aragonite/low-Mg calcite by inorganic calcite, (3) precipitation of secondary inorganic calcite with concomitant grain coarsening, (4) development of porous secondary minerals, as well as (5) amalgamation of neighbouring mineral units. Amalgamation is the term chosen to name the phenomenon when two neighbouring grains of slightly different crystallographic orientation merge to form one coherent crystallographic lattice. Nucleation and growth of thermodynamically most stable (inorganic) calcite was observed in all marine calcareous hard tissues at locations which allowed for fluid-solid contact such as shell surfaces, endopunctae and open pore systems. All findings in experimentally altered biogenic carbonate hard parts could also be observed in natural, diagenetically altered fossil specimens, which either showed preserved pristine areas next to overprinted parts or severe overprint expressed by distortion of delicate structural features on the micrometre scale and formation of inorganic calcite.

The application of CL and FE-SEM on naturally and hydrothermally altered biogenic carbonate hard tissues allowed for preliminary observations of the degree of diagenetic alteration, however, EBSD and AFM were necessary tools in order to obtain a more comprehensive assessment of the degree of overprint. Diagenetic changes as well as degrees of overprint down to the micrometre scale could be visualised by unequivocal identification of highly-detailed alteration features within the microstructure (e.g., amalgamation of neighbouring mineral fibres or nacre tablets), and the occurrence and amount of inorganic calcite replacing biogenic calcium carbonates by dissolution-reprecipitation reactions. In summary, preservation of initial biogenic mineralogy and

delicate biogenic microstructural features combined with the absence of secondary calcite formation are strong indicators for an unaltered specimen. These indicators can commonly be found in hard tissues comprised of metastable $CaCO_3$ subjected to low diagenetic temperatures. The promising preservation potential qualifies such specimens as ideal archives for palaeoenvironmental studies. In contrast, moderate to severe diagenetic alteration observed in (fossil) biogenic carbonates caused by aggressive conditions and long experimental/geological time scales, respectively, resulted in poor preservation of the initial mineralogy and microstructural features. Thus, these marine carbonate hard tissues are not resistant to diagenetic alteration, and more importantly, not suitable for reconstruction studies of past climate dynamics.

Abstract

Zusammenfassung

Biomineralisierte Hartteile wie Schalen und Skelette fossiler mariner Invertebraten bilden das wichtigste materielle Archiv vergangener Umweltbedingungen. Jedoch stehen lebende Organismen im thermodynamischen Ungleichgewicht mit ihrer Umwelt und erzeugen lokale chemische Kompartimente innerhalb ihrer Körper, in denen physiologische Prozesse stattfinden. Nach dem Tod des Organismus werden physiologische Bedingungen, die während des Biomineralisationsprozesses vorhanden waren, nicht mehr aufrechterhalten, so dass sich das System in Richtung Gleichgewicht mit dem umgebenden anorganischen, physikalisch-chemischen System bewegt. Während Diagenese können die Hartteile über geologische Zeiträume erhöhten Druck- und Temperaturbedingungen sowie Fluiden ausgesetzt sein. Dadurch wird die ursprünglich biogene Struktur der Hartteile durch anorganische Strukturmerkmale ersetzt, die oftmals durch das Auftreten von Sekundärcalcit charakterisiert sind. Diagenetische Überprägung biogener Materialien wird desweiteren häufig vom Zerfall der Biopolymer-Matrix, Verzerrung der ursprünglichen Morphologie und der mikrostrukturellen Eigenschaften begleitet. Dabei kann der Grad der Alteration mariner Hartteile signifikant variieren und primär von den Bedingungen der jeweiligen diagenetischen Umgebung abhängen. Die korrekte Bewertung der Paläoumweltentwicklung und -dynamik auf der Basis von Element- und Isotopeneigenschaften ist jedoch nur möglich, wenn ursprüngliche, unveränderte Hartgewebe analysiert werden. Daher ist die eindeutige Unterscheidung zwischen unveränderten und diagenetisch veränderten Hartschalen von grundlegender Bedeutung für die Zuverlässigkeit von Rekonstruktionen der Paläoumwelt, die auf solchen Proben beruhen.

Um das Verständnis der diagenetischen Alteration zu verbessern und den Grad der diagenetischen Überprägung von biogenen Aragoniten und (niedrig-Mg) Calciten zu bestimmen, wurden ausgewählte rezente Bivalven (*Arctica islandica*, *Mytilus edulis*), Brachiopoden (*Terebratalia transversa*), Steinkorallen (*Porites* sp.) und Gastropoden (*Haliotis ovina*) hydrothermalen Alterationsexperimenten unterworfen, um eine diagenetische Veränderung zu simulieren. Experimente wurden zwischen 100 und 175 °C für 1 bis 84 Tage in Lösungen, die entweder meteorische oder Versenkungsfluide simulierten, durchgeführt. Basierend auf den experimentellen Befunden wurde der Einfluss verschiedener Mikrostrukturen auf den Grad der diagenetischen Alteration, und damit ihr Potenzial der diagenetischen Überprägung zu widerstehen, evaluiert. Gleichzeitig wurden niedrig-Mg Calcit Schalen ausgewählter fossiler, diagenetisch überprägter Brachiopoden (*Digonella digona*, *Lobothyris punctata*, *Platystrophia laticostata* und *Quadratirhynchia attenuata*) in gleicher Hinsicht untersucht. Die verwendeten

fossilen Proben unterschieden sich in ihrer Mikrostruktur (punktat/impunktat), im geologischen Alter und waren unterschiedlichen Versenkungstiefen sowie -bedingungen ausgesetzt.

Die qualitative Bewertung des Grades der diagenetischen Veränderung basiert auf optischen Überprägungssignalen auf Makro- bis Nanometerebene, die mit Feldemissions-Elektronenmikroskopie (FE-SEM), Kathodolumineszenz (CL) und Rasterkraftmikroskopie (AFM) erfasst wurden. Änderungen in Kristallorientierungsmustern wurden mittels Elektronenrückstreubeugung (EBSD) untersucht. Dieser multianalytische Ansatz wurde durch eine statistische Auswertung der Kristallkoorientierung und Korngrößenverteilung unterstützt, die es ermöglichte den marinen Kalskelettteilen qualitative Grade der (nachgeahmten) diagenetischen Alteration zuzuordnen. Die für die rezenten und hydrothermal alterierten biogenen Carbonate erhaltenen Ergebnisse ermöglichten einen Vergleich mit denen für natürlich alterierte, fossile Teststücke.

Während der hydrothermalen Alteration bei 100 °C wurde die Erhaltung ursprünglicher Skelettmorphologien, Mikrostrukturen und Mineralogie bis in den Submikrometerbereich sowie eine partielle Zersetzung der Biopolymer-Matrix beobachtet. In hydrothermalen Experimenten bei 175 °C wurde die ursprüngliche biogene Mineralogie nach einer inaktiven Phase von einigen Tagen aufgrund von Lösungs-Repräzipitationsreaktionen durch anorganischen Calcit ersetzt. Aragonit-Hartteile waren im Vergleich zu ursprünglich (niedrig-Mg) Calciten und Perlmutt jedoch deutlich anfälliger für diese Reaktionen, was zu unterschiedlichen Alterationsgraden der verschiedenen Mikrostrukturen führte. Mit zunehmender experimenteller Zeit schritt die Veränderung fort und führte zu (1) vollständiger Zerstörung von Biopolymeren, (2) fast vollständigem Ersatz von ursprünglichem Aragonit/Mg-Calcit durch anorganischen Calcit, (3) Ausfällung von sekundärem, anorganischem Calcit mit gleichzeitiger Kornvergröberung, (4) Entwicklung poröser Sekundärminerale sowie (5) Amalgamation benachbarter Mineraleinheiten. Der Begriff Amalgamation wird verwendet, um das Phänomen, wenn zwei benachbarte Körner mit einer geringfügig anderen kristallographischen Orientierung sich zusammenfügen, um ein kohärentes kristallographisches Gitter zu formen, zu bezeichnen. Keimbildung und Wachstum thermodynamisch stabilstem (anorganischem) Calcit wurde in allen marinen kalkhaltigen Hartteilen an Stellen beobachtet, die einen Fluid-Feststoff-Kontakt erlaubten, wie beispielsweise Schalenoberflächen, Endopunctae und offene Porensysteme. Alle Befunde an experimentell alterierten biogenen Carbonat-Hartschalen konnten auch in natürlichen, diagenetisch veränderten Fossilien beobachtet werden, die entweder erhaltene, unberührte Bereiche neben überprägten Bereichen aufwiesen oder eine starke Überprägung zeigten, die durch Veränderungen delikater Strukturmerkmale

auf der Mikrometerskala sowie Bildung von anorganischem Material zum Ausdruck kamen.

Die Anwendung von CL und FE-SEM an natürlich und hydrothermal alterierten biogenen Carbonat-Hartschalen ermöglichte direkte Beobachtungen des Grades diagenetischer Überprägung. Jedoch sind EBSD und AFM notwendige Tools, um den Grad diagenetischer Überprägung umfassend zu beurteilen. Diagenetische Veränderungen sowie Grade der Überprägung können bis in den Mikrometerbereich durch eine eindeutige Identifizierung hochdetaillierter Alterationsmerkmale innerhalb der Mikrostruktur (z. B. Amalgamation benachbarter Fasern oder Tafeln) und dem Auftreten und der Menge an anorganischem Calcit, der biogene Calciumcarbonate durch Auflösung-Repräzipitationsreaktionen ersetzt, visualisiert werden.

Zusammenfassend sind die Erhaltung der ursprünglichen biogenen Mineralogie und der feinen biogenen, mikrostrukturellen Merkmale in Verbindung mit der Abwesenheit sekundären Calcits starke Indikatoren für eine unveränderte Probe. Diese Indikatoren können üblicherweise in Hartschalen aus metastabilem $CaCO_3$ gefunden werden, die niedrigen diagenetischen Temperaturen ausgesetzt waren. Das vielversprechende Erhaltungspotenzial qualifiziert solche Proben als ideale Archive für Paläoumweltstudien. Im Gegensatz dazu führt eine moderate bis starke diagenetische Veränderung durch aggressive Bedingungen und lange experimentelle/geologische Zeitskalen zu einer schlechten Erhaltung der ursprünglichen mineralogischen und mikrostrukturellen Eigenschaften (fossiler) biogener Carbonate. Aus diesem Grund sind solche Carbonat-Hartteile nicht für Rekonstruktionsstudien der vergangenen Klimadynamik geeignet.

Zusammenfassung

Table of contents

Table of contents

XII

1   Introduction

The work presented in this dissertation is part of the first phase of the collaborative research initiative "CHARON: Marine C̲arbonate Arc̲h̲ives: Controls on C̲a̲rbonate Precipitation and Pathways of Diagenetic Alterati̲o̲n̲" (DFG *Forschergruppe* 1644) funded by the German Research Council (*Deutsche Forschungsgemeinschaft* DFG).

   A consortium of interdisciplinary research teams from Germany, Austria, and Switzerland, formed by groups from *Ruhr-Universität Bochum*, *Helmholtz-Zentrum für Ozeanforschung* (*GEOMAR*) *Kiel*, *Technische Universität Graz*, *Westfälische Wilhelms-Universität Münster*, *Universität Bern*, and *Ludwig-Maximilians-Universität München*, set the objective to obtain improved knowledge and understanding of complex diagenetic processes and pathways of marine carbonates. In detail, these are (1) microbiological, physical and geochemical parameters of marine settings of the Phanerozoic, which control the microbial- induced as well as inorganic precipitation of carbonates, and (2) a quantitative comprehension of (post-mortem/post-depositional) diagenetic processes, which have an influence on geochemical properties and mineralogy of marine carbonate archives. By combining innovative and multidisciplinary approaches of experts in geochemistry, sedimentology, palaeontology, microbiology, crystallography, as well as materials science, CHARON provides a unique opportunity to reach these goals.

   Biogenic carbonate hard tissues are formed with direct influence of living organisms during the process of biomineralisation. After the animal´s death, the corpse is deposited on the seafloor. With increasing time, degradation of biopolymer matrices and sedimentation are taking place leading to the burial of marine biocarbonates. With increasing sedimentary cover and under the influence of endogenic geological processes, buried biogenic hard tissues undergo diagenetic alteration as well as dissolution-reprecipitation, and mineral replacement reactions. These processes are considered to be taking place up to 20 km in depth, can be accompanied by the occurrence of fluids, and last until the final uplift of the geologic formation to the Earth´s surface.

   Fossil materials like belemnites or bivalves are essential in reconstruction studies of the palaeoclimate and have potentially undergone diagenetic overprint. The determination of their preservation state as well as suitability in research studies regarding estimation of seawater temperatures of the geologic past, however, proves to be difficult to impossible by macroscopic observations. To overcome this obstacle, this thesis covers mainly materials science and crystallographic aspects of diagenetic alteration in biogenic carbonate hard tissues as well as some geochemical data. The investigations focus on microstructure and texture within a variety of naturally and experimentally altered biocarbonate specimens. Based on a variety of analytical screening methods, the present dissertation shows to which degree as well as probability

laboratory-based and naturally occurring diagenesis has an effect on the preservation state of several marine biogenic carbonates with differing microstructures and mineralogy. Crystallographic studies covering EBSD orientation maps, textures, possibly fractal distributions of grain size, and multiples of uniform distribution are the first steps in empirically assessing the degree of diagenetic alteration, thus, enabling new insights on the suitability of fossil materials for reconstruction studies of the palaeoclimate.

To finalise the introductory words and to point out the interdisciplinary teamwork of the CHARON project, this subchapter ends with a citation from Leadbeater and Riding (1987):

"Biomineralization links soft organic tissues, which are compositionally akin to the atmosphere and oceans, with the hard materials of the solid Earth. It provides organisms with skeletons and shells while they are alive, and when they die these are deposited as sediment in environments from river plains to the deep ocean floor. It is also these hard, resistant products of life which are mainly responsible for the Earth´s fossil record. Consequently, bio-mineralisation involves biologists, chemists, and geologists in interdisciplinary studies at one of the interfaces between Earth and life."

1.1 Calcium carbonate phases in biological and geological environments

Calcium is one of the most abundant cations on the Earth's surface and occurs in about 50 % of the 64 known biominerals (Lippmann 1973; Lowenstam and Weiner, 1989; Knoll, 2003; Weiner and Dove, 2003). Most calcium is present as calcium carbonate ($CaCO_3$) which is formed by organisms (e.g., brachiopods, molluscs, foraminifera; Mann, 2001) for several purposes, such as protective shield against predators (Gosling, 2003; Mackenzie et al., 2014) or enhancement of respiration (Alexander, 2001). Table 1.1 gives an overview on biogenic calcium carbonates which are formed by several organisms. Given the importance and prevalence in Earth´s history, (fossil) marine organisms with biogenic carbonate hard tissues (e.g., brachiopods, bivalves) were selected as specimens for investigations in the framework of the present dissertation.

Calcite is the most abundant biogenic and rock-forming carbonate mineral on Earth (Lippmann, 1973; Reeder, 1990; Smyth and Ahrens, 1997). This can be attributed to the fact that anhydrous calcite is the $CaCO_3$ polymorph thermodynamically most stable at ambient conditions (Plummer and Busenberg, 1982; Radha and Navrotsky, 2013; Casella et al., 2017). Biogenic calcite is represented by, e.g., shells of bivalves (Checa et

al., 2013; Casella et al., 2018c) or brachiopods (Griesshaber et al., 2007a; Pérez-Huerta et al., 2007; Schmahl et al., 2012; Casella et al., 2018a, 2018b).

Table 1.1: Examples of biogenic calcium carbonate which can be found in the corresponding organisms.

Polymorph	Chemical Formula	Organism	Reference
Calcite	$CaCO_3$	Argonauts	Wolfe et al., 2013
			Stevens et al., 2015
		Belemnites	Hoffmann et al., 2016
			Stevens et al., 2017
		Brachiopods	Schmahl et al., 2004
			Griesshaber et al., 2007a
			Casella et al., 2018a, 2018b
		Coccolithophores	Beaufort et al., 2008
			Yin et al., 2018
		Crustaceans	Hild et al., 2008
			Huber et al., 2015
		Foraminifera	de Nooijer et al., 2009
			Branson et al., 2013
			Naganuma et al., 2014
Magnesian calcite	$Ca_{1-x}Mg_xCO_3$	Brachiopods	Cusack et al., 2008a
			Butler et al., 2015
		Echinoderms	McClintock et al., 2011
			Griesshaber et al., 2012
		Red Corals	Vielzeuf et al., 2013
			Floquet et al., 2015
		Red Coralline Algae	Aharon, 1991
			Burdett et al., 2012
Aragonite	$CaCO_3$	Cephalopods	Brand ,1987
			Rexfort and Mutterlose, 2009
		Gastropods	Checa et al., 2016
			Casella et al., 2018c
		Molluscs	Schöne et al., 2005a
			Casella et al., 2017
		Scleractinian Corals	Böhm et al., 2006
			Krief et al., 2010
			Casella et al., 2018c
Vaterite	$CaCO_3$	Bivalves	Cerrato, 2000
			Spann et al., 2010
		Sea Squirts	Novoa et al., 2008
			Pokroy et al., 2015
Amorphous Calcium Carbonate (ACC)	$CaCO_3 \cdot nH_2O$	Crustaceans	Becker et al., 2003
			Sato et al., 2011
		Plants	Levi-Kalisman et al., 2002
			Gal et al., 2012

Introduction

The crystal structure of calcite was determined by Bragg in 1914 (Lippmann, 1973). Calcite is categorised into the trigonal crystal class with the space group $R\bar{3}c$ and unit cell parameters $a = b = 4.990$ Å, $c = 17.00$ Å (Chessin et al., 1965; Rachlin et al., 1992). The pseudohexagonal structure of calcite can be described as alternating layers of Ca^{2+} and CO_3^{2-} groups aligned perpendicular to the c-axis. Between layers, the bonding is interionic, CO_3^{2-}-groups within a layer have identical orientations and are co-planar, whereas CO_3^{2-}-layers show a rotation of 180 ° with respect to the neighbouring layers below and above (Bragg, 1914). Calcite cleaves perfectly at the $\{10\bar{1}4\}$ atomic plane forming rhombohedra (Rachlin et al., 1992; Lüttge and Conrad, 2004). In addition to pure calcite, magnesium-bearing calcites are known to occur as solid solution. This was discovered by X-ray studies on skeletal tissues in the 1950´ies (Chave, 1954; Goldsmith et al., 1955; Lippmann, 1973). Magnesian calcites are not restricted to biogenic carbonates and may appear as purely inorganic counterpart in nature such as dolomitic marbles or calcareous tufa (Lippmann, 1973). A content of up to 4 mol% $MgCO_3$ is referred to as low Mg-calcite which is more stable at Earth´s surface conditions than high-Mg calcite with contents ≥4 mol% $MgCO_3$ (Chave, 1954; Milliman, 1974; Reeder, 1990; Brand, 1994; Stanley et al., 2002; Morse et al., 2006).

Aragonite is the high-pressure polymorph of $CaCO_3$ (Le Chatelier, 1893; Helgeson et al., 1978; Frisia et al., 2002; Radha and Navrotsky, 2013) and thermodynamically less stable compared to calcite (Falini et al., 1996). This mineral is reported to be the most abundant $CaCO_3$ mineral in marine carbonate-rich sediments found at shelf depths below 200 metres (Morse et al., 2006). Furthermore, it constitutes hard tissues of certain organisms, e.g., madreporian corals (Lippmann, 1973) and scleractinian corals (Böhm et al., 2006; Wombacher et al., 2011). Aragonite also forms nacre which can be found in bivalves (Carpenter, 1848; Schmidt, 1924; Wada, 1972; Checa et al., 2006; Griesshaber et al., 2013; Maier et al., 2014; Casella et al., 2018c), gastropods (Wise, 1970; Mutvei, 1978, 1980; Nakahara, 1983, 1991; Checa et al., 2006, 2009; Casella et al., 2018c), and oyster pearls (Hatchett, 1799; Watanabe, 1965; Bevelander and Nakahara, 1969; Saruwatari et al., 2009; Naganuma et al., 2014). Aragonite is assigned to the orthorhombic crystal system with the space group Pmcn and the lattice constants $a = 4.9614$ Å, $b = 7.9671$ Å and $c = 5.7404$ Å (De Villiers, 1971). The crystal structure of aragonite was assessed by Bragg (1924) and Wyckoff (1925) and is described as alternating layers of Ca^{2+} and non-planar CO_3^{2-} groups, which are oriented perpendicularly to the c-axis (Dickens and Bowen, 1971).

Vaterite is reported to be the least stable crystalline calcium carbonate polymorph (Lippmann, 1973; Falini et al., 1996; Radha and Navrotsky, 2013). The mineral is less commonly formed by organisms (Lowenstam, 1981; Lowenstam and Weiner, 1989; Falini et al., 1996; Schenk et al., 2014; Pokroy et al., 2015), but plays an important role as transient phase during the formation of $CaCO_3$ from solutions (Lippmann, 1973;

Lowenstam and Abbott, 1975; Sawada, 1997; Grasby, 2003; Rodriguez-Blanco et al., 2011). This calcium carbonate polymorph can also be found in environments, which exhibit high concentrations of sulphate and salinity (Lippmann, 1973). Rare occurrences of vaterite as biomineral include multicrystalline spicules of solitary tunicates (e.g., *Herdmania momus*) or tablets in lacklaster pearls (Qiao et al., 2007; Schenk et al., 2014; Pokroy et al., 2015). After more than 50 years of research, the crystal structure of vaterite is still highly debated. Until the present day, over a dozen crystal structure models have been suggested (Demichelis et al., 2013), thus, many different space groups with varying lattice parameters can be found in literature (Tang et al., 2009), such as orthorhombic space group *Ama2* and lattice parameters a = 8.4721 Å, b = 7.1575 Å, c = 4.1265 Å (Le Bail et al., 2011) or monoclinic structure C2/c and lattice parameters a = 12.17 Å, b = 7.12 Å, c = 25.32 Å (Mugnaioli et al., 2012). Data derived from neutron powder diffraction suggests the best fit among all proposed structure models, with the space group $P6_522$ and corresponding lattice parameters $a = b$ = 7.1443 Å and c = 25.350 Å (Chakoumakos et al., 2016). The structure of hexagonal vaterite is a disordered structure with an ABC sequence along the c-axis (Wang and Becker, 2009).

The highly unstable amorphous calcium carbonate (ACC) is found in organisms where it is assumed to act as a transient precursor phase (Addadi et al., 2003; Lam et al., 2007; Han and Aizenberg, 2008). Despite the metastable properties of ACC, it is formed by some organisms as skeletal hard tissues (Aizenberg et al., 1996, 2002; Han and Aizenberg, 2008). The amorphous $CaCO_3$ phase was first discovered in chiton teeth (Towe and Lowenstam, 1967; Cartwright et al., 2012) and can also be found in crustaceans (Raz et al., 2002; Sugawara et al., 2006), echinoderms (Beniash et al., 1997; Raz et al. 2003), molluscs (Weiss et al., 2002; Xiang et al., 2014) and even between organic membranes in the innermost part of the secondary layer of the terebratalia brachiopod *Megerlia truncata* (Griesshaber et al., 2009). The stabilisation of ACC is assumed to be controlled by factors such as ionic molecules, membranes, macromolecules, and water (Loste et al., 2003; Xu et al., 2005; Guillemet et al., 2006; Politi et al., 2006; Huang et al., 2007). It has been demonstrated that the usage of citrate, inorganic phosphate, and phosphoenol pyruvate exert control on the stabilisation process of ACC in cuticles of crustaceans (Akiva-Tal et al., 2011; Sato et al., 2011). The detailed mechanism how these organisms produce stable ACC, however, remains unsolved.

Two amorphous calcium carbonate phases differing in their solubility and structure are known to exist, i.e., ACC I and ACC II. ACC I is characterised by higher stability as well as a short-range order which resembles that of calcite, whereas ACC II exhibits a lower stability and a short-range order analogous to vaterite (Gebauer et al., 2008). Following this analogy, Gebauer and co-workers (2010) established the notion of polycrystalline structuring in amorphous calcium carbonate as follows: ACC I is declared as proto-calcite and ACC II as proto-vaterite.

More amorphous and hydrous calcium carbonate forms are known to exist next to the polymorphs, i.e., the monohydrate ($CaCO_3 \cdot H_2O$) and hexahydrate ($CaCO_3 \cdot 6H_2O$) which is also known as ikaite (Brooks et al., 1950; Lippmann, 1973). As these two modifications play no important role in terms of biomineralisation, microstructure and texture evolution under diagenetic conditions, they are not further discussed in the present thesis. A widespread current paradigm on 'non-classical nucleation' of calcite (e.g., Gebauer and Cölfen, 2011) invokes an alledged sequential reaction pathway (Fig. 1.1) originally proposed by Gower (2008). This author proposes that calcite formation in aqueous solutions can be described in relation to activation energy barriers as well as Gibbs free energy by following reaction pathways (Fig. 1.1). Pathway I is represented by a single-step reaction which requires overcoming of a large activation energy barrier, whereas pathway II is characterised by a sequence of intermediate phases with smaller energy barriers (Ostwald´s 'rule of stages').
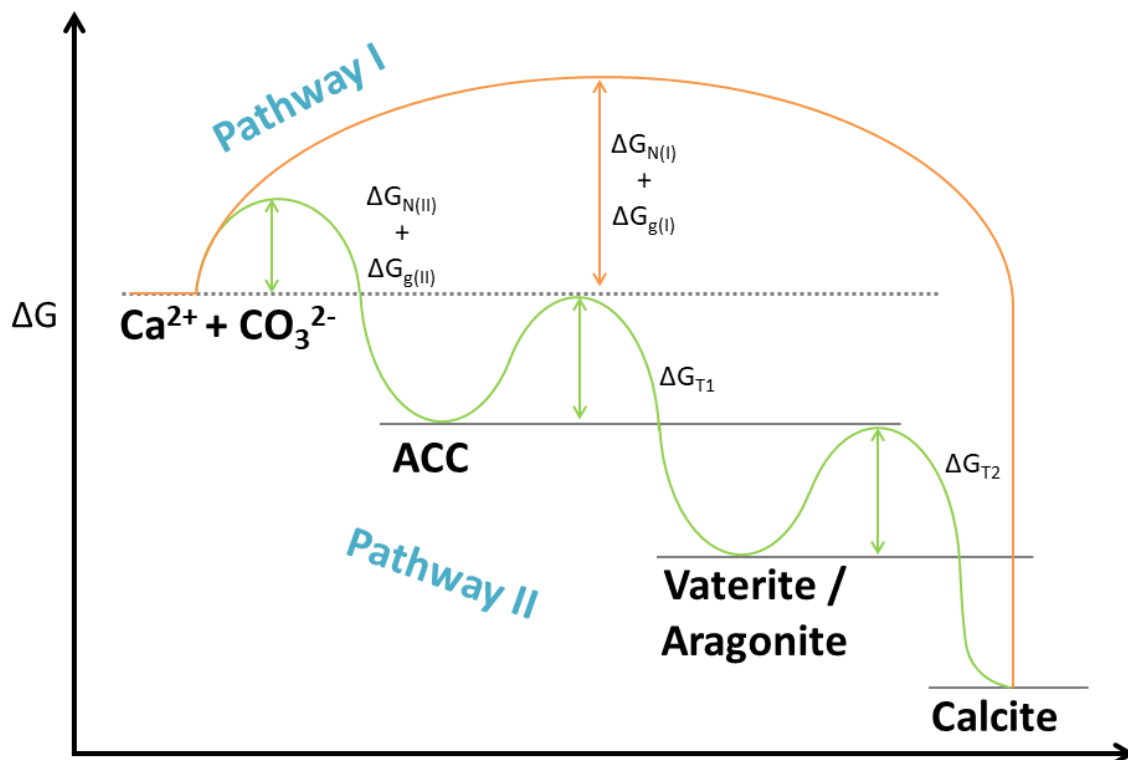
Figure 1.1: Schematic drawing illustrating the reaction pathways of calcite formation with the associated change in Gibbs free energy and energy barriers as proposed by Gower (2008). Pathway I describes classical crystallisation whereas Pathway II implies calcite formation via a multi-step route starting with the formation of ACC, vaterite and/or aragonite with interjacent steps (Ostwald´s 'rule of stages'). $\Delta G_{N(I)}$ is the activation energy barrier associated with nucleation, $\Delta G_{g(I)}$ is the activation free energy associated with growth, and ΔG_T is the activation energy barrier related to phase transformation (modified after Gower, 2008).

The thermodynamic stability of the intermediate phases increases with ever step starting with the formation of unstable ACC, which then changes to more stable vaterite or aragonite and lastly to calcite. However, this scenario completely disregards the mechanism of dissolution-reprecipitation reactions (Putnis, 2009) and supposes direct solid/solid transformations of each metastable solid phase into the next energetically more favourable phase as a step-by-step reaction (more information on dissolution-reprecipitation reaction is given in chapter 1.3).

1.2 Fundamentals of diagenesis

The term diagenesis describes chemical (elemental, isotopic), physical, mineralogical, and structural (macro- to nanoscale) changes in sediments during and after their deposition and subsidence to greater depths. Due to post-depositional processes, the initial sedimentary assemblages as well as their interstitial pore fluids follow reactions leading to geochemical and textural equilibrium with their respective environments (Curtis et al., 1977; Burley et al., 1985; Brand, 1994; Wilson and Pollard, 2002; Worden and Burley, 2009; Press et al., 2011). These reactions lead to changes in mineralogy, microstructure, and texture[1] and determine the final state (i.e., destruction or preservation) of the buried and altered sediment (Wilson and Pollard, 2002). Furthermore, compaction and lithification transforms initially unconsolidated sediments, e.g., quartz, grains or biogenic and inorganic calcium carbonate particles, into solid rocks, e.g., sandstone or limestone, respectively (Tucker, 1990a; Worden and Burley, 2009; Press et al., 2011).

The process of diagenesis persists until the solid rock is either subjected to weathering or metamorphism. Figure 1.2 illustrates the pressure and temperature regime which distinguishes diagenesis from metamorphism. As variations in pressure and temperature play a major role in diagenetic processes, the transition from diagenesis to metamorphism is seamless without a clear division (Sujkowski, 1958; Ali et al., 2010; Press et al., 2011). Due to the catalytic behaviour of fluids originating from either oceanic/marine or continental/meteoric environments or a combination of both realms during diagenesis, concomitant alteration processes proceed at faster rates in terms of geological time scales. Variations in the chemistry of pore waters, temperature, and

---

[1] Note here that the term texture has a different meaning in geological communities compared to its crystallographic meaning, which is mainly utilised in the present dissertation if not declared otherwise. The former definition refers to as the entire appearance of a rock due to the arrangement, shape and size of its constituent mineral grains (Altree-Williams et al., 2015). The latter refers to crystallographic preferred orientation of mineral grains (Wenk and Van Houtte, 2004).
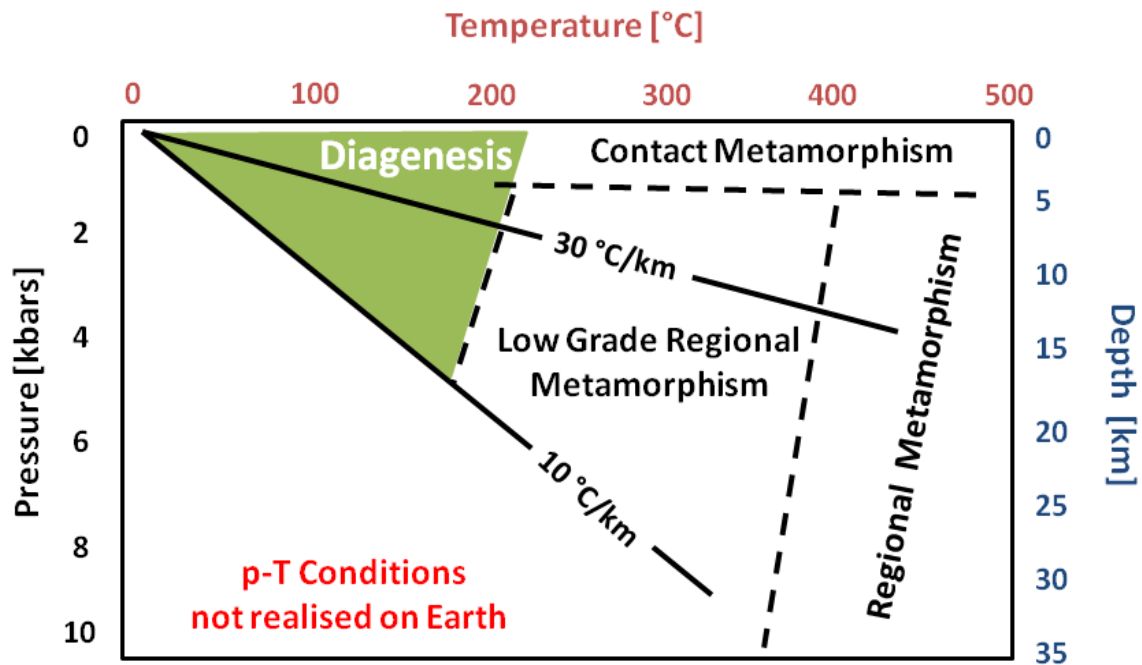
Figure 1.2: Pressure-temperature diagram illustrating the conditions at which diagenesis (green area) and metamorphism take place. The crustal geotherms of 10 °C/km and 30 °C/km are typical for stable cratons and rifted sedimentary basins, respectively. Modified after Worden and Burley (2009).

pressure control reactions during diagenetic processes with decreasing impact and built the driving force for diagenetic alteration or overprint (Takahashi and Broecker, 1977; Emerson et al., 1980; Sayles, 1980; Morse, 2003; Worden and Burley, 2009).

Within the Earth´s crust, the increase in temperature accounts to 30 °C/km in average. Hence, sediments located at 4 km below the surface of the Earth may be exposed to temperatures of around 120 °C. Organic substances like algae and bacteria which are exposed to these environmental conditions are transformed to fossil oil and natural gas (Press et al., 2011).

The transformation of unconsolidated sediments into solid rock is mainly caused by compaction via lithospheric pressure which generally increases by 1 hPa each 4.4 m in depth. However, it can be also induced by the chemical process of cementation. Reprecipitation processes result in a decrease in porosity of the sediment (Bathurst, 1975; Brand and Veizer, 1980; Press et al., 2011).

A broad spectrum of post-depositional modifications in sediments is encompassed by diagenetic processes including:

[1] **Lithification** of the sediment due to the weight of superimposed layers of new, loose sediment.

[2] **Cementation**, a process in which new minerals precipitate inside cavities between the deposited components. Processes (1 – 2) take place during burial.

[3] **Weathering** processes in sub-aerial environments.

[4] **Dissolution** of solid host rock by an aqueous solution penetrating voids and pores, subsequently creating new cavities within the host sediment.

[5] **Recrystallisation** which implies modification in shape and size of crystals as result of thermodynamic equilibration.

[6] **Neomorphism** describes changes which are taking place due to either polymorphic transformations and/or recrystallisation. Processes (4-6) require the presence of an aqueous medium (Schmidt and Mcdonald, 1979; Burley and Kantorowicz, 1986; Worden and Burley, 2009; Boggs, 2010; Press et al., 2011).

[7] **Dolomitisation** describes the replacement reaction of calcite by dolomite due to the exchange of Ca^{2+} by Mg^{2+} ions at Ca^{2+}-sites within the carbonate crystal structure.

[8] Carbonate deposits can undergo either chemical or mechanical **compaction** due to increased overburden pressure, if cementation has not yet taken place.

Diagenetic processes are not only limited to inorganic carbonates but also occur in bioclasts which undergo alteration caused by organisms as long as they reside on the seafloor or even below. Drill holes created by marine organisms at the surface of biogenic carbonates are then filled with fine-grained marine cement after the death of the boring organism. This process is known as **microbial micritisation** (Bathurst, 1975; Machel and Mountjoy, 1986; Taylor and Sibley, 1986; Tucker, 1990a; Brand, 1994; Morse, 2003; MacDonald et al., 2015).

1.2.1 Diagenetic regimes

Diagenetic processes are known to occur in three major environments, so called diagenetic regimes (see Figure 1.3):

[1] The **meteoric regime** includes all environments above and below the ground-water table, and underlying mixed freshwater-seawater environments. Meteoric diagenesis can have an impact on sediments directly after their deposition. Alteration processes arise from microbial activities as well as water-mineral interactions. The transition to the burial regime is smooth.

[2] The **burial regime** includes all environments, in which voids are filled with fluids initially originating from evaporative, fresh water, or marine sources. These pore waters were modified due to the interaction with other diagenetic fluids and minerals under the elevated pressure and temperature conditions of the burial realm. All processes of burial diagenesis are generally a result of water-mineral interactions and overburden compaction.

[3] The diagenetic **synsedimentary marine realm** occurs in environments which include the seafloor and sediments submerged in seawater. Alteration processes in the marine regime are driven by chemical changes caused by mineral-seawater

interactions, as well as microbial activity (Tucker, 1990a; Moore, 1997; James and Jones, 2016).

As the present study mainly focuses on (natural and mimicked) burial and meteoric diagenesis on (fossil) marine biogenic carbonates, details on the synsedimentary marine regime are not further discussed here.
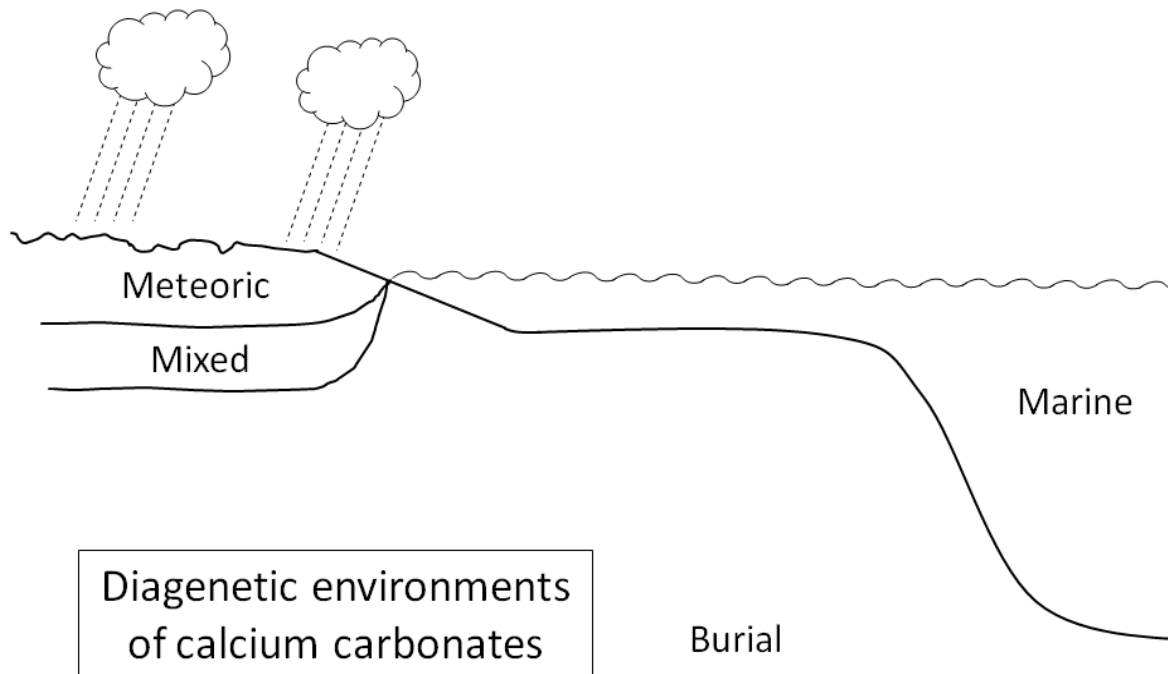
Figure 1.3: Schematic drawing illustrating the spatial relationships of carbonate diagenetic realms (after James and Jones, 2016).

The burial regime

The regime of burial diagenesis was defined by Schmidt and Mcdonald in 1979 (see Worden and Burley, 2009) and encloses all biological, chemical, and physical processes which affect a sediment during burial. By these processes, the influence of the depositional setting on the sediment is gradually removed. Burial diagenesis endures either until the advent of metamorphic processes or structural uplift, and thus, exposure to meteoric fluids.

In the burial realm, nearly all ancient rocks are covered by an accumulation of geologically younger sediments and, thus, undergo compaction due to overburden pressure. The upper several hundred metres of the burial environment are characterised by physical compaction by which unconsolidated sediments are subjected to squeezing processes. This causes dewatering, reduction of initial porosity by 50-60 %, fracturing of

grains, as well as closer packing of sediment grains with concomitant reduction in layer thickness by ≤50 %. These values apply for calcareous sediments undergoing physical compaction at approx. 100 m in depth. In contrast, chemical compaction typically occurs at depths in the range of several 100 m to km and involves dissolution at grain boundaries and accompanying precipitation in open pores (e.g., as cements). Furthermore, diagenetic dissolution of the host rock by aqueous pore fluids induces the creation of cavities or new spaces within the host sediment. The long-term trend of alteration processes in the burial realm is the reduction of permeability and porosity at increasing pressure and temperature conditions over the timeframe of millions to hundreds of millions of years (Tucker, 1990a; James and Jones, 2016).

Predominant features of burial diagenesis are dissolution margins, precipitated cements, as well as stylolites (Schmidt and Mcdonald, 1979; Burley and Kantorowicz, 1986; Worden and Burley, 2009; James and Jones, 2016).

Burial diagenesis can be described using two scenarios occurring either in basins or domains of shelf-platforms.

[1] In basins, sediments with marine water-filled voids are directly merged into the burial environment in which reactions (e.g., with burial waters, organic material) result in the modification of the original marine pore fluids. Physical compaction and subsequent compaction by pressure solution follow after the initial marine fluids within pores were removed. Cementation in basinal burial domains commonly begins at depths varying between 200-250 m and is dominant at depths below 1 km.

[2] Neritic deposits of shelf-platform domains are either subjected to diagenetic processes of the synsedimentary marine realm or meteoric realm prior to passing into burial diagenesis. Thus, these sediments show a substantial alteration, as well as large chemical variation which have taken place prior to burial overprint. Pores commonly contain meteoric ground water which may be replaced by fluids with differing chemistry during burial. These pore fluids typically undergo an evolution from freshwater-marine origin to primarily saline or hypersaline brines. Therefore, features caused by burial processes are mostly defined by their previous history of diagenetic events (James and Jones, 2016).

Burial temperatures range from 40 to 200 °C and vary commonly between 50 and 150 °C, whereas pressures can reach up to 200,000 kPa. However, the processes of burial diagenesis are not limited in time as these may persist for a few thousands up to several millions of years (James and Jones, 2016).

Burial diagenesis is controlled by intrinsic and extrinsic factors. The former include

[1] grain sizes (faster compaction in the case of small particle sizes)

[2] previous diagenetic processes (dolomitisation, early precipitated cements prevent easy compaction)

[3] permeability

[4] porosity (larger volumes and flow rates of transmitted fluids present in coarse-grained sediments lead to faster diagenetic overprint compared to fine-grained sediments)

[5] sediment purity (organic matter and clay minerals present in the sediment are more prone to compaction events).

The most significant extrinsic factors of the burial realm are

[1] burial time (longer exposure to burial diagenesis will cause more pervasive diagenetic overprint)

[2] chemistry of pore waters (chemistry of pore fluids determines the types of minerals which can be precipitated during burial)

[3] pressure (hydrostatic, lithostatic, and tectonic-directed pressure)

[4] temperature (common temperature gradients: 15-35 °C/km)

[5] calcite precipitation

[6] dehydration of hydrous minerals (e.g., gypsum)

[7] change of sedimentary unstable to stable organic matter

[8] release of organic acids at elevating temperatures (Tucker, 1990a; Brand, 1994; Haszeldine et al., 2000; James and Jones, 2016).

During physical compaction shells of (marine) organisms are rotated to a horizontal alignment, muddy carbonates expose fracturing features in early lithified layers, whereas carbonates comprised of grains experience mainly plastic deformation and fracturing of grains (Tucker, 1990a; James and Jones, 2016). The latter commonly occurs at depths of several hundred of metres (e.g., in cores of shallow water limestones taken from atolls in the Pacific from the Quaternary-Tertiary; see Schlanger, 1964; Saller, 1984; Tucker and Wright, 1990).

In contrast to physical compaction, chemical compaction commonly occurs at several hundred meters of burial depth when physical compaction has already taken place. This process may result in further reduction of layer thicknesses by 20-35 %. Stress generated by tectonics or load is concentrated at contact points between grains, where dissolution processes may arise of increased solubilities of the stressed grain. Thus, an extremely thin solution film with a chemical potential gradient is created due to pressure-induced solubility. Consequently, ions are transported to areas with lower stresses via diffusion or follow the chemical potential gradient by solution transfer, and finally precipitate as calcitic cement at sites with lower solubility as well as stress. These ions can also be carried to more distant sites via pore fluid transport (Tucker, 1990a; James and Jones, 2016).

The meteoric regime

Diagenetic processes of the meteoric realm of thick sedimentary deposits which were formed by layer by layer accumulations on the seafloor occur at continental areas, along shelf margins, upon island-developing platforms, as well as on atolls and isolated platforms with sediments rising above the seawater level (Tucker, 1990a; James and Jones, 2016). Due to time-dependent vicissitudes of seawater level fluctuations or tectonic processes, carbonate sediments above and beneath the Earth´s surface are periodically exposed to meteoric fluids. This process leads to a number of pervasive changes (e.g., in chemical and mineralogical composition, fabric and texture) in the deposits. Furthermore, carbonate dissolution by weakly acidic rainwater, and precipitation of other carbonates (e.g., ankerite, siderite) under lacustrine conditions are common in surface meteoric environments (Brand, 1994; James and Jones, 2016).

Alteration of magnesian calcite during *meteoric diagenesis* commonly occurs on the micro- or nanoscale via dissolution-reprecipitation processes and results in the formation of diagenetic low-Mg calcite. It is known that initially calcitic components do not undergo a crystallographic change, thus, the initial microtexture remains preserved in the newly formed $CaCO_3$ mineral. Nevertheless, the application of SEM imaging reveals diagenetic changes (e.g., increased grain sizes, porosity; see McAllister and Brand, 1989; Reeder, 1990; Brand, 1994; James and Jones, 2016). Meteoric alteration of metastable carbonates (e.g., aragonite) can take place in two ways: (1) dissolution of entire grains, components, cements and even fossils occurs on the macroscale, and results in the creation of pores. (2) Aragonitic grains are altered by exposition to nm to µm thick fluid fronts. This results in dissolution of aragonite and precipitation of (low-Mg) calcite and is known as *mineral-driven diagenesis* which results in dissolution, cementation, and formation of porosity of $CaCO_3$ sediments. Due to recrystallisation of metastable carbonates, calcite crystals which crosscut the initial fabric of the sediment are formed. However, relicts of insoluble matter (e.g., organic matter) can be encased in the newly formed calcite. As aragonitic particles are dissolved and reprecipitated as low-Mg calcites, they undergo crystallographic changes (Reeder, 1990; James and Jones, 2016).

Further modifications of diagenetically overprinted sediment can be additionally caused by microbial activity. However, once the alteration of carbonate sediments or solid rocks to diagenetic low-Mg calcite has occurred, these stay mainly unchanged during the upcoming geological time (James and Jones, 2016).

In contrast to *mineral-driven diagenesis*, *water-controlled diagenesis* occurs simultaneously in meteoric realms and is caused by changes in water composition (e.g., increasing and decreasing contents of carbon dioxide, ion concentrations, water temperature).
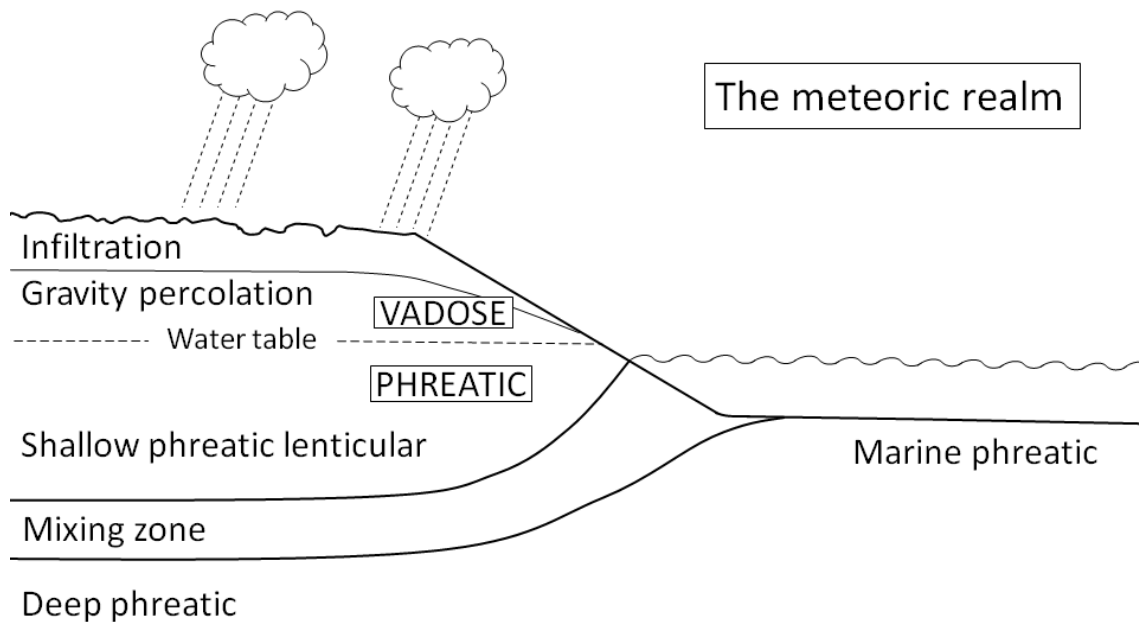
Figure 1.4: Schematic drawing illustrating major zones found in the environments of meteoric diagenesis (after James und Jones, 2016).

In general, meteoric diagenesis leads to formation of calcareous soils, enormous subsurface karsts, calcareous cave deposits (i.e., speleothems, spelean carbonates; see White, 1967; Ford, 1988; James and Choquette, 1988; Tucker, 1990a; Moore, 1997; Taborosi and Stafford, 2003; James and Jones, 2016). The replacement reaction of aragonitic speleotherms by calcite is reported to take place <1000 yrs and, thus, is more rapid than calculated for diagenesis occurring in the vadose zone of the meteoric realm (Frisia et al., 2002).

The meteoric regime of the *shallow subsurface environment* is subdivided into the two zones, above and below the water table, i.e., *vadose zone and phreatic zone*, respectively (see Fig. 1.4). These zones are further divided into sub-zones (Brand, 1994; James and Jones, 2016).

In the *vadose zone*, the subsurface is either directly or indirectly permeated (e.g., via bare rock, by percolation through calcrete or soil zones) by meteoric fluids (i.e., melt water, rainwater, runoff) and may be a zone dissolution-reprecipitation reactions with concomitant geopodal cementation and sedimentation processes. The *zone of infiltration* is characterised by complex interactions between water, carbonates, as well as microbes (Tucker, 1990a; Brand, 1994; James and Jones, 2016), whereas the *zone of gravity percolation* is distinguished by voids which can be occupied by different media (e.g., air, water, a mixture of air and water, organically-produced gases; see Moore, 1997; James and Jones, 2016). In contrast, the *zone of vadose flow* describes rapid downward movements or sinking of water directly to the water table via large fissures, joints or sinkholes in the soil. Cementation processes of the vadose zone occur mainly via

evaporation of seawater, and can be also caused by microbial activity (e.g., at beaches, tidal flats; Tucker, 1990a; James and Jones, 2016).

In the *phreatic zone*, water movement occurs (sub-) horizontally either towards the base level of the local water (e.g., lake, river, spring) or the ocean. Voids which can be found in the *phreatic zone* are water-filled and exhibit active water flow. The *phreatic* marine realm can be subdivided into three zones: the *lenticular zone, transition/mixing zone, and deep phreatic zone* (Tucker, 1990a; Brand, 1994; James and Jones, 2016).

The *lenticular zone* is located directly beneath the water table and constitutes a common scenario of regions near coastlines. The lenticular lense-like geometry of freshwater, which fills the interparticle voids, is eponymous for this meteoric subzone and 'floats' on seawater due to its lower density. A special case occurs on islands or isolated cays where meteoric fluids flow on top of marine waters with higher density. In these unconfined aquifers, the depth of the *lenticular zone* extends below the sea level by approx. 40 times of the fresh water level which is above sea level. This phenomenon is known as the Ghyben-Herzberg relationship (Verruijt, 1968; James and Jones, 2016). Fluctuations of the water table level leading to its (slight) increase have a pervasive impact on diagenesis of sediments or rocks as elevated water table levels can result in a deeper penetration of meteoric fluids (Davis and DeWiest, 1966; Todd, 1980; Tucker, 1990a; James and Jones, 2016).

The *mixing or transition zone* can reach greater thicknesses compared to the *lenticular zone*, especially in locations which are comprised of permeable carbonates (e.g., oceanic islands). This zone is characterised by diffusive and physical mixing which is most effective in sediment/rock layers with high permeability. Thus, greater thicknesses of the *mixing zone* can be achieved (Back et al., 1979, 1984; Tucker, 1990a; James and Jones, 2016). Characteristic diagenetic products of the mixing zone of meteoric and marine waters are, e.g., dolomite and other carbonate species (Hanshaw et al., 1971; Brand, 1994).

In the *deep phreatic zone*, saline waters typically exhibit slow movements or can be almost stagnant. In general, fabrics generated by diagenetic processes occurring in the phreatic and vadose zones differ from each other, thus, they are distinguishable throughout geological records (James and Jones, 2016).

1.2.2 Diagenesis of geologic and biogenic carbonates

Diagenesis of geologic carbonates

Carbonate diagenesis encompasses diverse reactions, e.g., dissolution, recrystallisation processes, as well as replacement reactions. Often the presence of aqueous solutions is crucial (e.g., Hesse, 1987; McAllister and Brand, 1989; Morse and Mackenzie, 1990; Brand, 1994; Morse et al., 2007).

Since the 1950′ies diagenesis of carbonates was defined not only as variance in chemical distributions (e.g., in minor and trace elements) but also as mineralogical and textural changes of sediment accumulations. These changes are assumed to occur at conditions of the Earth′s surface. Brand and Veizer (1980) tried to find a correlation between variations in chemical composition of sediments and the degree of diagenetic overprint.

The wet dissolution and reprecipitation reaction occurring during diagenesis leads to a substitution of Ca^{2+} present in the $CaCO_3$ crystal lattice by cations such as Fe^{2+}, Mg^{2+}, Mn^{2+}, Na^+, Pb^{2+}, Sr^{2+} and Zn^{2+} in varying degrees. Due to the widely deviant partition coefficients of Mn and Sr (ions/isotopes), their ability to act as substituent for Ca in the $CaCO_3$ lattice, as well as their enormous concentration differences in marine and meteoric fluids, these elements were assumed to be very useful as diagenetic indicators (Bodine et al., 1965; Kinsman, 1969; Peterman et al., 1970; Turekian, 1972; Brand and Veizer, 1980; Burke et al., 1982; Brand, 1994). Carbonate phases which initially precipitated from seawater tend to incorporate stable isotopes and trace elements from ambient seawater. Carbonates partially or even fully dissolve upon exposure to meteoric fluids causing mixing and exchanging processes of trace elements as well as isotopes with those present in interstitial fluids resulting in reprecipitation. Consequently, the elemental and isotopic composition of diagenetic low-Mg calcite shows a shift in the direction of equilibrium with intermediate meteoric fluids when compared to pristine calcite (Brand and Veizer, 1980; Morse, 2003). Due to the fact that interstitial meteoric waters exhibit decreased values for Mg^{2+}, Na^+, and Sr^{2+} and increased values for Fe^{2+}, Mn^{2+}, and Zn^{2+} compared to marine waters (Turekian, 1972), reprecipitation of diagenetic low-Mg calcite results in depletion of Na^+, and Sr^{2+}, as well as enrichment in Fe^{2+}, Mn^{2+}, and Zn^{2+} (Brand and Veizer, 1980).

Magnesian calcites appear to be stable in the original depositional marine realm and exhibit a higher resistance to alteration, thus, keeping their initial chemical imprint (Berner, 1966; Land, 1967; Schroeder, 1969; Winland, 1969; Bathurst, 1975; Möller and Kubanek, 1976; Brand and Veizer, 1980; Morse, 2003). Aragonite and high-Mg calcite, however, are metastable, thus, rapidly undergo alteration processes into

thermodynamically more stable low-Mg calcite during meteoric diagenesis (Land, 1967; Schroeder, 1969; Bathurst, 1975; Brand and Veizer, 1980). It is assumed that alteration of marine carbonates occurs in burial and continental phreatic realms (Taylor and Sibley, 1986). Surface-adsorbed inhibitors (e.g., Mg^{2+}, PO_4^{3-}) may affect the rate of diagenetic alteration by forming complexes with dissolved ions, and occupation of high-energy lattice sites on the mineral grain surface which are preferred for dissolution reactions (Sjöberg, 1978; Lahann, 1978; Reddy and Wang, 1980; Morse, 1983; Brand, 1994).

The majority of ancient as well as modern marine carbonate sediments initially are a combination of carbonate polymorphs (i.e., aragonite, low-Mg and high-Mg calcites). As aragonite and high-Mg calcite are thermodynamically metastable, they are commonly replaced by calcite during the history of limestones, whereas thermodynamically more stable low-Mg calcite directly precipitates from meteoric fluids. Apart from previous dolomitisation processes, ancient limestones are completely comprised of low-Mg calcite (Tucker, 1990a; Flügel, 2004). As carbonate phases found in ancient sedimentary rocks are dominated by calcite and dolomite, it can be assumed that these sedimentary carbonates originating from shallow water were subjected to major diagenetically-induced changes (Morse, 2003). Numerous studies on limestone and carbonate sediment diagenesis deal with the identification of diagenetic processes in rock samples (Alexandersson, 1978; Morse, 2003; Munnecke et al., 2008; Armenteros, 2010; Ali and Mohamed, 2013). However, the diagenetic history of the investigated carbonate sediments usually remains unsolved (Munnecke et al., 2008).

Thermodynamically unstable $CaCO_3$ polymorphs (i.e., aragonite, magnesian calcites) of deposited carbonate sediments undergo relatively rapid reactions to either form diagenetic (low-Mg) calcite or dolomite when they are in contact with fresh water (Brand, 1994; James and Jones, 2016). However, the formation process of dolomite is still under debate as it has not yet successfully been grown at ambient conditions (e.g., Lippmann, 1973). During meteoric diagenesis, metastable carbonates are altered to calcite by the following pathway (James and Jones, 2016):

[1] Precipitation of small calcite crystals starts on grain surfaces with the beginning of fresh water percolation.

[2] Microscale dissolution-reprecipitation processes of magnesian calcite grains result in alteration and, thus, in the replacement by diagenetic low-Mg calcite cement.

[3] When the majority of grains are completely surrounded by calcitic cement, aragonitic particles most commonly start to dissolve, thus, porosity is created within the sediment. Furthermore, aragonitic particles become subject to calcification processes which may result in the preservation of initial grains.

[4] Large amounts of Ca^{2+} and CO_3^{2-} ions are released into the groundwater due to aragonite dissolution. These may reprecipitate as diagenetic low-Mg calcite cement inside moulds which were formed by the dissolution of aragonitic minerals.

[5] Diagenetic low-Mg calcite cements transform into solid calcitic limestones.

[6] The original interparticle porosity is transformed into secondary interparticle mould porosity.

In the meteoric realm, carbonate dissolution events and subsequent transport of resultant ions out of the system (e.g., transport to the ground water) are described by following equation:

$$CaCO_3 + H_2O + CO_2 \leftrightarrow Ca^{2+} + 2\ HCO_3^- \qquad \text{(eq. 1)}$$

Diagenesis of biogenic carbonates

Numerous studies aiming for reconstructions of environmental changes and climate dynamics of the past are mainly founded on chemical and isotopic signatures in biogenic marine carbonate archives comprised of benthic and nektonic organisms (e.g., bivalves, brachiopods, and cephalopods; Grossman et al., 1993; Khim et al., 2000a; Korte et al., 2005).

Numerous studies have shown that burial environments can be identified by using compositions of rare earth elements in fossil bones (Williams, 1988; Trueman, 1999, 2013; Kemp and Trueman, 2003; Metzger et al., 2004). Diagenetic overprint of fossil marine carbonates (including endo- and exoskeletons of benthic, nektonic, as well as planktonic living organisms), however, is the most substantial obstacle for the comprehension of palaeoclimate dynamics as all chemical and isotopic signatures may have been altered during diagenesis (Grossman et al., 1993; Richardson, 2001; Korte et al., 2005; Immenhauser et al., 2015; Casella et al., 2017). Therefore, research on carbonate diagenesis has been conducted with a broad set of imaging and analytical tools (e.g., SEM, CL, EBSD, elemental and isotope geochemistry; see Steuber, 1999; Brand, 2004; Brand et al., 2011; Ullmann and Korte, 2015; Casella et al., 2018a, 2018b) for more than a century, however, most of the controlling factors and processes are conceived in a qualitative manner (Brand and Veizer, 1980, 1981; Swart, 2015). As determination of the degree of diagenetic overprint of fossil biogenic carbonates still remains unsolved, this dissertation focuses on the qualitative and partially quantitative assessment of the degree of natural and simulated diagenetic overprint of marine biocarbonates using a multi-analytical combination of imaging and measurement tools.

Systems of living matter are not in thermodynamic equilibrium and induce local chemical environments, in which physiologic processes (e.g., biomineralisation) are taking place. Concholin which is comprised of several polysaccharides and proteins is a common organic component enclosing individual crystallites in calcareous hard tissues (e.g., shells, skeletons) and may lead to suppression of early diagenetic alteration during

degradation and disarticulation after demise of the animal (Grégoire et al., 1955; Brand, 1994). During diagenesis, carbonate hard tissues undergo alteration processes due to equilibration with the surrounding environment as the organism´s disequilibrium is no longer sustained after its death. Thus, metastable biogenic carbonates (e.g., aragonite, high-Mg calcite) underlie chemical driving forces which result in the replacement by thermodynamically more stable (low-Mg) calcite (Morse et al., 2007; Casella et al., 2017; 2018c) via dissolution-reprecipitation processes of (fossil) carbonate material (e.g., bivalves (Casella et al., 2017; Ritter et al., 2017), brachiopods (Cusack and Williams, 2001; Pérez-Huerta et al., 2007; Casella et al., 2018a, 2018b), and corals (McGregor and Gagan, 2003; Sayani et al., 2011; Gothmann et al., 2015; Casella et al., 2018c)) in diagenetic environments. Diagenetically altered hard tissues commonly show changes in microstructures and may unveil new information about the site of deposition (Rollins et al., 1971; Brand, 1994; Trueman, 2013; Casella et al., 2017, 2018a, 2018b, 2018c).

Due to increasing degree of diagenetic alteration, biogenic structures gradually disappear and are replaced by inorganic features. Hence, recrystallisation of the initial organism-specific skeleton microstructure of fossil marine invertebrates and their mineral disorder are unambiguous indicators for the extent of diagenetic overprint (Trueman, 2013; Casella et al., 2017). The rate of diagenetic alteration may be influenced by grain morphology and overall grain size of biogenic carbonates (Anderson et al., 1973; Walter and Morse, 1984a; Brand, 1994). In addition to the chemistry of the diagenetic fluid, and thermodynamic stability of the carbonate species, water/rock ratios are assumed to exert the ultimate control on the alteration type and degree of carbonate hard tissues during diagenesis. Alteration processes involving high water/rock ratios result in the destruction of the original microstructure, and development of intraskeletal and moldic porosity which may be filled with fine- to coarse-grained calcite crystals. Geochemical imprint of diagenetic carbonate and its degree of alteration is mainly controlled by that of the bulk aquifer fluids (Pingitore, 1976; Brand and Veizer, 1980; Brand, 1989a, 1994). A prominent characteristic of intermediate water/rock ratio alterations is the formation of a chalky appearance of the fossil material. This may be associated with early degradation of organic matters coating, e.g., individual crystallites, and entire carbonate shells/skeletons. Intermediate water/rock ratios commonly result in the development of microscopic intraskeletal porosity during mineral replacement reactions (e.g., in corals and molluscs; see Pingitore, 1976; Brand, 1989a, 1994). Geochemical signatures and microstructural features of the depositional environment in biogenic carbonates are preserved in their diagenetic product during alteration processes occurring in low water/rock systems, and commonly result in the development of ghost structures. The controlling factor of dissolution of initial carbonate is the removal rate of ions from solution due to the precipitation of the diagenetic calcareous product (Carlson, 1983; Brand, 1994). Trace elements and concomitant redistribution patterns support the

identification of pathways and the degree of diagenetic processes of biogenic carbonates. Thus, elemental concentrations in seawater and diagenetic fluids (e.g., meteoric water) result in the depletion and enrichment of specific elements (e.g., heavy metals, strontium, magnesium) in the solid phase during diagenetic alteration (Veizer, 1983; Brand and Morrison, 1987; Mucci and Morse, 1990; Brand, 1994; Morse, 2003).

Perfect preservation of fossil hard tissues during diagenetic processes implies not only preservation of their macro- and microstructures but also of the initial geochemistry and mineralogy of their hard tissues. Fossil hard tissues may most likely remain preserved when a surrounding matrix of, e.g., amber, chert, fine-grained sediments, effectively reduces biological interaction, and seals out air or diagenetic fluids. The protection from the catalytic effect of diagenetic fluids, which is further governed by dissolved complexes, compounds, and ions, results in a decelerated replacement reaction from meta-stable aragonite or magnesian calcites to more stable calcite (Morse et al., 1980; Plummer and Busenberg, 1982; Sjöberg and Rickard, 1985; Mucci et al., 1989; Brand, 1994; McCoy et al., 2018). Due to the thermodynamic stability of low-Mg calcite, brachiopod shells of the same rock unit may exhibit a good preservation in their pristine state compared to molluscs which may be only retained as moulds or filled with calcitic spar. Fossils with initially high-Mg calcite hard tissues, however, exhibit normally well-preserved macrostructures, whereas more delicate microstructures and mineralogy are replaced by low-Mg calcite. Simultaneously, low-Mg calcite shells are still well-preserved within the same rock unit after diagenetic alteration. Only a few initially high-Mg calcite hard tissues with $MgCO_3$ contents >7 mol% are preserved from before the Mesozoic. Initially aragonitic hard tissues are more prone to diagenetic alteration, thus, biogenic aragonite is reported to be preserved as ghost microstructures and relicts in Devonian/Silurian horizons (Stehli, 1956; Grandjean et al., 1964; Rollins et al., 1971; Richter, 1974; McAllister and Brand, 1989; Brand, 1981, 1994).

A number of case studies showed that the degree of diagenetic overprint of the surrounding sediment has an influence on the preservation state of fossils under the given environmental conditions.

[1] Marine successions of the Castell'Arquato Formation (northern Italy; assumed thermal heat flow <50 °C) from the Pleistocene period are highly fossilferous mudstones, sandstones and siltstones containing barnacles, bivalves, brachiopods, bryozoans, corals, echinoids, gastropods, scaphopods, as well as serpulis. Aragonitic and calcitic bivalve shells present in these marine successions show an exceptional good preservation state in which the original fabric and mineralogy have survived. (Pelosio and Raffi, 1977; Dominici, 2001, 2004; Crippa, 2013; Crippa and Raineri, 2015).

[2] Thermal modelling studies of the Pennine Basin in Central England (U.K.), which has one of the most extensively studied burial and thermal histories in Great Britain

(Ewbank et al., 1995), revealed maturation temperatures in the range of 100-120 °C (Andrews, 2013). Brachiopods, corals, echinoderms, and molluscs are present in the mud mound facies in the Eyam Limestone Formation which is comprised of grey limestones (Gutteridge, 1995). Changes in the preservation state of the fossil brachiopod *Gigantoproductus* sp., which is commonly found in the shell beds of the Eyam Limestone as well as Monsal Dale Limestone Formations, exhibited slight diagenetic overprint as preserved pristine calcite can be observed next to altered calcite in the identical shell (Angiolini et al., 2012).

[3] Fossil material (i.e., brachiopods, corals, echinoderms, foraminifera and molluscs; Angiolini, 1995, 1996, 2001; Gaetani et al., 1995, 2004) trapped inside Carboniferous to Permian marine successions of the Karakoram Basin, northern Pakistan, were exposed to estimated high temperatures of 200-350 °C based on CAI of conodonts[2], cleavage, history of deformation, organic maturity, as well as mineral paragenesis of the Karakoram Basin (Gaetani et al. 1995, 2013; Gaetani, 1997; Zanchi and Gaetani, 2011). According to Angiolini and co-workers (1999) as well as Gaetani and co-workers (2004), brachiopod specimens of the species *Afghanospirifer* sp. and *Gypospirifer* sp. which are both present in the Lupsuk and Ribat Formation of the Ribat and/or Karambar Lake section, northern Pakistan, are poorly preserved.

Diagenesis may also occur in modern marine environments where diagenetic and depositional processes take place simultaneously to sedimentary processes, such as in reefs which are subjected to: growth of the coral reef, cementation, erosion by waves, and biogenic alteration by activities of boring organisms (e.g., clionid sponges, lithophagid bivalves and microbes; see Bromley, 1978; Tucker, 1990a; Morse, 2003). These processes result in the degradation of the coral framework. Furthermore, diagenesis in corals is also expressed by internal sedimentation of fine-grained detritus found in cavities in which marine organisms (e.g., foraminifera, serpulids) exist and contribute to the sediment. However, cementation plays the major role in terms of reef diagenesis as precipitated cements are characteristic for the majority of recent and many ancient coral reefs. As marine cements appear in great extent in a number of ancient reefs, the term 'cement-stone' was introduced. These cemented reefs show a frequent occurrence in modern coral reefs including those located in Belize (James et al., 1976; James and Ginsburg, 1979), Bermuda (Ginsburg et al., 1971; Schroeder, 1972), Great

---

[2] Conodont Colour Alteration Index (CAI) is utilised in order to estimate thermal maturity of carbonate rocks derived from the colour of minute apatitic remains (microfossils) of the feeding apparatus of the extinct animal class of Conodonta (commonly present in oceans of the Cambrian to Triassic). Increasing temperatures lead to a successive carbonisation process of the elements of the conodonts. Thus, unaltered conodonts can be recognised by a pale yellowish colour and a smooth surface exhibiting a silky brightness. Increasing temperatures result in a colour sequence ranging from light brown via dark brown up to a black colour (Voldman et al., 2010).

Barrier Reef, Australia (Marshall and Davies, 1981; Marshall, 1983, 1986), French Polynesia (Aissaoui and Purser, 1985; Aissaoui et al., 1986) and Jamaica (Macintyre and Mountjoy, 1968; Land and Goreau, 1970; Tucker, 1990a).

Despite numerous morphologies found in cements of modern reefs, they can be reduced to the two carbonate mineral phases, aragonite and high-Mg calcite. The former occurs as acicular crystals in isopachous fringes, in a mesh of needles, as well as micrite, whereas high-Mg calcitic cement can be observed as equant crystals, micrite, as well as acicular isopachous fringes. The latter are comprised of fibrous calcite and strikingly occur in ancient reef cements from the Mid-Palaeozoic but especially in those dated back to the Devonian. Furthermore, cements are also very common in reefs from the Permian and Triassic, e.g., Permian Basins found in the U.S. States New Mexico and Texas (Tucker, 1990a). Numerous reefs from the Devonian (e.g., Canning Basin, western Australia (Kerans et al., 1986), Golden spike, Leduc reef, western Canada (Walls, 1983; Walls and Burrowes, 1985; Tucker, 1990a) exhibit zones of marine cements inside their frameworks.

During diagenesis original biogenic carbonates may not only be replaced by a diagenetic carbonate product but may also underlie replacement diagenesis in which entire substitution of initial and diagenetic carbonate by another mineral takes place. In some instances, macro- and microstructural features may be preserved in the replacing mineral by mimicking the initial features. Major processes of replacement diagenesis are dolomitisation, phosphorisation, pyritisation, and silicification.

Dolomitisation replaces biogenic carbonates (e.g., in crinoids) of all ages by dolomite ($CaMg(CO_3)_2$) by the equation

$$2\ CaCO_3 + Mg^{2+} \rightarrow CaMg(CO_3)_2 + Ca^{2+} \qquad\qquad (eq.\ 2)$$

and commonly results in poor preservation of initial microstructures, whereas the morphology of the exoskeleton/shell may be well-retained. Depending on the availability of Fe in the source environment, variable Fe-amounts may be incorporated into the dolomite lattice, thus, forming a solid solution between dolomite and its isotype ankerite ($CaFe(CO_3)_2$; see Reeder, 1990; Brand, 1994).

Phosphorisation is known to be found in diagenetically altered molluscs from the Cambrian and describes a direct massive and disruptive replacement reaction of biogenic carbonates by an undefined phosphate mineral species destroying the original microstructure of the organism (almost) entirely. However, in some instances surficial and internal microstructures have been retained in altered mollusc shells. The dissolution of biogenic carbonate and replacement by a phosphate mineral is assumed to proceed simultaneously through a thin-film front which is supersaturated with

phosphate and not in equilibrium with the bulk aquifer fluids (Runnegar, 1985; Brand, 1994).

During pyritisation biogenic carbonates (e.g., in crinoids) are rapidly replaced by pyrite (FeS_2) and macrostructures are commonly well-preserved, whereas shell/skeletal microstructures are partially to entirely disrupted. The pyritisation process mainly takes place soon after the animal´s demise within the shallow burial environment of the sediment column. Commonly, Fe and S are contributed by the local environment prior to pyrite formation. Carbonate dissolution and pyrite formation proceed simultaneously in a thin-film front (Berner, 1964; Howarth, 1979; Raiswell and Berner, 1985; Brand and Morrison, 1987; Brand, 1994).

Silification (chertification) describes a common diagenetic replacement process of biogenic carbonate of all ages by silica (SiO_2) and was observed, e.g., in belemnites. Macrostructures are preserved during silification, whereas microstructural features are trapped in carbonate hard tissues. The silification process is assumed to occur at any time during diagenesis of biogenic carbonates; however, evidence has shown that this process takes place prior to substantial cementation. It still remains unclear, whether silification occurs before, during or after aragonite/high-Mg calcite replacement by calcite. Silification of carbonate hard tissues takes place via a thin-film front in bulk pore fluids (Choquette, 1955; Jacka, 1974; Richter, 1974; Hesse, 1987, 1990; Maliva and Siever, 1988a; Brand, 1994).

1.3   Fundamentals of dissolution-reprecipitation reactions

Dissolution-reprecipitation reactions describe processes which result from solid-fluid-interactions occurring at rock or mineral grain surfaces. First direct evidence for dissolution-reprecipitation processes was observed in AFM in-situ measurements and recently with interferometric methods, e.g., vertical scanning interferometry (Dove and Hochella, 1993; Pina et al., 1998; Teng et al., 2000; De Yoreo et al., 2009; Lüttge and Arvidson, 2010; Ruíz-Agudo and Putnis, 2012; Ruíz-Agudo et al., 2014¸ Altree-Williams et al., 2015).

Dissolution-reprecipitation reactions may range from the molecular scale up to several metres and can be subdivided into following processes:

[1] **dissolution of the parent mineral** due to contact with an undersaturated fluid

[2] **supersaturation** with respect to a thermodynamically more stable phase at interfacial layers due to parent dissolution

[3] **nucleation and growth of the product phase** at the parent mineral´s surface controlled by the local supersaturation at the interface of the occurring replacement reaction.

As these processes of host dissolution and precipitation of a secondary mineral phase are presumed to be coupled in space and time, they are referred to as coupled dissolution-reprecipitation (CDR) reactions (e.g., Putnis, 2009). Although replacement reactions can occur at low temperatures even in dry systems it is known since the 1960´ies that they proceed up to ten orders of magnitudes faster when fluids are involved (Brown et al., 1962; Putnis, 2009; Altree-Williams et al., 2015). The Earth´s surface and the upper crust therefore provide characteristic conditions for the occurrence of fluid-mediated mineral replacement reactions, which play a significant role in a myriad of large-scale geological processes, e.g., weathering, metamorphism, metasomatism, and formation of ore deposits and their accompanying alteration (Hellmann et al., 2003, 2012; Oliver et al., 2004; Putnis and Putnis, 2007; Putnis, 2002, 2009; Putnis and Austrheim, 2010, 2013; Putnis and John, 2010; Jamtveit et al., 2011; Oberthür et al., 2013; Putnis and Ruíz-Agudo, 2013; Ruíz-Agudo et al., 2014; Altree-Williams et al., 2015). Dissolution-reprecipitation reactions may also occur during fossilisation and diagenetic overprint, and in mild hydrothermal environments, e.g. magnesite replacement by aragonite, anhydrite replacement in dolomite hosts by calcite, and biogenic aragonite and (magnesian) calcite replacement by inorganic calcite (Brand, 1994; Wordon et al., 2000; Putnis, 2002; Smit et al., 2008; Putnis and Fernández-Díaz, 2010; Altree-Williams et al., 2015; Casella et al., 2017, 2018a, 2018b, 2018c). Furthermore, fluid-mediated CDR reactions are relevant for sequestration of CO_2, synthesis of novel materials, the environmental remediation of contaminated soil and groundwater, development of novel treatments for wastewater, surface preservation of monuments, and durability of materials arising from nuclear waste disposal (Yang et al., 1999; Lackner, 2002; Ben-Nissan, 2003; Turner et al., 2005; Xia et al., 2008, 2009a; Sassoni et al., 2011; Wang et al., 2012; Ruíz-Agudo et al., 2014; Geisler et al., 2015).

During CDR reactions newly formed minerals crystallise along cracks, cleavages, and grain boundaries and may create sharp replacement fronts with concomitant rim to core progressions within individual grains, e.g., pseudomorphic replacement of potassium bromide by potassium chloride, or calcite single crystals showing a magnesitic rim and dolomitic core after reacting with an aqueous $MgCl_2$ solution (Jonas et al., 2013, 2014, 2015; Ruíz-Agudo et al., 2014; Altree-Williams et al., 2015). Hydrothermal pseudomorphic replacement reactions commonly start at internal cracks and from the outer surface of the parent, proceed towards the grain centre and may lead to complete replacement (Xia et al., 2008, 2009a). Similar observations were made on marine biogenic carbonates after hydrothermal treatment simulating diagenetic alteration (Casella et al., 2017, 2018c).

The development of sharp reaction fronts between the initial and product phases are commonly characterised by genesis of intracrystalline porosity (with concomitant pore inclusions) within the host. Due to the interface-controlled nature of CDRs the reactions may result in pseudomorphic replacement with concomitant preservation of the external morphology and crystallographic orientations across the replacement interface of the parent phase (Putnis, 2009; Xia et al., 2009a, 2009b; Álvarez-Lloret, 2010; Brugger et al., 2010; Putnis and John, 2010; Qian et al., 2010; Raufaste et al., 2011; Altree-Williams et al., 2015). This structural feature was observed in initially calcitic ammonites which retained their shell macrostructure and finest details of internal microstructure after replacement by pyrite (Putnis, 2002). Development of pseudomorphism during CDR reactions requires close coupling of dissolution and nucleation rates at the parent-product interface (Maliva and Siever, 1988b; Putnis and Mezger, 2004; Putnis et al., 2005; Putnis and Putnis, 2007; Putnis, 2009).

However, textural diversity may arise from CDR reactions which are controlled by localised conditions at the interface of reaction or by non-equilibrium processes, and may also be caused by occlusion of pores as well as matrix cementation and compaction. Generally, prediction of CDR reactions is intricate as a number of complex interactions occurring at the reaction interface are involved (e.g., kinetics of the dissolution process, nucleation rate, growth mechanisms, solute transport, change in volume) and assumed to be of greater importance than global pressures, temperatures, and chemical factors (Brand and Veizer, 1980; Altree-Williams et al., 2015). Consequently, complex replacement textures are formed, e.g., grain coarsening in biogenic calcium carbonate minerals and feldspars (Norberg et al., 2011; Altree-Williams et al., 2015; Casella et al., 2017, 2018a, 2018b, 2018c).

Mineral dissolution-reprecipitation processes are driven by the minimisation of the Gibbs free energy of the system in response to changing system parameters, e.g., local fluid chemistry, pressure, temperature, and/or strain (Nakamura and Watson, 2001; Putnis, 2009; Milke et al., 2013; Putnis and Ruíz-Agudo, 2013; Altree-Williams et al., 2015). The local fluid composition at the interface governs the saturation state and chemistry of the initial and product phase. Thus, the precondition for CDR reactions can be described by disequilibrium of a single mineral or a mineral assemblage with respect to a present fluid phase. Re-equilibration is principally driven by dissolution and reprecipitation, and may be achieved by crystallisation of a `different´ mineral phase with concomitant change in chemistry or texture (Putnis, 2002, 2009; King et al., 2010; Putnis and Ruíz-Agudo, 2013; Ruíz-Agudo et al., 2014). As CDR reactions do not necessarily involve large volumes of reacting fluids and even limited dissolution of the initial solid phase can result in supersaturation of the interfacial fluid with respect to a secondary solid phase, the relative solubility is a critical factor (Hövelmann et al., 2012; Putnis et al., 2005; Putnis, 2009; Ruíz-Agudo et al., 2014; Altree-Williams et al., 2015).

Changes in growth patterns, however, may be directly ascertained at the nanometre scale when ions other than those of the participating mineral are present in the reaction solution (Ruíz-Agudo et al., 2012; Putnis and Ruíz-Agudo, 2013).

Ions released by parent dissolution can be transported by the fluid phase, thus, CDR reactions are sustained by solute transport from and to the reaction front. This process occurs through diffusion due to the development of a chemical gradient at the fluid-solid-interface (Xia et al., 2008; Putnis and Fernandez-Díaz, 2010; Zhang, 2010; Altree-Williams et al., 2015; Pedrosa et al., 2016). Furthermore, the rate of mineral dissolution, which depends on solution chemistry and specific surface area of the dissolved solid, plays a key role in CDR reactions due to the generation of new space, and supply of chemical components to the fluid phase (Altree-Williams et al., 2015). Non-stoichiometric dissolution of numerous multi-component minerals (e.g., dolomite) has been explained by favoured release of one component into the solution resulting in development of an enriched surface layer, which further affects dissolution and precipitation rates (Busenberg and Plummer, 1986; Pokrovsky and Schott, 2001; Zhang et al., 2007; Putnis and Ruíz-Agudo, 2013).

An activation energy barrier determines the threshold supersaturation for nucleation and hinders nucleation at small supersaturations (e.g., Steefel and van Cappellen, 1990; Prieto et al., 1993; Putnis et al., 1995; Scherer, 1999; Putnis and Mauthe, 2001; Harlov et al., 2011; Stack et al., 2014). Below the threshold value, product formation is defined by crystal growth of present nuclei, whereas above the threshold value product formation is dominated by nucleation events (Steefel and van Cappelin, 1990; Putnis et al., 1995). The crystal growth mechanism of the product is therefore controlled by the availability of attachment sites (e.g., kink and step positions) as well as on the degree of supersaturation (Sunagawa, 1981; Otálora and García-Ruiz, 2014).

Changes in mineralogy caused by CDR reactions are assumed to be closely related to the evolution of the system towards an equilibrium state through numerous polymorphs of the product phase. This process is referred to as Ostwald´s step rule in which the first precipitating phase may be comprised of either nanoclusters or a metastable phase (Cardew and Davey, 1985; Morse and Casey, 1988; Threlfall, 2003; Pouget et al., 2009; Demichelis et al., 2011; Gebauer et al., 2014; Altree-Williams et al., 2015). Thus, the system is driven towards a thermodynamically more stable product phase via amorphous and crystalline polymorphs of lower stability, e.g., gypsum replacement by calcite through the $CaCO_3$ polymorphs ACC, vaterite, and aragonite (Ogino et al., 1987; Fernández-Díaz et al., 2009; Rodriguez-Navarro et al., 2015).

For the proceeding of pseudomorphic replacement fronts, pathways for mass transfer must be sustained at the fluid-solid interfaces. Differences in molar volume between the initial and the product phase, and the relative solubilities of the phases in the fluid at the reaction interface are responsible for porosity formation. Due to the

development of porosity, further fluid penetration into the grain is enabled and, thus, CDR reactions are promoted (Pollok et al., 2011; Putnis and Ruíz-Agudo, 2013). Fractures in the parent and product phases can be induced by substantial changes in the volume (e.g., expansion and shrinkage) followed by the generation of stresses (Ruíz-Agudo et al., 2014). Rapid fluid movements through solids during CDR reactions are commonly present at fractures and grain boundaries, whereas CDR reactions occurring at mineral-fluid-interfaces lead to the generation of porosity within the newly formed phase and ultimately advance the mobilisation and exchange of ions (Putnis and Ruíz-Agudo, 2013). Fracture and porosity development during CDR reactions were detected in leucite replacement by analcime (Putnis et al., 2007; Jamtveit, 2009), rutile replacement by ilmenite (Jannsen et al., 2010), aragonite replacement by calcite (Perdikouri et al., 2011, 2013, Casella et al., 2017, 2018c; Ritter et al., 2017), and replacement of calcite by calcium oxalate (Ruíz-Agudo et al., 2013).

An alternative explanation for the occurrence of dissolution-reprecipitation processes may be Ostwald ripening; a process in which smaller crystals are dissolved and, subsequently, reprecipitate as larger crystals in order to reduce the surface free energy (Morse and Casey, 1988). Hover and co-workers (2001) reported that originally dissolved high-Mg calcite was reprecipitated with similar contents in Mg, thus, changes in mineralogy are not necessarily involved in Ostwald ripening processes (Burdige et al., 2010). Furthermore, experimental studies simulating diagenetic alteration of biogenic carbonates have shown that dissolved biogenic aragonites were replaced by newly formed coarse calcite grains. It was shown that not only the mineral phase but also microstructure and concomitant crystallographic texture have changed with increasing experimental duration due to dissolution-reprecipitation reactions (Putnis, 2009; Casella et al., 2017, 2018c).

CDR reactions in carbonates caused by solubility differences between carbonate polymorphs may occur during early diagenetic processes. Involved pore fluids can be undersaturated with respect to metastable phases and still supersaturated with respect to another carbonate phase. Hence, more soluble $CaCO_3$ phases underlie dissolution processes, whereas thermodynamically more stable phases are precipitated (Brand, 1994; Hu and Burdige, 2007; Burdige et al., 2010).

Low Mg-calcites (0-4 mol% $MgCO_3$) are the calcium carbonate polymorph most resistant to dissolution processes. With increasing Mg-contents, calcite solubility increases exponentially, thus, high-Mg calcites are less stable at conditions of the Earth´s surface (Chave, 1954; Milliman, 1974; Brand, 1994). However, morphological and textural features as well as primary porosity of biogenic carbonates may have a great impact on alteration processes and dissolution kinetics (Martin et al, 1986; Brand, 1994; Cubillas et al., 2005). Though low-Mg calcites are most stable at conditions of the Earth´s surface, geochemical and physical evidence has shown their potential for

postdepositional alteration processes (Al-Aasm and Veizer, 1982; Brand and Logan, 1991; Brand, 1994).

Aragonite by calcite replacement is one of the most studied CDR reactions due to the importance of calcium carbonate for geosciences and was observed, e.g., in cave environments and biogenic carbonates. In the latter case, aragonite by calcite replacement is commonly accompanied by a loss in lustre and pigmentation (Cabrol, 1978; Cabrol and Coudray, 1982; Brand, 1994; Frisia, et al., 2002; Putnis, 2009). Metastable aragonite is prone to calcite replacement when aragonitic speleothems with porous fabrics are infiltrated by water. Calcite nucleation and replacement is assumed to be favoured on calcite cement located between aragonitic rays and needles of speleothems as well as by fluctuations in the saturation state (i.e., undersaturation with respect to aragonite with simultaneous supersaturation with respect to calcite) of the involved fluid (Frisia, 1996; Frisia, et al., 2000, 2002).

$CaCO_3$ replacement by apatite has been observed during natural hydrothermal reactions and chemical weathering (Kasioptas et al., 2008). Hydrothermal experiments using aragonite and calcite single crystals in phosphate solutions at 200 °C showed that calcium carbonates are replaced by polycrystalline hydroxylapatite, while the overall morphology of both single crystals was retained. Furthermore, hydrothermal alteration experiments using aragonite single crystals between 140-200 °C have shown that partial aragonite replacement by polycrystalline calcite occurred at elevated temperatures (≥180 °C) and resulted from interface-coupled dissolution-reprecipitation reactions. The usage of ^{18}O tracer in the solutions shed light on the replacement mechanism. Aragonite by calcite replacement proceeded by fracture development which allowed mass transport between the reaction front and fluid reservoir. Randomly oriented calcite crystallites nucleated within generated fractures, thus, no systematic relationship between the crystallographic orientations of the two $CaCO_3$ polymorphs could be observed (Perdikouri et al., 2008, 2013). Similar findings were made on mollusc and gastropod aragonite where replacement of aragonite by randomly oriented calcite crystals could not be detected below 175 °C (Casella et al., 2017, 2018c; Ritter et al., 2017).

1.3.1 Dissolution-reprecipitation-reactions in diagenetic environments

Rocks are prone to chemical alteration processes from their time of deposition up to the present day (Walter, 1986). During diagenesis dissolution-reprecipitation processes may occur in clay minerals present in sedimentary basins, and carbonates mainly produced in settings of modern shallow seawater. Carbonaceous sediments are replaced by phases with higher stability (e.g., calcite, dolomite) under given conditions during short-term

(early-diagenetic) diagenesis close to the Earth´s surface (i.e., <1 m in depth) and long-term (burial/post-depositional) diagenesis (Morse and Mackenzie 1990; Rude and Aller, 1991; Brand, 1994; Patterson and Walter, 1994; Melim et al., 2002; Fowler and Yang, 2003; Morse, 2003; Walter et al., 2007; Hu and Burdige, 2007; Burdige et al., 2010). Micritisation and development of calcareous cements are assumed to involve CDR reactions (Reid and Macintyre, 1998; Morse, 2003).

CDR reactions may be caused by intergranular pressure solution at grain boundaries due to overburden pressure in burial environments, e.g., in quartz sedimentary deposits. Induced by the weight of overlying sediments grain-grain contacts experience higher stresses resulting in increased solubilities and mineral dissolution at grain contacts, material transport into the fluid phase, and reprecipitation processes at sites of low stress. Thus, sediment compaction and lithification is ultimately caused by CDR reactions (Rutter, 1983; Gratier and Guiget, 1986; Renard et al., 2000; Revil, 2001; Chester et al., 2004; Putnis, 2009).

In the 1980´ies, Maliva and Siever (1988b) developed a model for replacement reactions taking place in diagenetic environments where free grain surfaces of the host are in contact with fluids which are not necessarily undersaturated nor supersaturated with respect to the host and new forming phase, respectively. The authors proposed that the controlling factor in this model is the force of crystallisation by which the crystal growing from a supersaturated solution exerts pressure on its surrounding resulting in dissolution of adjacent minerals/rocks due to pressure induced dissolution. Preserved microstructural features of the parent indicate that rates of parent dissolution and product precipitation were equal (Nahon and Merino, 1997; Putnis, 2009).

2 Results and discussion

2.1 Experimental diagenesis: insights into aragonite to calcite transformation of *Arctica islandica* shells by hydrothermal treatment

Laura A. Casella[1], Erika Griesshaber[1], Xiaofei Yin[1], Andreas Ziegler[2], Vasileios Mavromatis[3,4], Dirk Müller[1], Ann-Christine Ritter[5], Dorothee Hippler[3], Elizabeth M. Harper[6], Martin Dietzel[3], Adrian Immenhauser[5], Bernd R. Schöne[7], Lucia Angiolini[8], and Wolfgang W. Schmahl[1]

[1] Department of Earth and Environmental Sciences and GeoBio-Centre, Ludwig-Maximilians-Universität München, 80333 Munich, Germany

[2] Central Facility for Electron Microscopy, University of Ulm, 89081 Ulm, Germany

[3] Institute of Applied Geosciences, Graz University of Technology, 8010 Graz, Austria

[4] Géosciences Environnement Toulouse (GET), CNRS, 31400 Toulouse, France

[5] Institute for Geology, Mineralogy and Geophysics, Ruhr University Bochum, 44801 Bochum, Germany

[6] Department of Earth Sciences, University of Cambridge, CB2 3EQ Cambridge, U.K.

[7] Institute of Geosciences, University of Mainz, 55128 Mainz, Germany

[8] Dipartimento di Scienze della Terra "A. Desio", Università degli Studi di Milano, 20133 Milan, Italy

2.1.1 Abstract

Biomineralised hard parts form the most important physical fossil record of past environmental conditions. However, living organisms are not in thermodynamic equilibrium with their environment and create local chemical compartments within their bodies where physiologic processes such as biomineralisation take place. In generating their mineralised hard parts, most marine invertebrates produce metastable aragonite rather than the stable polymorph of $CaCO_3$, calcite. After death of the organism the physiological conditions, which were present during biomineralisation, are not sustained any further and the system moves toward inorganic equilibrium with the surrounding inorganic geological system. Thus, during diagenesis the original biogenic structure of aragonitic tissue disappears and is replaced by inorganic structural features.

In order to understand the diagenetic replacement of biogenic aragonite by inorganic calcite, *Arctica islandica* mollusc shells were subjected to hydrothermal alteration experiments. Experimental conditions were between 100 and 175 °C, with the main focus on 100 and 175 °C, reaction durations between 1 and 84 days, and alteration fluids simulating meteoric and burial waters, respectively. Detailed microstructural and geochemical data were collected for samples altered at 100 °C (and at 0.1 MPa pressure) for 28 days and for samples altered at 175 °C (and at 0.9 MPa pressure) for 7 and 84 days. During hydrothermal alteration at 100 °C for 28 days most but not the entire biopolymer matrix was destroyed, while shell aragonite and its characteristic microstructure were largely preserved. In all experiments up to 174 °C, there are no signs of a replacement reaction of shell aragonite to calcite in X-Ray diffraction bulk analysis. At 175 °C the replacement reaction started after a dormant time of 4 days, and the original shell microstructure was almost completely overprinted by the aragonite to calcite replacement reaction after 10 days. Newly formed calcite nucleated at locations which were in contact with the fluid, at the shell surface, in the open pore system, and along growth lines. In experiments with fluids simulating meteoric water, calcite crystals reached sizes up to 200 μm, while in the experiments with Mg-containing fluids the calcite crystals reached sizes up to 1 mm after 7 days of alteration. Aragonite is metastable at all applied conditions. Only a small bulk thermodynamic driving force exists for the replacement by calcite. We attribute the sluggish replacement reaction to the inhibition of calcite nucleation in the temperature window from ca. 50 to ca. 170 °C or, additionally, to the presence of magnesium. Correspondingly, in Mg^{2+}-bearing solutions the newly formed calcite crystals are larger than in Mg^{2+}-free solutions. Overall, the aragonite by calcite replacement occurs via an interface-coupled dissolution–reprecipitation mechanism, which preserves morphologies down to the sub-micrometre scale and induces porosity in the newly formed phase. The absence of aragonite replacement by calcite at temperatures lower than 175 °C contributes to explaining why

aragonitic or bimineralic shells and skeletons have a good potential of preservation and a complete fossil record.

2.1.2 Introduction

The skeletons of marine calcifiers are considered high resolution archives of proxies to understand the evolution of the Earth system. They are widespread in the fossil record and are sensitive to changes in seawater composition (e.g., Brand et al., 2003; Parkinson et al., 2005; Schöne and Surge, 2012; Brocas et al., 2013). However, diagenetic alteration of fossil biogenic carbonates is a significant obstacle in understanding past climate dynamics (Grossmann et al., 1993; Richardson, 2001; Immenhauser et al., 2005; Korte et al., 2005). Despite more than a century of research on carbonate diagenesis, many of the controlling processes are still only understood in a qualitative manner (Brand and Veizer, 1980, 1981; Swart, 2015). One of the main problems is that diagenetically altered carbonates occur as the product of a complex alteration pathway with an unknown number of intermediate steps and controlling factors (Immenhauser et al., 2015; Swart, 2015; Ullmann and Korte, 2015). Motivated by the lack of quantitative data on rates and products of marine, meteoric, and burial diagenesis, we performed laboratory-based alteration experiments with *Arctica islandica* shells with the aim to obtain time series data sets. The bivalve *A. islandica* has been studied in several scientific disciplines, e.g., biology (Taylor, 1976; Oeschger and Storey, 1993; Morton, 2011; Strahl et al., 2011). *Arctica islandica* has also gained profound attention in palaeoclimatology due to its long lifespan and its use as a high-resolution long-term archive (e.g., Marchitto et al., 2000; Schöne et al., 2004, 2005b, 2005c; Wanamaker et al., 2008, 2011; Butler et al., 2009, 2013; Karney et al., 2012; Schöne, 2013). From a long-term perspective, *A. islandica* plays an important role in palaeontology, not only as a Neogene palaeoecological and palaeoclimatic archive (e.g., Marchitto et al., 2000; Schöne et al., 2004, 2005b, 2005b; Wanamaker et al., 2008, 2011; Butler et al., 2009, 2013; Karney et al., 2012; Schöne, 2013; Crippa et al., 2016) but also as a biostratigraphic tool. Formerly considered a marker for the Pliocene-Pleistocene boundary (Raffi, 1986) in the Mediterranean region, its first appearance is now regarded as an indicator of the Gelasian-Calabrian (early Pleistocene) boundary, around 1.7 Ma (Crippa and Raineri, 2015). The potential of this species for palaeontology is strictly dependent on its preservation, and thus, the dynamics of diagenetic shell alteration.

At ambient conditions calcite is the stable, and thus, the least soluble polymorphic phase of $CaCO_3$ (Plummer and Mackenzie, 1974; Plummer and Busenberg, 1982; Sass et al., 1983; Walter and Morse, 1984b; Bischoff et al., 1987, 1993; Redfern et al., 1989; Navrotsky, 2004; Morse et al., 2007; Gebauer et al., 2008, Gebauer and Cölfen, 2011;

Radha and Navrotsky, 2013), while at higher pressures aragonite forms the stable calcium carbonate polymorph (Redfern et al., 1989; Radha and Navrotsky, 2013). Accordingly, calcite crystallises from aqueous solutions below ca. 50 °C (if no calcite-inhibitors are present). However, even in pure Ca^{2+}/HCO_3^- solutions, at temperatures above ca. 50 °C metastable aragonite rather than calcite is obtained (Kitano et al., 1962; Taft, 1967; Ogino et al., 1987). There is no sharp tipping point but rather a gradual change of fraction of the precipitating phases (Ogino et al., 1987; Balthasar and Cusack, 2015). Furthermore, inhibitors of calcite nucleation and/or growth decrease the temperature of this regime shift in precipitation even further; in marine and diagenetic environments the most important inorganic inhibitor is Mg^{2+} (Kitano et al., 1972; Katz, 1973; Berner, 1975; Morse et al., 1997; Choudens-Sánchez and Gonzáles, 2009; Radha et al., 2010; Balthasar and Cusack, 2015; Sun et al., 2015).

The replacement reaction of aragonite by calcite in aqueous systems was investigated by Bischoff and Fyfe (1968), Metzger and Barnard (1986), Yoshioka et al. (1968), Bischoff (1969), Kitano et al. (1972), Katz (1973), Oomori et al. (1987), and more recently by Perdikouri et al. (2011, 2013). It was recognised by Fyfe and Bischoff (1965) that the aragonite by calcite replacement reaction in aqueous environments occurs by dissolution and reprecipitation reactions. Except for Metzger and Banard (1968), and Perdikouri et al. (2011, 2013), most authors have used powdered samples of geological or powdered synthetic aragonite. For these powdered samples, they claim a rapid replacement reaction of aragonite to calcite within hours or very few days at temperatures of ca. 100 °C or above, depending on temperature and the Mg content of the solution.

Metzger and Banard (1968) and Perdikouri et al. (2011, 2013) investigated aragonite blocks or single crystals and report that temperatures in excess of 160-170 °C are required to replace aragonite by calcite within a couple of days, whereas below 160 °C aragonite remains present over many weeks.

The present study describes first experimental data of the replacement reaction of BIOGENIC aragonite to inorganic calcite and investigates the kinetics of the replacement reaction of aragonite by calcite in shell material, geochemistry, nano- and microstructure alteration, and crystallographic texture variation. During biomineralisation, living organisms create local micro-environments for physiological generation of their composite hard tissues. After the death of the organism, all tissues become altered by equilibration with the surrounding environment – part of the complex set of processes called diagenesis. Thus, as diagenetic alteration proceeds, the species-specific fingerprint of the biogenic structure disappears and is replaced by inorganic features. Despite the fact that the evolutionary line of *A. islandica* dates back to the Jurassic (Casey, 1952), only a limited number of studies have dealt with *A. islandica* specimens due to the thermodynamically unstable nature of their aragonitic shells. The aim of the present

paper is to describe analysis-based detailed microstructural, geochemical, phase, and texture data observed in the experimental simulation of diagenesis by hydrothermal treatment of modern *A. islandica* shell samples. With this study, we gain quantitative insight into processes that take place along pathways from early marine pore water diagenesis to the pervasive recrystallisation under burial conditions. The targets of the present study are the analysis of microstructural features, the preservation of the organic matrix in the shell, and the kinetics of the replacement reaction of aragonite by calcite as investigated by X-ray diffraction, scanning electron microscopy (SEM), and crystallographic microanalysis determined by electron backscatter diffraction (EBSD). Element maps of Cl, Mg, Na, and Sr were determined by electron probe micro-analysis (EPMA).

2.1.3 Materials and methods

Test materials

For this study, shells of *A. islandica* were collected from the recent shell middens of a fishing company in northern Iceland and from Loch Etive waters in Scotland. On average, shells were between 8 and 10 cm in size and represent adult specimens. Major morphological features of the shell of *Arctica islandica* are displayed in Fig. 2.16; see also Schöne (2013).

Methods applied

Organic matrix preparation by selective etching

To image the organic matrix in modern reference and hydrothermally altered shell samples, as well as the mineral part in the reference specimens (i.e., inorganic and biogenic aragonite), shell or mineral pieces were mounted on 3 mm thick cylindrical aluminium rods using super glue. The samples were first cut using a Leica Ultracut ultramicrotome with glass knives to obtain plane surfaces within the material. The cut pieces were then polished with a diamond knife (DiATOME) by stepwise removal of material in a series of 15 sections with successively decreasing thicknesses (90, 70, 40, 20, 10 and 5 nm; each step was repeated 15 times) as reported in Fabritius et al. (2005). The polished samples were etched for 180 s using 0.1 M HEPES (4-(2-hydroxyethyl)-1-piperazineethanesulfonic acid) at pH 6.5 containing 2.5 % glutaraldehyde as a fixation solution. The etching procedure was followed by dehydration in 100 % isopropyl three

times for 10 min each, before the specimens were critical point dried in a BAL-TEC CPD 030 (Liechtenstein). The dried samples were rotary-coated with 3 nm of platinum and imaged using a Hitachi S5200 field emission-secondary electron microscope (FE-SEM) at 4 kV.

Hard tissue characterisation methods

For FE-SEM and EBSD analyses, 5 mm × 5 mm thick pieces were cut out of the shell and embedded in epoxy resin. The surface of the embedded samples was subjected to several sequential mechanical grinding and polishing steps down to a grain size of 1 μm. The final step was etch polishing with colloidal alumina (particle size ~0.06 μm) in a vibratory polisher. For EBSD analysis, the samples were coated with 4-6 nm of carbon, and for SEM visualisation and electron probe micro analysis (EPMA) with 15 nm. EBSD measurements were carried out on JEOL JSM 6400 field emission SEM, equipped with a Nordlys EBSD detector. The SEM was operated at 20 kV and measurements were indexed with the CHANNEL 5 HKL software (Schmidt and Olesen, 1989; Randle and Engler, 2000). Information obtained from EBSD measurements is presented as band contrast images and as colour-coded crystal orientation maps with corresponding pole figures.

The EBSD band contrast gives the signal strength of the EBSD–Kikuchi diffraction pattern and is displayed as a greyscale component of EBSD scanning maps. The strength of the EBSD signal is high when a crystal is detected (bright), while it is weak or absent when a polymer such as organic matter is scanned (dark/black).

Co-orientation statistics is derived from pole figures obtained by EBSD scans and is given by the MUD (multiple of uniform (random) distribution) value. The MUD value is a measure of crystal co-orientation (texture sharpness) in the scanned area. High MUD values indicate a high crystal co-orientation (in this study calcite), whereas low MUD values reflect a low to random co-orientation.

In order to trace the infiltration and percolation of fluids into and through the shells, pristine and hydrothermally altered shell samples were scanned with EPMA (Goetz et al., 2014). Chemical data were obtained by using a CAMECA SX100 EPMA system equipped with a LaB_6 cathode. An accelerating voltage of 15 keV at a current of 40 nA were used as operative settings. All elements were analysed with wavelength-dispersive X-ray spectrometers. The Sr-Kα, Mg-Kα, and Na-Kα were measured on a TAP (thallium acid phthalate) crystal and Cl-Kα measured on an LPET (large pentaerythritol) crystal. Lα emission lines of Mn and Fe were detected with a LLIF (large lithium fluoride) crystal. A step size in the range of 1-2 μm with a dwell time of 150 ms was chosen for the element mappings. Celestine (Sr), dolomite (Ca, Mg), ilmenite (Mn), apatite (P), albite (Na), benitoite (Ba), vanadinite (Cl), and hematite (Fe) were used as

standard materials. Matrix correction was carried out using the PAP procedure (Pouchou and Pichoir, 1984).

Alteration experiments

Hydrothermal alteration experiments mimicked burial (and meteoric) diagenetic alteration of recent *A. islandica* under controlled laboratory conditions. Chemical and experimental information on hydrothermal experiments utilised in the present study are given in Table 2.1. All fluids were spiked with ^{18}O-depleted oxygen in order to trace fluid-solid exchange reactions and isotopic studies investigated by Ritter et al. (2017).

Details of the experimental protocol can be found in Riechelmann et al. (2016). Briefly, pieces (2 cm × 1 cm) of recent *A. islandica* specimens were placed in a PTFE (polytetrafluoroethylene) liner together with 25 mL of either the meteoric (10 mM NaCl aqueous solution) or burial fluid (100 mM NaCl + 10 mM $MgCl_2$ aqueous solution) and sealed with a PTFE lid. Each of the PTFE liners was placed in a stainless steel autoclave, sealed and kept in the oven at temperatures of 100, 125, 150 and 175 °C for different periods of time ranging between 1 day and 84 days (see Table 2.1, Fig. 2.26 and Table 2.2 for experiments; main focus was on 100 and 175 °C). Obviously, this temperature regime is far beyond natural meteoric diagenetic environments (Lavoie and Bourque, 1993) but is typical for the burial realm (Heydari, 1997). Nevertheless, elevated fluid temperatures were applied to meteoric experiments, too, as reaction rates under surface conditions are too slow for experimental approaches. After the selected time period, an autoclave was removed from the oven, cooled down to room temperature and then opened. The aqueous fluid that had passed through a 0.2 μm cellulose acetate filter was subjected to further chemical and isotopic analyses. Recovered solids were dried at 40 °C overnight.

X-Ray diffraction analysis

X-ray diffraction analysis of pristine and hydrothermally treated samples was performed with Mo-Kα_1 radiation in transmission geometry and with Cu-Kα_1 radiation in reflection geometry on a General Electric Inspection Technologies XRD3003 X-ray diffractometer with an incident beam Ge111 focussing monochromator and a Meteor position-sensitive detector. The diffractograms were analysed by Rietveld analysis with the software package FULLPROF (Rodríguez-Carvajal, 2001) using the aragonite structure data of Jarosch and Heger (1986) and calcite structure data of Markgraf and Reeder (1985).

Table 2.1: Detailed conditions used in hydrothermal alteration experiments of modern *Arctica islandica*. Major and minor element chemical data of pristine *Arctica islandica* aragonite and the calcite obtained after treatment are given in Table 2.3.

Sample name	Fluid type	NaCl content [mM]	MgCl$_2$ content [mM]	Temp. [°C]	Experimental time	Alkalinity [mM]	pH	Mg-content of fluid after experiment [mg/L]
CHA-M-040 AI21	meteoric	10	-	100	28 days	1.69	7.91	3
CHA-M-042 AI 23	meteoric	10	-	175	7 days	7.72	-	0
CHA-M-046 AI27	meteoric	10	-	175	84 days	10.75	7.78	1
CHA-M-043 AI24	burial	100	10	100	28 days	2.02	8.39	112
CHA-M-041 AI22	burial	100	10	175	7 days	9.96	-	84
CHA-M-046 AI 27	burial	100	10	175	84 days	6.99	7.51	165
CHA-M-044 AI29	burial	100	10	125	1 day	-	-	-
CHA-M-044 AI29	burial	100	10	125	14 days	-	-	-
CHA-M-044 AI29	burial	100	10	150	2 days	-	-	-
CHA-M-044 AI26	burial	100	10	175	1 day	-	-	-
CHA-M-044 AI20	burial	100	10	175	3 days	-	-	-
CHA-M-044 AI28	burial	100	10	175	4 days	-	-	-
CHA-M-044 AI28	burial	100	10	175	4 ¼ days	-	-	-
CHA-M-044 AI28	burial	100	10	175	4 ¾ days	-	-	-
CHA-M-044 AI20	burial	100	10	175	5 days	-	-	-
CHA-M-044 AI20	burial	100	10	175	6 days	-	-	-

Table 2.2: Crystal co-orientation (texture) strength expressed as multiple of uniform (random) distribution (MUD) of modern and experimentally altered *Arctica islandica* shells. Ar: aragonite, Cc: calcite.

Sample name	Fluid type	Temp. [°C]	Experimental time	MUD value of the outermost shell part	MUD value of the central shell part	MUD value of the innermost shell part
Modern reference	-	-	-	12 Ar/32 Ar	58 Ar	88 Ar
altered specimen *CHA-M-040 AI21 B2*	meteoric	100	28 days	7 Ar	27 Ar	94 Ar
altered specimen *CHA-M-043 AI24 B2*	burial	100	28 days	4 Ar	-	99 Ar
altered specimen *CHA-M-042 AI23 B2*	meteoric	175	7 days	18 Cc	15 Cc	-
altered specimen *CHA-M-046 AI27 B1*	meteoric	175	84 days	25 Cc	32 Cc	-
altered specimen *CHA-M-041 AI22 B2*	burial	175	7 days	36 Cc	90 Cc	80/81 Cc
altered specimen *CHA-M-046 AI27 B2*	burial	175	84 days	64 Cc	62 Cc	-

2.1.4 Results

The shell ultrastructure of modern *Arctica islandica*

Figures 2.1 to 2.5 show characteristic ultrastructural features of the shell of modern *A. islandica*. Images of the pristine shell are given in Figs. 2.1-2.3, while Figs. 2.4 and 2.5 present structural features of the hydrothermally altered shells. The valve of *A. islandica* is layered, with various shell parts showing different internal structural features (Fig. 2.1). The distribution patterns of porosity, pore sizes and the dimensions of basic aragonitic crystal units vary significantly along the cross section of the shell. The outer shell layer, indicated with yellow stars in Figs. 2.1A-B, consists of aragonite crystal units in the 5 μm size range (Fig. 2.2A). This shell layer is highly porous (see the white dotted features in Fig. 2.1B), and pore diameters range within a few micrometres (Fig. 2.17, see chapter 2.1.9). The inner shell layer, i.e., the part very close to the soft tissue of the animal (indicated with white rectangles in Figs. 2.1A, C), is dense and composed of very few small aragonite crystallites with pore sizes of less than 1 μm (Fig. 2.2B). The dimension of pores in this shell region is in the 1 to 2 μm range. However, the innermost shell layer, the layer that is in contact with the mantle tissue of the animal (white stars in Figs. 2.1A, C), contains large (up to 12 μm in diameter) and elongated pores which are oriented perpendicular to the rim of the shell (see white arrows in Fig. 2.1C). Growth lines are clearly visible in the cross section through the shell (white arrows in Fig. 2.1A) as thin layers are characterised by higher accumulations of organic material (this study and Richardson, 2001).

Figures 2.2 and 2.3 show, at increasing magnification, structural features of modern *A. islandica* shells which were made visible by slight etching of the mineral and simultaneous chemical fixation of the organic matrix. Structural characteristics of the reference material (inorganic aragonite grown from solution), treated chemically in a similar way as the biogenic aragonite samples, are shown in chapter 2.1.9 (Fig. 2.18). Figure 2.2A shows features which are characteristic of the outer shell layer, whereas Fig. 2.2B depicts internal characteristics of the tissue-adjacent side of the shell (the region marked by white rectangles in Fig. 2.1). Etching brings out the outlines of the aragonite grains, revealing the fabric of the biopolymer matrix within the hard tissue and its interlinkage with the mineral. The mineral units (crystals) in the outer shell layer are highly irregular in shape with dimensions in the 1-5 μm range (Fig. 2.2A). In contrast, although the mineral units (crystals) in the dense layer of the shell also have irregular morphologies, they are of significantly smaller dimensions, mainly in the 1-2 μm range and below (Fig. 2.2B). The predominant fabric of the organic matrix in the shell of *A. islandica* is a network of intracrystalline fibrils (Fig. 2.3, yellow arrows in Figs. 2.3A, B)

which interconnect the mineral units across the grain boundaries. However, organic membranes are occasionally also present and surround the mineral units (white arrows in Fig. 2.3A). Like all other biological carbonate hard tissues, at the finest scale, the shell of *A. islandica* is composed of nanoparticles which are a few tens of nanometres in diameter (white arrows in Fig. 2.3C). In order to check the validity of nanoscale structural features observed in pristine *Arctica islandica* shells, we prepared inorganic aragonite grown from solution in a similar way (microtome-cut, polished, etched slightly only for 180 s, critical-point-dried). As is visible in Fig. 2.18, etch pits develop in inorganic aragonite grown from solution and nanoparticulate features are absent.
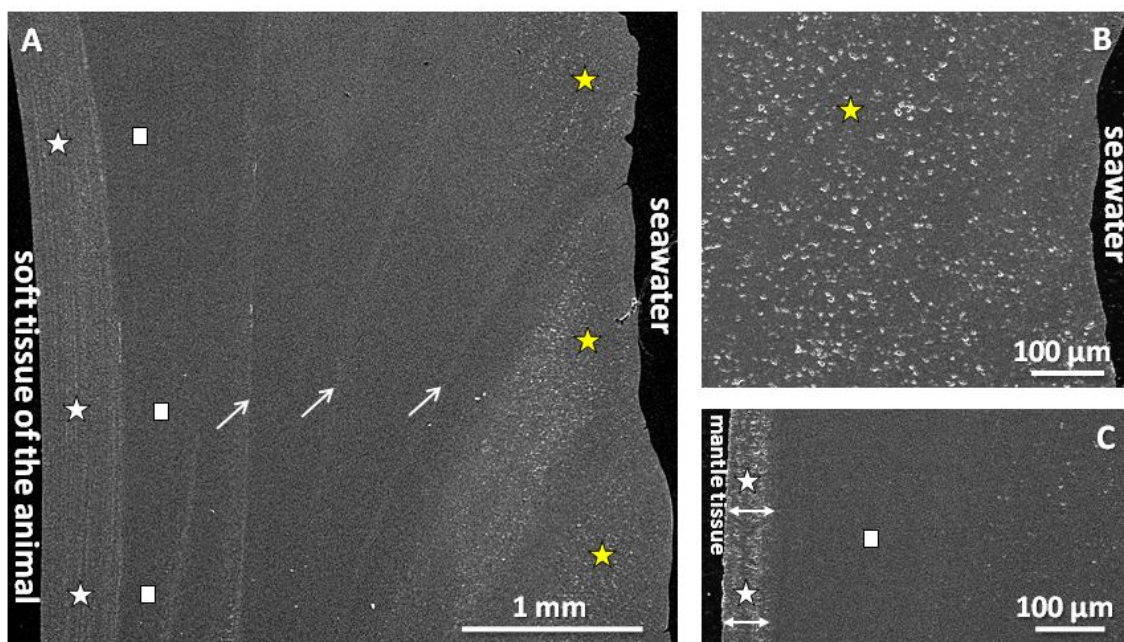
Figure 2.1: FE-SEM image showing ultrastructure characteristics of the shell of modern *Arctica islandica* (A), its high porosity in shell layers facing seawater (yellow stars in A, B) and the denser shell layers (white stars in A, C) close to the soft tissue of the animal. The innermost shell layers contain elongated pores (white stars in C) with the long axis of the pores oriented perpendicular to the inner surface of the shell (white arrows in C). Highly dense shell parts are also present (white rectangles in A, C), in which pore density and size is very low and where minute aragonite crystals are closely packed. White arrows in (A) indicate the location of growth lines.
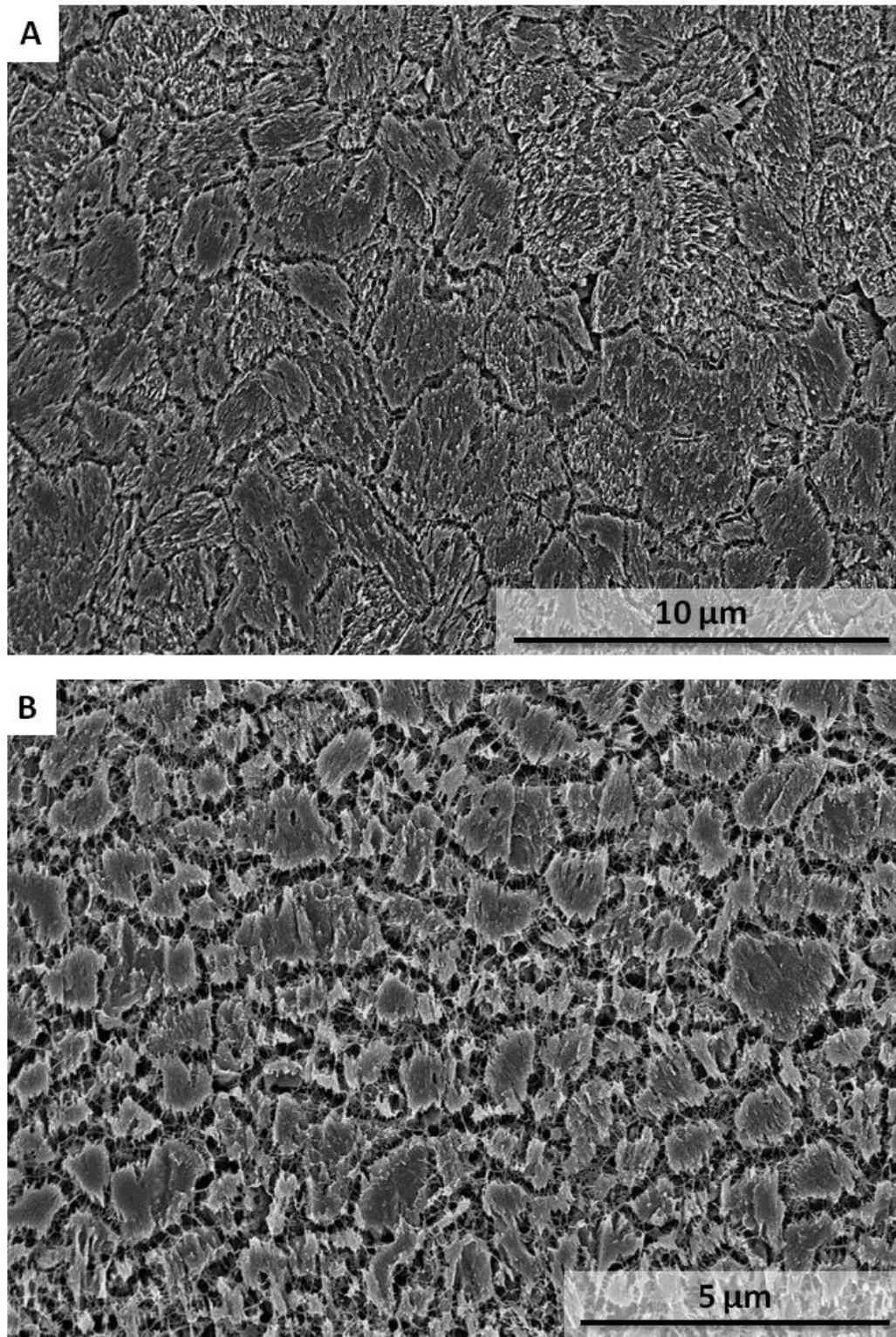
Figure 2.2: FE-SEM micrograph of microtome cut, microtome polished, etched, and critical-point-dried surface of the shell of modern *Arctica islandica*: (A) the outer shell layer and (B) inner shell layer. Etching occurred for 180 s and was applied to remove aragonite in order to visualise the spatial distribution of (glutaraldehyde-stabilised) biopolymers within the shell. The outer shell layer consists of large and irregular mineral units, connected to each other and is infiltrated by a network of organic fibrils. The inner shell layers consist of significantly smaller mineral units. These are also interconnected by organic fibrils.
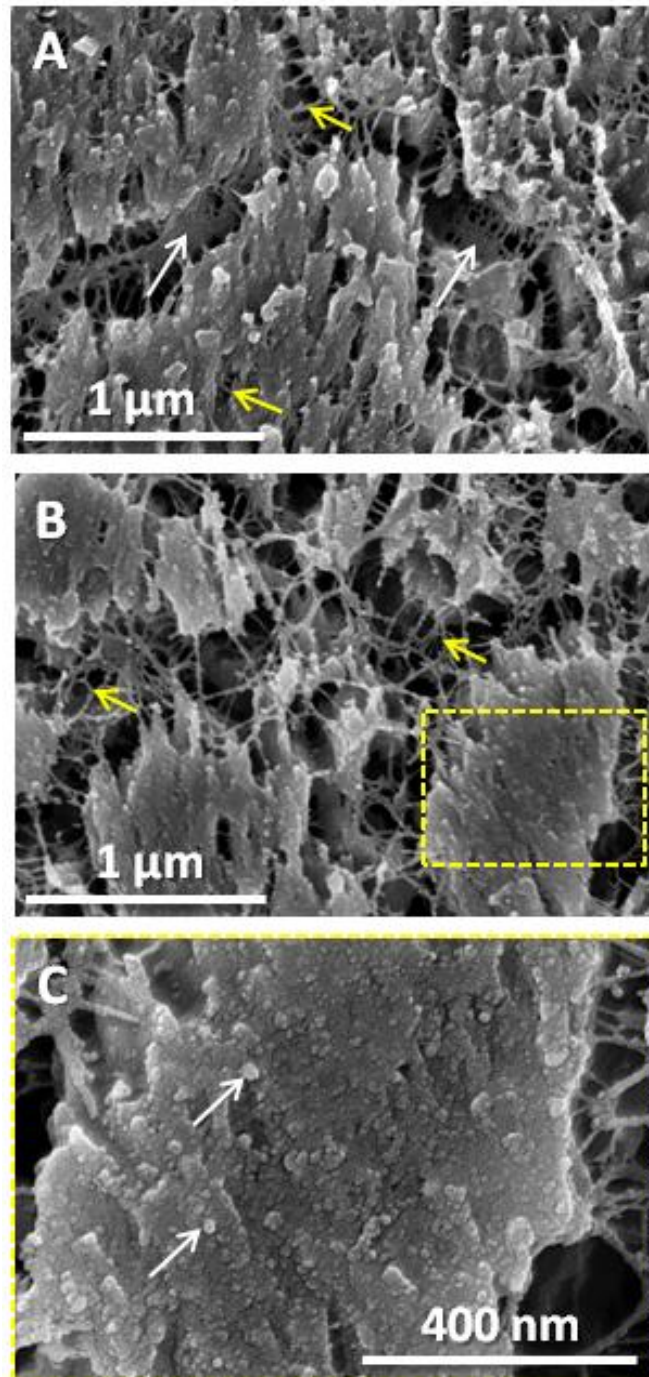
Figure 2.3: FE-SEM micrographs of cut, microtome-polished, etched, and critical-point-dried surfaces of modern *Arctica islandica* next to seawater (A) and close to the soft tissue of the animal (B, C). Etching occurred for 180 s and slightly removed aragonite in order to visualise the spatial distribution of (glutaraldehyde-stabilised) biopolymers within the shell. Readily visible is the nanoparticulate consistency of the aragonitic hard tissue (white arrows in C) and the presence of biopolymer membranes (white arrows in A) and fibrils (yellow arrows in A, B) between and within the mineral units.

The ultra- and microstructure of experimentally altered *A. islandica* shells

Pieces of pristine *Arctica islandica* shells were altered at 100, 125, 150 and 175 °C for 1 to 84 days in fluids simulating meteoric and burial (Mg-rich) fluids (Table 2.1). As X-Ray diffraction (XRD) measurements in Fig. 2.26 show, shell aragonite remains stable for the first 3 days of alteration, even at alteration temperatures of 175 °C. Alteration times up to 14 days at 125 °C do not cause the mineral replacement reaction of *A. islandica* shell aragonite by calcite (Fig. 2.26). In our experiments calcite formation started on the fourth day of alteration.

In order to trace fluid infiltration into and their percolation through the shell we performed major and minor element chemical analyses by EPMA. The distribution patterns of sodium, chlorine and strontium are shown as characteristic examples (Figs. 2.19-2.21). Fluids enter the shell through pores and along growth lines, as demonstrated by the perfect correspondence between increased Na and Cl contents and the outlines of annual growth lines indicated by elevated Sr contents (Fig. 2.19).
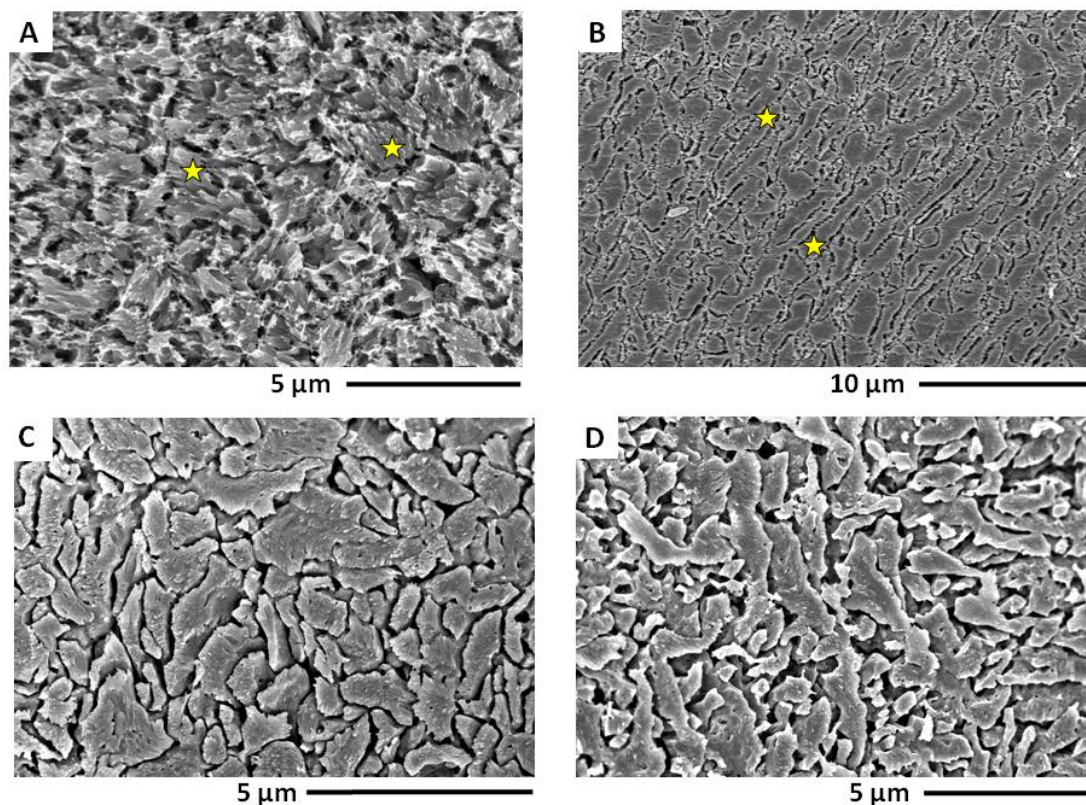
Figure 2.4: FE-SEM micrographs of cut, microtome-polished, etched, and critical-point-dried surfaces of experimentally altered *Arctica islandica* shell materials: (A, C) outer shell layer and (B, D) inner shell layer. Etching occurred for 180 s and was applied for the visualisation of the spatial distribution of (glutaraldehyde-stabilised) biopolymers within the shell; 10 mM NaCl + 10 mM MgCl$_2$ aqueous solution (burial fluid) was used for alteration at 100 °C for 28 days (A, B) and at 175 °C for 7 days (C, D). Yellow stars in (A) and (B) indicate mineral units.
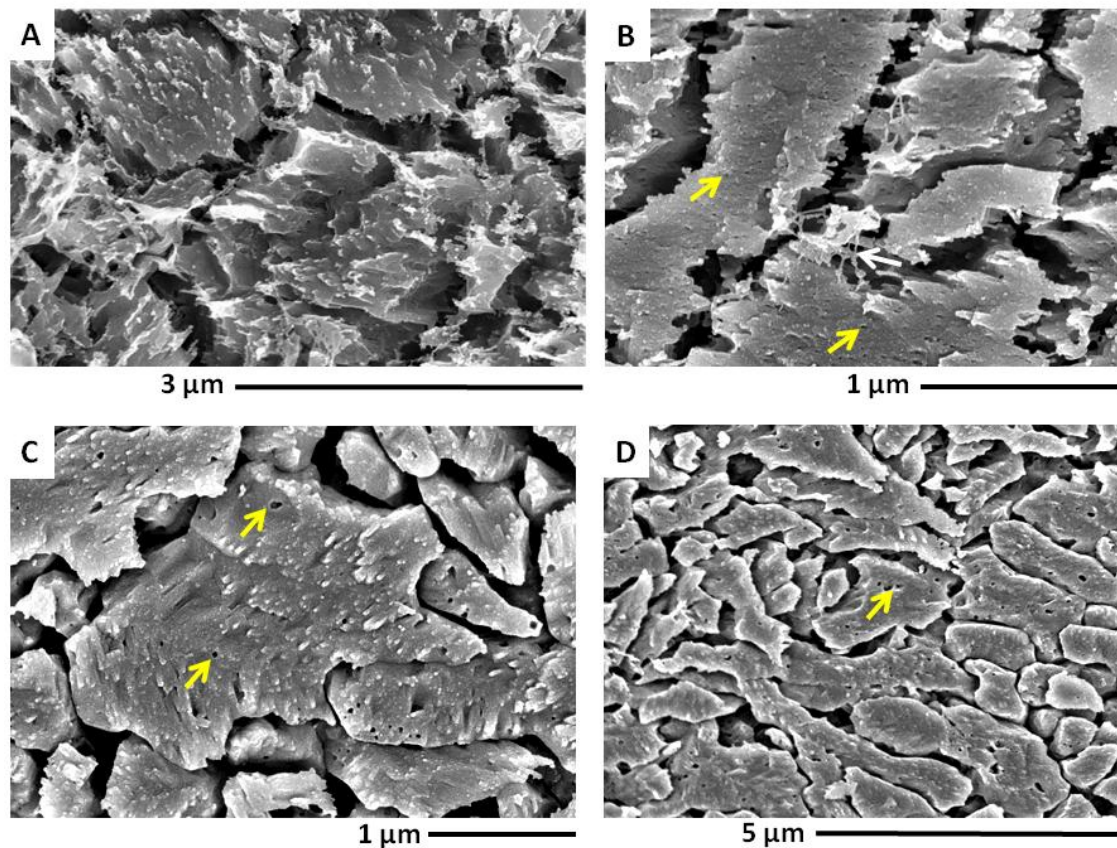
Figure 2.5: FE-SEM micrographs that zoom into experimentally altered *Arctica islandica* shell material shown in Fig. 2.4. 10 mM NaCl + 10 mM MgCl$_2$ aqueous solution (burial fluid) was used for alteration at 100 °C for 28 days (A, B) and at 175 °C for 7 days (C, D). Panels (A) and (C) show the outer shell layers; (B) and (D) depict material from the inner shell layers. The biopolymers have decomposed and dissolved in the material treated at 175 °C (C, D). Readily observable are minute round holes within the mineral units (yellow arrows in B, C, D) which were filled in the pristine shell, prior to alteration, by biopolymer fibrils. For further details concerning the interlinkage between mineral units and nanoparticles with organic matrices, see Figs. 2.22 and 2.23.

These growth lines are readily detected by an increase in Sr contents in pristine (Fig. 2.19A) as well as in hydrothermally altered shell samples (Figs. 2.20-2.21; see also Shirai et al., 2014). However, neither the temperature of hydrothermal alteration nor the chemistry of the alteration fluid has an influence on the amount of Sr present along growth lines. Relative to neighbouring shell increments, the Sr content along the growth lines is always higher (Shirai et al., 2014). Maximal concentrations (along annual growth lines) in pristine and altered shells vary between 0.4 and 0.6 wt % Sr (Figs. 2.19-2.21).

FE-SEM images of Figs. 2.4-2.5 highlight the grain structure and remnants of the organic matrix in hydrothermally altered *A. islandica* shells. In the case of the samples shown in Figs. 2.4-2.5, burial water was used as alteration solution; the hydrothermal treatment conditions were 100 °C for 28 days (Figs. 2.4A-B, Figs. 2.5A-B) and 175 °C for 7 days (Figs. 2.4C-D, Figs. 2.5C-D). SEM images on the left-hand side of Figs. 2.4 and 2.5

are taken of the outer shell layer, while SEM images on the right-hand side of Figs. 2.4 and 2.5 are taken of the dense inner shell layer. Alteration at 100 °C for 28 days did not change the internal ultrastructure of the shell significantly. The shape and size of the mineral units are retained and they are still interconnected with a few organic fibres (Figs. 2.4A-B, Fig. 2.5B). However, at 175 °C for 7 days, the formerly present network of biopolymer fibres and membranes has vanished completely (Figs. 2.4C-D, Figs. 2.5C-D). At higher magnification a multitude of tiny holes (indicated with yellow arrows in Figs. 2.5C-D and enlarged in Figs. 2.22A and 2.23B) become readily visible. In the unaltered shell, these holes were filled with the network of biopolymer fibrils interconnecting the mineral units (e.g., Fig. 2.3B). The tiny holes in the mineral units start to become visible even in the samples altered at 100 °C (yellow arrows in Fig. 2.5B). Although at 175 °C shell aragonite has been replaced by large calcite crystals (see following the description of results), etching still outlines a grain fabric on the size scale of the former bio-aragonite crystal units (Figs. 2.4C-D). The newly formed fabric resembles that of a fine-grained inorganic ceramic material.

Aragonite crystal orientation patterns of modern *A. islandica* shells and those altered at 100 °C are presented in Figs. 2.6, 2.24, and 2.25 with EBSD greyscale band contrast images (upper images of Figs. 2.6A-C, Fig. 2.24), EBSD colour-coded orientation maps (lower images of Figs. 2.6A-C), and corresponding pole figures. Figure 2.6E gives grain area information deduced from the EBSD measurements which are shown in Figs. 2.6A-C. Alteration occurred at 100 °C, over a period of 28 days, and took place in simulated meteoric (Fig. 2.6B) and burial fluid (Fig. 2.6C, Fig. 2.24), respectively. The microstructure and texture of pristine *A. islandica* shell material is shown in Fig. 2.6A. The crystallographic co-orientation in pristine and altered *A. islandica* shells is axial with the c-axes (setting a = 4.96 Å, b = 7.97 Å, c = 5.74 Å, space group *P*mcn) pointing approximately perpendicular to the growth lines. Co-orientation of the aragonite crystallites in the outer shell layer, even in the modern *A. islandica*, is very low with MUD values of 12 (Fig. 2.6A) and 32 (Fig. 2.25A).

Hydrothermal treatment of *A. islandica* at 100 °C does not produce a significant change in aragonite co-orientation pattern, texture, grain fabrics, and grain size distributions. The pristine and hydrothermally treated shell materials appear to be quite similar. Small changes in MUD values may be attributed to the fact that it was impossible to locate the EBSD scan fields on the different samples in exactly corresponding spots with respect to the outer shell margin and to the patterns of annual growth lines. Figure 2.7 and Figures 2.24B-C show microstructure and texture characteristics deeper within the shell (Fig. 2.7A, Figs. 2.24-2.25) and at the innermost margins next to the inner shell layer (Figs. 2.7C-D; alteration in simulated meteoric fluid: Figs. 2.7A-D; alteration in simulated burial fluid: Figs. 2.7E-F). In the EBSD band contrast map of Fig. 2.7A we clearly see the change in microstructure from the outer shell layer
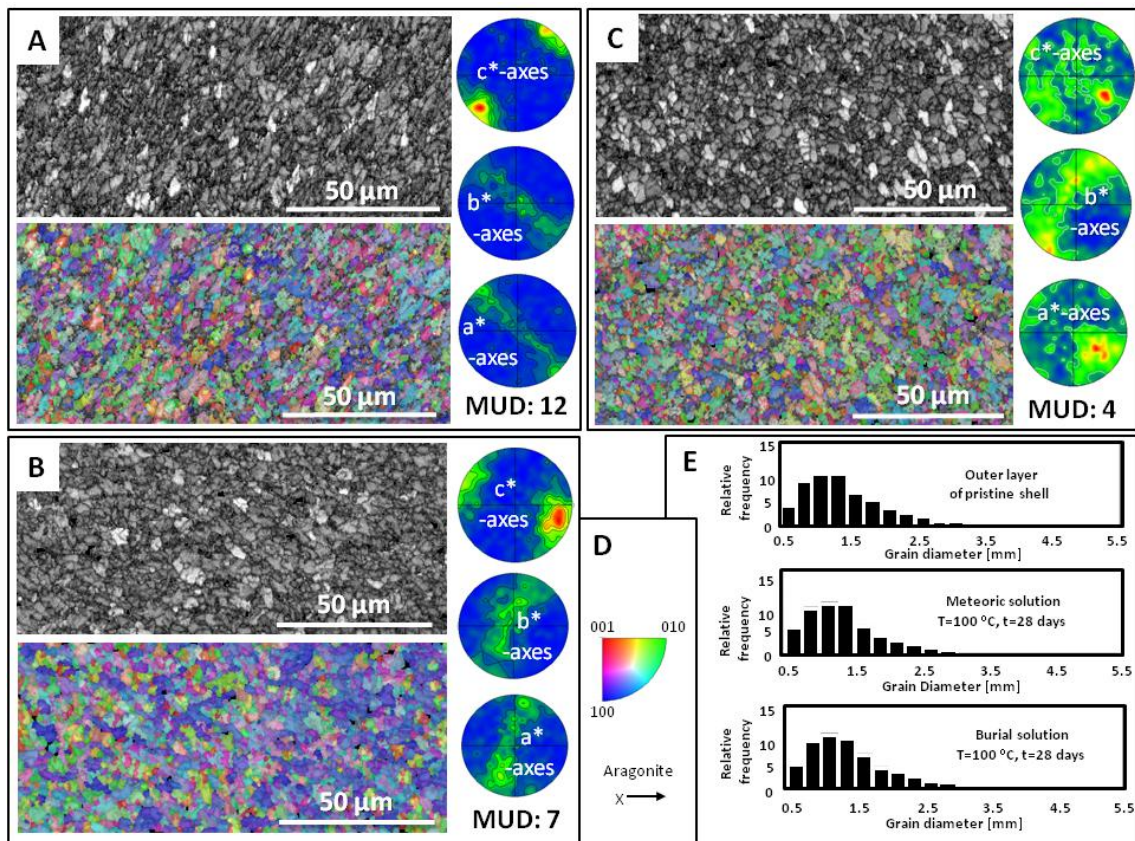
Figure 2.6: EBSD band contrast images (greyscale) and orientation maps (coloured; colour code given in panel D) with corresponding pole figures of pristine (A) and experimentally altered (B, C) *Arctica islandica* shell material. In the pole figures, colour is coded for pole density, with the maximum in red corresponding to the given MUD value for each set of pole figures, respectively. All EBSD measurements were taken on the outer shell layer. Hydrothermal alteration was applied for 28 days at 100 °C. The solutions used were artificial meteoric fluid in (B) and artificial burial fluid in (C). As the pole figures show, in comparison to the microstructure of pristine *A. islandica* (A), the crystal orientation pattern in the skeleton is not affected by treatment with the solutions. (E) Grain diameter statistics for pristine and experimentally altered *A. islandica* shell material obtained from the EBSD measurements are shown in (A)–(C). There is no significant difference in grain size between pristine and hydrothermally altered *A. islandica* shells.

with the larger aragonite crystals (yellow star in Fig. 2.7A) to the inward shell layer where aragonite crystals become small to minute (white star in Fig. 2.7A, Figs. 2.24B-C). As the pole figures and MUD values demonstrate, the axial *c-* and *a*-axes' co-orientation increases gradually towards the inner shell layer where MUD values of almost 100 are reached (Figs. 2.7D and F, Figs. 2.24-2.25).

Using XRD we obtained an overview of the kinetics of the *A. islandica* biogenic aragonite by calcite replacement under hydrothermal conditions up to 175 °C in artificial burial solution (Figs. 2.8A-B, Fig. 2.26). A representative Rietveld plot of the analysis of the XRD data obtained for the 6-day alteration is given in Fig. 2.27. As Fig. 2.24 demonstrates, experiments below 175 °C show no signs of a replacement reaction of bio-aragonite to inorganic calcite in the XRD bulk measurements. At 175 °C in simulated

burial solution, calcite formation starts after a passive period of about 4 days (Figs. 2.8A-B, Fig. 2.26) and then proceeds rapidly. After 7 days only a few patches of aragonite in the dense shell layer are not yet completely replaced by calcite (as seen in the EBSD investigations, unaltered shell areas are indicated with white rectangles in Fig. 2.1A). After 8 days the replacement by calcite is complete.
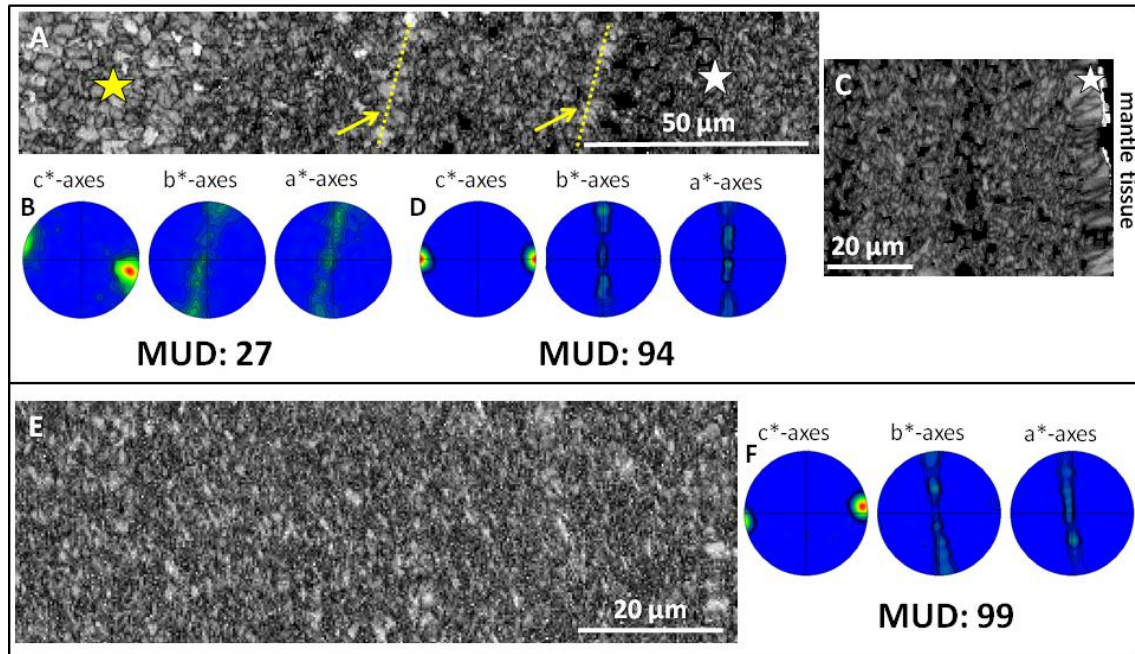
Figure 2.7: EBSD band contrast images (greyscale) and corresponding pole figures of hydrothermally altered (100 °C for 28 days) *Arctica islandica* shell material with artificial meteoric fluid (A, B, C, D) and artificial burial fluid (E, F). In (A) the change in shell microstructure is visible from the outer shell layer which contains large aragonite crystals (yellow star in A) and many pores, in contrast to the inner shell layer, which consist of densely packed small aragonite crystallites (white star in A). In (C) and (E) band contrast maps and pole figures are shown that were taken on the inner shell layer. As the pole figures and the high MUD values in (D) and (F) highlight, this part of the shell remains almost unaltered, and the pristine *A. islandica* microstructure is kept. In (A) two yellow arrows and two dashed lines indicate the location of former growth lines where, in pristine shells, an increased amount of organic material is present. As the latter is destroyed during hydrothermal alteration, space becomes available for infiltration of fluids. For further details, see Fig. 2.24.
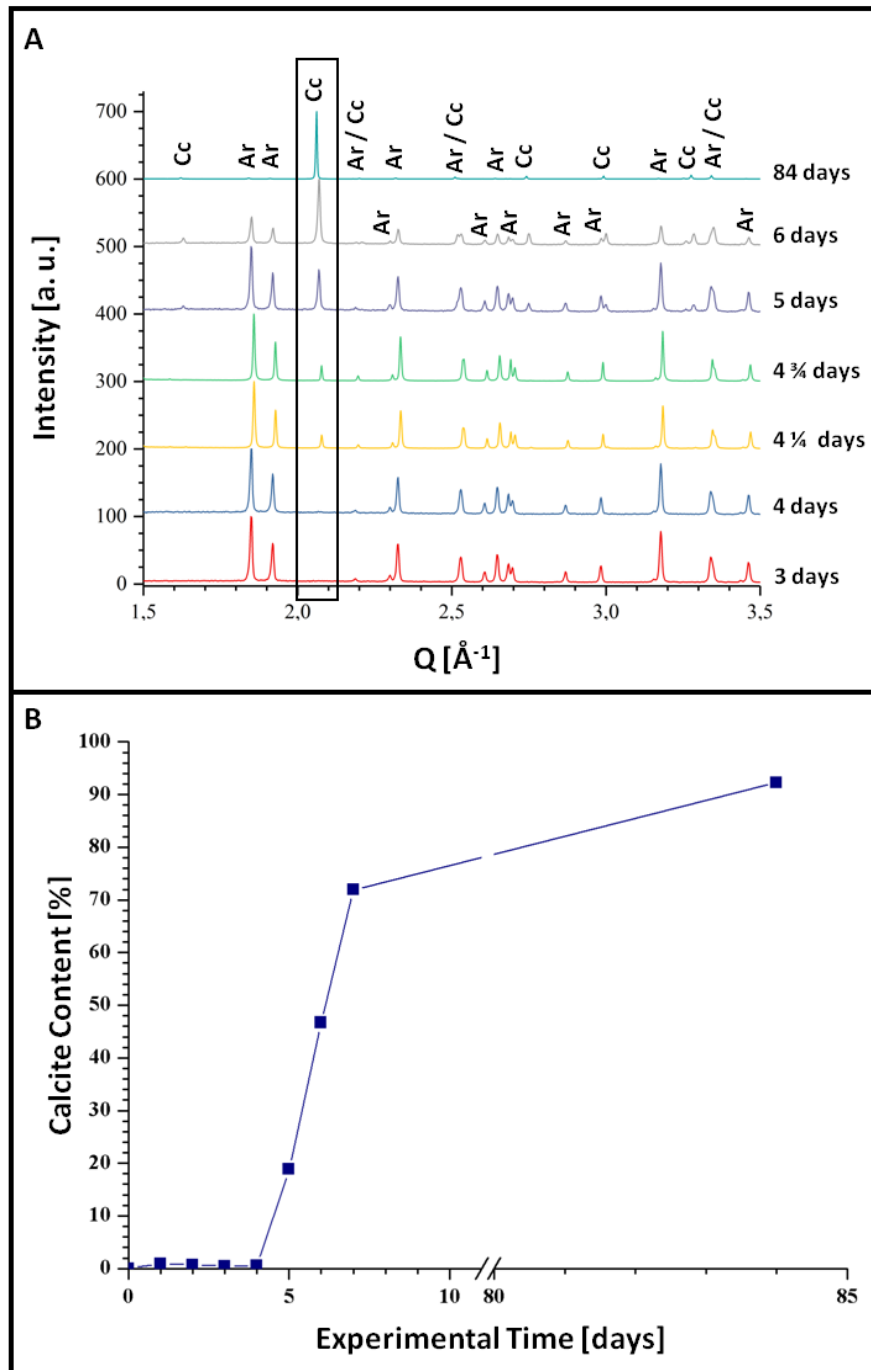
Figure 2.8: (A) Selected X-ray diffractograms for 3 to 84 days of alteration of *Arctica islandica* shell material. Alteration took place in artificial burial solution at 175 °C. (B) Newly formed calcite content relative to alteration time (days) calculated from Rietveld analyses of the XRD measurements.
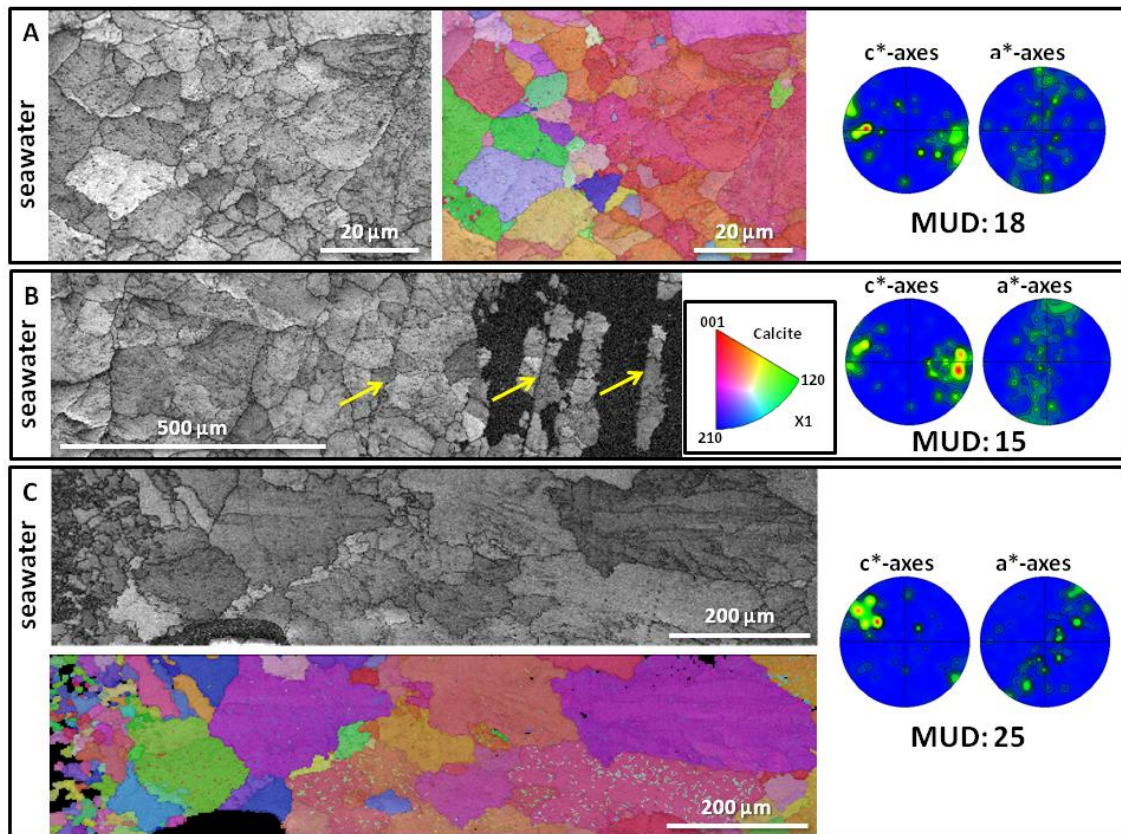
Figure 2.9: EBSD band contrast maps, colour-coded orientation maps, and corresponding pole figures highlight the microstructure and texture of *Arctica islandica* shells altered at 175 °C in artificial meteoric solution. EBSD measurements shown in (A) and (B) were taken on shells which were subject to hydrothermal alteration for 7 days. Measurements shown in image (C) refer to shells where alteration lasted for 84 days. At 175 °C, for both alteration times, aragonite was almost completely replaced by calcite, and the shell microstructure is characterised by large and randomly oriented calcite crystals. The initial growth of calcite is visible at the location of former growth lines (yellow arrows in B). For further microstructural details of the pristine shell material, see Fig. 2.24.
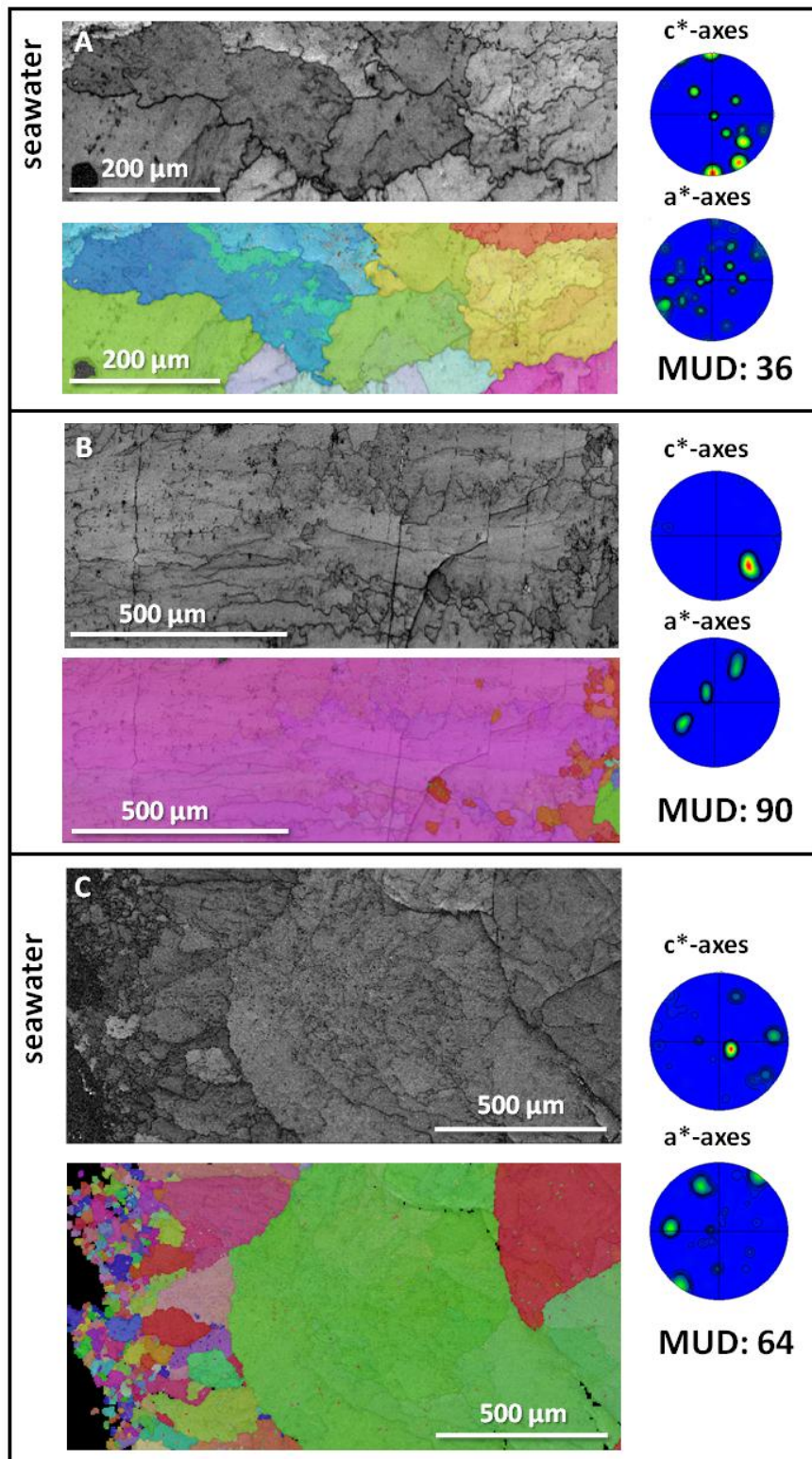
Figure 2.10: EBSD band contrast maps and colour-coded orientation maps with corresponding pole figures for hydrothermally altered *Arctica islandica* shells at 175 °C in water simulating burial diagenesis. EBSD measurements shown in (A) and (B) were taken on shells which were subject to hydrothermal alteration for 7 days, while the measurement shown in (C) was performed on shells where alteration lasted for 84 days. At 175 °C, for both alteration times, most of the aragonite has been replaced by calcite.
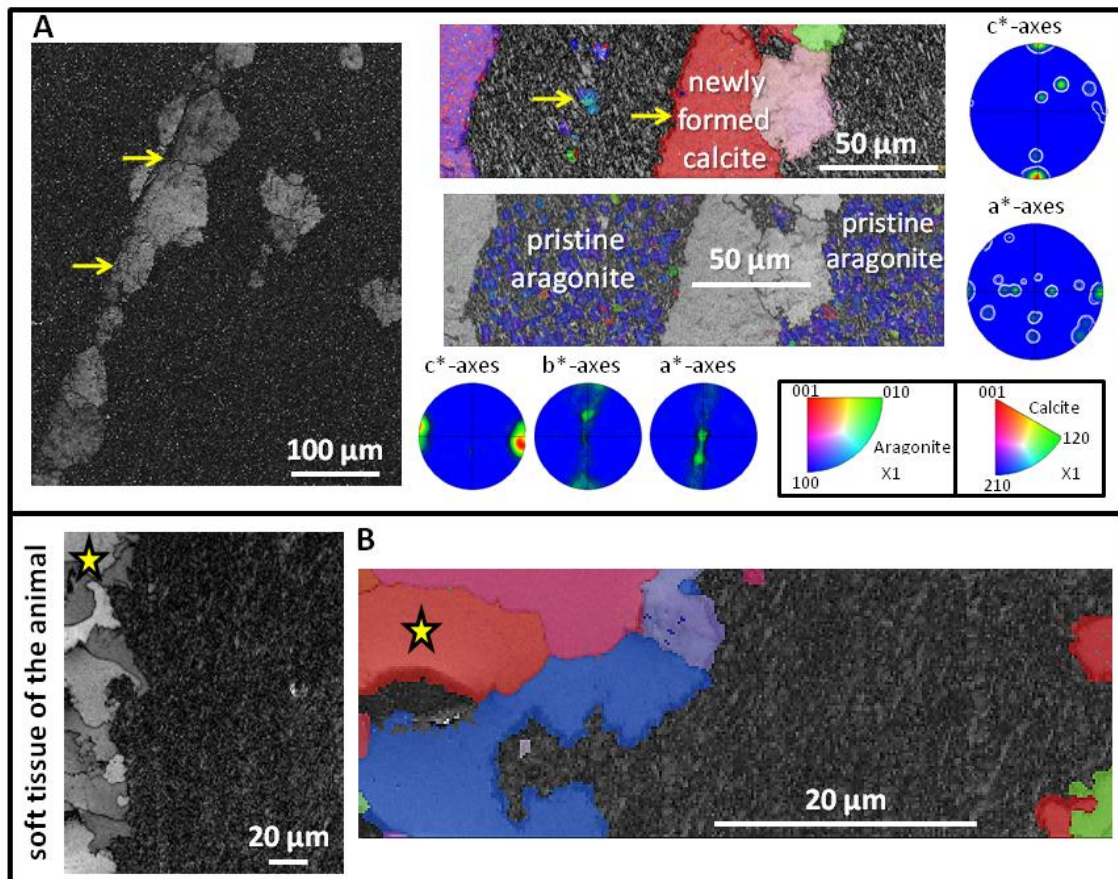
Figure 2.11: EBSD band contrast (in grey), crystal orientation (colour-coded for orientation) maps, and corresponding pole figures of altered *Arctica islandica* shells at 175 °C in artificial meteoric (A) and burial (B) solution. Clearly visible is the initial formation of calcite at the location of former growth lines (yellow arrows in A) and the growth of large calcite crystals (yellow stars in B) which formed at the shell area which is in direct contact with the alteration solution. Note that some pristine aragonite in the dense shell layer is still present.

EBSD data clearly shows that after a hydrothermal treatment at 175 °C, with either simulated meteoric or burial fluid, shell aragonite is replaced by calcite (Figs. 2.9-2.11). In the outer shell layer the replacement reaction to calcite is complete with the development of large crystal grains; some reaching sizes of hundreds of micrometres (see EBSD maps in Figs. 2.9-2.10). In contrast, dense shell regions devoid of pores still retain patches of the original aragonitic microstructure and texture (coloured EBSD maps in Figs. 2.11A-B). The MUD values for the newly formed calcite material are high (Figs. 2.9-2.10), but this is related to the fact that, within the range of the EBSD scan, just a small number of large, newly formed, individual crystals is encountered. Figure 2.11 shows shell regions where patches of aragonite have survived which contain first-formed calcite. Calcite nucleation sites are the locations where the experimental fluid has access to the shell: at its outer and inner surfaces (yellow stars in Fig. 2.11B) and at growth lines (yellow arrows in Fig. 2.11A). Figure 2.11A demonstrates how calcite crystals form strings along linear features, which correspond to growth lines in the pristine shell material.

51

2.1.5 Discussion

<u>Driving force in comparison to nucleation barrier</u>

In sedimentary environments the fate of metastable biogenic aragonite or high-Mg calcite can follow two scenarios: (1) the metastable biogenic matter can be completely dissolved and removed by fluid transport to form moulds which are later filled by cement or other neogenic minerals or (2) the metastable minerals may be replaced by stable low-Mg calcite in situ through a process which involves dissolution of the metastable phase into a nano- to microscale local fluid volume (e.g., a thin fluid film) from which the stable low-Mg calcite precipitates without long-range transport (Brand and Veizer, 1980, 1981; Brand, 1991, 1994; Bathurst, 1994; Maliva, 1995, 1998; Maliva et al., 2000; Titschak et al., 2009; Brand et al., 2010). The latter process may preserve original morphological boundaries and microstructures such as prisms, tablets and fibres in bivalve shells. The replacement reaction from aragonite to stable low-Mg calcite is driven by the higher solubility (free energy) of the metastable phase compared to the stable phase. Thus, as the replacement reaction proceeds, the reactive, percolating experimental or diagenetic pore fluid becomes undersaturated with respect to aragonite owing to its relative supersaturation with respect to calcite, the less soluble mineral phase in the system. In a fluid which draws its calcium and carbonate ions from the dissolution of aragonite, the maximal supersaturation Ω_{max} with respect to calcite can be described as

$$\Omega_{max} \; = \; \frac{K_{sp} \, (\text{aragonite})}{K_{sp} \, (\text{calcite})}, \tag{eq. 3},$$

where K_{sp} stands for the ion activity products of the respective phase in the relevant pore fluid. The free energy difference or thermodynamic driving force is given by $\Delta G_{max} = -RT \ln \Omega_{max}$. To obtain an estimate we used the data of Plummer and Busenberg (1982) and calculated the solubility products for calcite and aragonite for 25, 100, and 175 °C (Fig. 2.12). The maximal supersaturations Ω_{max} thus obtained are 1.39 (25 °C), 1.26 (100 °C), and 1.18 (175 °C). The replacement reaction first requires a nucleation step: the formation of the first calcite crystallites larger than the critical size r^* (Morse et al., 2007). Empirical nucleation theory relates the activation energy $\Delta G_A(r^*)$ necessary to form a nucleus of critical size to the specific surface energy σ needed to form the interface between the nucleating phase and the matrix phase as

$$\Delta G_A(r^*) \propto \frac{\sigma^3}{(-RT \ln \Omega)^2} \tag{eq. 4}.$$
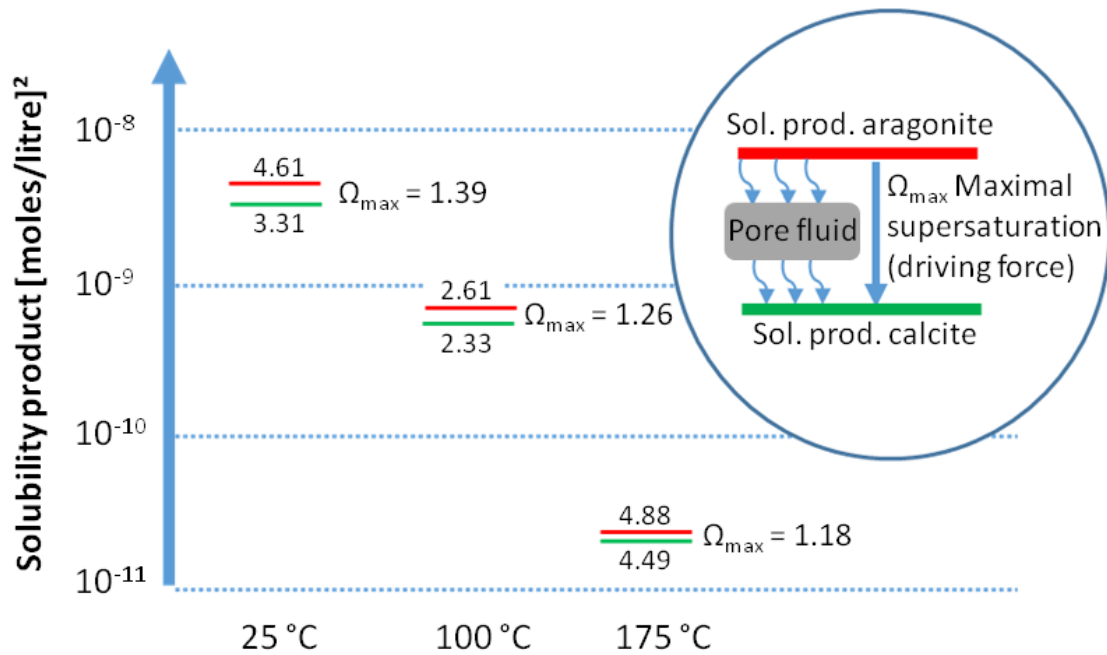
Figure 2.12: Solubility products of aragonite and calcite calculated from the data of Plummer and Busenberg (1982). The labels at the ordinate give the powers of 10, and the numbers in the plot give the mantissa of the SP. Ωmax is the difference between the value for aragonite (red) and calcite (green), and it is the upper bound of the supersaturation available to drive calcite precipitation from aragonite dissolution (thermodynamic driving force Δmax = RT ln Ωmax). To drive dissolution of aragonite and precipitation of calcite at non-zero rates, the pore fluid needs to be undersaturated with respect to aragonite and supersaturated with respect to calcite.

Only supercritical nuclei or pre-existing seed crystals of size $r > r^*$ of calcite can lower their free energy as their volume of free energy gained by growth exceeds the adverse energy contributions of increasing interface area. To obtain a significant number of supercritical nuclei a critical supersaturation needs to be reached (Morse et al., 2007; Gebauer et al., 2008; Nindiyasari et al., 2014; Sun et al., 2015). Reported values for critical supersaturation levels Ω_{crit} required for calcite nucleation in various conditions range from the order of 3.7 (Lebron and Suárez, 1996; Zeppenfeld, 2003) to the order of 30 (Morse et al., 2007; Gebauer et al., 2008) or even several hundred in, for example, hydrogel matrices (Nindiyasari et al., 2014). The density functional theory study of Sun et al. (2015) arrives at Ω_{crit} = 5 for systems free of inhibitors such as Mg, and Ω_{crit} = 35 for modern seawater. Accordingly, the supersaturation produced by the dissolution of aragonite is very small compared to supersaturation levels typically required for the nucleation of calcite. Thus, we can expect that nucleation is a critical kinetic step in the replacement reaction of aragonite by calcite.

Aragonite metastability at 100 °C up to 160 °C

In our laboratory-based hydrothermal alteration experiments at 100 °C in both simulated meteoric and burial fluids, the aragonite mineral and the characteristic biological microstructure survive the hydrothermal treatment up to at least 28 days. In experiments at 125 °C and 150 °C we did not see any calcite formation from the bio-aragonite either. This is consistent with the findings of Ritter et al. (2017), who analysed the light-stable isotope signatures ($\delta^{13}C$, $\delta^{18}O$) of hydrothermally treated samples. In the 100 °C alteration experiments using isotope-doped experimental fluids, Ritter et al. (2017) found that the carbon and oxygen isotope ratios of the treated shells are within the same range as those measured in the pristine samples. Furthermore, no obvious patterns emerge from the comparison of sub-samples exposed to seawater, meteoric, and burial fluids. Most of the extensive literature on aragonite precipitation from aqueous solutions and aragonite-calcite replacement reactions in aqueous environments, as reviewed in the introduction, makes it clear that both temperatures around the boiling point of water and the presence of Mg^{2+} inhibit calcite nucleation. Thus, the inhibition of calcite nucleation favours the growth of aragonite if the solution is supersaturated with respect to the calcium carbonate phases. If supersaturation is exceedingly high and rapidly generated, vaterite or even amorphous calcium carbonate will precipitate and reduce the supersaturation below the levels required for aragonite or calcite nucleation (Navrotsky, 2004; Gebauer et al., 2008, 2011; Radha et al., 2010). However, it is unlikely that these levels of supersaturation are reached in our case, as aragonite is already present. We thus conclude that the absence of an aragonite by calcite replacement reaction in our 100-150 °C treatments is related to inhibition of calcite nucleation (Sun et al., 2015), a mechanism that has rarely been rigorously explored.

Dormant period followed by rapid reaction at 175 °C

At 175 °C the replacement reaction of biogenic aragonite to coarse-grained calcite occurs rapidly; it starts after a dormant period of about 4 days and proceeds rapidly almost to completion after 3 more days (Figs. 2.8 and 2.26). However, even after 84 days about 5 % of residual aragonite is still present. Calcite nucleation occurs (and replacement reaction proceeds) where the experimental fluid is in contact with the bio-aragonite: at the surfaces of the shell, in pores and along growth lines (Figs. 2.9B, 2.11, and 2.19-2.21).

Nucleation and the time lag of the aragonite by calcite replacement reaction at 175 °C

A certain time lag in the hydrothermal treatment experiments is expected for the initial dissolution of shell aragonite to build up a sufficiently high ion activity product in the solution to precipitate any calcite. However, the several-day dormant period followed by the rapid growth of calcite indicates that the nucleation of calcite is inhibited, at least initially. We discussed in the previous section that the thermodynamic potential (supersaturation) for the formation of calcite from a fluid which is able to dissolve aragonite is smaller than the critical supersaturation required to obtain a discernible nucleation rate for calcite in normal laboratory experiments. The presence of magnesium in the solution further inhibits calcite nucleation, as do high temperatures between 70 and 160 °C (Kitano et al., 1962, 1972; Taft, 1967; Katz, 1973; Berner, 1975; Morse et al., 1997; Choudens-Sánchez and Gonzáles, 2009; Radha et al., 2010; Perdikouri et al., 2011, 2013; Balthasar and Cusack, 2015; Sun et al., 2015), which is supported by the lack of calcite formation in our experiments between 100 and 150 °C (Table 2.1, Fig. 2.26). A possible scenario explaining the dormant period could be simply that the nucleation rate of calcite is extremely small due to the limited supersaturation but is non-zero. Once a few nuclei formed after a few days the actual growth process proceeds rapidly. Another scenario may be the initial, rapid formation of a passivation layer on the surface of the aragonite or on the surface of any calcite nuclei; the dormant period is then the time that is needed to dissolve this passivation layer, at least in some places, where subsequently calcite nuclei of critical size can form. In order to explain this second scenario we can only speculate that, after initial dissolution of the biogenic aragonite with excess free energy due to its hybrid nanoscale composite structure, an inorganic aragonite precipitates first on the surface of the biogenic aragonite.

Grain size and chemistry of the newly formed calcite

Compared to the nano- to microscale grain fabric of the original aragonite material, the newly formed calcite crystals are remarkably large. In meteoric solutions the grain size of the newly formed calcite reaches 200 μm (e.g., Fig. 2.9C), while in the Mg-bearing burial solution newly formed calcite crystals reach sizes in the 1 mm range, in both the 7- and 84-day treatments (e.g., Figs. 2.10B-C). The large calcite grains obtained can very likely be the result of the formation of very few calcite nuclei.

Other explanations for the formation of large calcite grains from the original nano- to microscale grain fabric may be Ostwald ripening or strain-driven grain growth of the newly formed calcite. The latter could be expected due to the 8.44 % volume

increase when the denser aragonite is replaced by calcite. To elucidate this possibility we determined the *local misorientation* within the calcite crystals from the EBSD data sets. Maps showing small lattice orientation changes between neighbouring measurement points highlight high dislocation densities and subgrain boundaries, which may have been introduced during the replacement reaction by stresses.

Figure 2.13 depicts the distribution pattern of local misorientation within five selected EBSD maps (Figs. 2.13B, E, H, K, N). Legends accompany all local misorientation maps (Figs. 2.13C, F, I, L, O). Blue colours indicate the absence of measurable internal misorientation, while light-green to yellow colours highlight areas where local misorientation is larger than experimental resolution. Grains in Fig. 2.13 are defined by a *critical misorientation* selected as 5 ° (i.e., tilts smaller than 5 ° are counted as subgrain boundaries in the mosaic structure of the crystals).
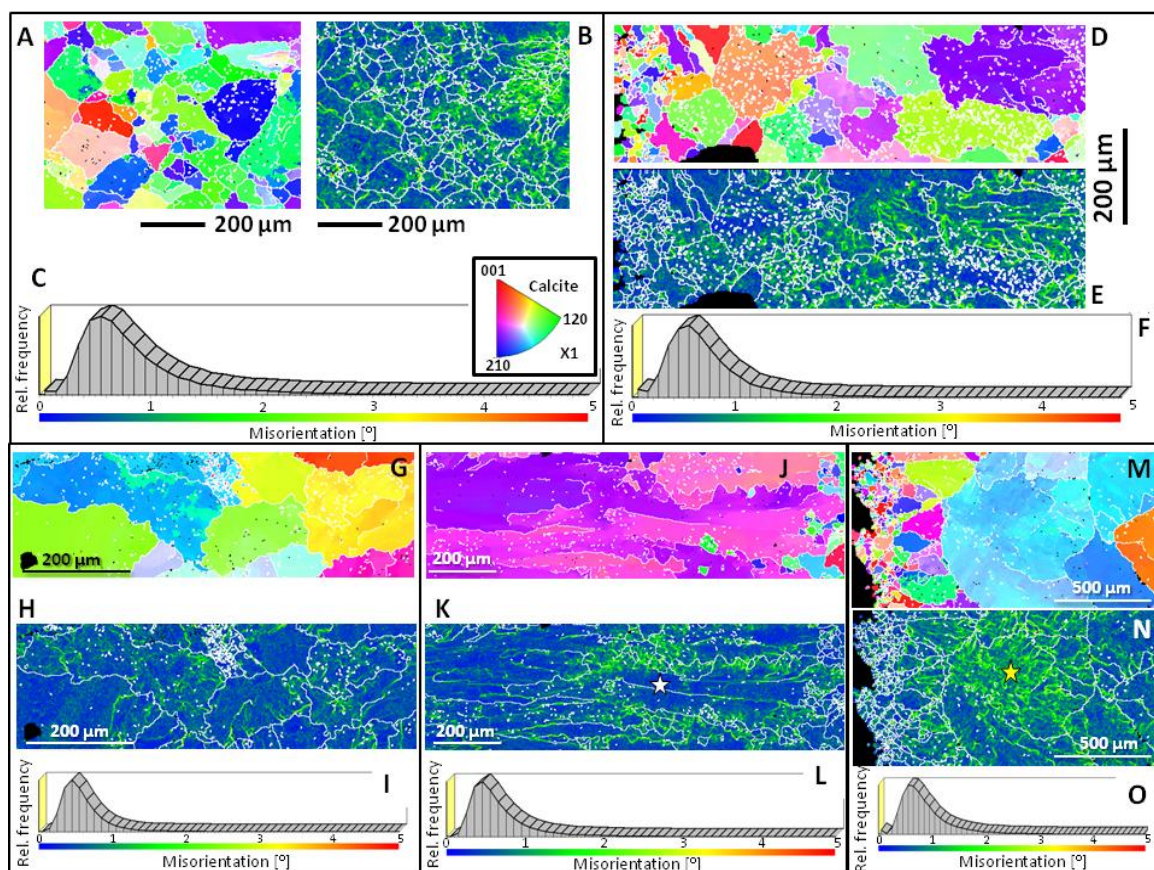
Figure 2.13: Calcite grain structure (A, D, G, J, M; inverse pole figures colours as indicated in the insert in C) and maps of grain-internal local misorientation distribution (B, E, H, K, N, scales and probability distributions given in C, F, I, L, O) for experimentally altered shells of *A. islandica* carried out in simulated meteoric solution at 175 °C for 7 (A-C) and 84 days (D-F), and in burial solution at 175 °C for 7 (G-L) and 84 days (M-O). Grains are defined by using a critical misorientation of 5 °. Local misorientation reaches up to 2-3 ° (see legends in C, F, I, L, O), irrespective of alteration duration and solution. The white star in (K) marks stress-free shell areas, while the yellow star in (N) indicates the location of an increased stress accumulation.

For better visualisation of individual grains, we outlined these with white lines. In Figures 2.13G, J, and M the mosaic structure in the grains is visible in inverse pole figure colouring reflecting lattice orientation. In all five investigated data sets the grain-internal local misorientation reaches up to 2 °; thus, neither alteration time nor the chemical composition of the alteration solution used shows any discernible influence on the degree of strain accumulation within the calcite grains. Figure 2.14 compares the subgrain (mosaic) structure of two large calcite grains obtained in the same experimental fluid at 175 °C, where one grain is from the 7-day treatment, and the other from the 84-day treatment. The grains are marked by stars in Figs. 2.13K and N, respectively. In these maps of Fig. 2.14 the colour is coded for misorientation relative to a common reference point, rather than for local misorientation. Corresponding legends are given below the grains. The internal misorientation (mosaic spread) for the grain obtained in the 84-day treatment is much higher than that in the grain obtained in the 7-day treatment. We find that the local misorientations are mainly curvilinear structures in the cross section (white arrows in Figs. 2.14A and C) and correspond to subgrain boundaries within the newly formed calcite crystals. These boundaries do not appear to heal or to disappear with an increased alteration time, an indication again of the negligible effect of alteration duration on the fabric and internal structure of calcite grains crystallised from *Arctica islandica* shell bio-aragonite.

To further investigate potential grain growth patterns, we took a statistical approach in the analysis of the EBSD measurements shown in Figs. 2.9-2.10 (alterations experiments carried out for 7 and 84 days at 175 °C in simulated meteoric and burial solution, respectively). Figures 2.14A and B show the statistics of grain area (again, we define a grain by a critical misorientation of 5 °) versus mean misorientation within a grain. Based on these statistics, we do not see major evidence for a specific calcite grain growth phenomenon with an increase in alteration time between 7 and 84 days, with the exception of three extremely large grains in the 84-day treatment in burial solution. However, we find that experiments conducted with the Mg-containing burial solution yield larger calcite crystals (black arrows in Fig. 2.15B) in comparison to the size of the grains obtained from experiments carried out with meteoric water (Fig. 2.15A). Grains obtained from alteration experiments with meteoric fluid show a significantly higher degree of mean misorientation (up to 10 °, black arrows in Fig. 2.15A), compared to the grains that grew in burial solution. Large mean misorientations of >4 ° occur notably in the grains grown in the 7-day treatment in meteoric solution, while the corresponding 84-day treatment does not show a significant increase in grain area compared to the 7-day treatment.

In summary, the observations do not support scenarios of Ostwald ripening or strain-driven anomalous grain growth as the reasons of the large calcite grains. We attribute the large calcite grains to the nucleation rate: the crystals growing from each

nucleus consumed the aragonite educt (the precursor, original aragonite) until they abutted each other. Thus, larger crystals in the experiment with burial solution result from a smaller number of calcite nuclei, which may be attributed to the presence of aqueous Mg in the experimental fluid. Note here that both the reduction in Mg concentration in the reactive fluid, compared to that in the initial burial fluid (see Table 2.1), and speciation calculations suggest that the formation of Mg-bearing carbonate minerals (magnesite and/or dolomite) is likely possible to occur at the experimental conditions. Indeed, we observe small patches of newly formed Mg-rich carbonates (Fig. 2.28). The formation of such minerals occurs at lower rates compared to pure Ca-bearing carbonates owing to the slow dehydration of aqueous Mg that is required prior to its incorporation in the crystal (e.g., Mavromatis et al., 2013) even at temperature as high as 200 °C (Saldi et al., 2009, 2012).

The newly formed calcite contains only small amounts of magnesium (Table 2.3) in the order of 0.1 wt% (or 0.006 in the formula unit), while the strontium content of the original aragonite in the order of 0.4 wt% is retained in the calcite (0.005 in the formula unit). The local formation of Mg-rich carbonates occurs at some places at the rim of the sample, where it is in direct contact with the bulk of the experimental fluid (Fig. 2.28B and Table 2.3). In these patches, measured Mg contents reach up to 19.7 wt% (0.716 in the formula unit, encountered in scan field 3 at the outer rim of the sample). The averaged composition in scan fields 4 and 9 in Fig. 2.28B may indicate dolomite, but like scan field 3, which has a Mg content exceeding that of dolomite, we more likely have magnesite with some calcite present, as judged from the EPMA map (Fig. 2.28B).

The aragonite by calcite replacement reaction kinetics

Inorganic experiments on aragonite replacement by calcite at 108 °C under hydrothermal conditions were reported by Bischoff and Fyfe (1968) and by Bischoff (1969). These authors used fine-grained powders as educts (the precursor, original material) and observed a comparatively rapid replacement by calcite which was complete within 48 h, depending on the composition of the fluid. For example, larger CO_2 partial pressure (leading to lower pH, and thus, larger solubility of the carbonates) accelerated, while the presence of Mg ions retarded the process. This rapid reaction kinetics as reported by Bischoff and Fyfe (1968) and by Bischoff (1969) is inconsistent with our observations. We do not see a replacement reaction of the biogenic aragonite by calcite at 100 °C even within 28 days. Hydrothermal experiments by Metzger and Barnard (1968) and by Perdikouri and co-workers (2011, 2013), however, who used aragonite single crystals in their experiments, report reaction kinetics which correspond very well to our observations. They do not observe any evidence of the replacement reaction at 160 °C even within 1 month but rather a partial replacement of their aragonite crystals by calcite
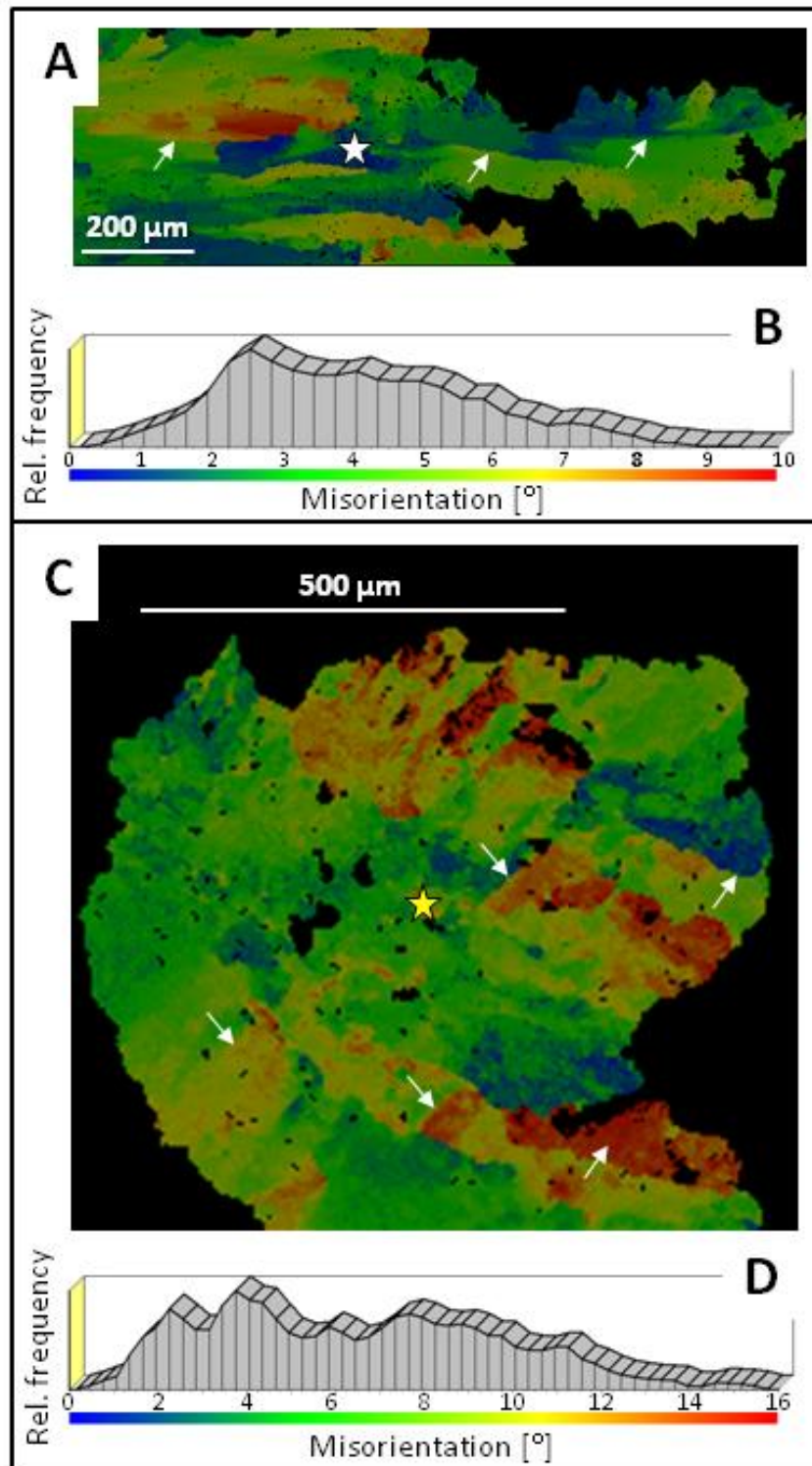
Figure 2.14: Colour-coded visualisation (A, C) and degree of internal misorientation (B, D) within two large, millimetre-sized grains which grew in simulated burial solution at 175 °C for 7 (A) and 84 (C) days. The grain shown in (A) contains some stress-free areas within its centre (indicated by blue colours and the white star in A), while internal misorientation in the grain shown in (C) is highly increased and occurs everywhere within the grain (D). The yellow star in (C) points to the region where, in this grain, stress accumulation is highest.
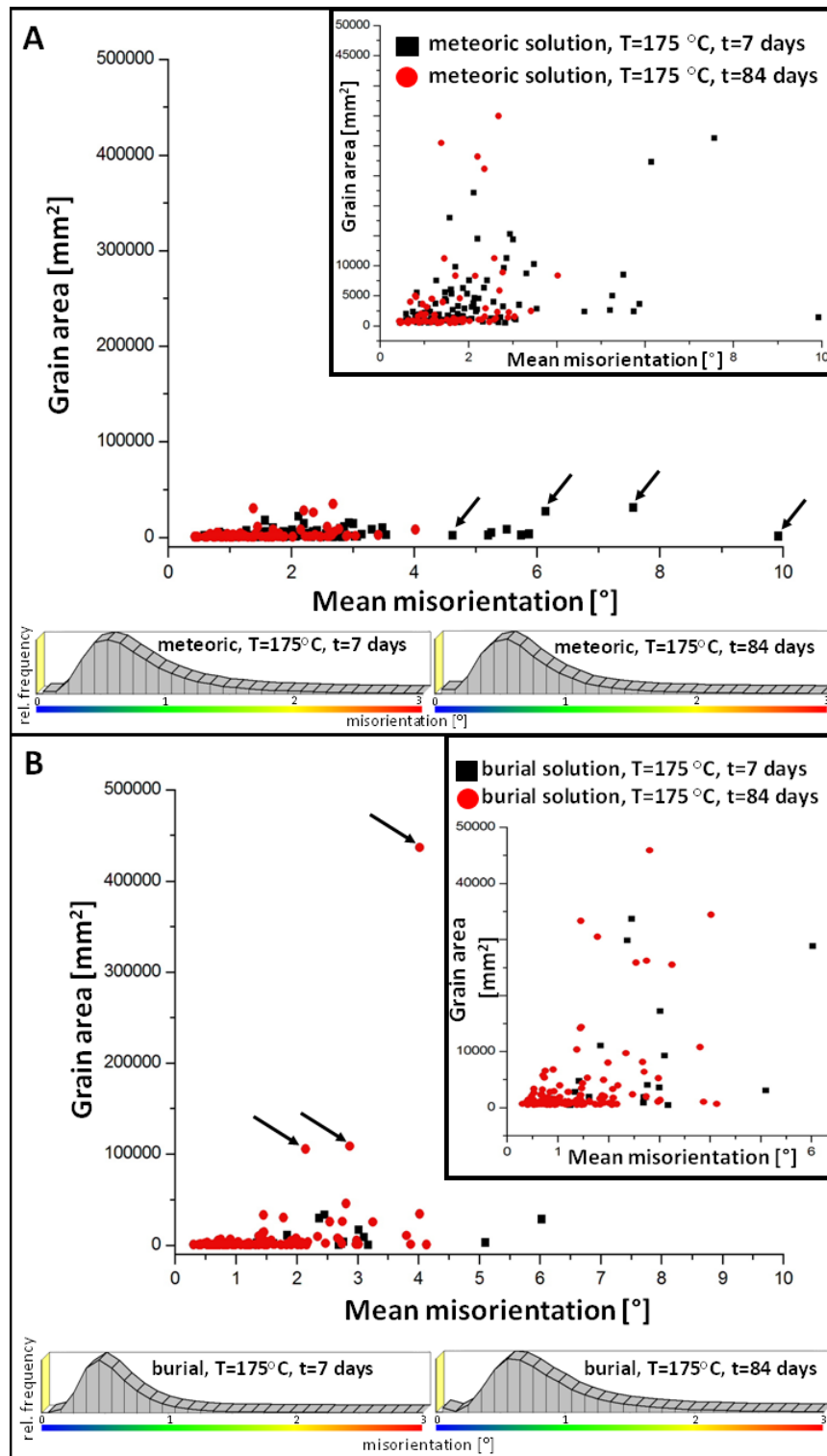
Figure 2.15: Grain area versus mean misorientation within individual grains obtained for newly formed calcite at alteration of *Arctica islandica* aragonite in artificial meteoric (A) and in burial (B) solutions at 175 °C and for 7 and 84 days, respectively. The Mg-containing (burial) alteration fluid induces the formation of large calcite grains that show a low degree of misorientation within the grains (B), while with artificial meteoric solution, the solution that is devoid of Mg, significantly smaller grains are obtained. However, the latter occur with a high mean misorientation within the individual, newly formed grains.

within 4 weeks at 180 °C. We observed that the fluids used (artificial meteoric and/or burial fluids) cause only a minor difference in replacement reaction kinetics in our experiments, with the $MgCl_2$-bearing artificial burial fluid reducing the nucleation rate of calcite, thus, leading to the observed significantly larger calcite crystals in the product. As compared to the work of Perdikouri et al. (2011, 2013) on aragonite single crystals, shell aragonite does not crack during the replacement of the aragonite by calcite. The reason for this difference may be ascribed to the porosity of the bio-aragonite, which results from the loss of its organic component. As Figures 2.5C-D, the band contrast and orientation maps of Figs. 2.6A-C illustrate, the (newly formed) calcite product reveals an internal structure which is very reminiscent of the original bio-aragonite–biopolymer composite. The structure arises as the solution penetrates along former sites of organic matrix (former aragonite grain boundaries), such that the structural features obtained after alteration still outline the former aragonite grains. Thus, limited grain sizes of the bio-aragonite together with the formerly biopolymer-filled spaces reduce any stresses which may be built up by the specific volume change of the $CaCO_3$ during the replacement reaction. The replacement process preserves original morphological features. Several studies (Putnis and Putnis, 2007; Kasioptas et al., 2008; Xia et al., 2009a; Putnis and Austrheim, 2010; Pollok et al., 2011) experimentally investigated mineral replacement reactions creating pseudomorphs, even reproducing exquisite structures such as the cuttlebone of *Sepia officinalis*. These studies conclude that the essential factor in producing pseudomorphs is the dissolution of the replaced parent material as the rate-limiting step once the replacement reaction proceeds, while the precipitation of the product phase and the transport of solution to the interface must be comparatively fast. The preservation of morphology – even as observed on the nano- to microscale – is ensured if nucleation and growth of the product immediately take place at the surface of the replaced material when the interfacial fluid film between the dissolving and the precipitating phase becomes supersaturated in the product after dissolution of the educt: an interface-coupled dissolution-reprecipitation mechanism (Putnis and Putnis, 2007). If dissolution of the educt is fast and precipitation of product is slow, more material is dissolved than precipitated, and the solutes can be transported elsewhere. Not only would this create an increased pore space which potentially collapses under pressure but the dissolved material would also eventually precipitate elsewhere with its own characteristic (inorganic) morphology rather than reproducing the educt morphology. The fact that some aragonite survives in the dense layers of the shell even after 84 days also points to a slow dissolution rate of aragonite at least in some parts of the shell. New medium-resolution techniques which are capable of mapping the space dependence of dissolution rates in situ (Fischer and Lüttge, 2016) may be able to shed some light on the different behaviour of different shell parts in the future.

A palaeontological perspective of our laboratory-based hydrothermal alteration experiments

The alteration experiments of recent *A. islandica* under controlled laboratory conditions are very important from a palaeontological perspective as they reproduce burial diagenetic conditions. The understanding of the diagenetic processes which control organism hard tissue preservation taphonomic, palaeoecological, and biostratigraphic studies (e.g., Tucker, 1990b). Most organisms have hard tissues composed of calcium carbonate, and its metastable form, aragonite, is one of the first bio-minerals produced at the Precambrian-Cambrian boundary (Runnegar and Bengtson, 1990), as well as one of the most widely used skeleton forming minerals in the Phanerozoic record and today. In fact, aragonitic shells/skeletons are produced by hyolithids, cnidarians, algae, and the widespread and diversified molluscs.

Several studies (Cherns and Wright, 2000; Wright et al., 2003; Wright and Cherns, 2004; James et al., 2005) have underscored that Phanerozoic marine faunas seem to be dominated by calcite-shelled taxa, the labile aragonitic or bimineralic groups being lost during early diagenesis (in the soft sediment, before lithification), potentially causing a serious taphonomic loss. Considering that most molluscs are aragonitic or bimineralic, this loss could be particularly detrimental both for palaeoecological and biostratigraphic studies. However, it has been shown that the mollusc fossil record is not so biased as expected (Harper, 1998; Cherns et al., 2008). This is due to abundant taphonomic scenarios such as early lithification/hardgrounds, storm plasters, anoxic bottoms, and high sedimentation rates that produce taphonomic windows allowing mollusc preservation (James et al. 2005; Cherns et al., 2008) by controlling organic matter content and residence time in the taphonomically active zone. Even if the factors that control aragonite dissolution are multiple and their interpretation is complex, the laboratory-based hydrothermal alteration experiments performed here offer very interesting insights into the fate of the aragonitic or bimineralic hard tissues that escape early dissolution during shallow burial and have the potential to enter the fossil record. In particular, the resistance of biogenic aragonite replacement by calcite up to a temperature of 175 °C during hydrothermal alteration offers an additional explanation for the preservation of aragonitic shells/skeletons once they have escaped early dissolution. The results of our experiments neatly explain the observation that the mollusc fossil record is good and allows restoration of evolutionary patterns.

2.1.6 Conclusions

1. Aragonite crystallite size, porosity, and pore size varies across the cross section of the valve of modern *Arctica islandica*. While the outer shell layer is highly porous, with pore sizes in the range of a few micrometres, and contains mineral units in the 1-5 μm size range, the inner shell layers are characterised by a dense shell structure with small (1 μm) mineral units and a very low porosity. The innermost section of the shell is penetrated by elongated pores oriented perpendicular to the inner shell surface. At annual growth lines, Sr contents are always high relative to shell increment between the growth lines in both pristine and experimentally altered shell samples. The chemistry of the alteration fluid and the duration of the alteration experiment do not exert a major effect on the concentration of Sr along the growth lines.

2. During hydrothermal alteration at 100 °C for 28 days, most, but not all, of the biopolymer matrix is destroyed, while shell aragonite and its microstructure are largely preserved.

3. During hydrothermal alteration at 175 °C for 7 days or more, the biopolymer shell fraction is destroyed, such that pathways for fluid penetration are created. At this temperature and time, shell aragonite is almost completely replaced by calcite.

4. When simulated meteoric solution is used for alteration, newly formed calcite crystal units reach sizes up to 200 μm, while alteration in simulated burial solution induces the formation of calcite crystals that grow up to 1 mm in 7 days. We attribute the latter, larger grains to the Mg content of the burial solution, which inhibits calcite nucleation. The formation of fewer nuclei leads to the growth of larger calcite crystals.

5. Geochemical results show that calcite nucleates and a replacement reaction proceeds where the experimental fluid is in contact with the aragonite: at the two shell surfaces, in pores, and at growth lines, which are thin, formerly organic-filled layers.

6. The replacement reaction of bio-aragonite by calcite does not proceed at temperatures much lower than 175 °C. At 175 °C, we observe a dormant time of about 4 days during which no XRD-detectable calcite is formed. The replacement reaction then proceeds within 2-3 days to almost completion with small amounts of aragonite still surviving after 84 days in the dense, proximal layer of the shell. The dormant period can be attributed to the low available driving force for calcite nucleation, but further studies dedicated to the nucleation process are necessary.

7. Between two tipping points – one between 50 and 60 °C (Kitano et al., 1962; Taft, 1967; Ogino et al., 1987; Balthasar and Cusack, 2015) and the other between 160 and 180 °C (Perdikouri et al., 2011, 2013, this paper) – aragonite appears to precipitate from supersaturated aqueous solutions rather than calcite, such that the

hydrothermal treatments of aragonite within this temperature bracket do not yield calcite.

8. The tardy kinetics of aragonite replacement by calcite at temperatures lower than 175 °C contributes to explaining why aragonitic or bimineralic shells and skeletons have a good potential of preservation and a complete fossil record.

2.1.7 Acknowledgements

2.1.8 Author contributions

LAC, EG and WWS designed the study. EG, VM, ACR, AI and DH provided sample material. LAC, XY and VM performed the experiments. LAC and DM conducted the analyses. LAC evaluated and merged the data. LAC, EG and WWS drafted the manuscript. All authors contributed to discussions and the final manuscript.

2.1.9 Appendix
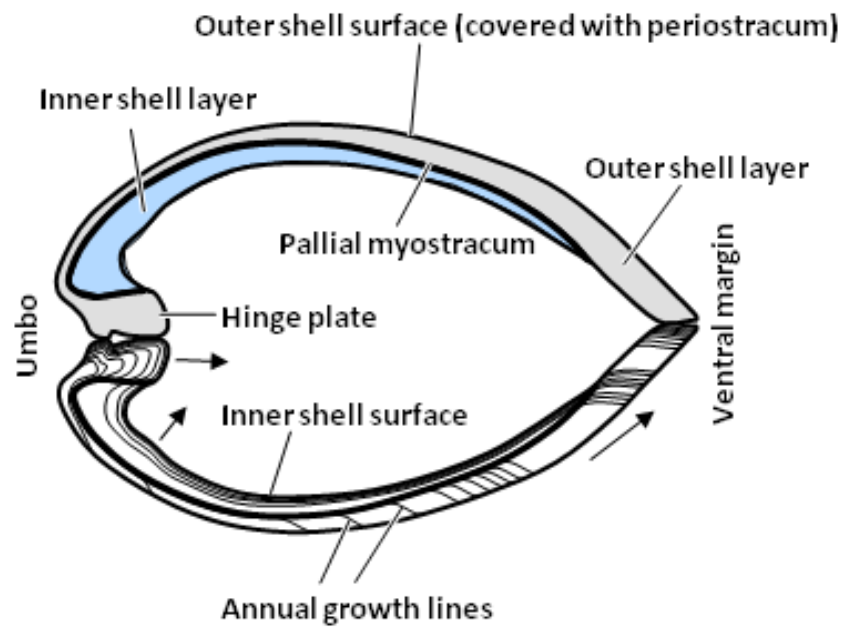
Figure 2.16: Morphological characteristics of the shell of the bivalve *Arctica islandica*. A detailed description is given in Schöne (2013).
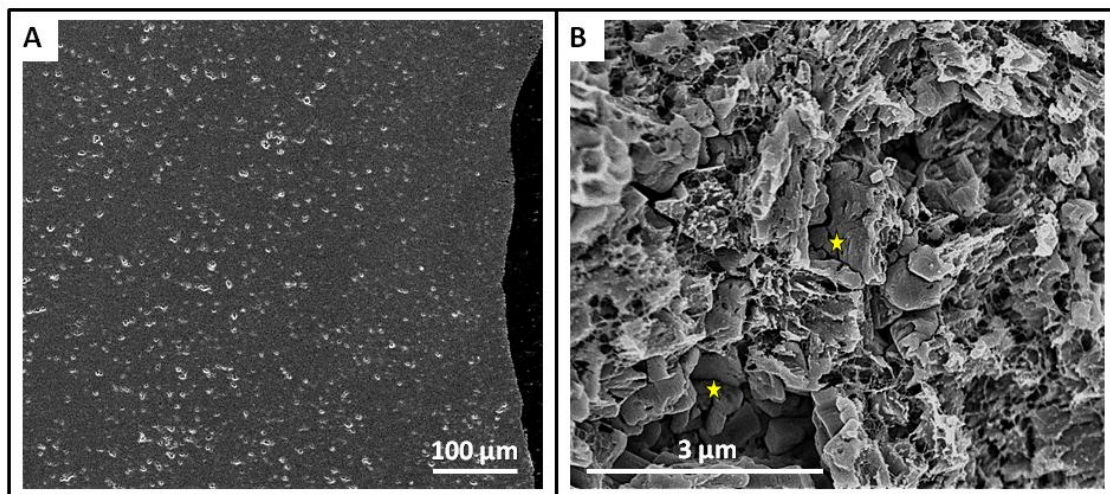
Figure 2.17: Accumulation of pores (whitish circular features) within the outer shell layers (A). Yellow stars in (B) point to the location of two nanometre-sized pores.
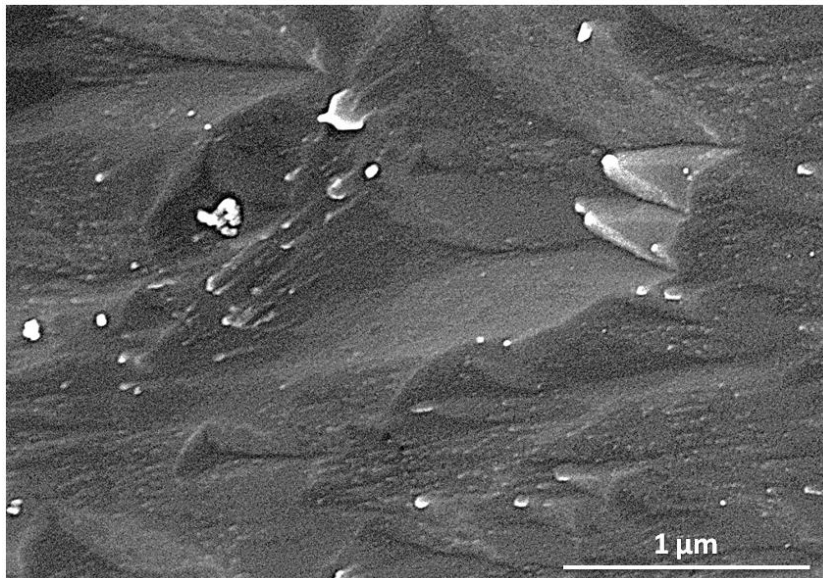
Figure 2.18: FE-SEM image of microtome-cut, polished, etched and critical-point-dried surface of inorganic aragonite grown from solution.
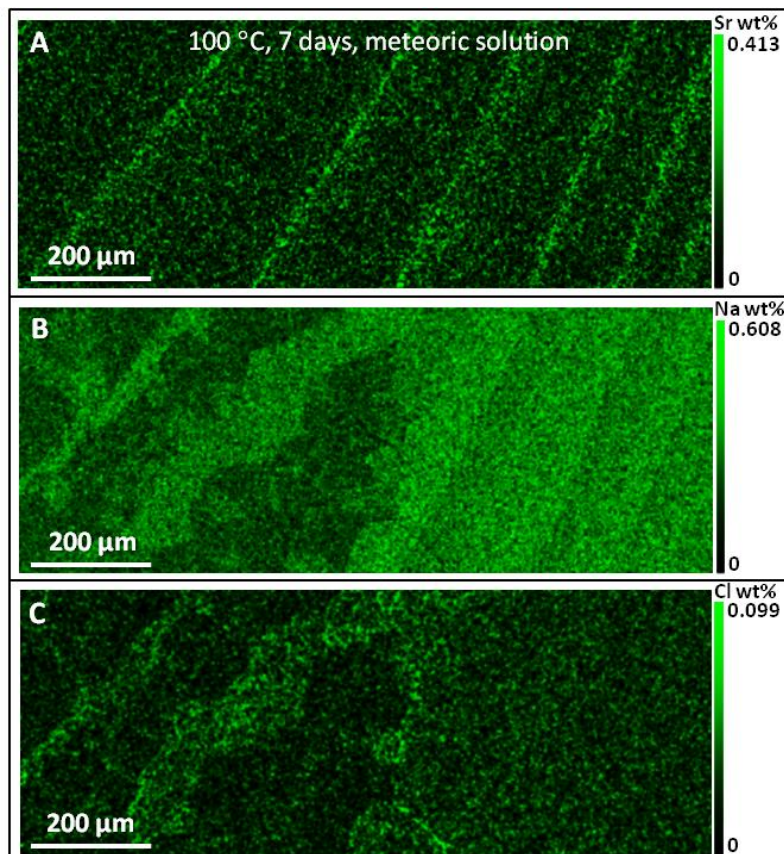
Figure 2.19: Sr^{2+}, Na^+, and Cl^- concentrations along annual growth lines in a hydrothermally altered shell area of *Arctica islandica*. The alteration fluid is enriched in NaCl simulating meteoric waters. The degree of fluid infiltration into and through the shell is well traceable with Na^+ and Cl^- concentrations. Infiltration occurs, in addition through pores, along growth lines which act as conduits for fluid circulation.
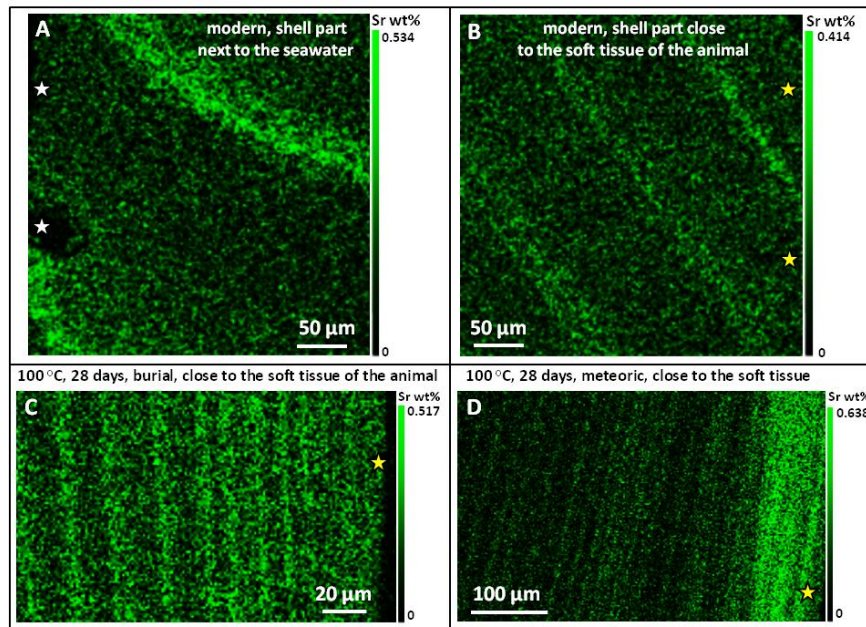
Figure 2.20: Sr²⁺ concentrations along annual growth lines in pristine (A, B) and hydrothermally altered (C, D) *Arctica islandica* shell areas. White stars in (a) indicate regions of the outer shell layer, while yellow stars in (B-D) point to the inner shell parts. Fluids enter the shell at its two surfaces (see enrichment in Sr²⁺ in D) and especially along growth lines. Neither the degree of hydrothermal alteration nor the chemistry of the alteration fluid significantly changes the Sr²⁺ contents along the growth lines. Maximal values for both pristine and altered samples range between 0.4 and 0.6 wt% Sr.
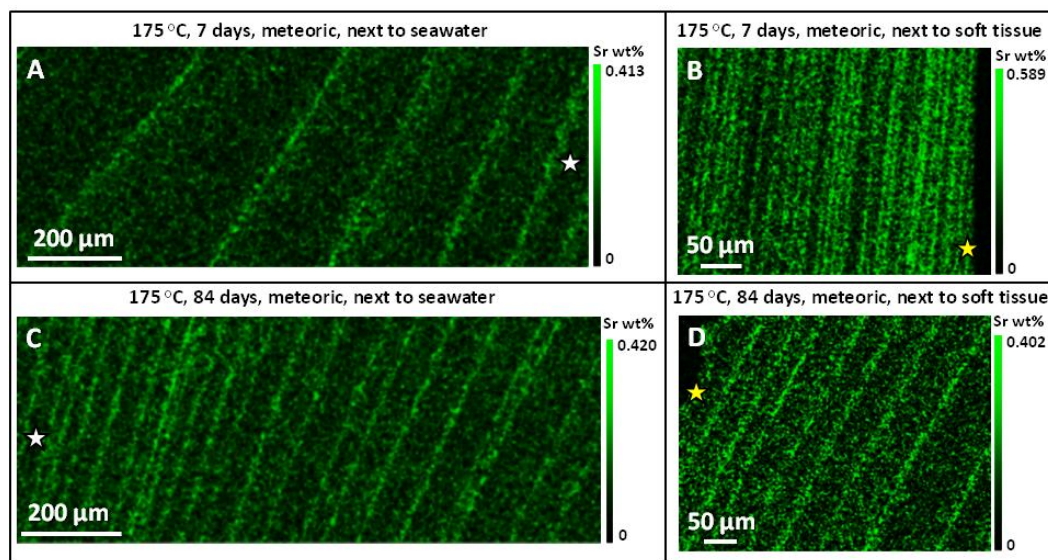
Figure 2.21: Sr²⁺ concentrations along annual growth lines in hydrothermally altered *Arctica islandica* shell areas. Hydrothermal alteration was conducted at 175 °C in meteoric water for 7 and 84 days (A–B). Sr²⁺ concentration scatters for both alteration times around 0.4 wt% Sr²⁺ and is similar to the value measured in the pristine *Arctica islandica* reference samples (see Figs. 2.20A and B).
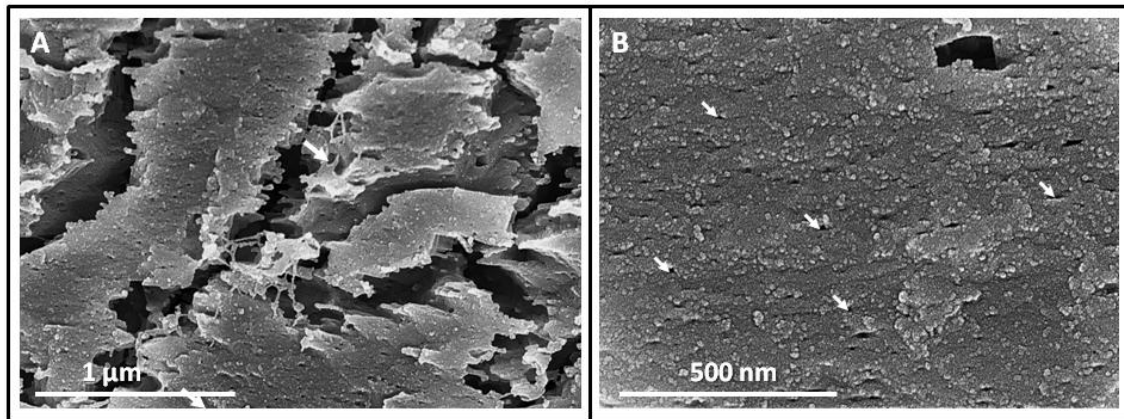
Figure 2.22: Hydrothermally altered *Arctica islandica* shell areas. Burial fluid was used for alteration carried out at 100 °C and for 28 days. (A) As the organic membranes and fibrils (white arrow in A) are destroyed by alteration, large gaps appear between and numerous minute holes (white arrows in B) within the mineral units. (B) The biogenic aragonite of *A. islandica* retains its nanoparticulate appearance after alteration.
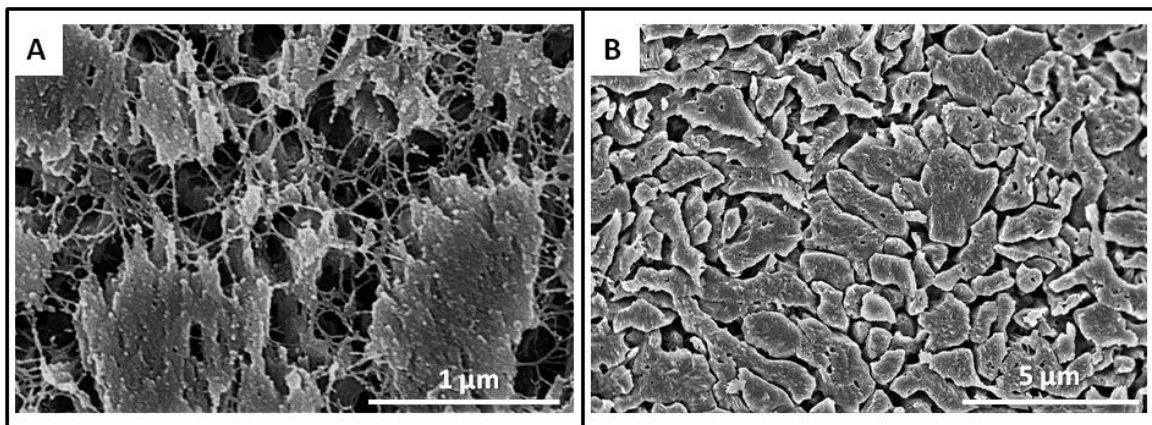
Figure 2.23: Pristine (A) and hydrothermally altered (B) shell layer of *Arctica islandica*. Alteration occurred in burial fluid at 175 °C and lasted for 7 days. (A) Network of biopolymer fibrils between and within pristine aragonite nanoparticles and mineral units. Organic matter is destroyed during alteration and numerous voids (B) become visible within the mineral units.
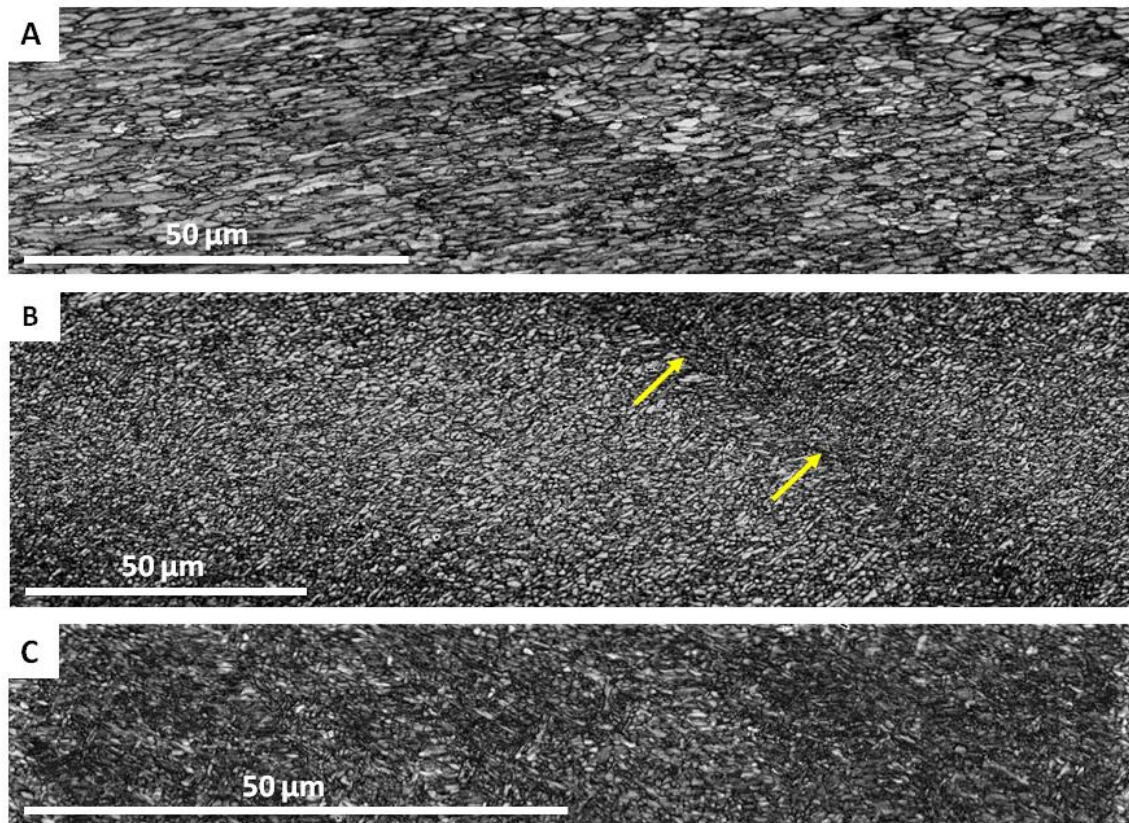
Figure 2.24: EBSD band contrast images taken along a cross section from different parts of the shell of pristine *Arctica islandica*. (A) Outer shell layer, (B) central shell layer, and (C) inner shell layer. Well visible is the difference in crystallite size. In contrast to the outer shell layer (A), the innermost shell section is highly dense and consists of minute aragonite crystals. Yellow arrows in (B) point to annual growth lines.
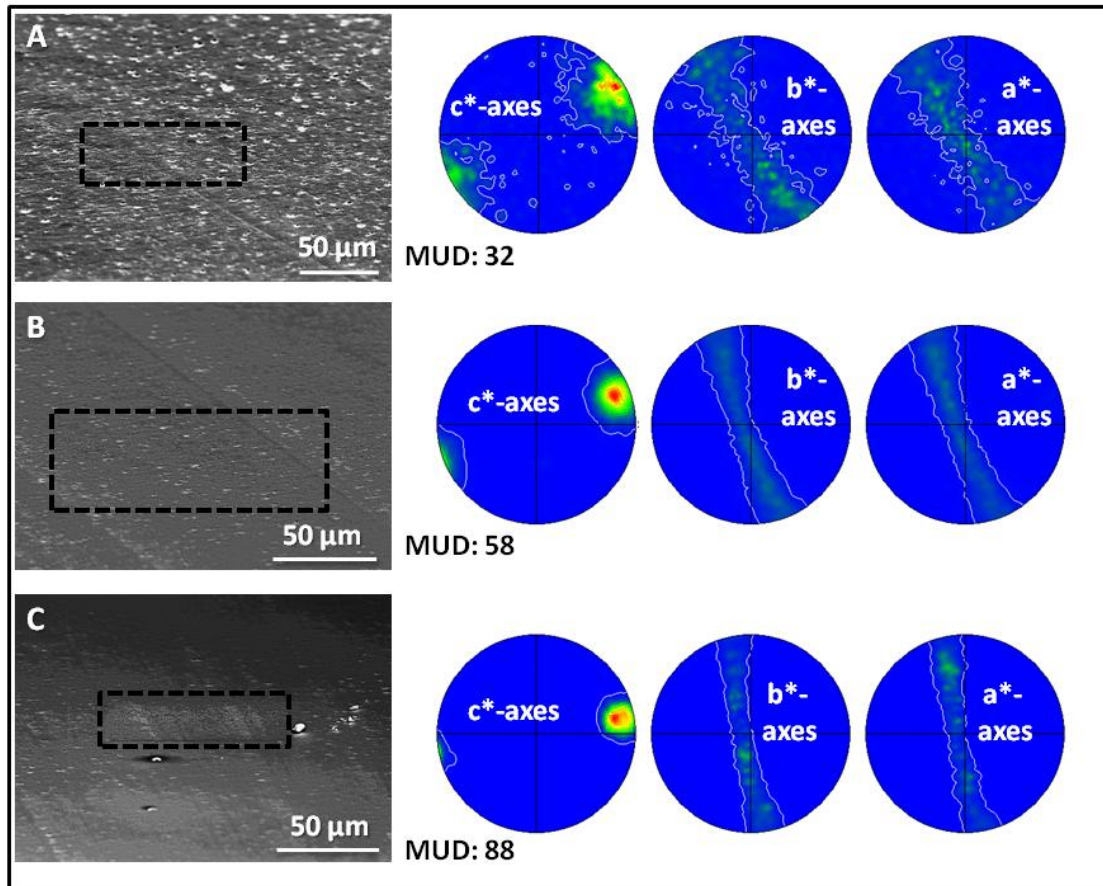
Figure 2.25: Pole figures obtained from EBSD measurements shown in Fig. 2.24. Measurements are performed on pristine *Arctica islandica*. SEM images on the left-hand side indicate the location of EBSD maps: (A) outer shell layer, (B) central shell layer, (C) inner shell layer. The pole figures and MUD values indicate clearly that aragonite co-orientation increases significantly towards innermost shell layers.
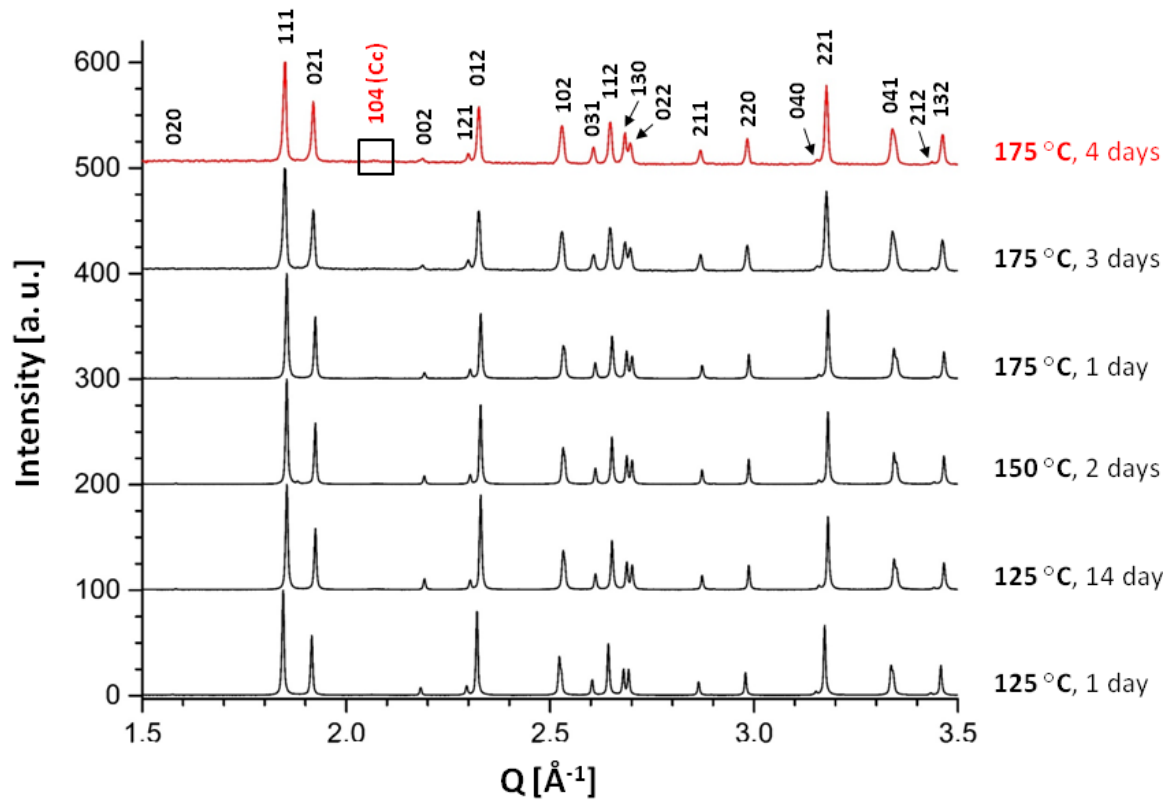
Figure 2.26: XRD measurements of experimentally altered *Arctica islandica* samples subjected to alteration temperatures between 125 and 175 °C for various lengths of time (1, 2, 3, 4 and 14 days). Calcite formation starts at 175 °C and an alteration time of 4 days. Miller indices for calcite (Cc) are given in red and those for aragonite in black.
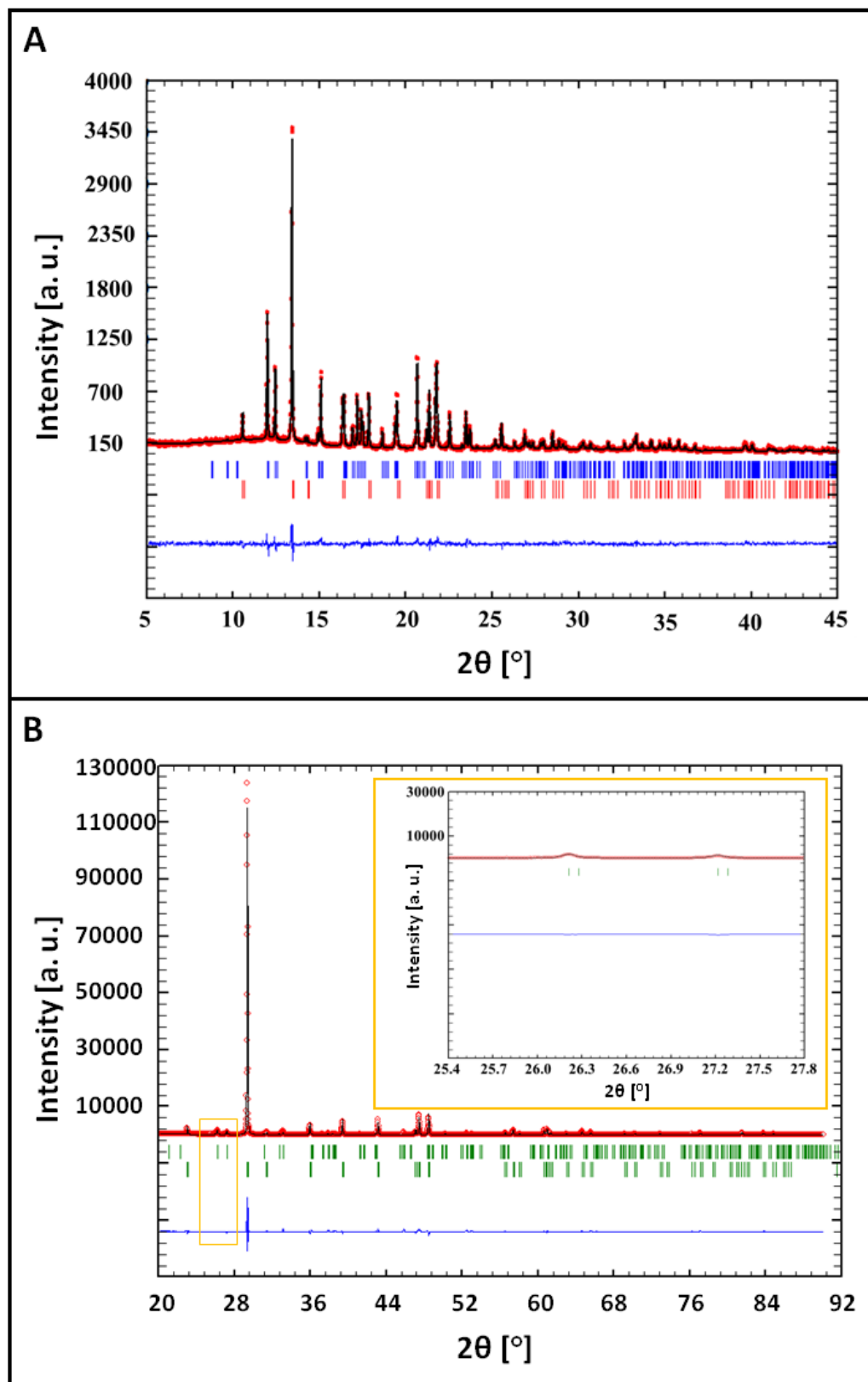
Figure 2.27: Representative Rietveld plot for the product of the alteration experiment performed at 175 °C for 6 (A) and 84 days (B) in artificial burial solution measured with MoKα_1 in transmission and with CuKα_1 in reflection, respectively. The diffuse amorphous signal peaking near 12.5 ° 2θ is due to the Lindemann glass capillary (Ø 0.3 mm) containing the sample.
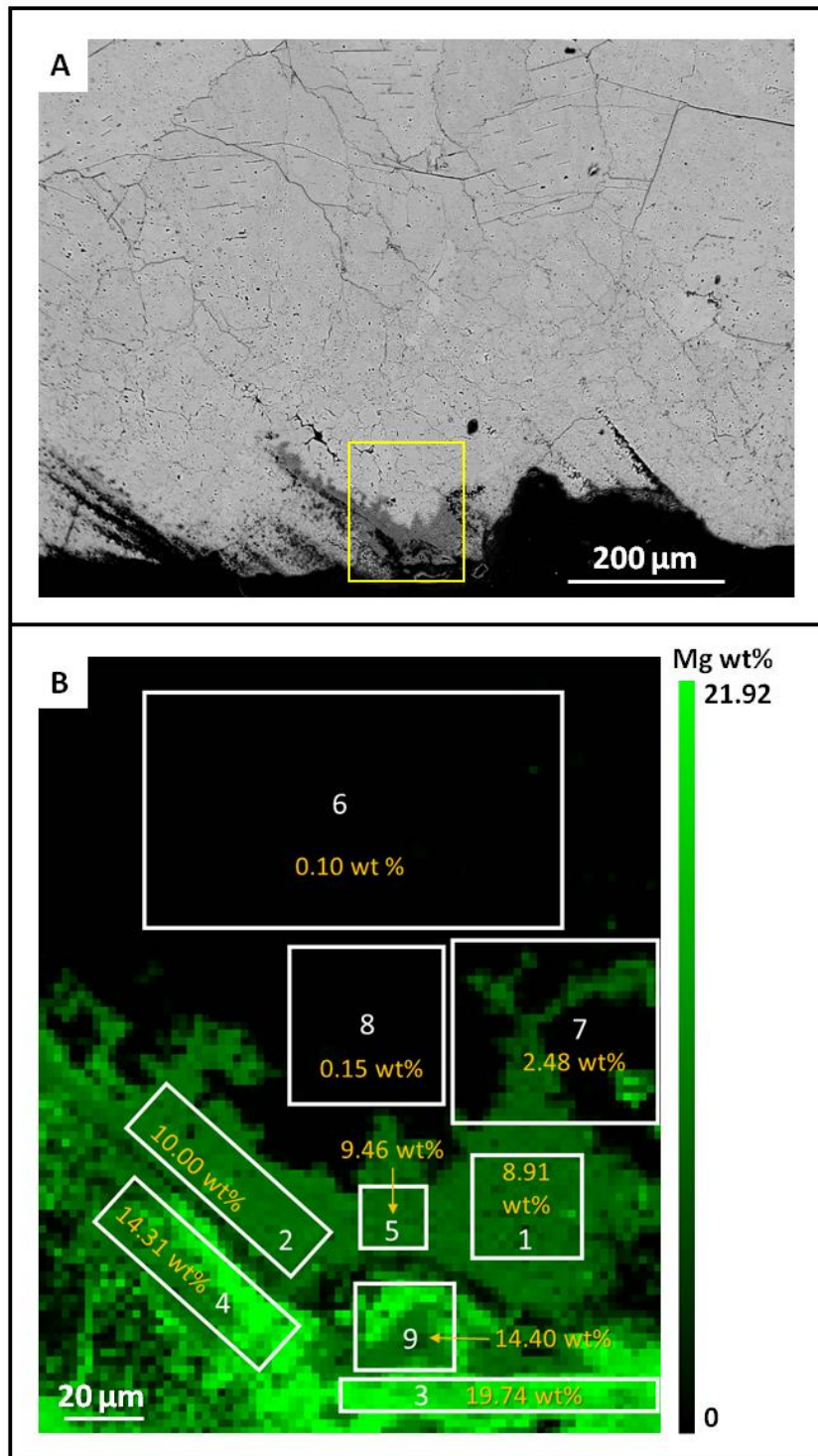
Figure 2.28: BSE image (A) and Mg concentrations (B) of hydrothermally altered *Arctica islandica* shell. Alteration occurred in burial solution at 175 °C for 84 days. The yellow rectangle in (A) indicates the shell area which is shown in (B) and scanned with EPMA. White rectangles in (B) highlight the extent of shell areas which were used for the determination of mean Mg concentrations given in yellow within each rectangle. Note the formation of magnesium-rich carbonates (see Table 2.3) along the outer rim of the sample.

Table 2.3: Electron microprobe analyses (CAMECA SX100 system and procedures described in Goetz et al., 2014) of the original pristine *Arctica islandica* aragonite and of the treated sample CHA-M046 AI27 B2 near the outer rim of the specimen. The analysed regions are shown in Fig. 2.28B. The [CO_3] content is nominal.

Analysed Region		Mg	Ca	Mn	Na	P	Sr	Fe(II)	O	C	Σ Cations (except P and C)
1	wt%	8.91	25.53	0.1	0.06	0.02	0.3	0.15	51.58	13.29	
	Formula	0.3425	0.596	0.0015	0.0025	0.0005	0.003	0.0025	3.018	1.034	0.9480
2	wt%	8.91	2.53	0.1	0.06	0.02	0.3	0.14	51.33	13.29	
	Formula	0.385	0.584	0.0015	0.002	0.0005	0.003	0.0025	3.007	1.014	0.9780
3	wt%	19.74	11.08	0.07	0.28	0.05	0.25	0.17	54.46	13.82	
	Formula	0.716	0.2445	0.001	0.011	0.0015	0.0025	0.003	3.007	1.015	0.9775
4	wt%	14.31	18.62	0.09	0.16	0.04	0.28	0.15	52.84	13.44	
	Formula	0.5305	0.4285	0.0015	0.006	0.001	0.003	0.0025	3.010	1.018	0.9720
5	wt%	9.46	25.49	0.1	0.06	0.02	0.29	0.16	51.29	13.05	
	Formula	0.365	0.5965	0.002	0.0025	0.0005	0.003	0.0025	3.01	1.019	0.9715
6	wt%	0.1	38.19	0.11	0.13	0.02	0.43	0.15	48.43	12.36	
	Formula	0.004	0.948	0.002	0.0055	0.0005	0.005	0.0025	3.011	1.022	0.9670
7	wt%	2.48	31.32	0.1	0.12	0.03	0.36	0.14	51.44	13.94	
	Formula	0.095	0.751	0.0015	0.005	0.001	0.004	0.0025	3.047	1.094	0.8590
8	wt%	0.15	38.26	0.11	0.12	0.02	0.43	0.15	48.37	12.32	
	Formula	0.006	0.949	0.002	0.005	0.0005	0.005	0.0025	3.010	1.020	0.9695
9	wt%	14.4	18.03	0.09	0.17	0.03	0.28	0.15	53.15	13.62	
	Formula	0.534	0.411	0.0015	0.0065	0.001	0.003	0.0025	3.013	1.027	0.9585
Original Aragonite	wt%	0.07	39.24	0.11	0.46	0.02	0.43	0.15	47.44	11.76	
	Formula	0.003	0.988	0.002	0.02	0.0005	0.005	0.0025	2.989	0.987	1.02

2.2 Micro- and nanostructures reflect the degree of diagenetic alteration in modern and fossil brachiopod shell calcite: a multi-analytical screening approach (CL, FE-SEM, AFM, EBSD)

Laura A. Casella[1], Erika Griesshaber[1], María Simonet Roda[1], Andreas Ziegler[2], Vasileios Mavromatis[3,4], Daniela Henkel[5], Jürgen Laudien[6], Vreni Häussermann[7,8], Rolf D. Neuser[9], Lucia Angiolini[10], Martin Dietzel[3], Anton Eisenhauer[5], Adrian Immenhauser[9], Uwe Brand[11], and Wolfgang W. Schmahl[1]

[1] Department of Earth and Environmental Sciences, Ludwig-Maximilians-Universität München, 80333 Munich, Germany

[2] Central Facility for Electron Microscopy, University of Ulm, 89069 Ulm, Germany

[3] Institute of Applied Geosciences, Graz University of Technology, 8010 Graz, Austria

[4] Géosciences Environnement Toulouse (GET), CNRS, 31400 Toulouse, France

[5] GEOMAR Helmholtz Centre for Ocean Research Kiel, Marine Biogeochemistry/Marine Systems, 24148 Kiel, Germany

[6] Alfred Wegner Institute, Biosciences/Bentho-Pelagic Processes, 27568 Bremerhaven, Germany

[7] Pontificia Universidad Católica de Valparaíso, Facultad de Recursos Naturales, Escuela de Ciencias del Mar, Valparaíso, Chile

[8] Huinay Scientific Field Station, Chile

[9] Institute of Geology, Mineralogy and Geophysics, Ruhr-Universität Bochum, 44801 Bochum, Germany

[10] Dipartimento di Scienze della Terra "A. Desio", Università degli Studi di Milano, 20133 Milan, Italy

[11] Department of Earth Sciences, Brock University, St. Catharines, Ontario, L2S 3S1, Canada

2.2.1 Abstract

Fossil carbonate skeletons of marine organisms are archives for understanding the development and evolution of palaeoenvironments. However, the correct assessment of past environment dynamics is only possible when pristine skeletons and their biogenic characteristics are unequivocally distinguishable from diagenetically altered skeletal elements and non-biogenic features.

In this study, we extend our work on diagenesis of biogenic aragonite (Casella et al., 2017) to the investigation of biogenic low-Mg calcite using brachiopod shells. We examined and compared microstructural characteristics induced by laboratory-based alteration to structural features derived from diagenetic alteration in natural environments. We used four screening methods: cathodoluminescence (CL), cryogenic and conventional field emission-scanning electron microscopy (FE-SEM), atomic force microscopy (AFM) and electron backscatter diffraction (EBSD). We base our assessments of diagenetic alteration and overprint on measurements of, a) images of optical overprint signals, b) changes in calcite crystal orientation patterns, and c) crystal co-orientation statistics.

According to the screening process, altered and overprinted samples define two groups. In Group 1 the entire shell is diagenetically overprinted, whereas in Group 2 the shell contains pristine as well as overprinted parts. In the case of Group 2 shells, alteration occurred either along the periphery of the shell including the primary layer or at the interior-facing surface of the fibrous/columnar layer. In addition, we observed an important mode of the overprinting process, namely the migration of diagenetic fluids through the endopunctae corroborated by mineral formation and overprinting in their immediate vicinity, while leaving shell parts between endopunctae in pristine condition.

Luminescence (CL) and microstructural imaging (FE-SEM) screening give first-order observations of the degree of overprint as they cover macro- to micron scale alteration features. For a comprehensive assessment of diagenetic overprint these screening methods should be complemented by screening techniques such as EBSD and AFM. They visualise diagenetic changes at submicron and nanoscale levels depicting the replacement of pristine nanocomposite mesocrystal biocarbonate (NMB) by inorganic rhombohedral calcite (IRC). The integration of screening methods allows for the unequivocal identification of highly-detailed alteration features as well as an assessment of the degree of diagenetic alteration.

2.2.2 Introduction

Benthic and nektonic marine carbonate archives (e.g., brachiopods, bivalves, cephalopods) represent the foundation of studies aiming at reconstructions of past climate dynamics and environmental change (e.g., Grossman et al., 1993; Khim et al., 2000b; Korte et al., 2005). Any assessment of geochemical, isotopic and petrographic proxy data from these archives is limited by three major obstacles: (i) metabolic processes affecting the transfer of ions from the external fluid media to the site of biogenic mineral nucleation and hard tissue formation (Griesshaber et al., 2007a; Takayanagi et al., 2013; Yamamoto et al., 2013; Immenhauser et al. 2015); (ii) kinetic processes that influence elemental and isotopic fractionation between fluid and biomineral (Auclair et al., 2003; Parkinson et al., 2005); and (iii) diagenetic overprint and weathering processes which blur or eradicate pristine elemental, isotopic and morphostructural signatures (Brand et al, 2011; Swart, 2015).

The present contribution focuses on the impact of diagenetic and laboratory-based alteration on brachiopod shell micro- and nanostructures. Brachiopods are amongst the most frequently used archive in palaeoecology and palaeoclimatology (e.g., Lowenstam, 1961; Veizer et al., 1986; Brand, 1989b; Bates and Brand, 1991; Grossman et al., 1991, 1996; Carpenter and Lohmann, 1995; Wenzel and Joachimski, 1996; Wenzel et al., 2000; Cusack and Williams, 2001; Samtleben et al., 2001; Pérez-Huerta et al., 2007, 2011; Angiolini et al., 2009; Garbelli et al., 2012, 2016; Nielsen et al., 2013; Roark et al., 2015; Smirnova and Zhegallo, 2016). They cover most of the Phanerozoic (Curry and Brunton, 2007) and live(d) in a wide range of marine habitats (Richardson, 1997; Logan, 2007). Particularly important is their rich record in the Palaeozoic, when brachiopods dominated benthic communities and reached their maximum diversity (Angiolini, 1993; Curry and Brunton, 2007; Williams and Cusack, 2007; Garbelli, 2017), making those invaluable tools in reconstructing deep-time seawater conditions. Previous studies used single (Grossman et al., 1991) or multiple (Brand, 2004; Brand et al., 2011) screening tools for discriminating between altered and pristine shell material. However, all of these approaches have problems (Steuber, 1999; Garbelli et al., 2012; Angiolini et al., 2012; Ullmann et al., 2015; Garbelli, 2017) and demonstrate our inability to accurately assess the degree of diagenetic alteration of fossil carbonate shells.

Understanding how diagenetic overprint influences microstructural and geochemical archival data is of fundamental importance in palaeoceanography. One approach is to establish basic knowledge about microstructural and textural patterns in modern brachiopod shells (e.g., Barbin et al., 1991; Schmahl et al., 2004, 2012; Griesshaber et al., 2007a, 2007b, 2007c, 2010; Cusack et al., 2008a, 2008b; Goetz et al., 2009, 2011; Cusack, 2015; Ye et al., 2018a, 2018b). It is important to note that fibres of the secondary layer of modern brachiopods consist of a single calcite crystal (Schmahl et al., 2004;

Griesshaber et al., 2007b, 2007c), which contains an occluded intra-crystalline network of organic matter (e.g., Nindiyasari et al., 2015). Thus, on fractured or etched surfaces these crystals (fibres) consist of crystallographically co-oriented calcite nanogranules (Cusack et al., 2008a, 2008b; Schmahl et al., 2012). Nanogranular biogenic calcite, aragonite and vaterite microcrystals are widely observed in many animals (e.g., Cuif and Dauphin, 2005a; Rousseau et al., 2005; Dauphin et al., 2008; Przeniosło et al., 2008; Cuif et al., 2011a; Griesshaber et al., 2013, 2017). Cölfen and Antonietti (2008; cf. Seto et al., 2012) coined the term "mesocrystal" for objects with such a structure. In our paper we adopt the term nanocomposite mesocrystal biocarbonate (NMB) without implying that the material might or might not form by the accretion of nanoparticles.

In this study, we assessed the micro- and nanostructural characteristics of laboratory-altered and naturally overprinted (fossil) brachiopod shells, and compared the altered/overprinted structural features to those present in modern pristine analogues. With this approach, we not only document micro- and nanostructural differences between pristine and altered/overprinted shells, we document major steps in the alteration process and also obtain a quantitative understanding of diagenetic alteration based on patterns of mineral orientation distribution and mineral misorientation statistics. We further discuss the application of the available screening tools on slightly to moderately altered carbonate hard tissue. An issue of major importance since recognition of highly altered shells is straightforward, whereas signs of moderate to low degrees of overprinting are, generally, difficult to detect and document. With this study, we present a process-oriented understanding of diagenetic alteration with an updated and integrated screening method required for more refined elemental, stable and clumped isotope investigations.

2.2.3 Materials and methods

Throughout the manuscript we first describe the reference material, the shells of pristine modern brachiopods. The overall aim of our study is to increase our understanding of diagenetic overprinting, and thus, describe characteristics of the hard tissue of fossil brachiopods which was subjected to different degrees of simulated and natural alteration and diagenetic conditions.

Laboratory-based alteration experiments (thermal and hydrothermal) were carried out to simulate diagenetic processes in order to better understand the generation of diagenetic micro- and nanostructural features in fossil shells. Thermal alteration was performed to investigate the dehydration and decomposition of biopolymers within the shells. Hydrothermal alteration was carried out to better understand calcite

reorganisation, such as the replacement of pristine nanocomposite mesocrystal biocarbonate (NMB) by diagenetic inorganic rhombohedral calcite (IRC).

Materials

In this study, we investigated the modern brachiopods *Terebratalia transversa* (Sowerby, 1846), *Magellania venosa* (Solander, 1789), and *Liothyrella uva* (Broderip, 1833), and fossil species of *Lobothyris punctata* (Sowerby, 1812), *Digonella digona* (Sowerby, 1815), *Platystrophia laticostata* (James, 1871) and *Quadratirhynchia attenuata* (Dubar, 1931).

The shells of the modern brachiopods were used as reference material for pristine conditions. All chosen specimens have two-layer shells. They come from different habitats which enable us, to some degree, evaluate and assess environment-induced microstructural variability (cf. Ye et al., 2018a, 2018b).

In the case of the fossil samples, we investigated the shells of both, terebratulid and rhynchonellid brachiopod shells. They lived in distinctly different habitats, at different geologic times and experienced distinct burial conditions and depths.

Modern specimens of *T. transversa*, *L. uva* and *M. venosa* collected live were used for establishing baseline pristine shell micro- and nanostructures, and subsequently to document microstructural changes which evolved in the course of the thermal and hydrothermal experiments and under natural diagenetic alteration conditions. The terebratulid brachiopod *T. transversa* was collected at Friday Harbor Laboratories, University of Washington, U.S.A.. Specimens of the terebratulid brachiopod *L. uva* were obtained from Signy and Rothera Islands, Antarctica. The terebratulid brachiopod *M. venosa* was collected at Huinay Field Station, Puerto Montt, Chile.

Fossil brachiopods were chosen from basins which experienced different burial depths, diagenetic alteration and overprint temperatures. We selected the ancient taxon Orthida to represent the ancestral form of the fibrous fabric in brachiopods, two Jurassic terebratulid brachiopods to represent the punctate fibrous fabric, a fabric common to most modern brachiopod species, and a rhynchonellid brachiopod from the Jurassic with an impunctate fibrous fabric.

The Orthide *P. laticostata* is from the Upper Ordovician Dillsboro Formation, Indiana, U.S.A.. *Lobothyris punctata* (Terebratulida) is from the Pliensbachian (Jurassic, 190-182 Ma) Hierlatz-type limestone of the Bakony Mountains in Hungary (Vörös, 1986). *Quadratirhynchia attenuata* (Rhynchonellida) is from the Lower Jurassic (Toarcian, 182–174 Ma) Ait Athmane Formation of the Central High Atlas Basin, Morocco (Ait Athmane section, Fig. 3 in Wilmsen and Neuweiler, 2008). *Digonella digona* (Terebratulida) is from highly bioturbated marlstones (Marnes a Rhynchonelles superieures) of Bathonian age (168-166 Ma), that lived at the coastal cliffs at Luc-Sur-Mer, Normandy, France (Brigaud et al., 2009, Fig. 2).

Sample preparation

Biochemical preparation and etching

To visualise the organic matrix, shell pieces of modern and fossil brachiopod shells were mounted with superglue on 3 mm thick cylindrical aluminium rods. Subsequently, the samples were cut using a Leica Ultracut ultramicrotome outfitted with glass knives and then polished with a DiATOME diamond knife. Surface polishing was stepwise and serially removed slices with successively decreasing thicknesses (90 nm, 70 nm, 40 nm, 20 nm, 10 nm and 5 nm), and each polishing step was repeated fifteen times (Fabritius et al., 2005). The polished sample surfaces were etched, while the organic matter was fixed in the shells. In this preparation step, shell pieces were immersed for 180 seconds in a solution of 0.1 M HEPES (4-(2-hydroxyethyl)-1-piperazineethanesulfonic acid) at pH 6.5 and 2.5 % glutaraldehyde. Etching was stopped by washing samples three times for 10 minutes with 100 % isopropyl. Subsequently, specimens were critical point dried in a BAL-TEC CPD 030 (Liechtenstein) device, and then rotary coated with 3 nm of platinum.

High-pressure freezing

Parts of minute-sized shells (2 to 3 mm in diameter and thickness) of live *M. venosa* were used for cryo-SEM imaging. About 1.5 mm large and 150 to 200 µm thick shell pieces, while immersed in seawater, were cut from the valves and subsequently placed with a drop of hexadecane into aluminium planchettes with an outer diameter of 3 mm, 200 µm deep inner cavity and 2 mm inner diameter. Samples were high-pressure frozen and cryo-transferred to a BAF 300 freeze etch and coating device. Hence, the planchette-shell-lid sandwiches were cleaved open, the high-pressure frozen shell samples were fractured, coated, mounted onto a Gatan cryo-holder and cryo-transferred for imaging to a Hitachi S5200 FE-SEM. For further experimental details see Yin et al. (2018).

Preparation for FE-SEM, AFM and EBSD

For FE-SEM and AFM imaging and EBSD measurements 2-3 mm sized-shell wafers were cut from along the longitudinal section from the umbo to the commissure of the shell. According to well-established metallurgical procedures (Petzow, 2006), wafers were embedded into cold mounting epoxy-based resin and polished in eight sequential mechanical steps decreasing in grain size down to 1 µm. The final preparation step consisted of etch-polishing with colloidal alumina (particle size ~0.05 µm) in a vibratory polisher, where about 10 nm of the sample surface was abraded to remove scratches and defects on the surface. Subsequently, the samples were rotary coated with 4-6 nm of carbon.

Two types of preparations were performed for AFM imaging: in the first, shell pieces were glued onto metal cylinders with superglue and highly even shell surfaces were obtained by cutting and polishing the samples with glass and diamond knives. In the second type of sample preparation for high-quality AFM images, the samples were polished following the protocol used for FE-SEM imaging and EBSD measurements, and then cleaned with high-purity deionised water in an ultrasonic bath for 10 minutes, rinsed with ethanol and dried immediately afterwards.

Alteration experiments

We performed two types of alteration experiments: thermal and hydrothermal to investigate the decomposition/overprint of the occluded organic matrix as well as that of the mineral. For the thermal alteration experiments, pristine brachiopod shells were heated under dry conditions at different alteration temperatures (100 °C, 200 °C, 300 °C, 400 °C) for 24, 48, 72 hours, one, three and four months, respectively. In the present contribution we show results of samples heated at 100 °C for 72 hours, and at 400 °C for 48 hours; heating at low and high temperatures for short durations. Samples heated at 100 °C for three and four months; heating at low temperature for long durations.

Hydrothermal alteration experiments were carried out in the presence of two different fluids to simulate meteoric and burial diagenetic overprints. Both alteration fluids were prepared by dissolving 10 mM NaCl and 100 mM NaCl + 10 mM $MgCl_2$ in high-purity deionised water (cf. Casella et al., 2017; Ritter et al., 2017). Sample material and 10 mL of fluid were inserted into a polytetrafluoroethylene (PTFE) crucible which was placed inside a metal autoclave. These experiments were carried out at 100 °C for 28 days and at 175 °C for 7 and 28 days. In all experiments, pressure conditions corresponded to the vapour pressure of water which develops at the experimental temperatures. Bisected valve fragments (1x1 cm) of modern brachiopod specimens were placed in a PTFE liner (volume: 68.7 cm^3) together with 25 mL of either artificial meteoric (10 mM NaCl aqueous solution) or burial (100 mM NaCl + 10 mM $MgCl_2$ aqueous solution) fluid. Each PTFE liner was placed into a stainless steel autoclave, sealed and heated to the desired temperature.

Analytical methods

Cathodoluminescence and atomic force microscopy

Cathodoluminescence (CL) microscopy was performed on modern and fossil shell samples to characterise different CL features of pristine conditions as well as different degrees of diagenetic overprint. For this purpose, a HC1-LM hot cathode

81

cathodoluminescence microscope, developed at Ruhr-University Bochum, was used (Neuser et al., 1995). Acceleration of the electron beam was 14 keV with a beam current of 0.2 mA. We distinguish between specific luminescence properties in the shells. The terminology used in this study is "non-luminescent/intrinsic", "patchy luminescent" and "bright luminescent". The observed luminescence colours of the biogenic calcite are classified as blue, magenta-red and orange-brown.

Atomic force microscopy (AFM) was conducted on modern, hydrothermally altered and fossil shells. Images were taken in contact mode with a JPK NanoWizard II AFM equipped with an n$^+$-silicon cantilever.

FE-SEM and cryo-FE-SEM imaging and EBSD analysis

FE-SEM imaging was performed at 4, 5 and 10 kV using a Hitachi S5200 electron microscope. Cryo-SEM imaging was performed on a Hitachi S5200 FE-SEM, with samples being investigated at temperatures of −100 °C and an accelerating voltage of 10 kV. Imaging was performed using scattered (SE) and backscattered (BSE) electron modes.

Electron backscatter diffraction (EBSD) measurements were carried out on a Hitachi SU5000 FE-SEM operated at 20 kV, equipped with a Nordlys II EBSD detector, and with AZTec acquisition and AZTec and CHANNEL 5 HKL evaluation software (Schmidt and Olesen, 1989; Randle and Engler, 2000). Crystal orientation information is presented with band contrast measurements, with colour-coded crystal orientation maps and corresponding pole figures. EBSD band contrast represents the pattern quality of the EBSD Kikuchi diffraction pattern of each measurement point. Thus, a strong EBSD signal yields a bright image point when a crystal is detected. A weak or absent signal results in a dark point, for example, from overlapping crystal boundaries, pores, organic material or amorphous calcium carbonate (ACC).

Crystallographic orientation patterns were derived from EBSD scans and corresponding pole figures. Contoured versions of the pole figures show the strength of the clustering of the poles. We used in this study the lowest possible degree for half width of five degrees and for cluster size of three degrees. The half width controls the extent of the spread of the poles over the surface of the projection sphere. A cluster comprises data with the same orientation. A measure of calcite crystal co-orientation strength for an EBSD map is obtained from the multiple of uniform distribution density (MUD) value. High MUD values indicate high crystallographic axes co-orientation, where single inorganic carbonate crystals have MUD values greater than 700 (Nindiyasari et al., 2015), whereas low MUD values reflect low crystal co-orientation, and a MUD value of 1 represents random crystallographic orientation of the scanned calcite crystals in the shell.

2.2.4 Results

Calcite crystal organisation in modern, fossil and altered brachiopod shells

Modern brachiopod shells

The shell of modern *T. transversa* is a structural material with hierarchical architecture where component assembly encompasses nanometre to millimetre levels. Nanoscopic bio-calcite entities comprise distinctly-shaped basic mineral units, the biocrystals. An assembly of these biocrystals constitutes the two layers of the shell, the primary and the secondary shell layers (Figs. 2.29, 2.30, 2.42 and 2.43 in chapter 2.2.9; see also Figure 2.51 in chapter 2.3).

The primary layer (Figs. 2.29B and 2.42A) consists of an array of interdigitating, irregularly-shaped micrometre-sized calcite biocrystals. In cross-section, these units are elongated with lengths of 2-6 μm and widths of 0.5-1.5 μm. The morphology of these units shows concave recesses analogous to those noted in dendritic crystals. As adjacent mineral units grow into the recess zones of abutting crystals, a dense and fracture-resistant microstructure forms consisting of interlocking crystals. Biopolymers are not intercalated in the primary layer (Fig. 2.42A), however, they are abundant in the secondary shell layer. An organic membrane separates the primary layer from the array of fibres forming the secondary layer (Fig. 2.42A), and biopolymer membrane forms sheaths around each calcite fibre (Figs. 2.29B-C and 2.42A-B; Casella et al., 2018b).

Stacks of calcite fibres form the secondary layer of the shell of *T. transversa*. Figure 2.29A shows an electron backscatter diffraction (EBSD) scan of a cross-section through a stack of fibres, where biocrystal (basic mineral unit) orientation is colour-coded. Since individual fibres have uniform colours, this indicates that the crystal lattice within the fibres has uniform orientation. However, high magnification images obtained by conventional and cryo-FE-SEM (Figs. 2.29B-D and 2.30) and AFM images of cross-sections of pristine *T. transversa* fibres (Fig. 2.43) clearly show that nanoscopic bio-calcite entities constitute the fibres and reveal their mesocrystal architecture. Nanoparticulate calcite crystals are usually a few tens of nanometres in size (Figs. 2.29D and 2.43), and are arranged in layers within the fibres and induce their conchoidal mode of fracturing on them (Figs. 2.30A and C; Casella et al., 2018b).

In contrast, Fig. 2.44 shows the classical rhombohedral morphology of inorganic calcite grown from solution and illustrates the immense distinction in nanostructure between biologically-formed nanocomposite mesocrystal biocarbonate (NMB) calcite and diagenetically-precipitated inorganic rhombohedral calcite (IRC). Nonetheless, the

rhombohedral symmetry of the atomistic crystal structure of calcite is often also apparent in the biological material (Fig. 2.29C). However, at the nanoscale, the pattern of calcite organisation in the pristine biological hard tissue is clearly distinct from that of calcite grown from diagenetic solution (compare Figs. 2.29C-D and 2.44).
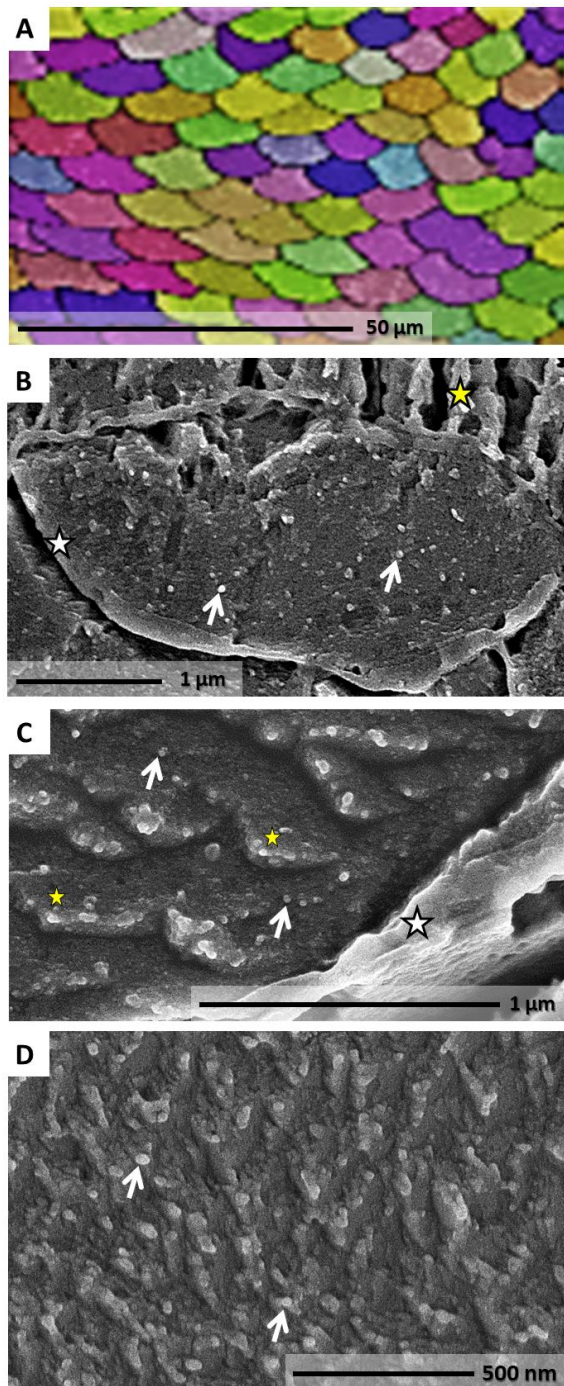
Figure 2.29; Electron backscatter diffraction (EBSD) scan (A) and FE-SEM images (B to D) of cross-sectioned fibres of modern *T. transversa*. (A) EBSD map of a cross section through a stack of brachiopod fibres showing the mineral units and biocrystals in the fibrous layer of brachiopod shells. Calcite orientation variation is colour-coded. Note that individual fibres are mostly single crystals in the sense that the crystallographic orientation of the calcite in the fibre is uniform. (B) Cross section through a calcite fibre crystal (nanocomposite mesocrystal biocarbonate, NMB), (C) close-up view showing the nanoscale entities within each NMB. Organic membrane (white stars in B and C) surrounding each calcite fibre is clearly visible and delicate membrane separates the nanoscale entities (white arrows in B to D) of the NMB fibres. Yellow star in (B) marks the primary shell layer, whereas yellow stars in (C) point to rhombohedrally-shaped nanoscale entities on an etched surface of a NMB.
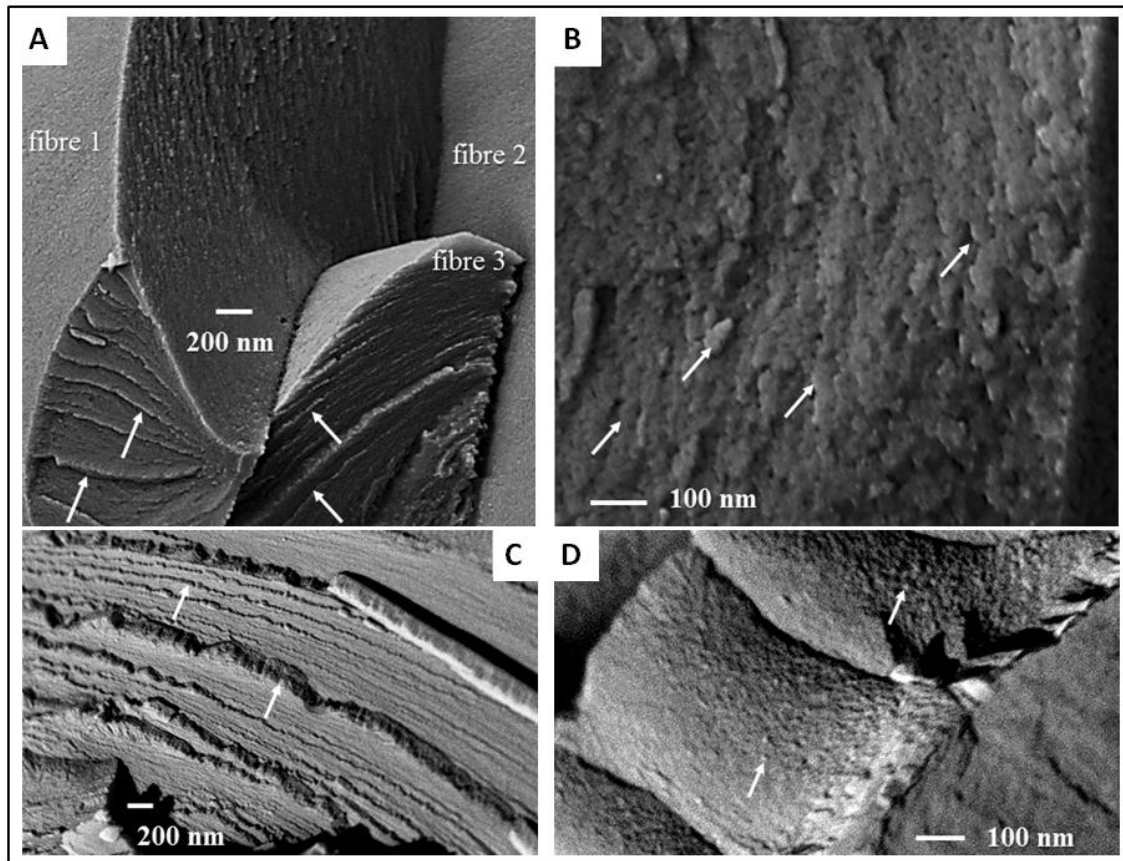
Figure 2.30: FE-SEM (A, B) and cryo-FE-SEM (C, D) images taken on fracture surfaces of the secondary shell layer of the modern brachiopods *T. transversa* (A, B) and *M. venosa* (C, D). As the shells are only fractured and not polished, artefacts due to surface preparation such as chemical etching are not induced. The conchoidal fracture behaviour of brachiopod calcite (white arrows in A, B) of the bio-calcite as well as the nanogranular appearance of the calcite within fibre crystals (white arrows in C, D) can be clearly observed. The size of calcite particles is less than 50 nm (B).

Preservation status of fossil brachiopod shells

Figures 2.31 and 2.32 show fibre morphology and nanoscale calcite crystal organisation in fossil brachiopod shells which were subjected to different degrees of diagenetic overprint. In Jurassic *L. punctata* (Fig. 2.31A-B) the primary layer is still discernible from the distinctly secondary layer. The morphology of the fibres (in cross-section) is well-preserved and resembles that of pristine fibres (cf. Ye et al., 2018a). Cavities developed in between fibres previously filled by organic mebrane (Fig. 2.31B). In the shell of the Jurassic brachiopod *D. digona* (Figs. 2.31C-D) the primary layer is indistinguishable from the secondary layer. Smooth sample surfaces were difficult to obtain, because when sectioned with a microtome knife, the altered shell material with loss of all organic matter became brittle (Figs. 2.31C-D). The shell of *D. digona* has a dense array of endopunctae which were filled with organic tissue in the live animal and which are now filled with inorganic crystallised calcite (Fig. 2.31C). Figures 2.31E and F show arrays of

diagonally cut fibres in the Ordovician brachiopod *P. laticostata*. Its fibre morphology is highly distorted; compare images of Figs. 2.31A and E. The organic membrane normally observed between fibres is absent, and neighbouring fibre surfaces are in contact (Fig. 2.31F). Cavities which may develop due to decomposition of the organic membrane were not observed in the fossil *P. laticostata* shell. Instead, neighbouring fibres amalgamated by recrystallisation of the NMB and formed new irregularly-shaped crystalline calcite units (Fig. 2.31E).

As a characteristic example, we highlight the shell of the fossil brachiopod *Q. attenuata* and its overall changes in fibre morphology and internal nanoscale structures (Fig. 2.32; Fig. 2.52 in chapter 2.3). When sectioned with a microtome knife, some of the fibres shattered, and clean microtome cuts are rarely possible through stacks of fossil fibres. The EBSD scan performed on a cross-sectioned stack of fibres of the fossil *Q. attenuata* (Fig. 2.32A) shows uniform colour for individual fibres indicating single crystallinity of each fibre. In this fossil sample the outline of the fibres is well-preserved (e.g., Fig. 2.52 in chapter 2.3). However, the organic membrane between fibres is absent (Fig. 2.32C) but, more importantly, the original nanogranular mosaic structure within the NMB calcite was replaced. Indeed, inorganic calcite crystals with rhombohedral morphology (IRC) make-up the fibres of the diagenetically impacted fossil shell (Fig. 2.32C). Thus, even though the original arrangement and outer micromorphology of the fibres are maintained, the significant change of the nanoscopic bio-calcite morphology within the biocrystals indicates that the biogenically formed NMB was recrystallised/replaced, and now appears as diagenetic IRC. In addition, new diagenetic calcite formed between adjacent fibres at the site of the former organic membrane (Fig. 2.32C).

Thermally altered modern brachiopod shells

To investigate the decomposition of organic material within shells, we thermally altered shells of some modern brachiopods. Modern *L. uva* shells were heated in a dry environment at 100 °C for 72 hours, for three and for four months, and at 400 °C for 48 hours (Figs. 2.33 and 2.45). Thermal treatment at 100 °C for 72 hours did not induce any marked microstructural change to the calcite fibres. Indeed, the organic membrane between the fibres is still preserved (Fig. 2.33A), however, thinned significantly by dehydration (Fig. 2.33B) and starting to detach from the mineral fibres (Fig. 2.33A). In contrast, thermal treatment at 100 °C for three months destroyed all organic matter within the shells (Figs. 2.33C-D). In addition, new massive calcite formation took place (Fig. 2.33C) with mineral units of primary and secondary shell layers growing together forming a new entity.
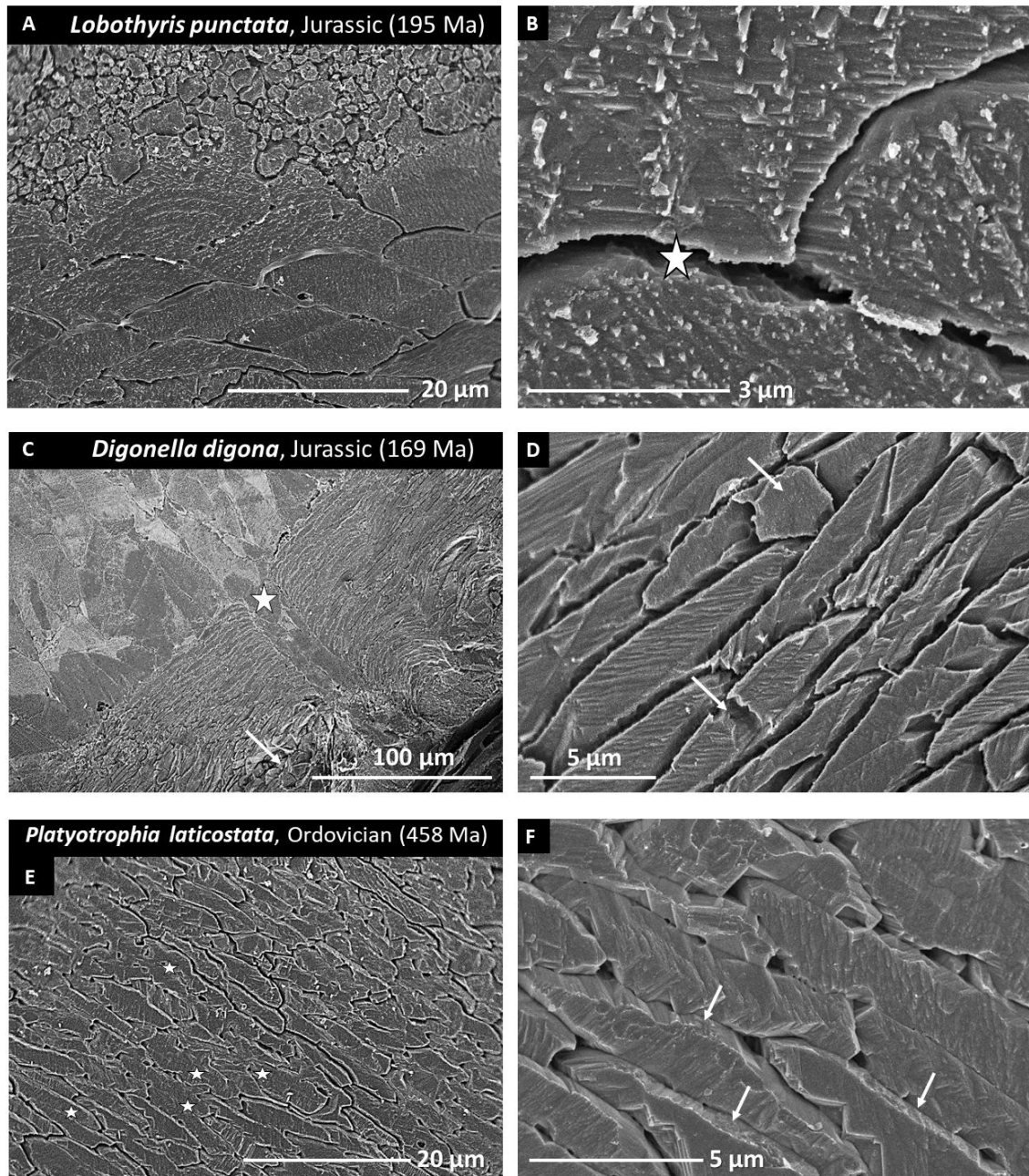
Figure 2.31: FE-SEM images showing microstructural characteristics of fossil brachiopod shells subjected to different degrees of diagenetic alteration. In *L. punctata* (A) the shell layers (primary and secondary) are well discernible and fibre morphology is regular (B). Cavities are present between neighbouring fibres (white star in B) at the sites of former organic membranes. The primary and the fibrous shell layers cannot be distinguished from each other (C, D). Endopunctae are filled with newly formed calcite (white star in C). As organic membranes decomposed cavities occur between fibres (D). Shell ultrastructure in *P. laticostata* is highly distorted (E), and cavities form after organic membrane decomposition (F) but with advanced alteration neighbouring fibres amalgamate (white stars in E; white arrows in C, D, F).
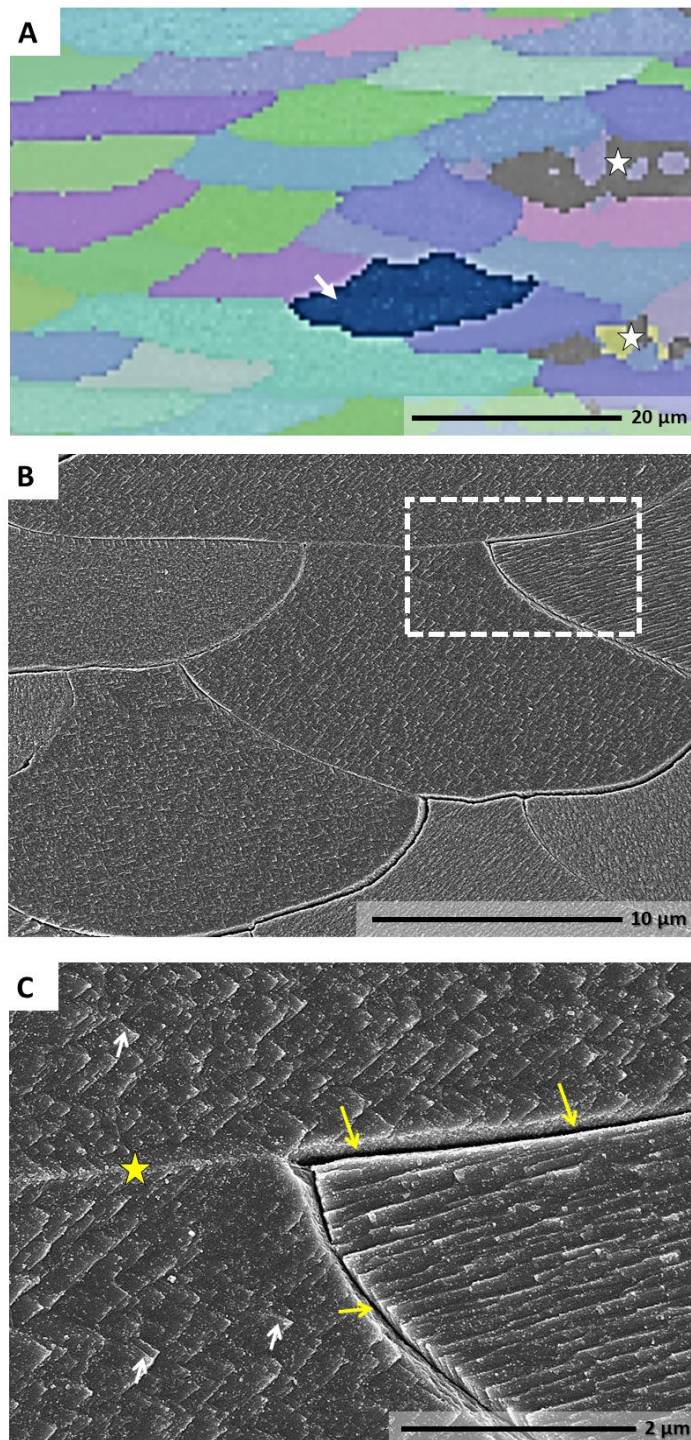
Figure 2.32: Electron backscatter diffraction (EBSD) map (A) and FE-SEM images (B, C) of cross-sections of fibres in the fossil brachiopod *Q. attenuata*. The EBSD scan is colour-coded for crystallographic lattice orientation; the white arrow points to a fibre with well-preserved morphology, whereas white stars point to fibres with poorly preserved shell morphology. (A). The white dashed rectangle in (B) indicates the position of the SEM image in (C). Organic membrane between fibres is absent (yellow arrows in C). New calcite formation occurs when neighbouring fibres grow together and form a new unit (yellow star in C). In the fossil shell calcite, some fibres are well-preserved but diagenetic crystallites are present - inorganic rhombohedral calcite (IRC; white arrows in C).

Thermal alteration at 400 °C for 48 hours destroyed most of the occluded biopolymers within the shells (Fig. 2.45). Large cavities were left behind at the location of organic membranes between neighbouring fibres. On rare occasion, highly-thinned membrane remnants can be still observed between adjacent fibres (Fig. 2.45D). The main effect of this alteration process was that biopolymers within the shell were degraded, the calcite of the fibres was highly porous, and the shell became highly brittle. New calcite formation started as adjacent fibres amalgamated, showing signs of pitting of fibres and change in their original microstructure.

Hydrothermally altered modern brachiopod shells: the effect of artificial meteoric fluid

Hydrothermal treatment at 100 °C for 28 days (Figs. 2. 34A-B), at 175 °C for 14 days (Figs. 2.34C-D, 2.35 and 2.46) and for 28 days was carried out in a solution of artificial meteoric fluid. At these alteration conditions, overall calcite fibre morphology and fibre stack arrangement were retained in all test specimens. The calcite was slightly etched at the fibre rims (Figs. 2.43A-B) and all organic material was destroyed within the shells (Figs. 2.34C-D and 2.35). The extracellular membrane vanished (Fig. 2.35) as well as the network of biopolymer fibrils normally occluded within the fibres of the pristine shell (Fig. 2.35). NMB calcite can be still observed in experiments using artificial meteoric fluid at temperatures of 175 °C after 14 days, and new calcite formation is minimal. However, IRC calcite formation was observed at alteration temperatures of 175 °C and alteration times of 28 days (Figs. 2.47 and 2.48). Under these conditions, we observed significant degradation of organic matter, amalgamation of fibres and more importantly, restructuring of the biogenic calcite at both, the nano- and microscale levels. Furthermore, degradation of the original biologic microstructural features within the shell was not uniform, and amalgamation of fibres was more extensive in some places than in others (Figs. 2.47 and 2.48).

Hydrothermally altered modern brachiopod shells: the effect of artificial burial fluid

Hydrothermal alteration at 100 °C and at 175 °C carried out in burial solution for 28 days (Fig. 2.36) greatly affects and changes the morphology of fibres, destroys all organics in and between the fibres, and induces the formation of large cavities within shell calcite. At 100 °C and 28 days of alteration, the microstructure of the primary and the fibrous shell layer mineral units and fibres is greatly disrupted by the hydrothermal treatment (Figs. 2.36A-B). Extensive dissolution as well as amalgamation is noticeable of the secondary layer fibres. At higher temperatures, the hydrothermal alteration experiment produced an even greater disruption, alteration and dissolution of brachiopod calcite fibres (Figs. 2.36C-D). In some places, alteration of the original microstructure was quite extensive with dissolution producing sharp zigzag-edged fibres (Fig. 2.36D).
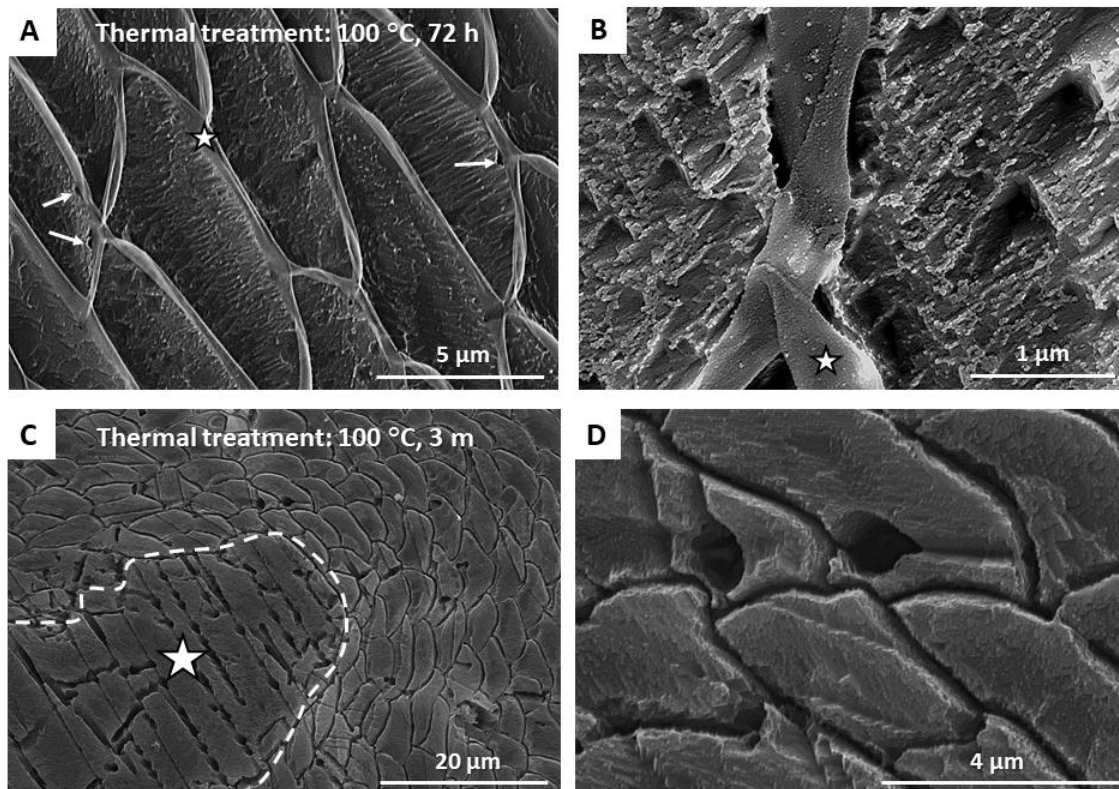
Figure 2.33: FE-SEM images of thermally altered modern *L. uva* shells at 100 °C. Thermal treatment at 100 °C for 72 hours dehydrates organic components but does not destroy them (white star in A and B). A thin biopolymer ribbon remains between neighbouring fibres. However, as the organic membranes shrink they become detached from the calcite of the fibres (white arrows in A). Thermal treatment at 100 °C for 3 months causes the disintegration of biopolymers (C, D), amalgamation of fibres, and new, inorganic calcite unit formation (white star and dashed line in C).
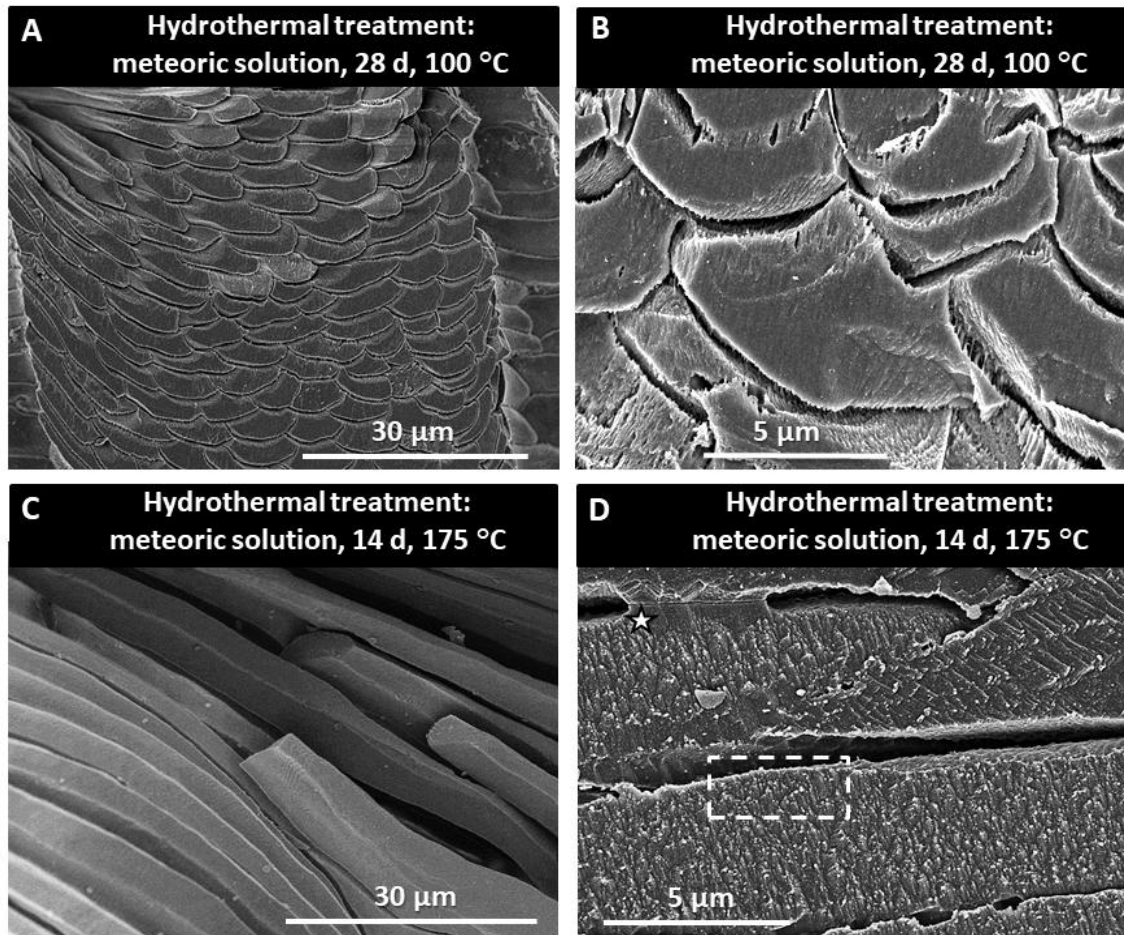
Figure 2.34: FE-SEM images showing hydrothermally altered modern *T. transversa* shells. Hydrothermal treatment occurred in a fluid simulating meteoric fluid (10 mM NaCl aqueous solution) at 100 °C for 28 days (A, B) and at 175 °C for 14 days (C, D), respectively. The well-preserved morphology of the fibres can be observed, as well as the well-kept stacks of fibres and the cavities between fibres which were filled in the pristine shell with organic membranes. Hydrothermal treatment, even at 100 °C, destroyed all biopolymers that were occluded within the shell. The white dashed rectangle in (D) indicates the position in the sample of SEM image (C). Slight amalgamation of fibres was observed in the specimen hydrothermally altered at 175 °C (white star in D).
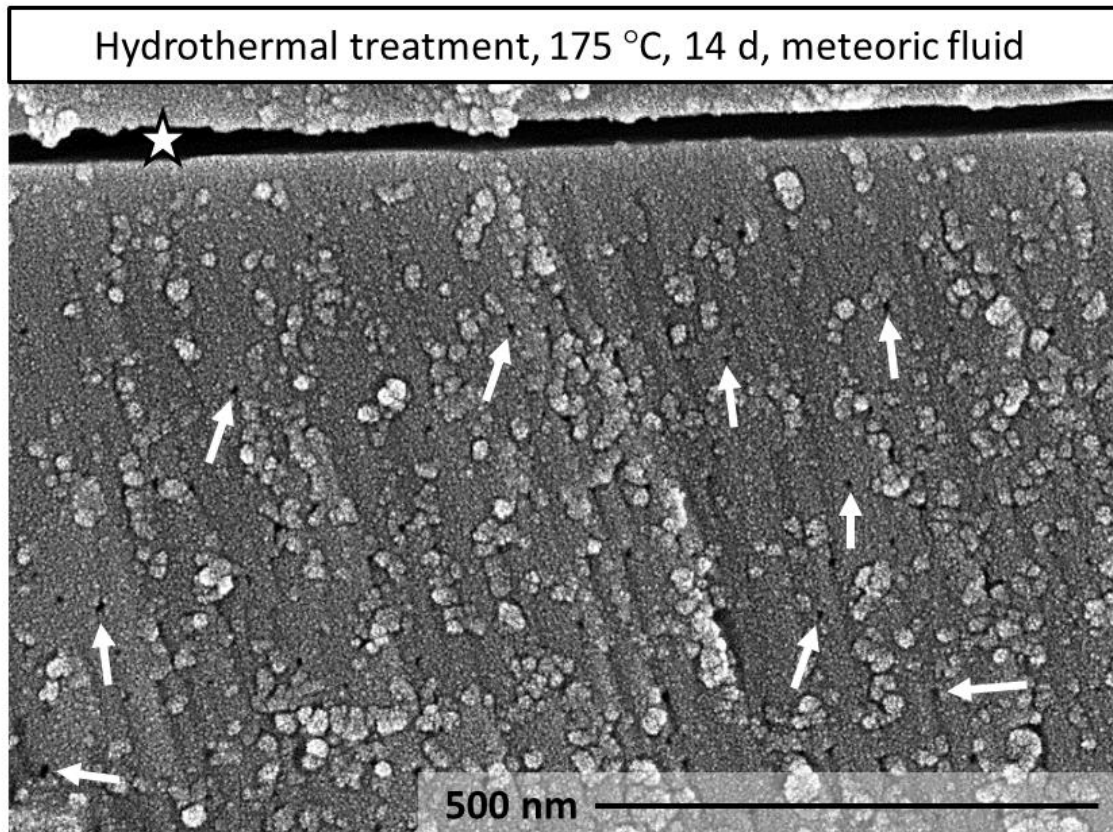
Figure 2.35: FE-SEM image of a hydrothermally treated shell part of modern *T. transversa*. Hydrothermal alteration occurred at 175 °C for 14 days in artificial meteoric fluid. At this stage of alteration all organics are destroyed (white star), however, new calcite formation has not yet taken place. The white star points to the location of an organic membrane which encased fibrous calcite in the pristine shell. White arrows point to minute holes within the calcite of the fibre which become visible after decomposition of the network of organic fibrils.
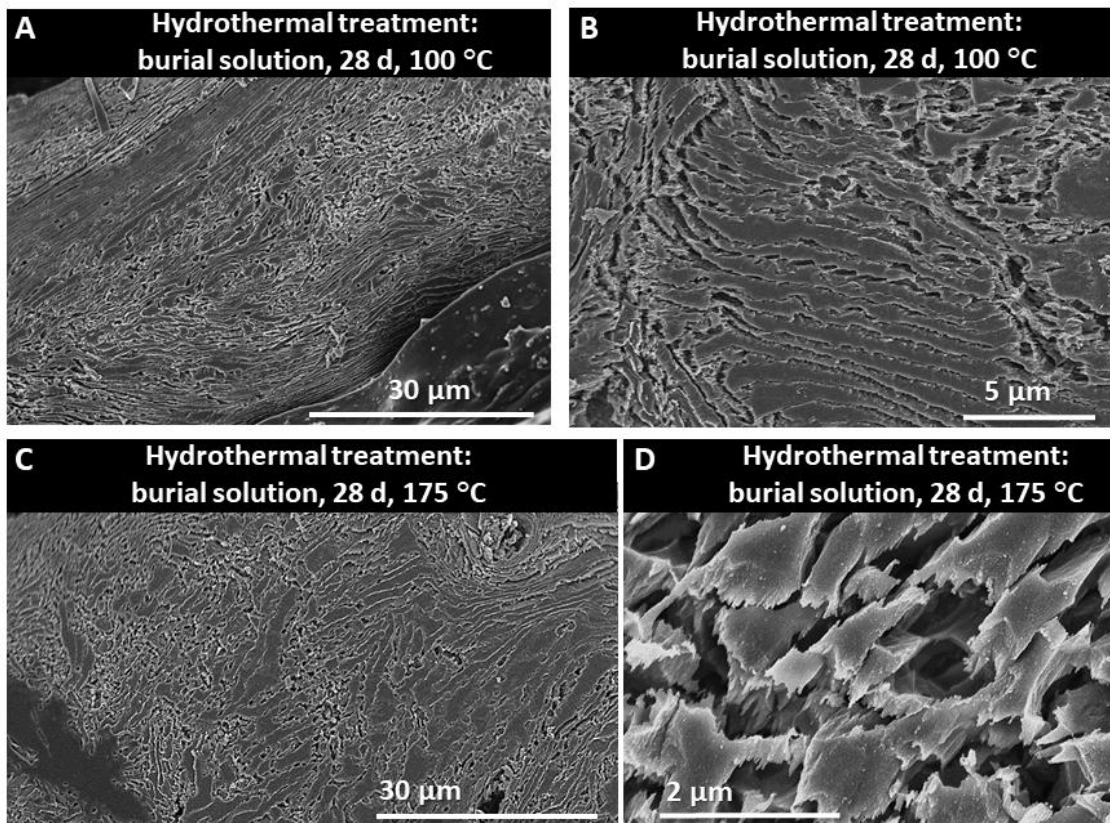
Figure 2.36: FE-SEM images show the effect of simulated burial fluid (100 mM NaCl + 10 mM MgCl$_2$ aqueous solution) on brachiopod shells during hydrothermal treatment (modern *T. transversa*). Alteration lasted 28 days at 100 °C (A, B) and 175 °C (C, D), respectively. Fibre morphology is severely distorted, and all occluded biopolymer membranes and network of fibrils are decomposed.

Cathodoluminescence evaluation

Cathodoluminescence (CL) has been used by researchers since the 1980's to characterise the preservation status of fossil brachiopod shell calcite (e.g., Popp et al., 1986; Rush and Chafetz, 1990; Grossman et al., 1996; Angiolini et al., 2012), and to distinguish whole rock chemistries (e.g., Brand, 1989b). Its use continues unabated in differentiating between preserved and altered carbonates. However, with the acquisition of high-definition trace elements, stable, radiogenic and clumped isotopes to characterise environmental effects, we require screening tools with enhanced resolution power in identifying the preservation status not only of shells, but of individual fibres and columns at the micro- and nanostructural levels.

Modern brachiopod shells, collected alive, luminesced dark blue for the shell and light blue in the punctae (intrinsic luminescence; Fig. 2.37A), which was termed 'background blue', indicative of an absence of quenchers (e.g., Fe) and activators (e.g.,

Mn; Amieux et al., 1989). Indeed, *T. transversa* from Friday Harbor contains about 27 and 26 µg/g Mn and Fe, respectively, and these contents are well below their activation and quenching potentials (Machel et al., 1991; Brand et al., 2003). As manganese was not added to the alteration solutions, the source of Mn is the modern brachiopod shells themselves. EPMA results give 0.2 wt% Mn for the pristine and 0.15 wt% Mn for the hydrothermally altered *T. transversa* shells.

The luminescence colour of the hydrothermally altered *T. transversa* shell is blue for the primary layer and the exterior part of the fibrous shell layer (Fig. 2.37B), while at the interior shell part (Fig. 2.37B) the blue luminescence is intercalated by thin orange-brown lines. Other than that there is little difference in luminescence between pristine and hydrothermally altered shells.

The fossil brachiopod shells (Figs. 2.37C-E) reveal decidedly different luminescence and luminescence distribution patterns. For all three fossil samples, we observed bright yellow to orange-brown luminescence for the primary layer and at the innermost shell part adjacent to the brightly luminescent whole rock cement (Figs. 2.37C-E). Luminescence for the shell of *D. digona* ranges from dark blue to orange-brown. The endopunctae and primary shell layer parts are always orange-brown (Fig. 2.37C), whereas the shell between the endopunctae exhibits dark blue luminescence (Fig. 2.37C). Similar observations were made in the CL pattern of *L. punctata* (Fig. 2.37D). The shell exhibits luminescence colours which vary from dark blue and near non-luminescent (intrinsic luminescence) to patchy luminescent (intrinsic with orange patches) for primary shell layer parts, and faint orange luminescence in the endopunctae (Fig. 2.37D). The primary shell layer in *P. laticostata* (Fig. 2.37E) is characterised by bright orange luminescence similar to that of the cement. Otherwise the fossil brachiopod *P. laticostata* shows dark blue and non-luminescent regions (upper Fig. 2.37E) concomitant with shell parts which are dark blue and intercalated with patchy orange luminescence (lower Fig. 2.37E).

Patterns of calcite crystal organisation in modern, fossil and altered brachiopod shells

Crystal orientation data are presented in colour-coded electron backscatter diffraction (EBSD) maps, and corresponding pole figures show orientation statistics of crystallographic c-axes ({00.1} poles) and a*-axes ({10.0} poles) either as data points or as pole density distributions. Shell microstructure is visualised with grey scale EBSD band-contrast measurement images, a contrast which gives the signal strength for each measurement point. Thus, when a mineral is hit by the electron beam, a strong diffraction signal is obtained, while, when polymers or nanometre-sized crystallites are

encountered, which are too small to be differentiated from each other by the electron beam, the diffraction signal is either absent or too weak to be interpretable. The strength of crystallographic axes co-orientation within biocrystals (fibres or basic mineral units of the primary layer) and within inorganic polycrystalline assemblies (e.g., secondary calcite, cement) is expressed by the multiple of uniform distribution (MUD) value. High MUD values indicate high crystallographic axes co-orientation as is the case in inorganic single crystals, whereas low MUD values reflect low crystallographic axes co-orientation down to an MUD value of 1, indicating random crystallographic orientation of crystals in the chosen EBSD scan field.

Calcite crystal orientation patterns in pristine, hydrothermally altered modern and in fossil brachiopod shells are presented in Figs. 2.38-2.39 and Figs. 2.47-2.49.
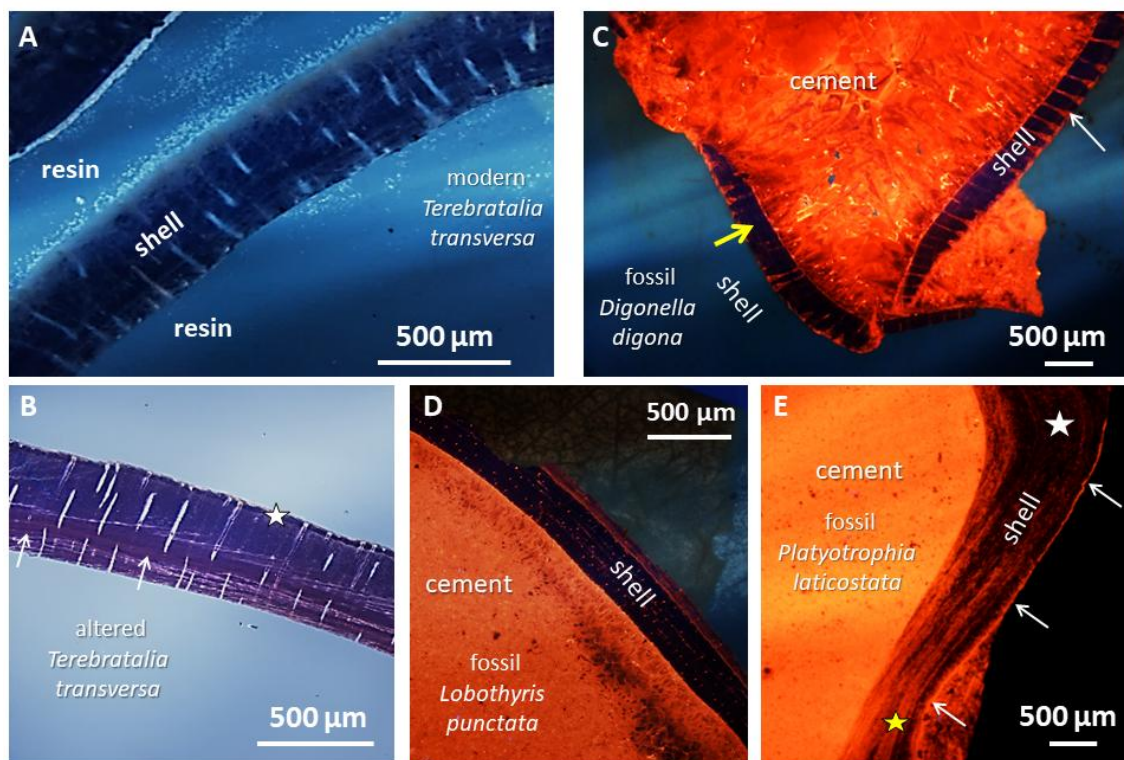
Figure 2.37: Cathodoluminescence images of modern, altered and fossil brachiopod shells (A: modern *T. transversa*, B: altered *T. transversa*, C, D, E: the fossil brachiopods *D. digona*, *L. punctata*, *P. laticostata*, respectively. The dark blue (A) and light blue, slightly orange luminescence colours (B) confirm the pristine state (A) of the modern shell and its very slight overprint (B) after treatment. Yellow to orange luminescence colours indicate a significant overprint, e.g., as it is the case for Ordovician *P. laticostata* (white arrows in C and E, yellow star in E). The orange luminescence in Jurassic *D. digona* from Normandy indicates the diagenetic calcite filling in the endopunctae (white arrow in C), however, the dark colours between the endopunctae indicate well-preserved shell parts (yellow arrow in C). Yellow star in (E) marks a shell part with orange luminescence, thus, a highly overprinted shell part. Patchy blue luminescence was observed within the same, severely overprinted shell part (white star in E).
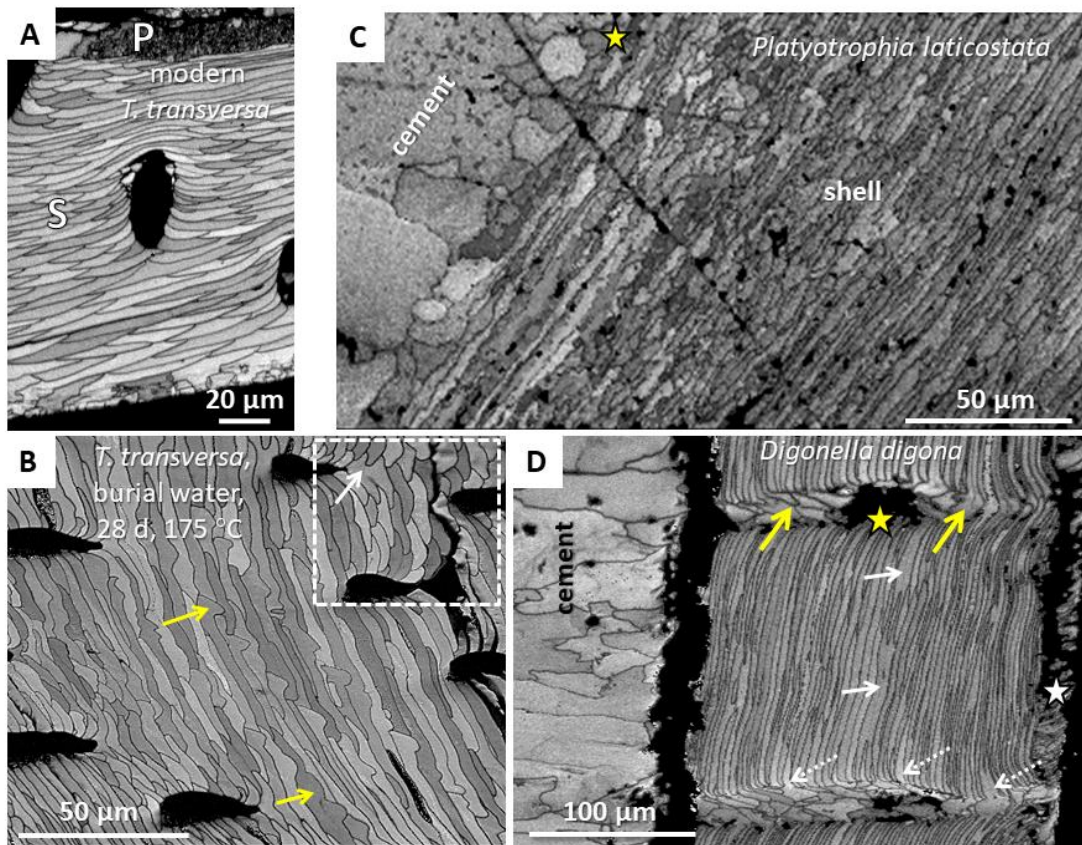
Figure 2.38: EBSD band contrast measurement images of modern (A), altered (B) and fossil (C, D) brachiopod shells. A, B: *T. transversa*; C: *P. laticostata*, D: *D. digona*. The characteristic cross section of transversely cut fibres which form well-organised stacks can be observed in the pristine shell (A). In the hydrothermally altered shell (B) stacks of longitudinally and transversely cut fibres can also still be observed, however, fibre morphology is distorted (yellow arrows in B) and neighbouring fibres fuse as these grow into each other. Within the same shell some stacks of fibres may keep their original morphology (e.g., shell part within the dashed white rectangle in B), even though their neighbouring fibres are fused (white arrow in the white dashed rectangle in B). C: Individual fibres in the highly overprinted shell of *P. laticostata* are not discernible any more. When in contact with the cement, the fibres fuse completely with the calcite of the cement (yellow star in C) and new, single-crystalline calcite units develop. D: Shell part of overprinted *D. digona*. Even though the fibrous fabric is discernible, the shell experienced some overprint: neighbouring fibres fuse (white arrows in D), empty endopunctae (yellow star in D) get filled with newly formed calcite (yellow arrows in D) which might spread from the endopunctae to empty space between two neighbouring fibres (dashed white arrows in D). White star in (D) points to remnants of the primary layer.

The EBSD band contrast measurement image shown in Fig. 2.38A highlights the characteristic shape of diagonally sectioned fibres and their stack arrangement (cf. Ye et al., 2018a, 2018b). In contrast, EBSD band contrast measurement image of Fig. 2.38B visualises the microstructure of hydrothermally altered shell parts of the formerly pristine brachiopod *T. transversa*. After alteration at 175 °C for 28 days in a Mg-rich solution we observe a significant change in microstructure. Even though the 'stacked fibre' appearance is still retained after the alteration process, some stacks of fibres have

undergone variable degrees of amalgamation, distortion and lateral elongation (Figs. 2.38B, 2.47 and 2.48), while in some other areas stacks of fibres retained their original (pristine) morphology and configurations. It is exceptional that on distances as short as two to three hundred micrometres shell parts with pristinely-shaped fibres can be observed next to stacks of fibres which show a distorted-shaped microstructure and new calcite formation. The pristinely shaped fibres subjected to hydrothermal conditions are indistinguishable from those not subjected to any alteration processes. At present, we are unable to say what exactly controls the distribution of pristine and altered fibres within the same shell specimen. Suffice to say that differential diagenetic alteration is a definite possibility for fossil material that could greatly complicate trace chemistry contents, as well as stable and clumped isotope compositions.

EBSD band contrast measurement images of Figs. 2.38C and D visualise the microstructure of two fossil brachiopod shells, *P. laticostata* (Fig. 2.38C) and *D. digona* (Fig. 2.38D). In *P. laticostata* the fibres are fused and highly distorted, whereas in *D. digona* longitudinally cut stacks of fibres are still discernible and may be interpreted to have escaped diagenetic overprinting or alteration. However, some signs of overprint such as amalgamated fibres are observed in the shell of *D. digona* (Fig. 2.38D), endopunctae filled with secondary calcite (Fig. 2.38D), and recrystallisation which extends from the endopunctae into the fibres (Figs. 2.38D and 2.49A).

In contrast to the selective alteration observed in *D. digona*, the fibres within *P. laticostata* experienced extreme alteration with extensive fibre distortion and amalgamation. When in contact with the whole rock cement, the fibres fuse completely with the calcite of the cement (Fig. 2.38C).

Colour-coded EBSD maps and corresponding pole figures document calcite crystal orientation patterns in pristine, hydrothermally altered modern, and in fossil brachiopod shells (Fig. 2.39). Grey-scaled band contrast and colour-coded orientation measurement images are superimposed in order to highlight both: the microstructure of the skeleton as well as the orientation pattern of the calcite. A measure of co-orientation within crystals is given by the multiple of uniform distribution (MUD) values; a MUD of 1 indicates a random crystallographic orientation, whereas MUD values of 700 and higher indicate perfect or near-perfect co-orientation in 3-D of crystallographic axes. These are observed for the reference calcite crystal grown from solution or the recrystallised calcite crystals of the cement (Figs. 2.59 and 2.60 in chapter 2.3). In a polycrystalline assemblage with only axial (one-dimensional) preferred orientation such as calcite which grows under biologic control as is the case for the pristine shell of *T. transversa* we resolve a MUD value of 62 (Fig. 2.39A). MUD values of the hydrothermally altered *T. transversa* and of the fossil brachiopod shells Jurassic *L. punctata*, Jurassic *D. digona* and Ordovician *P. laticostata* are 50 (Fig. 2.39B) and 52, 41 and 16, respectively (Figs. 2.39C-E). The latter MUD values indicate that, in comparison to the pristine shell,

the pattern of original bio-controlled calcite crystal co-orientation is disturbed in the altered and in the fossil shells, as the pattern of crystal orientation becomes more random.

The scan field of the EBSD measurement of *D. digona* was subdivided into different subsets and subsequently determined their MUD values (Fig. 2.39D). The endopunctae of this brachiopod shell were filled with secondary calcite crystals during diagenesis. These are large compared to the cross-sectional diameter of the fibres. For these parts of the fossil shell MUD values of 58 and 62, respectively, are reached (Fig. 2.39D). The high MUD values are due to the large secondary calcite crystals, which each give strong peaks in the orientational distribution of the mapped area. Thus, higher MUD values are the result. In *D. digona* the fibrous shell part between the endopunctae has a MUD value of 50 (Fig. 2.39D), an indication that calcite co-orientation in this part of the shell is only slightly disturbed. The slight disturbance can be attributed to newly formed calcite which grew from the endopunctae into adjacent shell parts (Fig. 49). If the secondary precipitated calcite that extends from the endopunctae into adjacent shell parts is taken out of the EBSD data, a MUD value of 60 is obtained (Fig. 2.49B) indicating almost negligible overprint of that particular shell area. The entire EBSD measurement for the whole shell of *D. digona* has a MUD value of 41 (Fig. 2.39D). This MUD measurement includes well-preserved fibrous shell parts, recrystallised calcite of the primary shell layer as well as secondary calcite within the endopunctae and adjacent shell regions.

The lowest MUD value of 16 was obtained for the highly overprinted shell of the fossil brachiopod *P. laticostata* (Fig. 2.39F). In this instance, fibre morphology and their arrangement in parallel stacks was entirely reset by newly formed, more randomly oriented, inorganic calcite formed during post-depositional diagenesis.

2.2.5 Discussion

Biogenic carbonate archives are fundamental for studies of past climate dynamics and environmental change. The greatest challenge that all archives face is their capacity to retain original signatures, such as chemical (Brand et al., 2011) or microstructural (Casella et al., 2017). Alteration of the pristine archival material starts with the death of the organism. The immediate decay of the organic matter (biopolymers) is accompanied by the concomitant precipitation of inorganic mineral within and at the two surfaces of the shell (e.g., Patterson and Walter, 1994; Ku et al., 1999; Brand, 2004; Zazzo et al., 2004; Casella et al., 2017). As alteration progresses further, pristine biogenic signals are
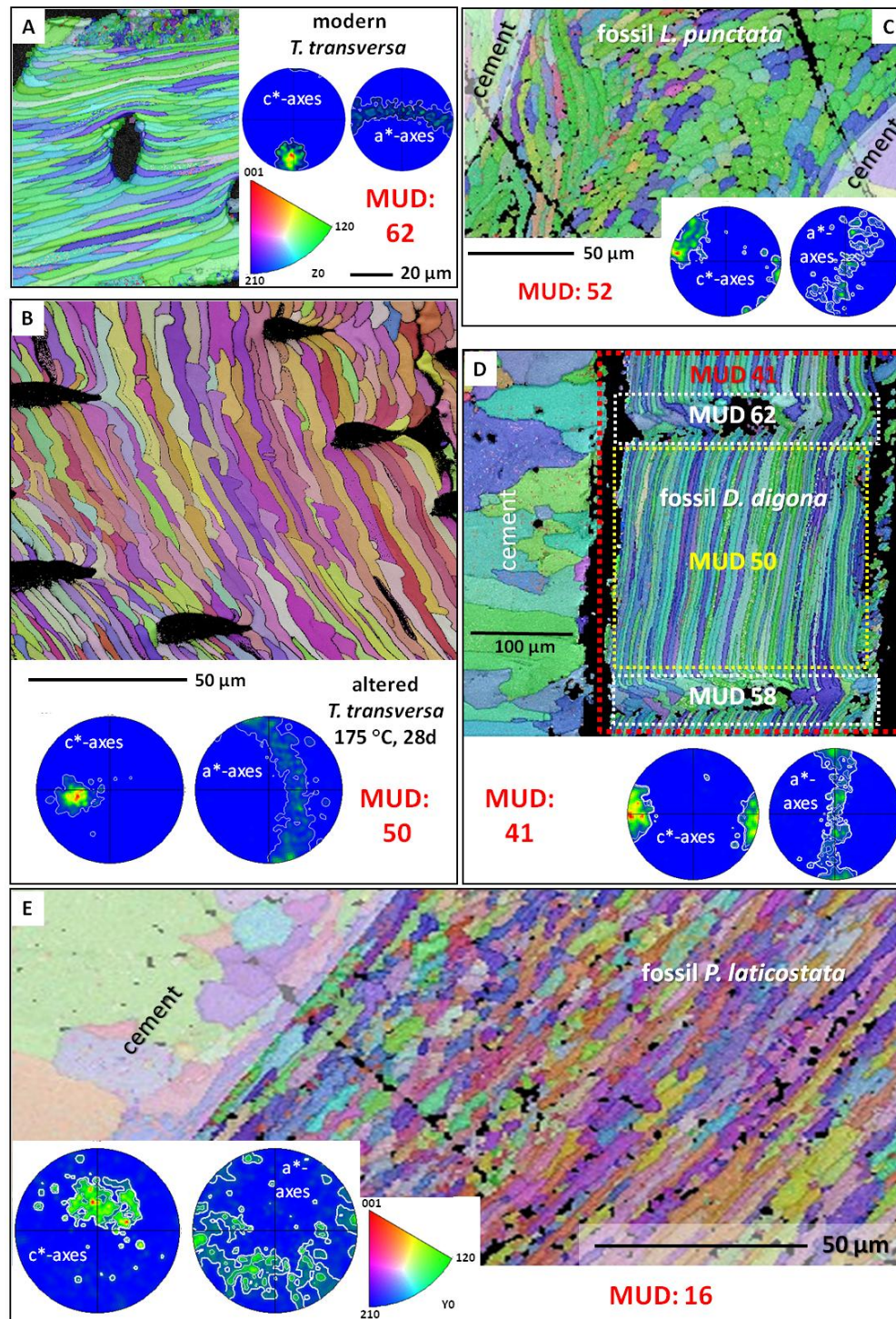
Figure 2.39: EBSD crystallographic orientation results shown as coloured EBSD maps with corresponding pole figures for modern and altered *T. transversa* (A, B) and the fossil brachiopods *L. punctata* (C), *D. digona* (D) and *P. laticostata* (E). Calcite co-orientation strength is given with MUD values (multiples or uniform random distribution) which are given at each EBSD map and corresponding pole figure. The measurement on the pristine shell has an MUD value of 62 due to axial-preferred crystallographic orientation induced by the biologically induced growth mechanism. The measurement on the highly overprinted shell has a MUD value of only 16, demonstrating the more randomly oriented nucleation of recrystallised calcite during diagenesis. Hydrothermal alteration at 175 °C (B) lowers the degree of calcite crystallographic preferred orientation in the overprinted shells, however, only slightly with a MUD value of 50. Note the

crystallographic amalgamation of adjacent calcite fibres in (B). The shell part of the fossil brachiopod *L. punctata* (C) is little affected by diagenetic overprint; fibre morphology is maintained with a MUD value of 52. Panel D shows the EBSD measurement on the fossil brachiopod *D. digona* (red dashed line in D). The entire measurement (the shell together with secondary calcite crystals in the endopunctae) has a MUD value of 41. As the secondary calcite crystals in the endopunctae are comparatively large single crystals (white dashed line in D), the MUD values for the measurements in the endopunctae are high with MUD values of 62 and 58, respectively, in comparison to the MUD value of the entire shell material. Calcite crystallographic preferred orientation in shell parts between the endopunctae has a MUD value of 50 (yellow dashed line in D), thus, overprint of these shell areas is moderate. Note that the secondary crystals filling the endopunctae share crystallographic orientation with calcite fibres in the shell.

replaced to various degrees by diagenetic chemistries (e.g., Brand and Veizer, 1980, 1981), and new microstructural characteristics (e.g., Casella et al., 2017).

Our alteration experiments were performed for 28 days. However, despite this relatively short time, we were able to trace and pinpoint the first major steps which occur with alteration. In addition, we found microstructural features which were observed in both, brachiopod shells overprinted by thermal/hydrothermal alteration as well as in brachiopod shells that were overprinted by natural diagenetic processes. Accordingly, we discuss subsequently micro- and nanostructural changes that developed in the course of laboratory-based hydrothermal alteration and conclude the discussion with structural features which were observed in the fossil shells. The comparison between modern and fossil brachiopod shells is feasible due to the similarity in shell microstructure between the two groups.

Pristine versus altered brachiopod shell micro- and nanostructures

At Earth surface conditions, calcite is the thermodynamically most stable calcium carbonate phase, and driving forces are not high for recrystallising biogenic low-Mg calcite. In contrast to inorganic carbonate, the composite nature and hierarchical organisation of biogenic carbonate provide both, surface-energy as well as strain-related driving forces for recrystallisation. The vast interface areas coupled to the nanocomposite formation principle of biologic hard tissues increases the free energy of the material. Likewise, micro- and nanopores, voids and cavities, which develop after the decay of the organic matrix and network, add to the driving force for recrystallisation. Accordingly, with alteration of biogenic calcite, in the laboratory and in nature, the surface/interface-rich features disappear first. For example, alteration at ONLY 100 °C induces the immediate dehydration and decomposition of organic matter and fibrils (high surface feature), whereas alteration at high temperatures such as 175 °C and for the first few weeks does NOT immediately cause the recrystallisation of the

nanocomposite mesocrystal biocarbonate to inorganic rhombohedral calcite. This process takes significantly longer.

Characteristics of the occluded biopolymers and specific nanostructural features of the bio-calcite of pristine (Figs. 2.40A-C) and hydrothermally altered *T. transversa* shells are juxtaposed in Fig. 2.40 (Figs. 2.40D-F; Fig. 2.61 in chapter 2.3). In addition, we show nano- and microstructural features of the calcite of two fossil brachiopods (Fig. 2.41; Figs. 2.62 and 2.63 in chapter 2.3): one is the slightly overprinted shell part between the endopunctae in Bathonian *D. digona* from Normandy, and the other is the highly overprinted shell of Upper Ordovician *P. laticostata.* Upon close inspection, the hydrothermally altered as well as fossil shells show that alteration starts with dehydration of the occluded organics (membranes: Fig. 2.40A, network of fibrils: Fig. 2.40B). Initially they shrink, and at a later alteration stage they decompose, and hence remnants may be irregularly distributed within the shell (Fig. 2.50; Fig. 2.61 in chapter 2.3). At a more advanced stage of alteration (e.g., at 400 °C or alteration at 100 °C for three or four months) all occluded organics have disintegrated and a multitude of multi-sized voids developed within the shells. These may serve as conduits for fluids into and through the biogenic hard tissue and supply the space for the precipitation of secondary minerals within and between the original mineral units.

The calcite fraction of the shells is influenced by the alteration process on different microstructural scales. It starts with fusion of nanoscopic entities within the NMBs (compare Figs. 2.40C-F) and it is accompanied by precipitation of secondary calcite, amalgamation of fibres and distortion of fibre morphology within the entire shell microstructure (Figs. 2.47 and 2.48). Recrystallisation of NMB calcite to IRC is not surprising as the replacement process reduces interface energy and some strain energy which is present in NMBs due to their nanocomposite nature. Our AFM results show that on the nanoscale we find similar features for the calcite of fossil shells (Fig. 2.41; Figs. 2.62 and 2.63 in chapter 2.3). NMB calcite is observed in the well-preserved fibres of the slightly overprinted shell part of *D. digona* (Figs. 2.41A and B), but this is not the case in the shell of the highly overprinted fossil brachiopod sample *P. laticostata*. Within this sample, at the micrometre scale level fibre morphology is almost erased (Fig. 2.41C), and at the nanoscale level nanoparticulate calcite was amalgamated to larger entities (Fig. 2.41D).

Contrasting to the microstructure of the primary layer with its interdigitating basic units and cavities the fibrous microstructure of the secondary shell layer is tight and withstands destruction or dissolution during the alteration treatment. At low alteration temperatures (100 °C) major changes in micro- and nanostructure are only observed when alteration times reach three to four months or even longer, whereas at high alteration temperatures (175 °C) a change in micro- and nanostructure is observed within two to four weeks. We find that calcite fibre morphology is maintained for a long

time during all alteration experiments carried out in this study. Because new calcite formation can only start in voids, the site of the former organics. As in the pristine material, the extracellular matrix determines the shape of the basic mineral units on the micrometre scale (e.g., that of brachiopod fibres), and at early stages of alteration the basic microstructural features of the hard tissue such as fibres are well-preserved. However, this does not mean that the (fossil) shell may not be overprinted (Fig. 2.49A). Depending on the aggressiveness and duration of the alteration process, the original microstructure does finally get distorted to varying degrees by recrystallisation and concomitant secondary mineral formation. At later stages of alteration, both, the primary as well as the secondary layer calcite is consumed, the fibrous microstructure is eradicated, and large, single crystalline, randomly oriented carbonate crystals develop (e.g., Fig. 2.38C).

Our alteration experiments clearly show that new calcite formation and fibre amalgamation are heterogeneous processes. In some instances profoundly altered and only slightly altered shell parts can be observed side-by-side. This is most probably caused by differences in fluid transmission through the shell and reflects the differential robustness and tightness of the fibre microstructure.

Modern versus fossil brachiopod shell micro- and nanostructures

In our integrated multi-analytical approach, we used extracellular organic matrix distribution patterns, morphological characteristics of biologically produced calcite and cathodoluminescence signals for distinguishing between highly overprinted and well-preserved shell parts and for devising a classification scheme of the degree of diagenetic and thermal/hydrothermal overprint. However, the aforementioned screening tools give only 'first approximation' results as they mainly cover *macro-* and *micrometre* scale levels. Integrating applied visualisation and characterisation techniques with crystal orientation measurements including information derived from MUD values on crystal co-orientation strengths yield a significantly more reliable assessment of the degree of alteration in biogenic calcite. We are able to measure changes in *micro-* and *nanostructure*s relative to those observed in pristine shell material, and thus, have a means of MEASURING diagenetic overprint. The slight differences in MUD values between pristine and hydrothermally altered *T. transversa* constrains the moderateness of the type of overprint. MUD values of laboratory-based alteration at 100 °C and 175 °C are 42 and 50, respectively, and are slightly lower than the MUD value of 62 measured for the pristine brachiopod shell. This observation is also affirmed by the only small difference in luminescence and luminescence pattern between pristine and altered brachiopod samples.
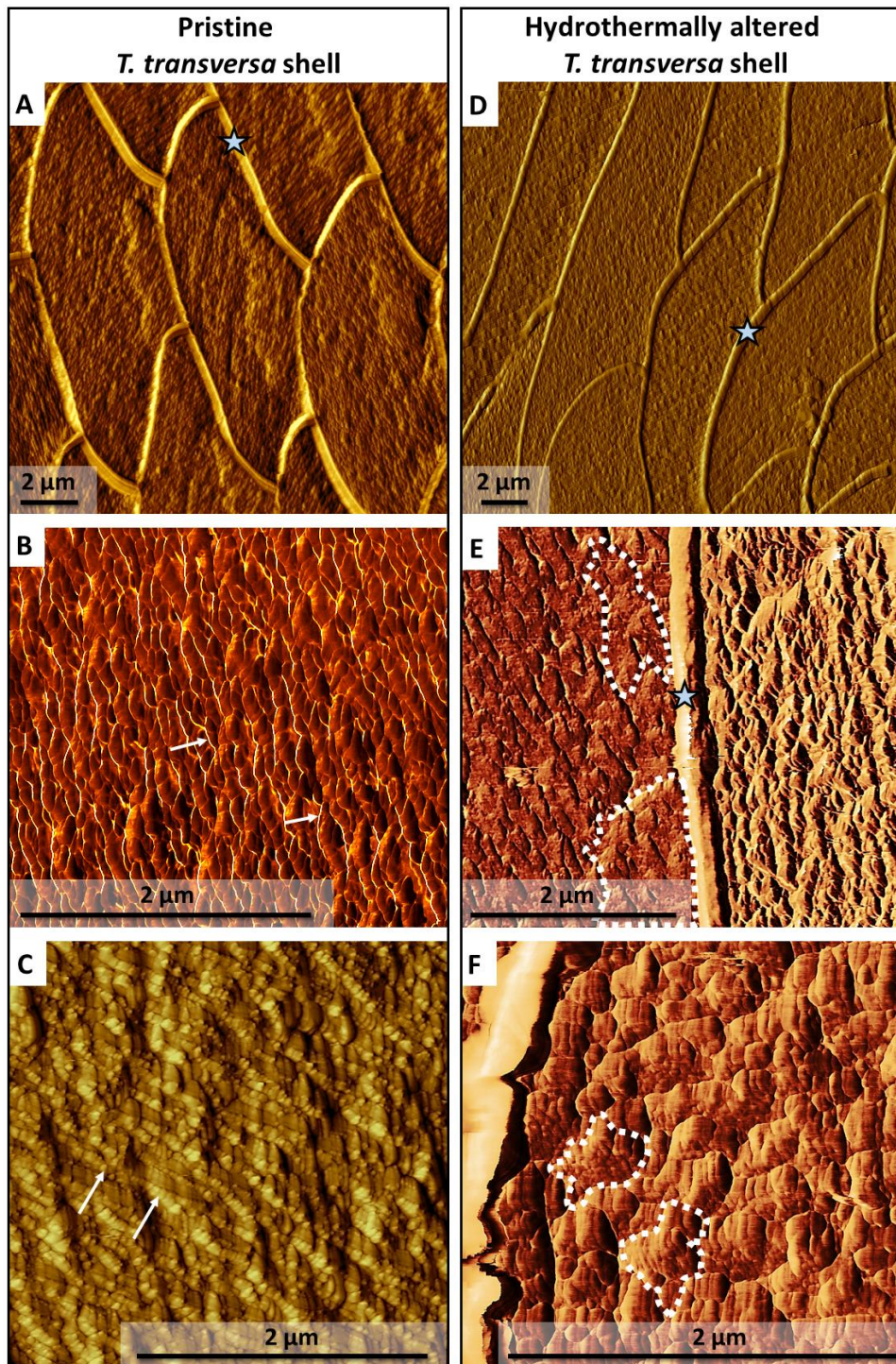
Figure 2.40: Vertical and lateral deflection AFM images showing with increasing magnification the difference in sub-micron scale structure of pristine (A, C) and hydrothermally altered (D, F) *T. transversa* shells. Organic membranes around the fibres are observed in the pristine and in the altered shell (blue stars in A, D, E), the network of organic fibrils within the fibres and the nanoparticulate appearance of calcite (white arrows in B, C) is only preserved in the pristine shell. In the altered shell, the network of organic fibrils is decomposed and calcite nanomosaic entities cannot be identified as these fused (recrystallised) to large units (highlighted with dashed white polygonal lines in E, F).
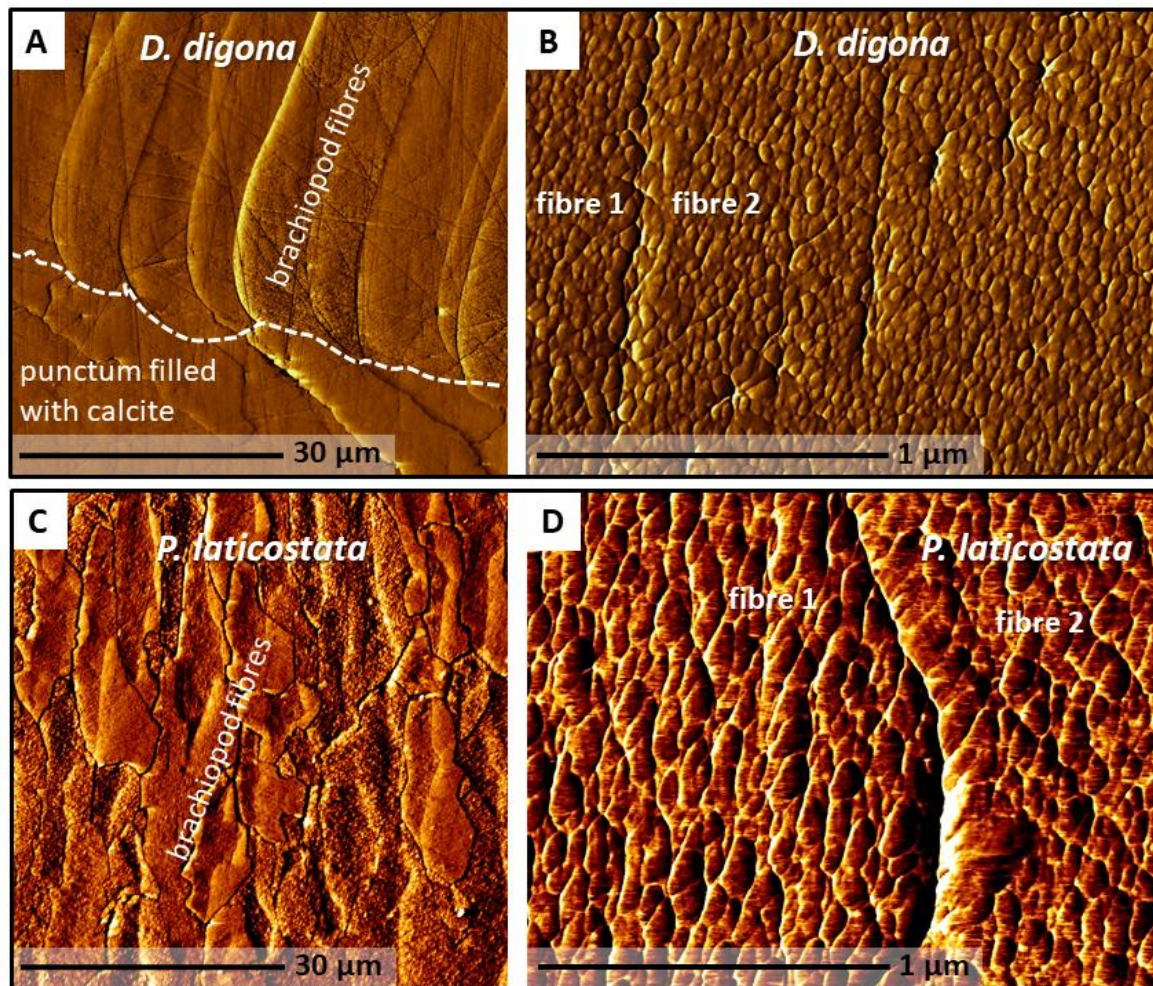
Figure 2.41: Vertical and lateral deflection AFM images showing with increasing magnification the difference in sub-micron scale structure of two fossil shells (A, B: *D. digona*, C, D: *P. laticostata*). The shell of *D. digona* is slightly overprinted between the endopunctae (white dashed line in A: fibre-punctum boundary). Fibre morphology (A) as well as the nanoscopic calcite within the fibres (B) is well-preserved. In contrast, the shell of *P. laticostata* is highly overprinted. Fibre morphology is distorted (C), and nanoscopic calcite particles within the fibres are fused (D).

The shell of modern *T. transversa* shows the typical nanocomposite mesocrystal biocarbonate structure of living biological, carbonate hard tissues, with the organic material occluded in the NMBs and the well-developed organic membranes between the NMB fibres. None of these features can be observed in the shell of the fossil brachiopod *P. laticostata*, where orange-brownish luminescence dominates and only minor parts of the shell appear intrinsic blue. In addition to the imaging tools, band contrast measurement images show a complete reset of the shell microstructure. Originally, fibrous crystals amalgamated by growing laterally at the expense of neighbouring fibres and new crystals formed with random orientations and irregular morphologies with respect to the original biogenic microstructure. Accordingly, the strength of the crystallographic preferred orientation decreases to a MUD value of 16 relative to 62 measured in pristine shells. Since shells are evolutionary-adapted functional materials,

the strength of the crystal co-orientation is high in their hard tissue. The low MUD value in *P. laticostata* and the broad distribution of c- and a*-axes in the pole figures proved the destruction of the original stacks of fibres and their crystallographic and morphologically preferred-orientation texture (Schmahl et al., 2004; Griesshaber et al., 2007b), while fibres amalgamated by lateral growth during diagenetic recrystallisation. Of the investigated fossil samples, *P. laticostata* is by far the oldest (Ordovician) and has been subjected to significantly deeper burial than any other fossil sample. In addition, the primitive fibrous fabric of this taxon originally consisted of softer material with respect to that found in Jurassic and more recent taxa. It was composed of large and uniformly radially oriented fibres below a very thin primary layer (Williams, 1968), and this less compact fabric is probably more susceptible to alteration with diagenesis (e.g., Garbelli et al., 2012; Garbelli, 2017).

Shell samples from the Jurassic of Normandy and Hungary are less overprinted, as expected for the two geologic settings and lower burial temperatures. All screening criteria suggest that the fossil shell of *L. punctata* experienced the least degree of overprint. Not much recrystallisation has taken place, as we still observe cavities between the fibres. The MUD value (Fig. 2.38D) is 52, which is only slightly less than that of pristine shell calcite. The MUD value and luminescence of *L. punctata* are comparable to those observed for hydrothermally altered samples. Filling of micrite in the shell of *L. punctata* probably enhanced the preservation of these specimens.

The shell of the Bathonian *D. digona* is a special case. Considering only the shell parts between the endopunctae, the degree of overprint is low, as indicated by the MUD value of 60 (when secondary calcite between the fibres is taken out of the evaluation, Fig. 2.49A) and the intrinsic, blue luminescence colour. However, in *D. digona* some recrystallisation has taken place observed by, (a) the amalgamation of fibres, and, even more significantly, (b) the epitactic growth of crystals of newly formed calcite in endopunctae which nucleated on some originally biogenic calcite fibres. The endopunctae are perforations through the shell which are filled by mantle tissue in the living animal. After death of the organism and decay of the organic material, endopunctae become passages for percolating diagenetic fluids and facilitate the alteration of neighbouring shell parts. This is documented by the bright orange cement in the endopunctae and in the cavity between the valves. Even though, in all *D. digona* shells of this study, the dense packing of the fibres impeded complete overprinting of the shell. Thus, even though the shell of *D. digona* was highly affected by diagenetic fluid circulation, it still retained some shell parts with well-preserved fibres. The advanced screening tools and high-definition identification of preserved and altered areas within brachiopod calcite provide us with important avenues in characterising 'pristine' material with original chemical signatures of past oceans. This is especially important to the oldest of the deep-time biogenic material used for reconstructing seawater curves of

carbon, oxygen, strontium isotopes. This will be especially beneficial and important to isotope studies, in particular for clumped isotopes, which are highly sensitive to minute degrees of diagenetic alteration. We anticipate with this combination of screening tools we will be able reconstruct deep-time seawater curves with highly improved fidelity and robustness. In summary, we can grade the degree of diagenetic alteration encountered in the studied fossil samples (Table 2.4). The impunctate shell of *P. laticostata* experienced the highest, whereas the punctate shell of *L. punctata* experienced the lowest degree of diagenetic overprint. *Digonella digona* contains well-preserved shell parts; however, these are interspersed with endopunctae filled with secondary calcite which is crystallographically continuous with the calcite of recrystallised fibres protruding into neighbouring shell regions. Two scenarios can explain this phenomenon: (a) the diagenetic calcite growing in the endopunctae may have nucleated on the originally biogenic NMB fibres or, (b) the recrystallisation process of NMB nucleated the diagenetic IRC crystals in the endopunctae. Nevertheless, fibre morphology was preserved to some extent in the impunctate shell of *Q. attenuata*. The shell shows major signs of overprint such as fibre amalgamation and diagenetic calcite formation between neighbouring fibres. In addition, within the fibres there is a change in calcite morphology from nanomosaic NMB to the typical crystal morphology of diagenetic IRC. *Quadratirhynchia attenuata* not only lacks punctae, but comes from low energy marly wackestones which should have favoured, to some degree, preservation of the brachiopod shell. The observed overprint degree may be related to high temperature fluids in the deep-burial realm, as observed by Wilmsen and Neuweiler (2008) for parts of this sedimentary succession.

Table 2.4: Degree of diagenetic alteration observed in the fibrous shell layer of pristine and altered brachiopods.

Method	Pristine	Alteration Stage 1	Alteration Stage 2	Alteration Stage 3
CL	Dark blue	Blue	Blue and minor orange	Orange
FE-SEM[1] (micro)	Sharp-distinct	Sharp-distinct, minor dissolution	Partly distorted, major dissolution	Distorted, recrystallised
FE-SEM/AFM[2] (nano)	NMB[4]	NMB	NMB-IRC	IRC[5]
MUD value[3]	$\geq$62	60-50	50-40	<40

[1] microstructural features visualised by scanning electron microscopy

[2] nanostructural features visualised by FE-SEM and atomic force microscopy

[3] multiples of uniform distribution values calculated from backscattered electron diffraction measurements (calculated from EBSD maps)

[4] nanocomposite mesocrystal biocarbonate (NMB)

[5] inorganic rhombohedral calcite (IRC)

2.2.6 Conclusions

1. Large differences in micro- and nanostructure exist between the three kinds of overprinted brachiopod shells: (i) thermally altered modern, (ii) hydrothermally altered modern shells, and (iii) naturally altered fossil shells. These differences were visualised and measured with a combination of analytical techniques: CL, FE-SEM, AFM, and EBSD. This method integration produces a reliable assessment of overprint as well as discloses different degrees of alteration and overprint of biogenic calcite.

2. During thermal or hydrothermal treatment and during natural diagenetic overprint, organic biopolymers are readily destroyed. Thermal biopolymer degradation was observed after 72 hours at 100 °C with the dehydration of the organic membrane and its detachment from the calcite fibres. Three months of thermal alteration at temperature of 100 °C destroys almost all biopolymers within shells. Consequently, cavities developed between adjacent fibres as well as a multitude of minute holes appeared within the calcite fibres.

3. Hydrothermal alteration fluid chemistry greatly influences the degree of destruction of fibres. In comparison to artificial Mg-free meteoric fluid, Mg-rich burial fluid affected the calcite to a significantly higher degree and caused distortion of the fibre morphology.

4. Hydrothermal alteration at 100 °C, after 28 days, did not induce major structural and morphological change to the calcite, nor did it lead to the formation of secondary (diagenetic) calcite. However, alteration at 175 °C for 28 days in Mg-containing burial fluid caused recrystallisation of the nanomosaic structure of the biocomposite mesocrystal (NMB) to classical mineral calcite (IRC) and concomitant amalgamation of fibres by lateral growth of the IRC into neighbouring NMB fibres. New calcite formation also took place between neighbouring fibres and at sites where calcite ingrowth occurred from one fibre into the other. However, fibre distortion and amalgamation were heterogeneous within the shell, and we found areas of highly and slightly altered fibres side-by-side.

5. Measuring crystal orientation patterns by EBSD combined with FE-SEM imaging of fibre morphology allowed for the assessment of the degree of diagenetic alteration (low, moderate, severe) in experimentally altered and fossil shells. It enabled the unequivocal identification of new calcite formation. The most severe natural diagenetic overprint of destruction of the fibre morphology and extensive new calcite formation was observed in the shell of Ordovician *P. laticostata*. The least diagenetic overprint in the investigated fossil shells was observed in the Pliensbachian *L. punctata* from the Jurassic of Hungary, where fibre morphology was still well-preserved and the site of former organic membrane between the fibres was

not filled with secondary calcite. The Jurassic brachiopods *D. digona* and *Q. attenuata* contained both, overprinted and near pristine shell areas. Overprinted regions in *D. digona* were the endopunctae, whereas the shell part between punctae was well-preserved. In the impunctate *Q. attenuata* fibre amalgamation and new calcite formation between neighbouring fibres was patchy.

6. Cathodoluminescence imaging and EBSD measurements indicate similar degrees of diagenetic overprint. However, even though cathodoluminescence is a fast and useful tool in obtaining a first impression on the degree of alteration it should not be used as a single screening tool. Instead the estimated degree of alteration by CL needs to be verified by EBSD microstructure and textural analyses, as well as by AFM nanostructure imaging. Thus, we fully endorse an integrated multi-analytical screening approach to characterising the preservation and degree of diagenetic alteration in biogenic calcite. This screening process should be important in identifying areas suitable for the most sensitive isotopes subjected to diagenetic change and influence.

2.2.7 Acknowledgments

2.2.8 Author contributions

LAC, EG and WWS designed the study. EG, VM, DH, JL, VH and UB provided sample material. LAC and VM performed the experiments. LAC and MSR conducted the analyses. LAC and MSR evaluated the data. LAC merged the data. LAC, EG and WWS drafted the manuscript. All authors contributed to discussions and the final manuscript.

2.2.9 Supplement
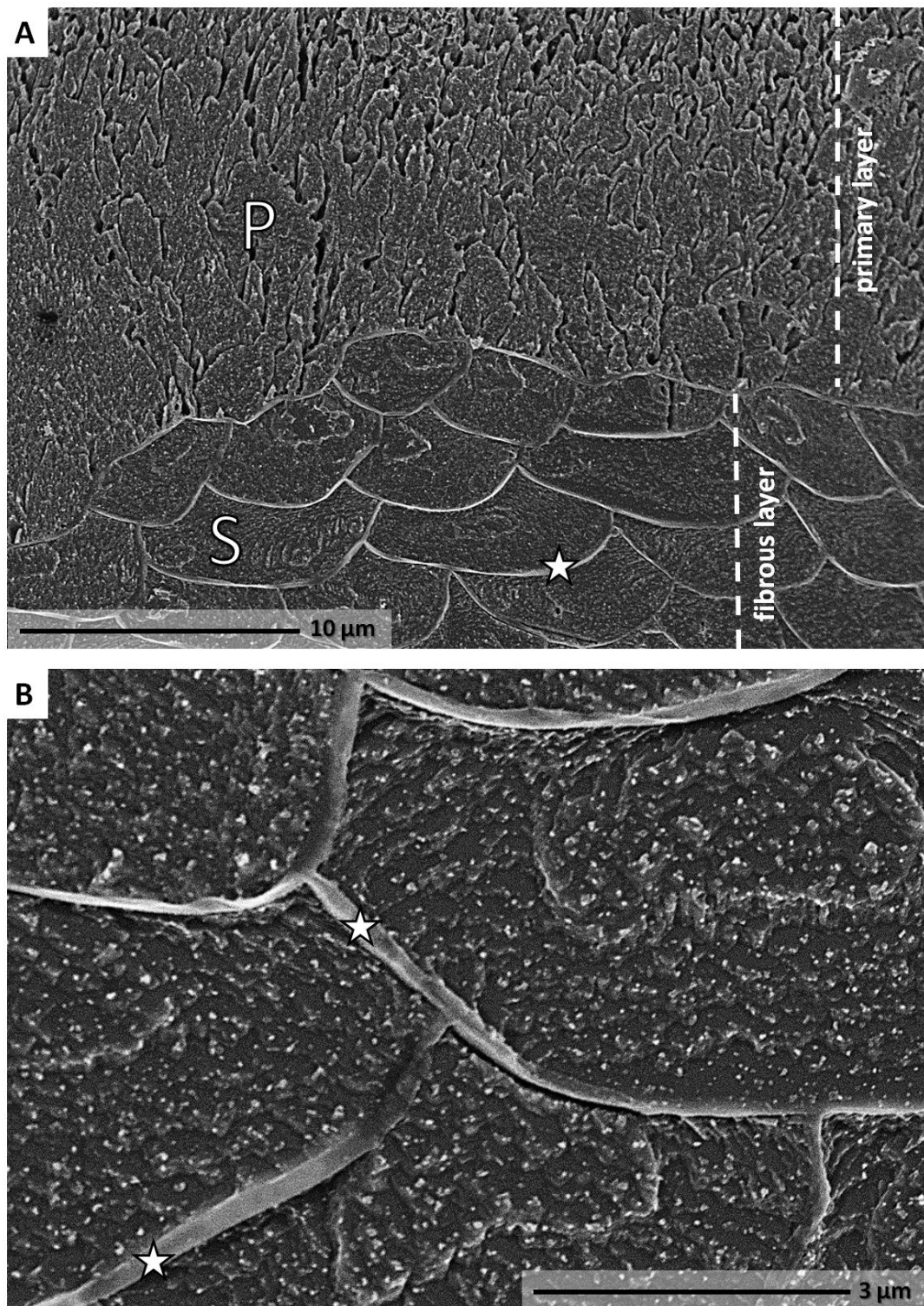
Figure 2.42: FE-SEM images of microtome cut, polished, etched and critical point dried surfaces of the modern brachiopod *T. transversa*. The distinctness in microstructure between the primary (labelled P in A), and the secondary (fibrous) labelled S in (A) and magnified in (B), as well as the organic sheaths (white stars in A, B) encasing the calcite of the fibres can be observed in the modern brachiopod.
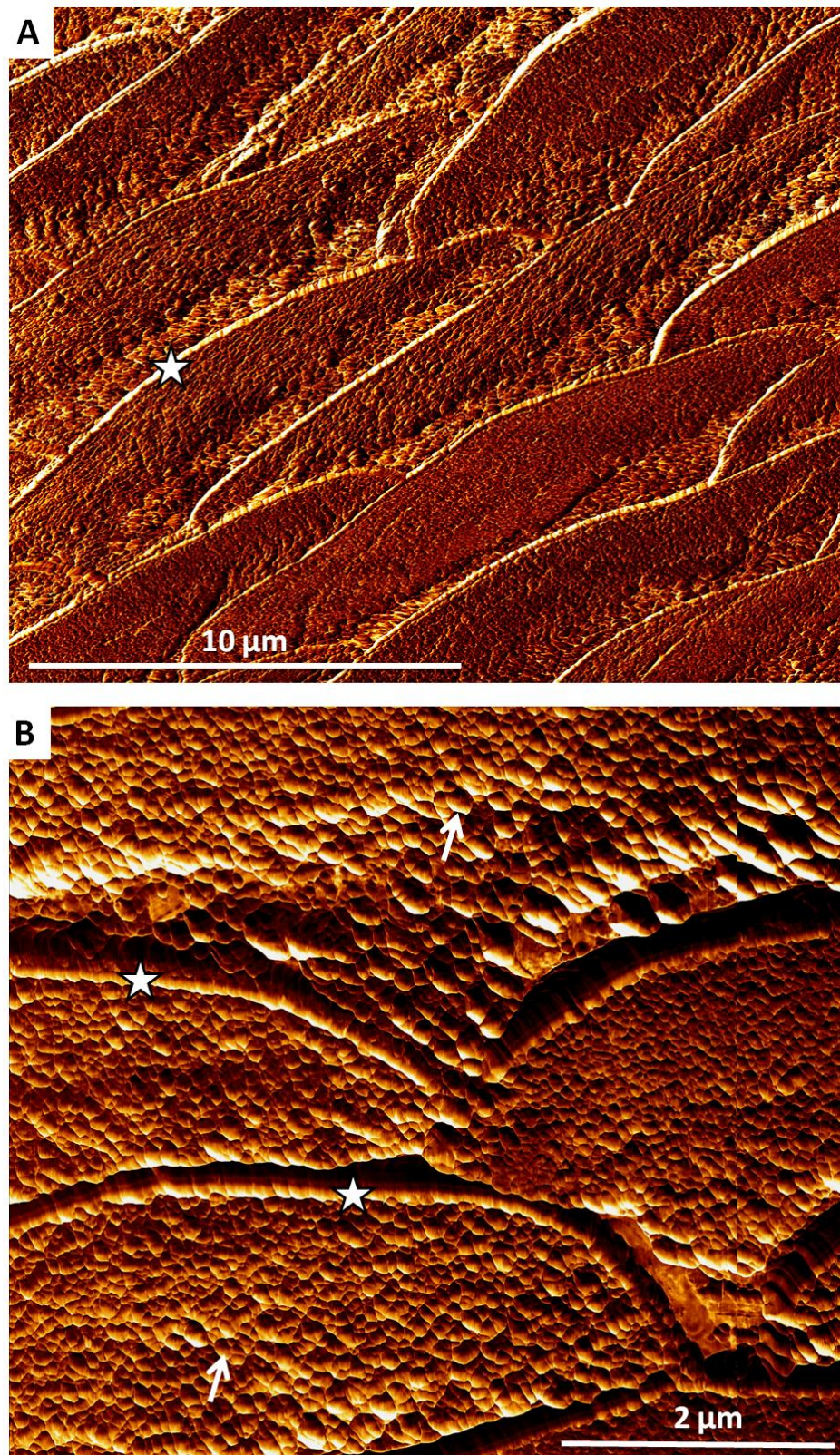
Figure 2.43: Lateral deflection AFM images of fibre morphologies within stacks of fibres in the shell of the modern brachiopod *T. transversa*. The calcite of the fibres is encased by biopolymer sheaths (white stars in A, B). Nanocomposite mesocrystal biocarbonates (NBM) constitutes the calcite of the fibres (white arrows in B).
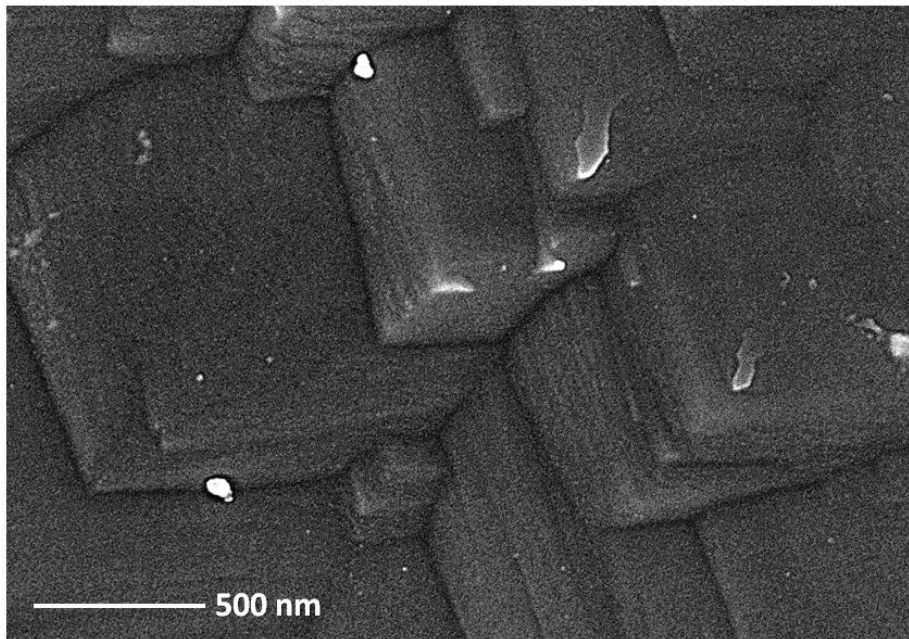
Figure 2.44: FE-SEM image of microtome cut, polished, etched and critical point dried surface of inorganic calcite grown from solution (IRC).
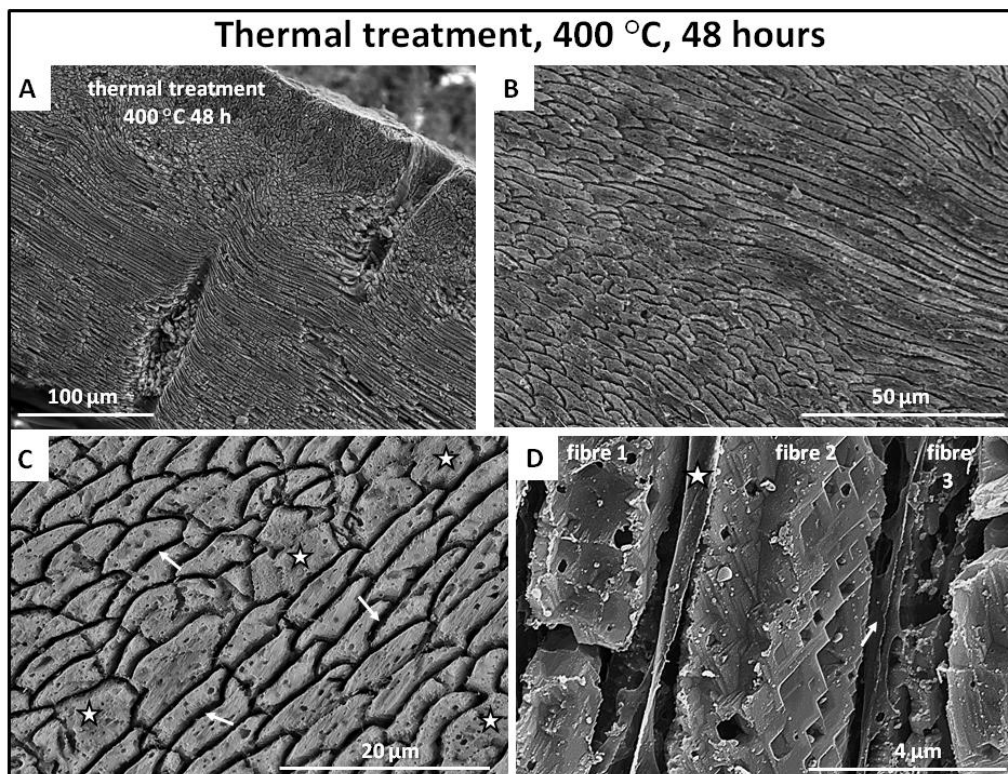
Figure 2.45: FE-SEM images with increasing magnification of thermally altered *L. uva* shells. The samples were heated at 400 °C for 48 hours. The shells become brittle (A) as organic membranes either decompose completely (B, white arrows in C) or, if still present, become highly thinned by dehydration (white star in D). Large voids (white arrow in D) developed between the fibres. Neighbouring fibres are often amalgamated (white stars in C).
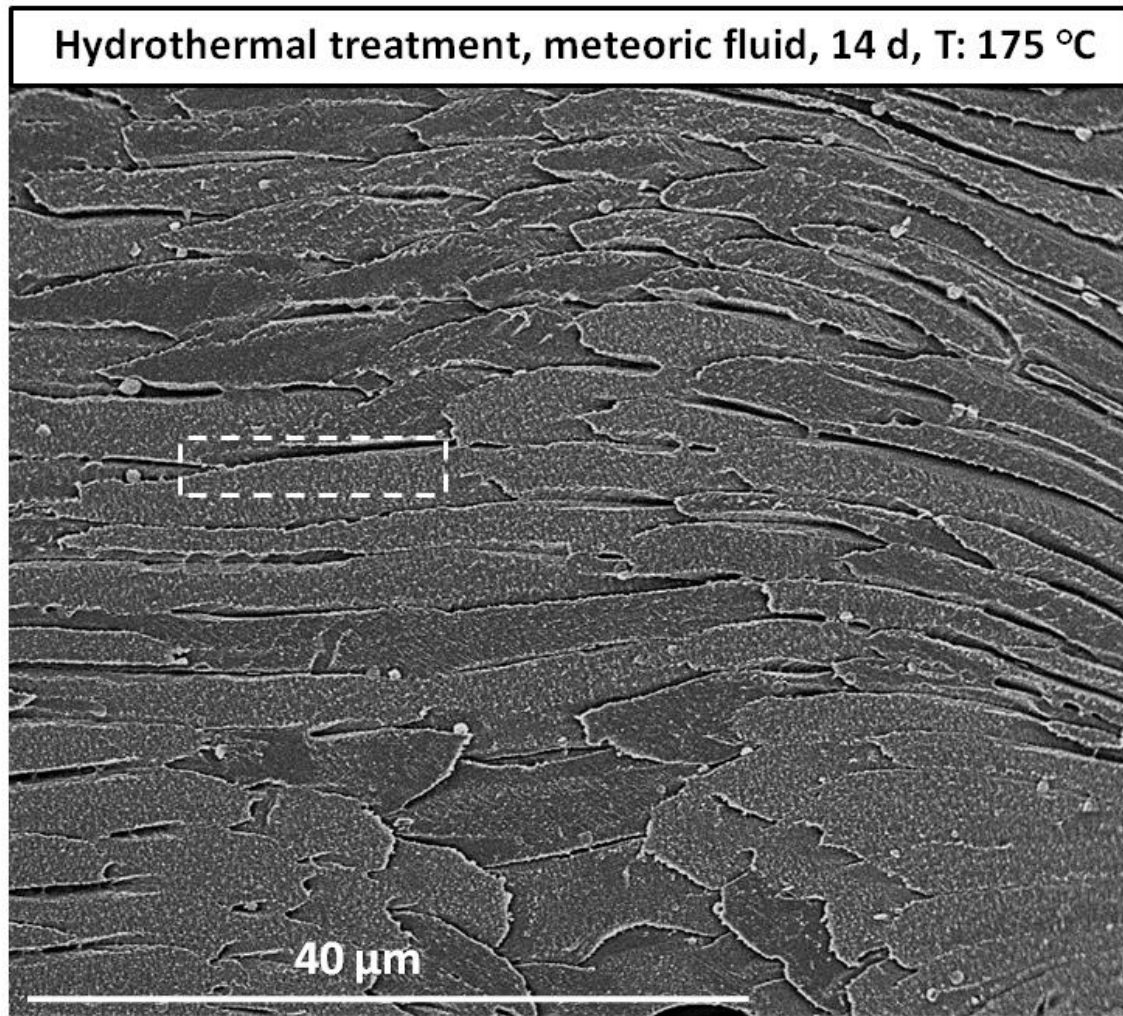
Figure 2.46: FE-SEM image showing an overview of a shell part of hydrothermally altered *T. transversa*. Alteration was carried out for 14 days at 175 °C in artificial meteoric fluid. All occluded organic polymers are decomposed and gaps developed between the fibres. The white dashed rectangle indicates the shell part where SEM image in Fig. 2.35 was taken.
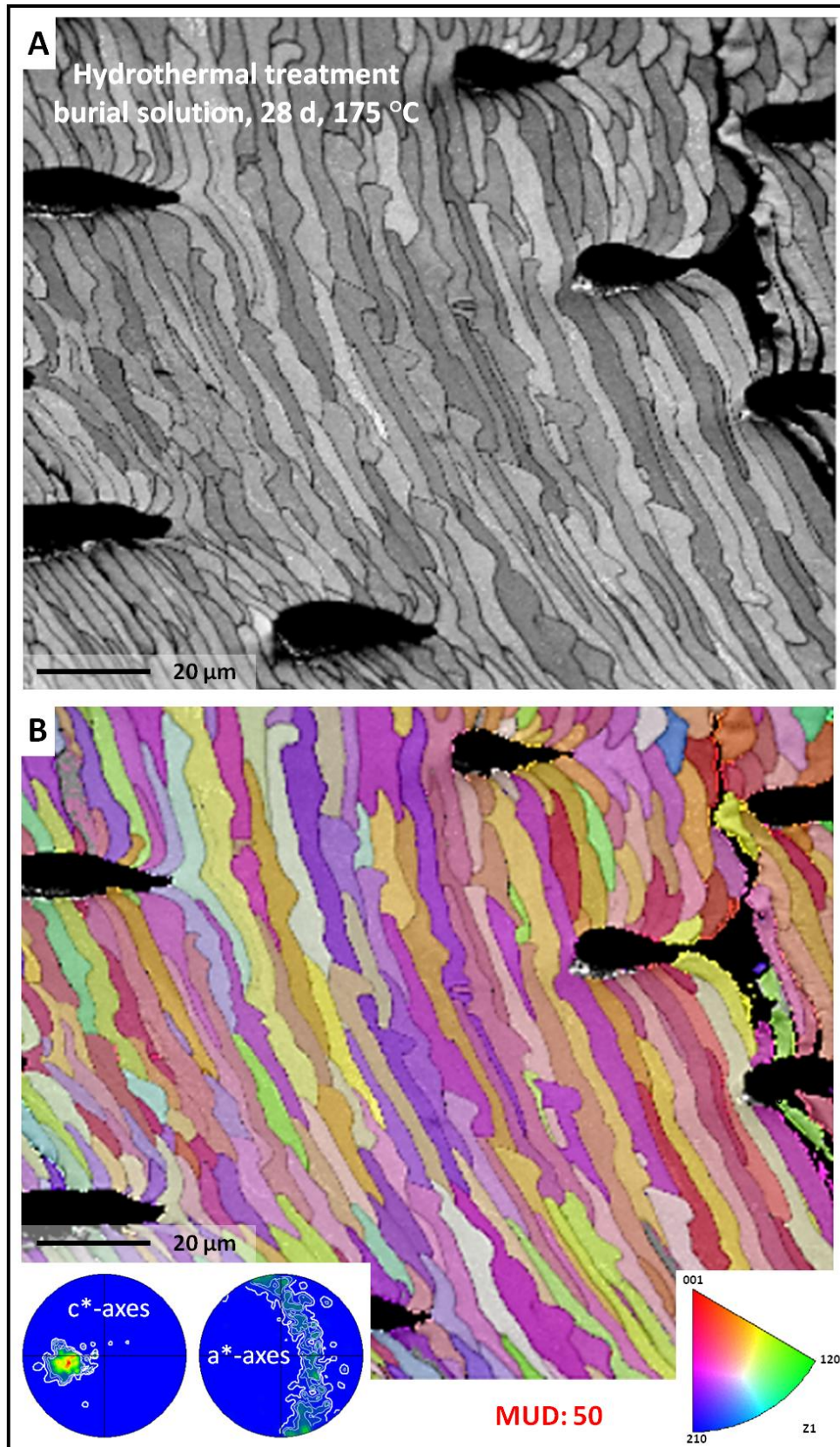
Figure 2.47: Enlargement of EBSD band contrast (A) and orientation (B) measurement images shown in Figs. 2.38B and 2.39B, respectively. Alteration of *T. transversa* occurred at 175 °C for 28 days and was carried out in simulated burial fluid. Note the high distortion of the altered fibres by new calcite formation and fibre amalgamation.
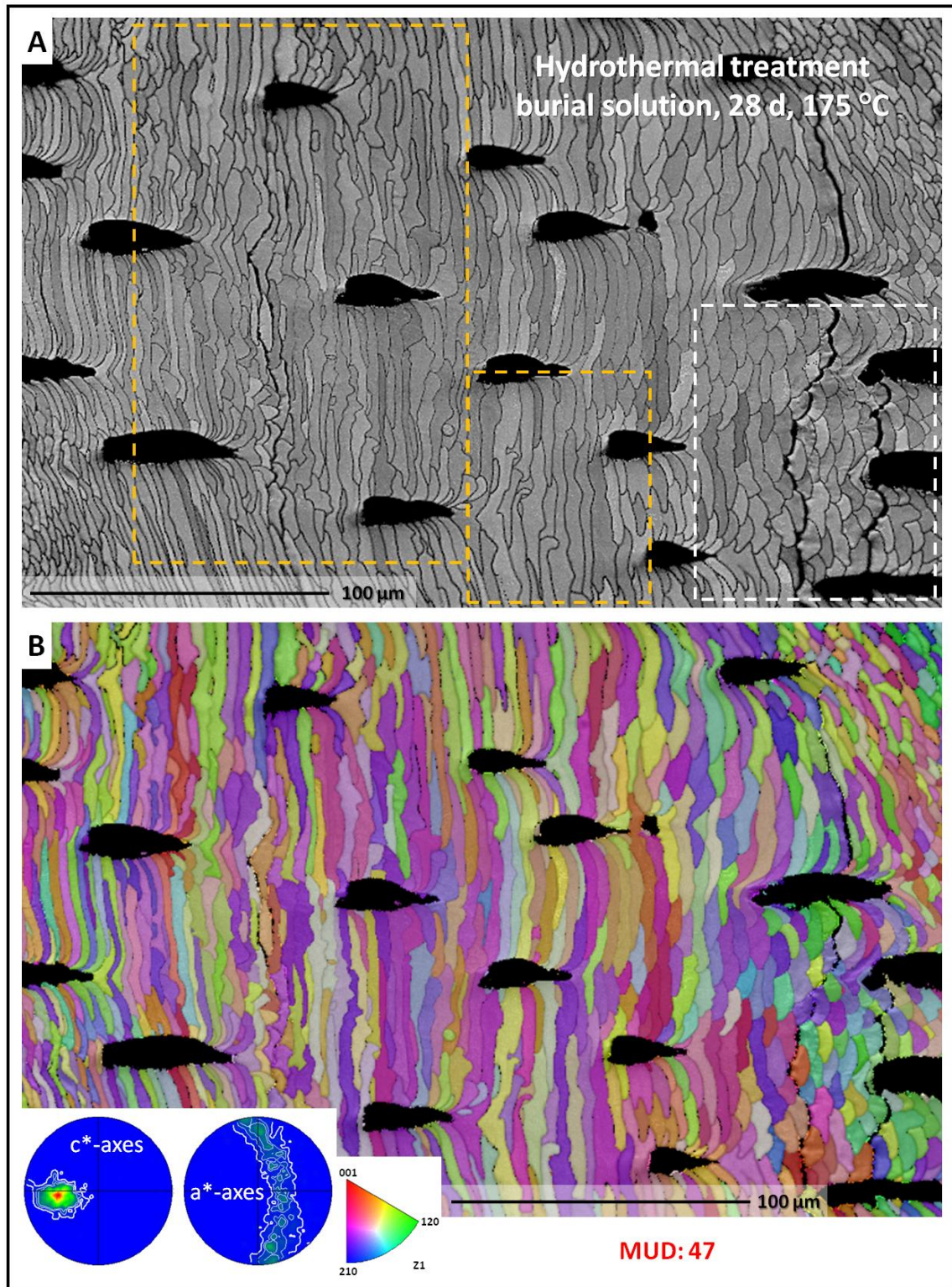
Figure 2.48: Enlargement of EBSD band contrast (A) and orientation (B) measurement images shown in Figs. 2.38B and 2.39B, respectively. Alteration of *T. transversa* occurred at 175 °C for 28 days and was carried out in simulated burial fluid. Note the high distortion of the altered fibres by new calcite formation and fibre amalgamation (slight fibre amalgamation: white dashed rectangle in A, severe fibre amalgamation: yellow dashed rectangles in A).
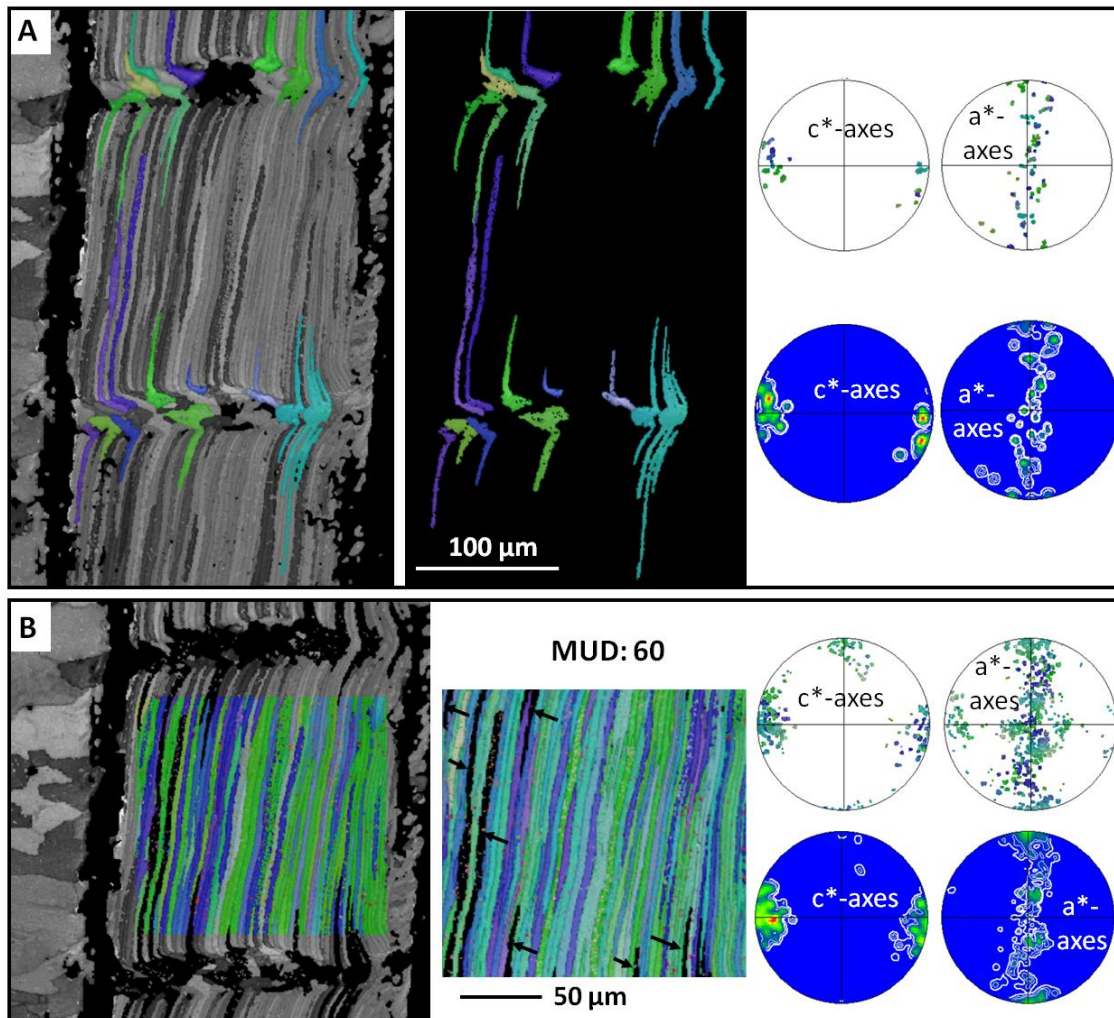
Figure 2.49: Subsets of EBSD measurements made on the shell of the fossil brachiopod *D. digona*. Calcite crystal orientation is colour-coded. The subset in (A) highlights the distribution of secondary calcite which extends from the endopunctae into adjacent shell parts. (B) Shell section between two endopunctae with most of the secondary calcite taken out of the measurement (see black arrows in B which point to fibres coloured in black). Note the rise in MUD when the orientation data of the secondary calcite are taken out of the evaluation.
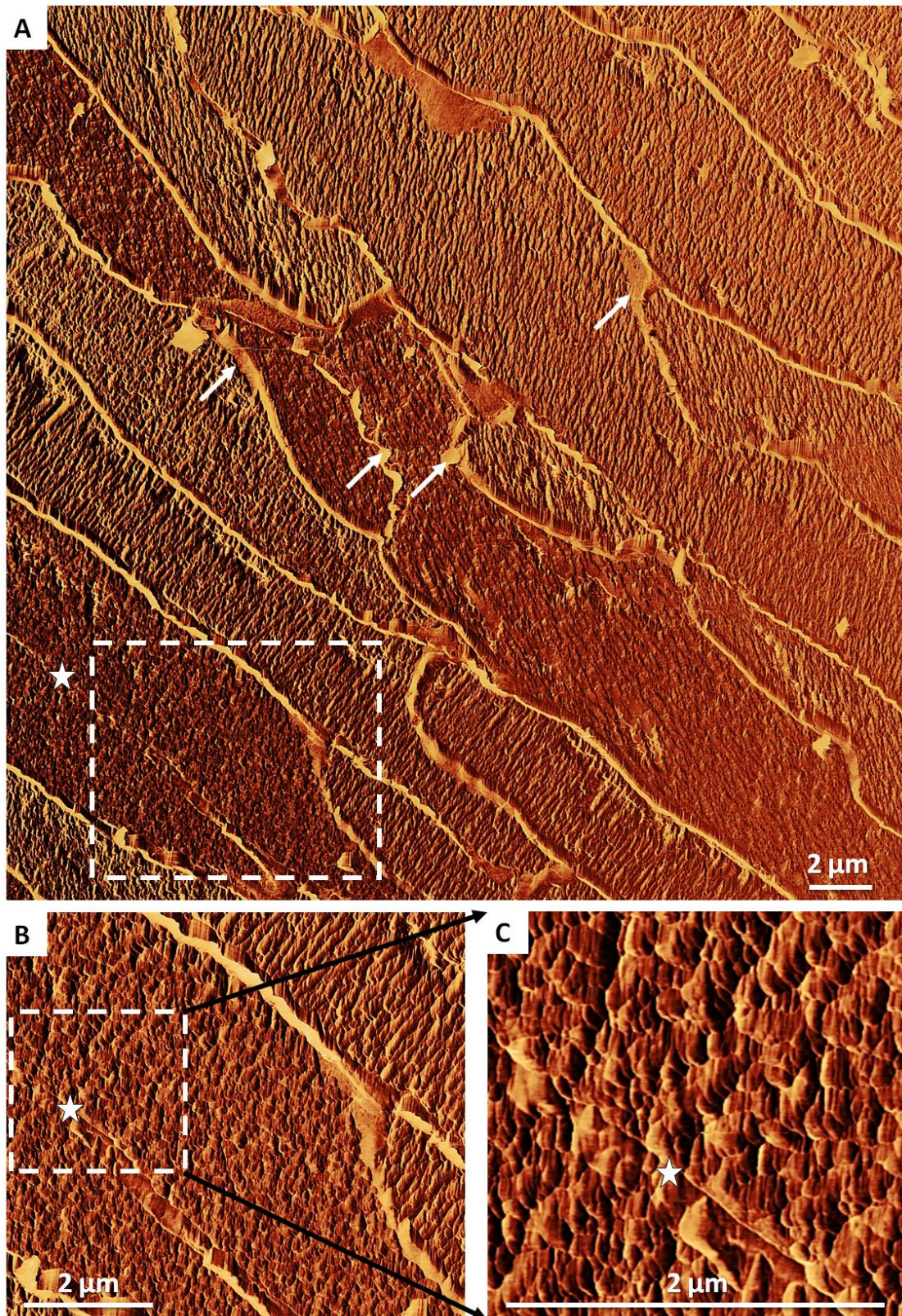
Figure 2.50: Lateral deflection AFM images of a hydrothermally altered *T. transversa* shell part. Alteration was carried out in artificial meteoric fluid at 175 °C for 28 days. The destruction of organic membrane between the fibres (see white arrows in A), the complete wearing of membrane (white star in A), and the amalgamation of fibres (white stars in B and C) can be observed. The white rectangle in (A) indicates the shell part which is shown in (B). The white dashed rectangle in (B) marks the shell region that is depicted.

2.3 Archival biogenic micro- and nanostructure data analysis: signatures of diagenetic systems

Laura A. Casella[1], María del Mar Simonet Roda[1], Lucia Angiolini[2],
Andreas Ziegler[3], Wolfgang W. Schmahl[1], Uwe Brand[4], and Erika Griesshaber[1]

[1] Department of Earth and Environmental Sciences, Ludwig-Maximilians-Universität München, 80333 Munich, Germany

[2] Dipartimento di Scienze della Terra "A. Desio", Università degli Studi di Milano, 20133 Milan, Italy

[3] Central Facility for Electron Microscopy, University of Ulm, 89069 Ulm, Germany

[4] Department of Earth Sciences, Brock University, St. Catharines, Ontario, L2S 3S1, Canada

2.3.1 Abstract

The present data in brief article provides additional data and information to our research article "Micro- and nanostructures reflect the degree of diagenetic alteration in modern and fossil brachiopod shell calcite: a multi-analytical screening approach (CL, FE-SEM, AFM, EBSD; Casella et al., 2018a). We present fibre morphology, nano- and microstructure, as well as calcite crystal orientations and textures found in pristine, experimentally altered (hydrothermal and thermal), and diagenetically overprinted brachiopod shells. Combination of the screening tools AFM, FE-SEM and EBSD allows to observe a significant change in microstructural and textural features with an increasing degree of laboratory-based and naturally occurring diagenetic alteration. Amalgamation of neighbouring fibres was observed on the micrometre scale level, whereas progressive decomposition of biopolymers in the shells and fusion of nanoparticulate calcite crystals was detected on the nanometre scale. The presented data in this article and the study described in Casella et al. (2018a) allows for qualitative information on the degree of diagenetic alteration of fossil archives used for palaeoclimate reconstruction.

2.3.2 Specifications table

Subject area	Crystallography
More specific subject area	Micro- and nanostructure of modern and fossil biogenic carbonate archives
Type of data	Figures, text file
How data was acquired	Microtome: Leica Ultracut equipped with glass knives and DiATOME diamond knife
	Critical Point Drying: BAL-TEC CPD 030
	FE-SEM: Hitachi S5200 field emission SEM
	EBSD: Hitachi SU5000 field emission SEM equipped with a Nordlys II EBSD detector and AZTec acquisition software
	AFM: JPK Instruments NanoWizard II equipped with an n^+-silicon cantilever, measurements were conducted in contact mode
Data format	Analysed
Experimental factors	Thermal and hydrothermal alteration experiments
Experimental features	Thermal alteration experiments on modern brachiopod specimens were performed under dry conditions at 100 °C (for 72 hours, and three months), and at 400 °C (for 48 hours).
	Hydrothermal alteration experiments on modern brachiopod specimens were conducted in either simulated meteoric or burial fluids at 175 °C for 28 days.

	Pristine, thermally and hydrothermally altered, and fossil brachiopod shell fragments were embedded in epoxy resin and successively ground and polished for further investigations (see Casella et al., 2017, 2018a)
Data source location	Friday Harbor Laboratories, University of Washington, U.S.A. (*Terebratalia transversa*), Signy and Rothera Islands, Antarctica (*Liothyrella uva*), Upper Ordovician Dillsboro Formation, Indiana, U.S.A. (*Platystrophia laticostata*), Lower Jurassic Ait Athmane Formation of the Central High Atlas Basin, Morocco (*Quadratirhynchia attenuata*), Luc-Sur-Mer, Normandy, France (*Digonella digona*) and, Bakony Mountains, Hungary (*Lobothyris punctata*).
Data accessibility	Data is with this article

2.3.3 Value of the data

The data provides fundamental, quantitative and qualitative information on the assessment of the degree of (diagenetic) alteration of brachiopod shells.

Hydrothermal alteration experiments mimicking diagenetic alteration may be applied to other biogenic hard tissues and inorganic mineral assemblages (e.g., rocks) in order to objectively compare the degree of diagenetic overprint.

Data analysed by multi-analytical screening methods (FE-SEM, EBSD, AFM) may provide crucial information on the history of fossils used in research fields such as reconstruction of the palaeoclimates and palaeoenvironments.

A comparison between microstructural and texture analyses of our data with isotope analysis may provide more detailed understanding of diagenetic overprint of fossil samples.

2.3.4 Data

Among marine biocarbonates, calcitic brachiopod shells are one of the most used archives in palaeoclimate and palaeoecological research (Lowenstam, 1961; Veizer et al., 1986; Brand, 1989b; Bates and Brand, 1991; Angiolini et al., 2009, Garbelli et al., 2012). In the past few decades, basic knowledge on microstructural and textural patterns of pristine brachiopod shells was established (Barbin et al., 1991; Schmahl et al., 2004, 2012; Griesshaber et al., 2007a, 2007b, 2007c, 2010; Cusack et al., 2008a, 2008b; Goetz et al., 2009, 2011; Cusack, 2015). Here, we focus on additional insights on microstructural and

nanostructural characteristics caused by (mimicked) diagenetic alteration by using biochemical etching (Figs. 2.51 and 2.52), SEM (Figs. 2.51 to 2.55), EBSD orientation and texture data evaluation (Figs. 2.56 to 2.60), and AFM imaging (Figs. 2.61 to 2.63) of pristine, thermally, hydrothermally and diagenetically altered brachiopod shells. Based on FE-SEM imaging and EBSD measurements, high-resolution data on pristine, (hydro-) thermally altered and fossil brachiopod specimens was obtained and subsequently analysed. We compare micro- and nanostructural data of pristine and (hydro-) thermally or diagenetically altered brachiopod shells, i.e., the presence of organic matrices, and the shape of calcite fibres of the fibrous secondary shell layer. Texture analysis deduced from EBSD measurements on fossil brachiopods with varying degrees of diagenetic overprint shows the relation between the degree of crystallographic co-orientation and diagenetic history experienced by biogenic minerals. AFM imaging of hydrothermally altered and fossil brachiopod shells provides supporting and more detailed data on fibre morphologies and their internal structure.

2.3.5 Experimental design, materials and methods

Experimental designs of simulated diagenetic alteration

Thermal alteration

Thermal alteration was carried out in order to observe the decomposition of the enclosing organic membranes. Sample material used in thermal alteration experiments was heated in an oven at 100 °C for 72 h and for three months, as well as at 400 °C for 48 h.

Hydrothermal alteration

Hydrothermal alteration experiments were performed in the presence of either simulated meteoric (10 mM NaCl aqueous solution) or simulated burial (100 mM NaCl + 10 mM $MgCl_2$ aqueous solution) fluid. Both solutions were prepared using high-purity deionised water (Casella et al., 2017, 2018a; Ritter et al., 2017). Sample material and 10 mL of fluid were inserted into a polytetrafluoroethylene crucible which was placed inside a metal autoclave. Experiments were conducted at 100 °C for 28 days using either simulated meteoric or burial fluid. Pressure conditions during the hydrothermal alteration experiments corresponded to the vapour pressure of water at the given temperature.

Pristine and fossil brachiopod materials

Investigated pristine brachiopods

Modern brachiopod specimens of *Terebratalia transversa* (Sowerby, 1846) and *Liothyrella uva* (Broderip, 1833) were utilised in biochemical studies for establishing baselines of pristine brachiopod shell micro- and nanostructures, as well as in thermal and hydrothermal alteration experiments mimicking diagenetic alteration of biogenic carbonates. Sampling sites of both live collected brachiopods were Friday Harbor Laboratories, University of Washington, U.S.A., and Signy and Rothera Islands, Antarctica, for *T. transversa* and *L. uva*, respectively.

Investigated fossil brachiopods

Four fossil equivalents were chosen from basins which experienced different burial depths and diagenetic temperatures. *Platystrophia laticostata* (James, 1871) was collected from the Upper Ordovician Dillsboro Formation, Indiana, U.S.A. The Jurassic brachiopods *Lobothyris punctata* (Sowerby, 1812) and *Quadratirhynchia attenuata* (Dubar, 1931) were collected at the Bakony Mountains, Hungary, and Ait Athmane Formation of the Central Atlas Basin, Morocco, respectively. *Digonella digona* (Sowerby, 1815) is the youngest of all Jurassic brachiopod samples and its sampling site was located at Luc-Sur-Mer, Normandy, France. Further information on all utilised brachiopod specimens is given in Casella et al. (2018a).

Microtome cutting and polishing

Brachiopod shell fragments of pristine and fossil brachiopod species were mounted on 3 mm thick cylindrical aluminium rods using super glue. In order to obtain plane surfaces, the samples were microtome cut using a Leica Ultracut ultramicrotome equipped with glass knives. Subsequently, the cut specimens were polished by stepwise removal of material in a series of slices with successively decreasing thicknesses (90 nm, 70 nm, 40 nm, 20 nm, 10 nm, and 5 nm) using a DiATOME diamond knife. Each step was repeated 15 times (Fabritius et al., 2005).

Selective biochemical etching

Microtome-polished shell surfaces were etched and the organic matter fixed, simultaneously, while immersed in a solution of 0.1 M HEPES (4-(2-hydroxyethyl)-1-piperazineethanesulfonic acid) at pH 6.5 and 2.5 % glutaraldehyde for 180 seconds. The

etching procedure was stopped by a dehydration step in 100 % isopropyl 3 times for 10 minutes each. Subsequently, specimens were critical point dried using a BAL-TEC CPD 030 (Liechtenstein) device and rotary coated with 3 nm of platinum.
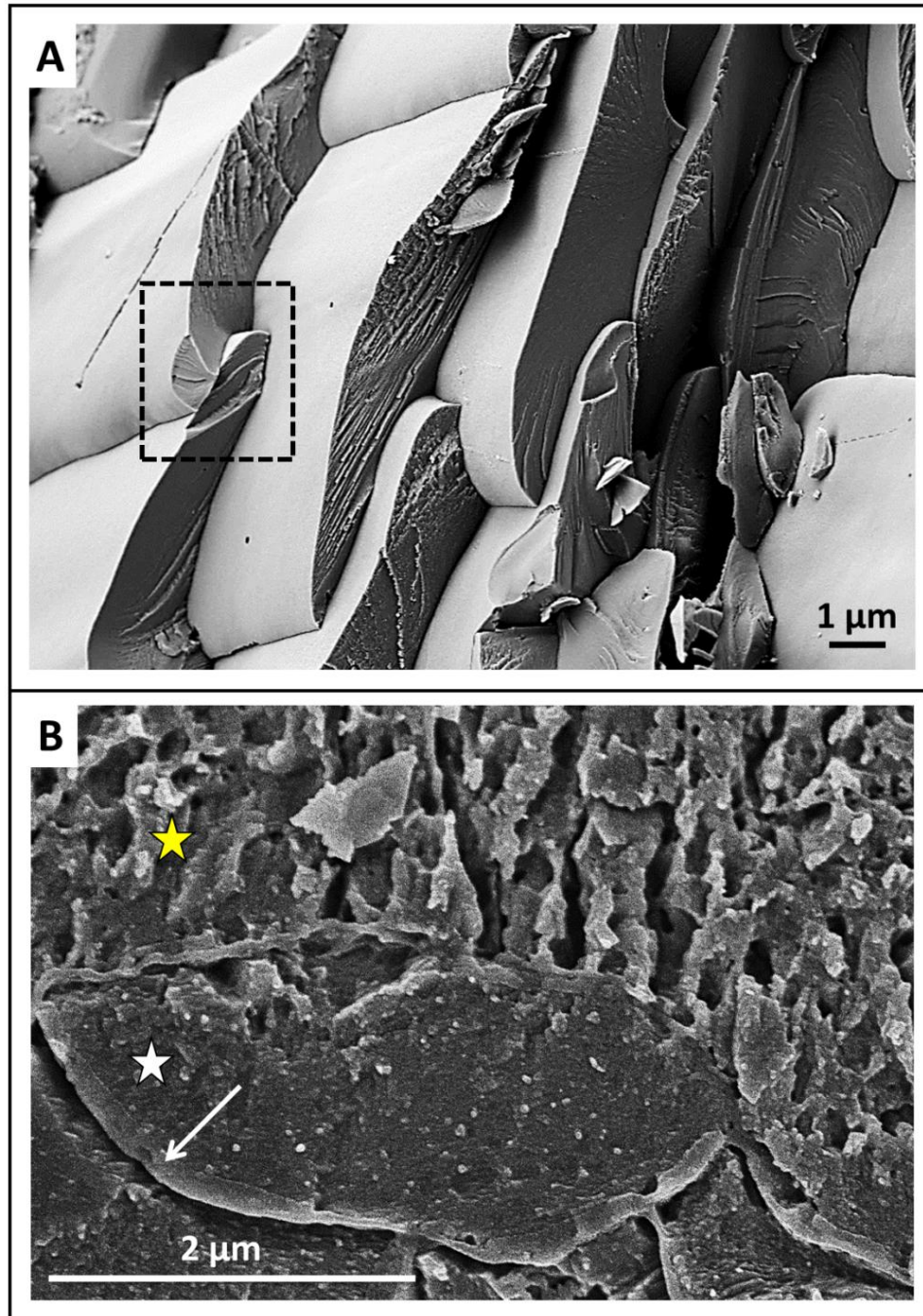
Figure 2.51: FE-SEM images of pristine *T. transversa* showing different fibre characteristics. (A) Fibres of the fibrous secondary layer exhibit uneven surfaces after mechanical fracturing (black dashed rectangle). (B) Irregularly shaped small mineral units as well as organic matrices can be observed in the primary layer (yellow star) of the *T. transversa* shell. Each single fibre of the fibrous secondary layer is surrounded by a biopolymer matrix (white arrow), and is comprised of nanoscopic biocomposite mesocrystals (white star).
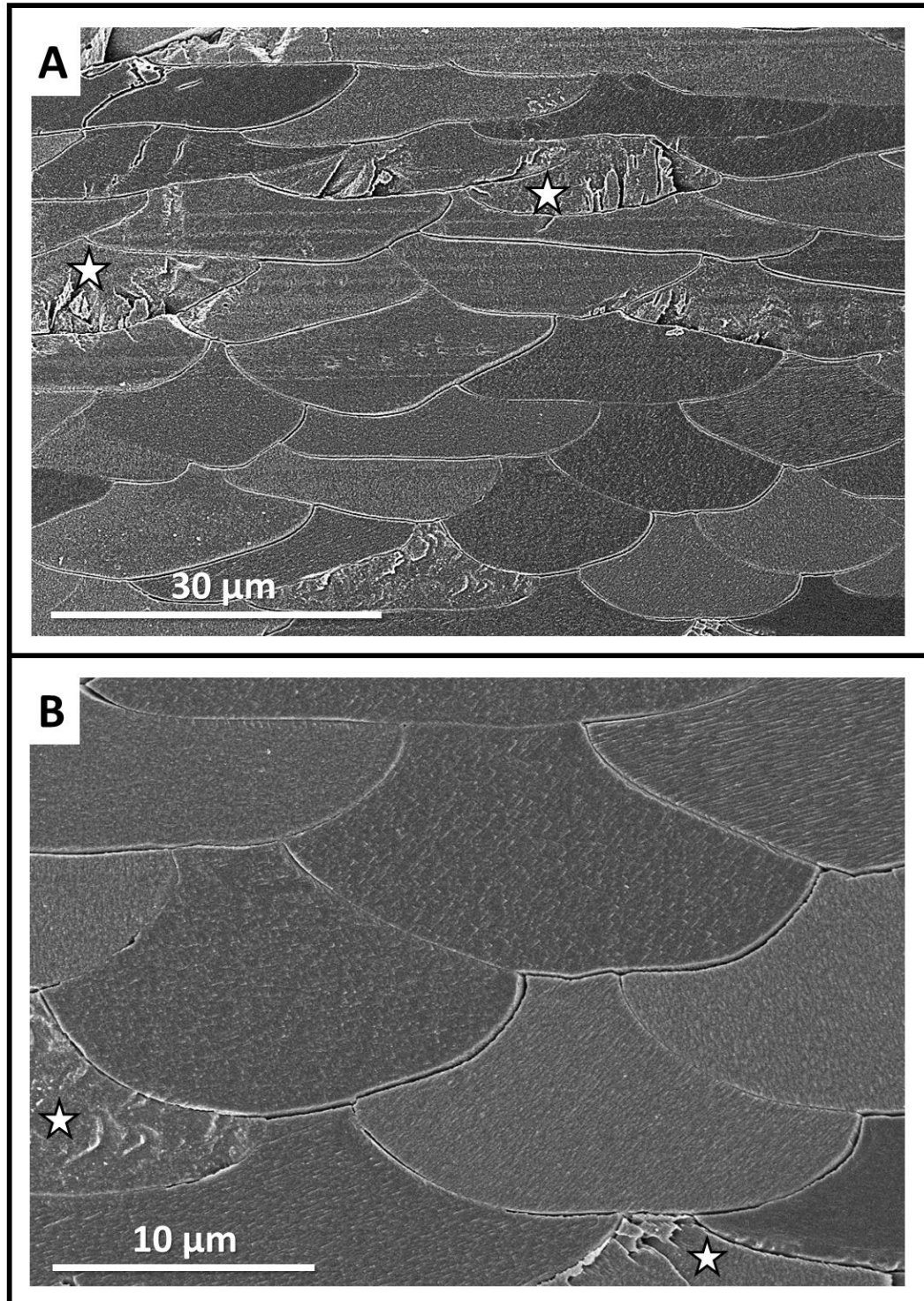
Figure 2.52: FE-SEM images of microtome cut, polished, etched and critical point dried surfaces of the fossil brachiopod *Q. attenuata*. As the fossil shell is devoid of organics (membranes around the fibres, network of fibrils within the fibres), it becomes brittle and fractures when cut with a microtome knife (white stars in A and B).

FE-SEM imaging

For FE-SEM imaging, selected sample material was prepared by microtome cutting and polishing following a selective biochemical etching treatment. However, the major preparation technique for SEM imaging and EBSD measurements of brachiopod samples was carried out as follows. Brachiopod shells were longitudinally cut from the umbo to the commissure, and subsequently, embedded in epoxy resin. Shell surfaces were conventionally ground and polished in sequential steps down to a grain size of 1 µm (particle size of polishing agent). The preparation was finalised by an etch-polishing step utilising colloidal alumina with particle sizes of approx. 0.05 µm in a vibratory polisher. Subsequently, sample surfaces were rotary coated with 4-6 nm of carbon.

FE-SEM imaging was carried out at 4, 5, or 10 kV using a Hitachi S5200 electron microscope.

EBSD measurements, band contrast and analysis of calcite orientation data

For EBSD measurements, brachiopod shells were conventionally ground and polished as described above. Sample surfaces were rotary coated with 4-6 nm of carbon. EBSD measurements were conducted at 20 kV using a Hitachi SU5000 FE-SEM equipped with a Nordlys II EBSD detector and AZTec acquisition. Obtained EBSD data was evaluated using CHANNEL 5 HKL evaluation software (Schmidt and Olesen, 1989; Randle and Engler, 2000).

Data on crystal orientation is shown as band contrast measurements and colour-coded crystal orientation maps with corresponding pole figures. EBSD band contrast represents the quality of the Kikuchi diffraction pattern in each measured point, thus, strong EBSD signals result in a bright image point and weak or absent signals (e.g., due to pores, organic matter, amorphous phases) result in dark image points. Crystallographic orientation maps were derived from EBSD scans. A measure of co-orientation within single crystals or assembly of crystals are given by the multiple of uniform distribution (MUD) value. High MUD values indicate highly co-oriented crystallographic axes (e.g., MUD of >700 in inorganic single crystals; Nindiyasari et al., 2015) and, thus, a strong texture. Low MUD values of down to 1.0 reflect randomly oriented crystallographic axes, thus, a weak or no texture.
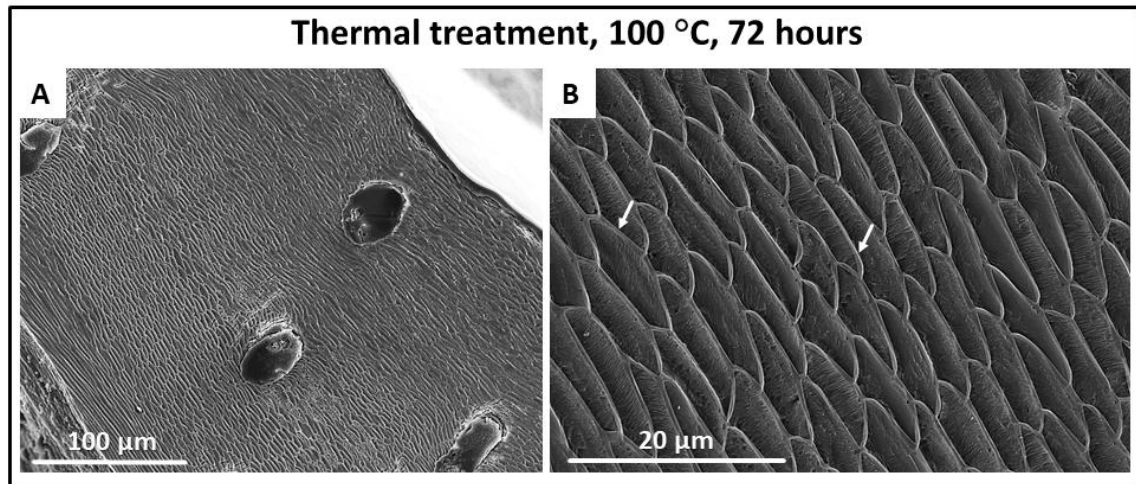
Figure 2.53: FE-SEM images of *L. uva* thermally altered under dry conditions at 100 °C for 72 hours. The morphology and arrays of fibres are well kept (A), and each fibre is surrounded by an organic membrane (white arrows in B).
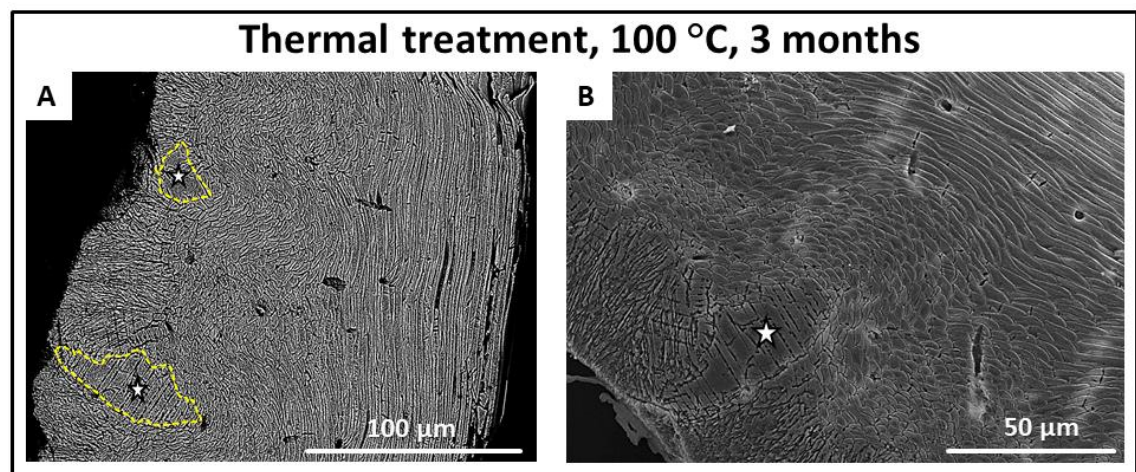
Figure 2.54: FE-SEM images of *L. uva* shells thermally altered under dry conditions at 100 °C for three months. New, large, irregularly shaped calcite units developed (white stars in A and B, yellow dashed outlines in A) as the original basic mineral units of the skeleton amalgamate.
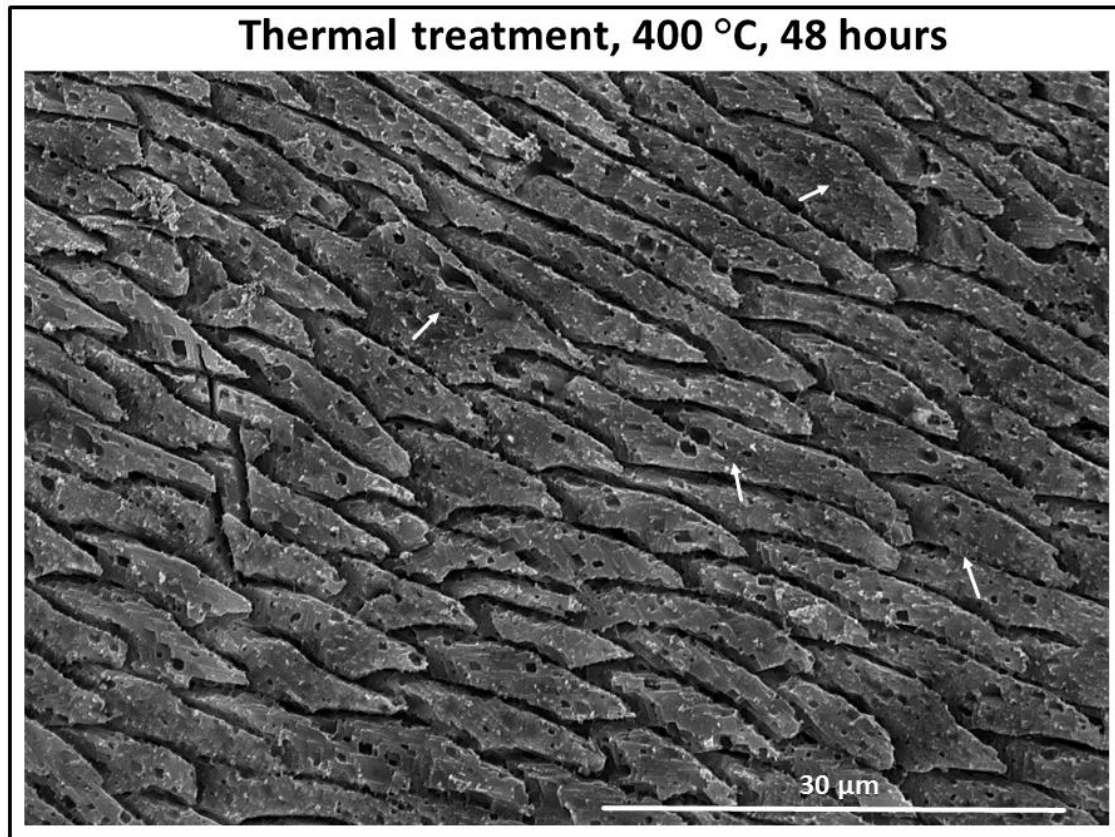
Figure 2.55: FE-SEM image of a *L. uva* shell thermally treated at 400 °C for 48 hours. Organic membranes are entirely decomposed; new calcite formation starts to occur as neighbouring fibres amalgamate (white arrows).
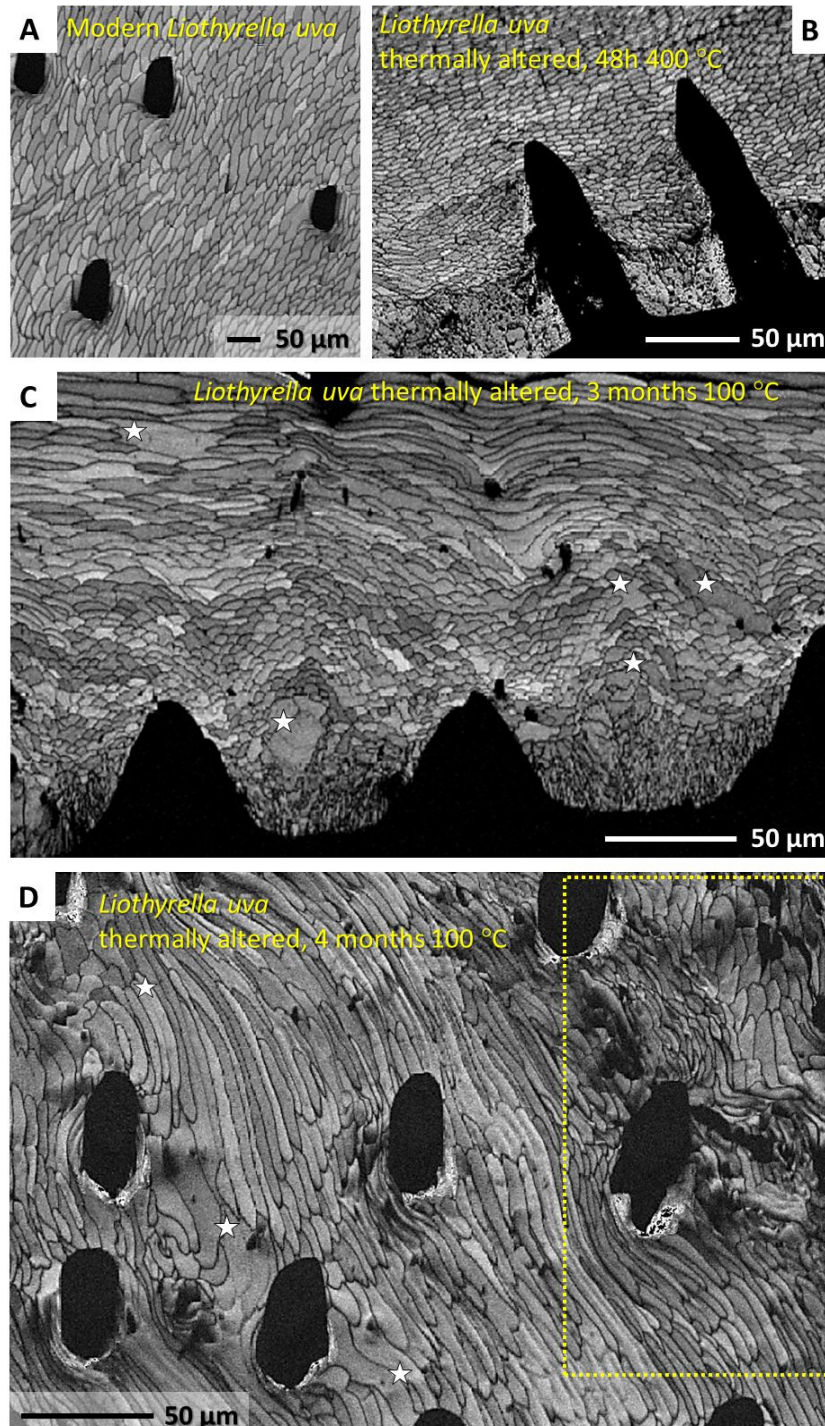
Figure 2.56: EBSD band contrast measurement images of pristine and thermally altered *L. uva* shells showing the change and distortion of microstructure of the fibrous layer with progressive alteration times and temperatures. Relative to pristine *L. uva* (A), a slight distortion of the microstructure can be observed in shell samples altered at 400 °C for 48 hours (B). New mineral formation and fibre amalgamation was observed at thermal alteration conditions of three months at 100 °C (white stars in C). Alteration for four months at 100 °C caused significant fibre amalgamation (white stars in D), microstructure destruction (yellow dashed rectangle in D) and new calcite formation.

127
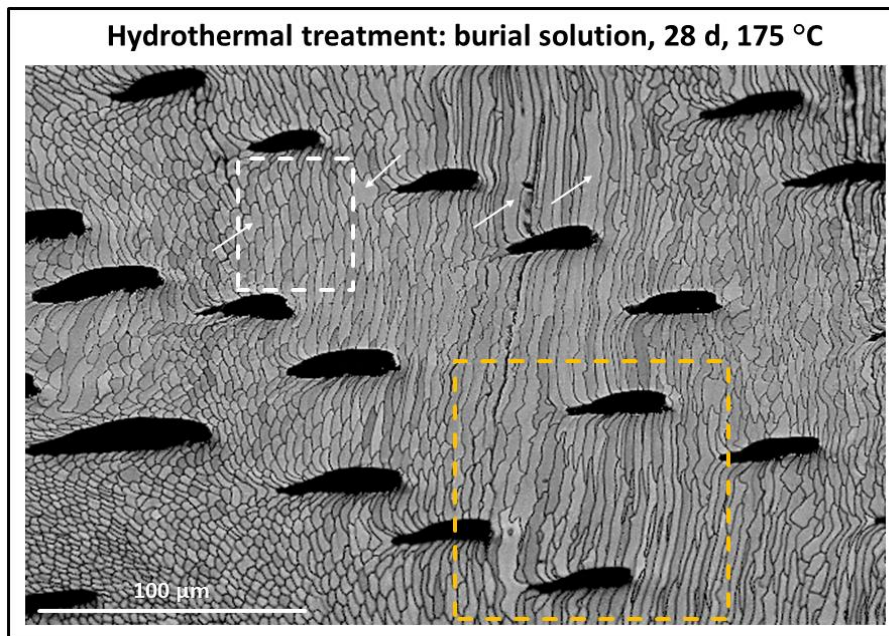
Figure 2.57: EBSD band contrast measurement images of hydrothermally altered *T. transversa* shell. Alteration occurred at 175 °C for 28 days and was carried out in simulated burial fluid. Shell areas where the original fibre morphology was distorted by alteration (yellow rectangle) can be observed close to regions where the shell microstructure was little affected (white rectangle). Note that amalgamation of fibres occurred occasionally (white arrows).
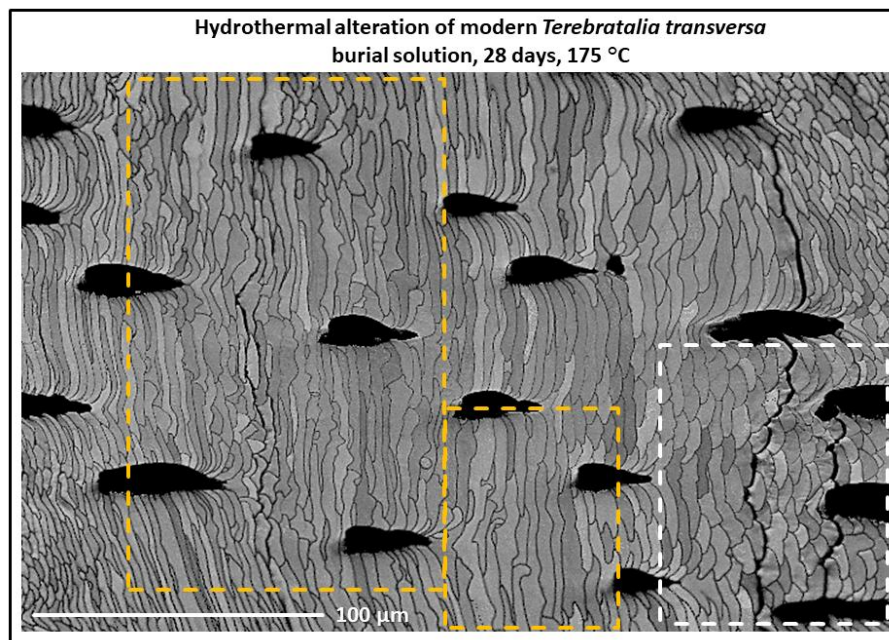
Figure 2.58: EBSD band contrast measurement image of hydrothermally altered *T. transversa* shell. Alteration occurred at 175 °C for 28 days and was carried out in simulated burial fluid. In some parts of the shell the original fibrous shell microstructure was distorted by the amalgamation of fibres due to alteration (yellow dashed rectangles). The amalgamation of fibres can be explained by lateral growth of the inorganic rhombohedral calcite (IRC) of one nanocomposite mesocrystal biocarbonate (NMB) fibre growing into the neighbouring fibre. Note that altered shell areas are next to shell areas which appear to be little affected by alteration (white dashed rectangle).
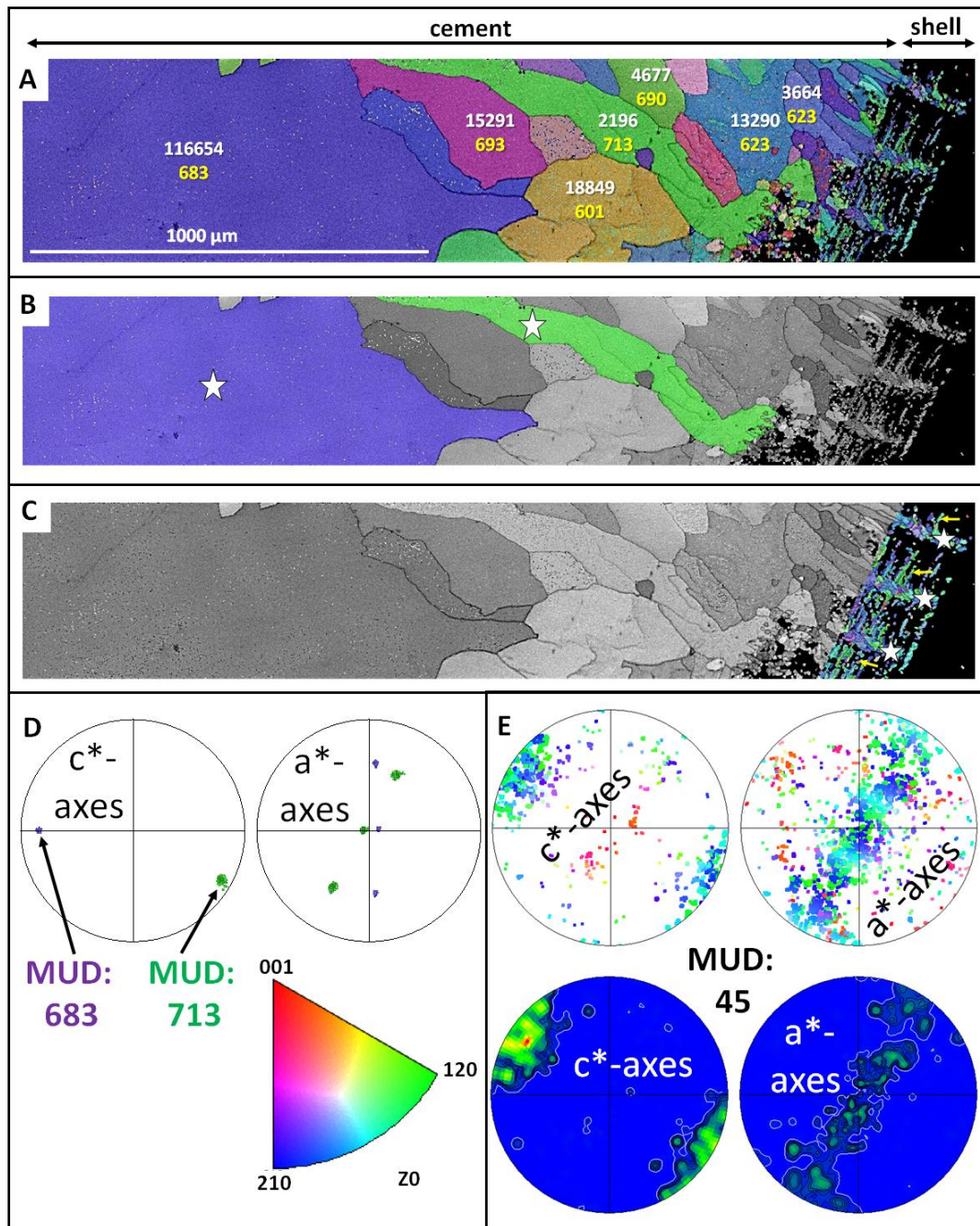
Figure 2.59: EBSD band contrast measurements and colour-coded orientation maps with corresponding pole figures of fossil brachiopod *D. digona* (A, C, E) and cement found between the pedicle and brachial valves (A, B, D; see Fig. 2.38 in chapter 2.2). Recrystallised calcite is present in the shell (white stars in C) and as precipitate within endopunctae (yellow arrows in C) of fossil *D. digona*, and within the cement (white stars in B). (A) Yellow numbers show MUD values of individual calcite grains found within the cement. The number of corresponding data points used for the calculation of each MUD value is given in white. (D) MUD values of two selected recrystallised calcite grains of the cement (coloured, white stars in B) are similar to each other (683 and 713) and show characteristics of a single crystalline phase due to the superposition of crystallographic axes on the pole figures. (E) In contrast, the crystallographic axes of newly formed calcite found within the shell of *D. digona* show high misorientation on the pole figures, and thus, a significantly lower MUD value of 45 is obtained.

129
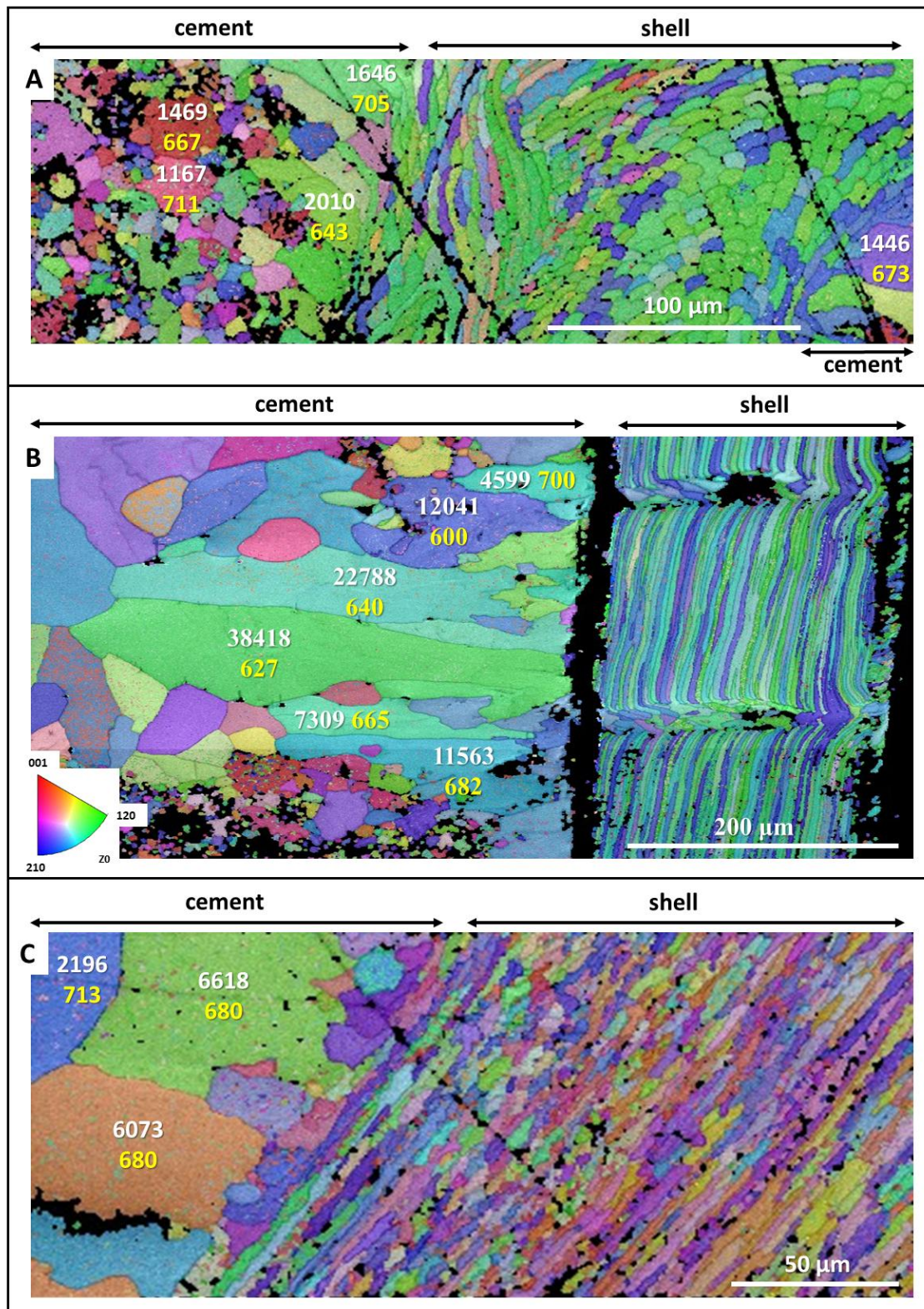
Figure 2.60: EBSD colour-coded orientation maps showing recrystallised calcite inside the shells of the fossil brachiopods *L. punctata* (A), *D. digona* (B) and *P. laticostata* (C). MUD values are given in yellow, the number of calcite data points within a large calcite crystal is shown in white.

AFM imaging

For AFM imaging, brachiopod specimens were prepared by two different preparation techniques, i.e., microtome cutting using glass knives and polishing using a diamond knife, as well as by conventional grinding and polishing as is described above. The latter includes an additional step, i.e., cleaning of the highly polished sample surface for 10 minutes using high-purity deionised water in an ultrasonic bath, rinsing with ethanol and subsequent air drying. Rotary coating was not applied for AFM imaging.

Atomic force microscopy was conducted on hydrothermally altered and fossil brachiopod shells. Images were taken in contact mode.
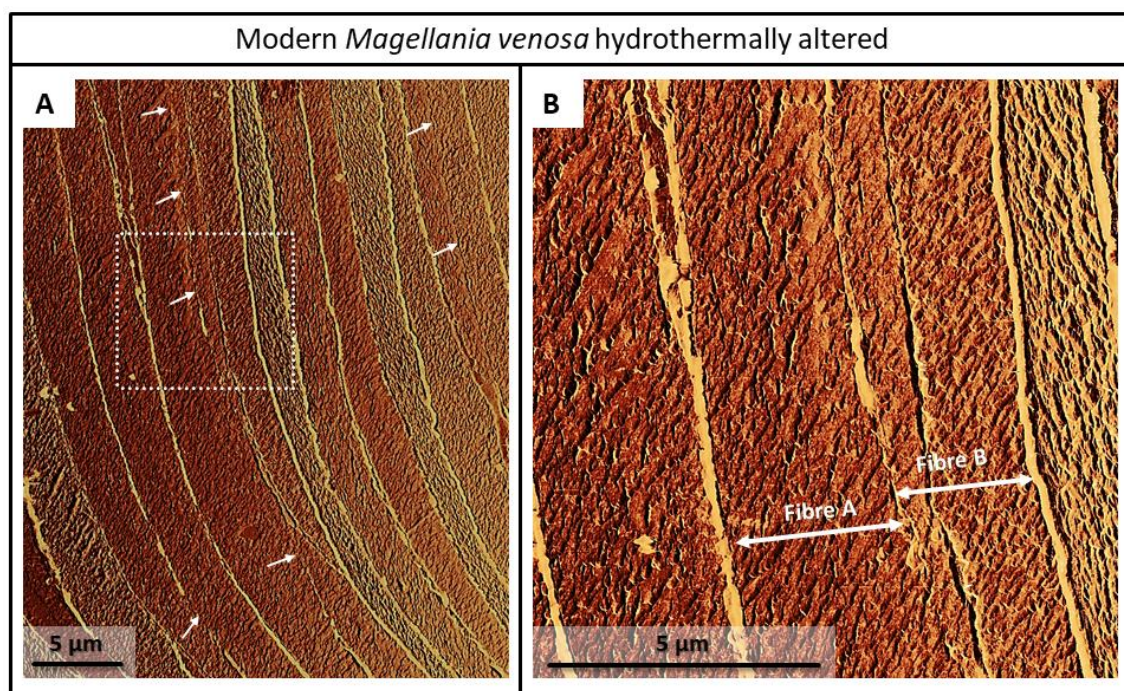
Figure 2.61: Lateral deflection AFM images of hydrothermally altered *T. transversa* shell pieces. Alteration was carried out in simulated meteoric fluid at 175 °C for 28 days. The degradation of organic membranes, the amalgamation of neighbouring fibres (white arrows in A), and new calcite formation (A, B) can be observed at the sites of former membranes located between two fibres. The dashed white rectangle in (A) indicates the location of the shell area shown in (B).
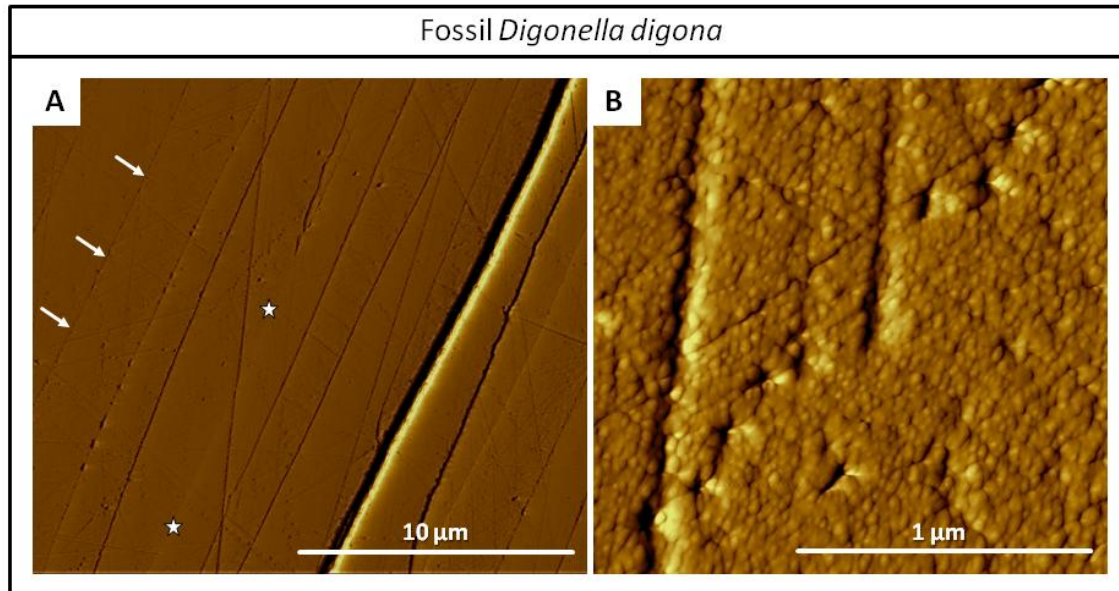
Figure 2.62: Vertical deflection AFM images of fossil *D. digona* shell pieces. Degradation of organic membranes (white arrows in A) and amalgamation of neighbouring fibres into larger units (white stars in A) can be observed in the Jurassic brachiopod specimen. (B) Formation of inorganic rhombohedral calcite (IRC) crystallites within a single calcite fibre of the fibrous secondary layer.
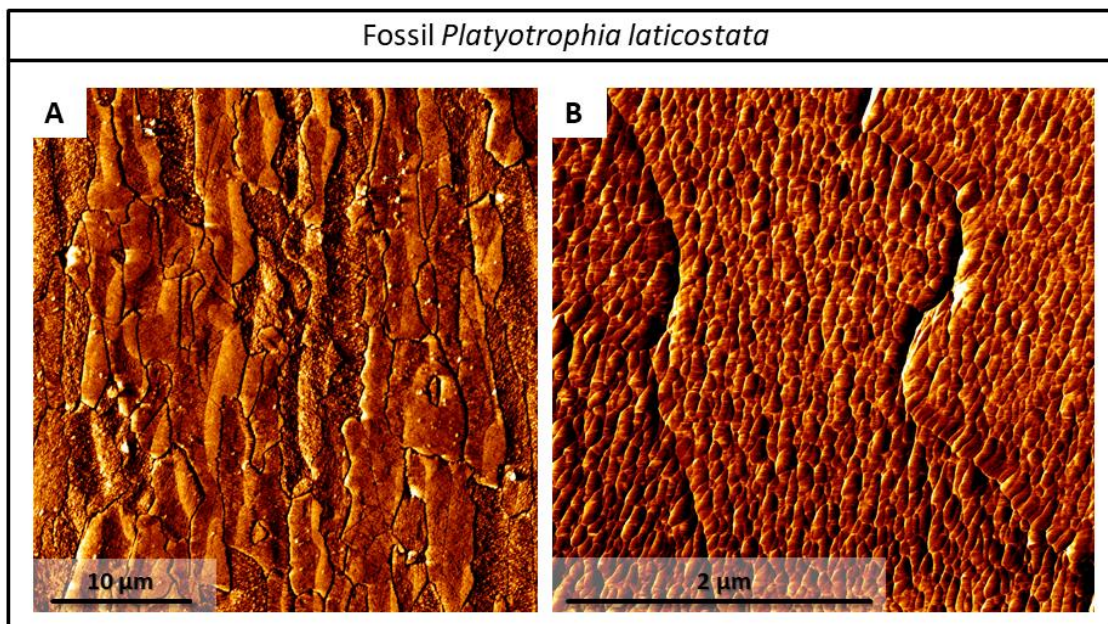
Figure 2.63: Lateral deflection AFM images of fossil *P. laticostata* shell pieces showing (A) the distortion of neighbouring calcite of the fibrous secondary layer caused by diagenetic overprint. (B) Fibres of fossil *P. laticostata* lack the enclosing organic membranes and consist of inorganic calcite crystallites.

2.3.6 Acknowledgements

2.3.7 Author contributions

LAC, EG and WWS designed the study. EG and UB provided sample material. LAC performed the experiments. LAC and MSR conducted the analyses and data evaluation. LAC merged the data. LAC drafted the manuscript. All authors contributed to discussions and the final manuscript.

2.4 Hydrothermal alteration of aragonitic biocarbonates: assessment of micro- and nanostructural dissolution-reprecipitation and constraints of diagenetic overprint from quantitative statistical grain-area analysis

Laura A. Casella[1], Sixin He[1], Erika Griesshaber[1], Lourdes Fernández-Díaz[2], Martina Greiner[1], Elizabeth M. Harper[3], Daniel Jackson[4], Andreas Ziegler[5], Vasileios Mavromatis[6], Martin Dietzel[6], Anton Eisenhauer[7], Sabino Veintemillas-Verdaguer[8], Uwe Brand[9], and Wolfgang W. Schmahl[1]

[1] Department of Earth and Environmental Sciences and GeoBio-Centre, Ludwig-Maximilians-Universität München, 80333 Munich, Germany

[2] Instituto de Geociencias, Universidad Complutense Madrid (UCM, CSIC), 28040 Madrid, Spain

[3] Department of Earth Sciences, University of Cambridge, CB2 3EQ Cambridge, U.K .

[4] Courant Research Center Geobiology, Georg-August University of Göttingen, 37077 Göttingen, Germany

[5] Central Facility for Electron Microscopy, University of Ulm, 89081 Ulm, Germany

[6] Institute of Applied Geosciences, Graz University of Technology, 8010 Graz, Austria

[7] GEOMAR-Helmholtz Centre for Ocean Research, Marine Biogeochemistry/Marine Geosystems, 24148 Kiel, Germany

[8] Instituto de Ciencia de Materiales de Madrid (ICMM, CSIC), 28049 Madrid, Spain

[9] Department of Earth Sciences, Brock University, St. Catharines, L2S 3A1 Ontario, Canada

Reprinted (adapted) version

2.4.1 Abstract

The assessment of diagenetic overprint on microstructural and geochemical data gained from fossil archives is of fundamental importance for understanding palaeoenvironments. The correct reconstruction of past environmental dynamics is only possible when pristine skeletons are unequivocally distinguished from altered skeletal elements. Our previous studies (see chapter 2.1) show (i) that replacement of biogenic carbonate by inorganic calcite occurs via an interfacecoupled dissolution-reprecipitation mechanism. (ii) A comprehensive understanding of alteration of the biogenic skeleton is only given when structural changes are assessed on both, the micrometre as well as on the nanometre scale.

In the present contribution we investigate experimental hydrothermal alteration of six different modern biogenic carbonate materials to (i) assess their potential for withstanding diagenetic overprint and to (ii) find characteristics for the preservation of their microstructure in the fossil record. Experiments were performed at 175 °C with a 100mM NaCl + 10mMMgCl$_2$ alteration solution and lasted for up to 35 days. For each type of microstructure we (i) examine the evolution of biogenic carbonate replacement by inorganic calcite, (ii) highlight different stages of inorganic carbonate formation, (iii) explore microstructural changes at different degrees of alteration, and (iv) perform a statistical evaluation of microstructural data to highlight changes in crystallite size between the pristine and the altered skeletons.

We find that alteration from biogenic aragonite to inorganic calcite proceeds along pathways where the fluid enters the material. It is fastest in hard tissues with an existing primary porosity and a biopolymer fabric within the skeleton that consists of a network of fibrils. The slowest alteration kinetics occurs when biogenic nacreous aragonite is replaced by inorganic calcite, irrespective of the mode of assembly of nacre tablets. For all investigated biogenic carbonates we distinguish the following intermediate stages of alteration: (i) decomposition of biopolymers and the associated formation of secondary porosity, (ii) homoepitactic overgrowth with preservation of the original phase leading to amalgamation of neighbouring mineral units (i.e., recrystallisation by grain growth eliminating grain boundaries), (iii) deletion of the original microstructure, however, at first, under retention of the original mineralogical phase, and (iv) replacement of both, the pristine microstructure and original phase with the newly formed inorganic product.

At the alteration front we find between newly formed calcite and reworked biogenic aragonite the formation of metastable Mg-rich carbonates with a calcite-type structure and compositions ranging from dolomitic to about 80 mol% magnesite. This high-Mg calcite seam shifts with the alteration front when the latter is displaced within the unaltered biogenic aragonite. For all investigated biocarbonate hard tissues we

observe the destruction of the microstructure first, and, in a second step, the replacement of the original with the newly formed phase.

2.4.2 Introduction

Biomineralised hard parts composed of calcium carbonate form the basis of studies of past climate dynamics and environmental change. However, the greatest challenge that all biological archives face lies in their capacity to retain original signatures, as alteration of them starts immediately upon death of the organism (e.g., Patterson and Walter, 1994; Ku et al., 1999; Brand, 2004; Zazzo et al., 2004; Casella et al., 2018a, 2018b).

Despite previous extensive research, carbonate diagenesis is still only partly understood (e.g., Bathurst, 1975; Brand and Veizer, 1980, 1981; Swart, 2015) as many studies addressing the evolution of parameters that influence diagenetic alteration, are discussed only in a qualitative manner (Brand and Veizer, 1980, 1981; Swart, 2015). In particular, deciphering the sequence of processes and, thus, pathways of alteration poses major problems in carbonate diagenesis (Immenhauser et al., 2015; Swart, 2015; Ullmann and Korte, 2015). Our previous study on the shell of the modern bivalve *Arctica islandica* has shown that laboratory-based, simulated diagenetic alteration discloses microstructural and geochemical features that are comparable to those found in fossil specimens (Casella et al., 2017; Ritter et al., 2017). However, the cited studies were performed on the hard tissue of only one taxon. For a more comprehensive understanding of microstructural and chemical controls at diagenesis we extend our studies to hard tissues of other modern marine carbonate biomineralisers such as the bivalve *Mytilus edulis*, the coral *Porites* sp., and the gastropod *Haliotis ovina*. With these we cover the major calcium carbonate phases, and with the inclusion of the shell of *A. islandica*, six distinct microstructures. When selecting organisms for this study, strict care was taken to investigate those taxa where fossil counterparts are often used for palaeoclimate and palaeoenvironmental reconstruction.

The bivalve *A. islandica* has been studied extensively in many scientific fields such as palaeontology, palaeoecology, biostratigraphy, and palaeoclimate research (e.g., Marchitto et al., 2000; Ridgway et al., 2011; Strahl et al., 2011; Wanamaker Jr. et al., 2011; Karney et al., 2012; Krause-Nehring et al., 2012; Butler et al., 2009, 2013; Schöne, 2013). The first occurrence of *A. islandica* in the Mediterranean Sea is of historical importance and was used until 2010 to mark the former Pliocene–Pleistocene boundary (e.g. Crippa and Raineri, 2015; Crippa et al., 2016). As long-lived organisms, stony corals attract great interest for the reconstruction of palaeoclimates derived from skeletal oxygen isotopic compositions and major element abundances, as these geochemical signals vary in response to changes in seawater temperature (e.g., Heiss, 1994; Cohen et al., 2001;

Results and discussion

McGregor and Gagan, 2002; Schöne et al., 2004, 2005a, b; Korte et al., 2005; Böhm et al., 2006; Allison et al., 2007; Meibom et al., 2007; Rüggeberg et al., 2008; Morton, 2011). For example, it is assumed that δ^{234}U in sea water has remained constant in the past. Thus, the comparison between present-day and decaycorrected δ^{234}U in sea water and in coral skeletons is a major tool for the detection of diagenetically altered corals. δ^{234}U values of the latter are higher relative to present-day sea water (Hamelin et al., 1991; Stirling et al., 1995; Delanghe et al., 2002), while pristine corals exhibit a ^{234}U/^{238}U activity ratio similar to modern sea water (Henderson et al., 1993; Blanchon et al., 2009). Shells of molluscs (e.g., *M. edulis*), and gastropods (e.g., *H. ovina*) represent important archives for studies of palaeo- and present environmental change (Raffi, 1986; Richardson, 2001; Elliot et al., 2003; Wanamaker Jr. et al., 2008; Hippler et al., 2009; Schöne and Surge, 2012). The work of Hahn et al. (2012, 2014) has shown that environmental reconstruction can be derived from microstructural information, as well as stable isotope and major element data (Jackson et al., 1988; Cartwright and Checa, 2007; Gries et al., 2009).

In order to detect low to moderate degrees of alteration as well as to identify intermediate steps for the reconstruction of major pathways of overprint we investigated the behaviour of biocarbonate skeletal microstructure at laboratory-based hydrothermal overprint. We conducted alteration experiments for time spans between 1 and 35 days, at a temperature of 175 °C and in the presence of a Mg-rich fluid. We investigated the skeletons of two modern bivalves (*A. islandica* and *M. edulis*), one modern stony coral (*Porites* sp.), and one modern gastropod (*H. ovina*). With this selection of hard tissue we are able to highlight the influence at alteration of variations in mineral surface area, control by primary (inherent) and secondary (induced) porosity, the effect of biopolymer fabric and pattern of distribution within the skeleton, and the impact of size, form, and mode of organisation of biomineral units such as granules, fibres, tablets and prisms. We discuss differences between biogenic to inorganic carbonate replacement kinetics, and illustrate differences in structure and porosity between original and overprinted product phases. Overprint strongly affects the size of mineral units in the alteration product, and we evaluate this characteristic for pristine and altered skeletons using statistical evaluation. Based on statistical grain-area analysis, we present a new and reliable tool for the detection of diagenetic overprint in biological carbonate hard tissues. This tool is sufficiently sensitive to characterize low degrees of diagenetic alteration.

2.4.3 Materials and methods

Test materials

Shells of the modern bivalve *Arctica islandica* were collected from Loch Etive, Scotland (U.K.). The shells are 8-10 cm in size and represent adult specimens. Pristine specimens of the scleractinian coral *Porites* sp. were collected at Mo'orea, French Polynesia (Rashid et al., 2014). Live specimens of the gastropod *Haliotis ovina* were collected from the reef flat of Heron Island, Queensland, Australia. All shell pieces used in this study were taken from the shell of one adult specimen with dimensions of approximately 8 × 6.5 cm. Shells of the modern common blue mussel, *Mytilus edulis*, were collected from 5-7 m depth in the subtidal zone of Menai Strait, Wales, UK. Shell sizes varied from 5 to 6 cm and represent adult animals.

Methods

Selective etching of organic matrix

In order to image the organic matrix in modern (reference) and hydrothermally altered shell samples, as well as the mineral reference (inorganic aragonite), shells or mineral pieces were mounted on 3 mm thick cylindrical aluminium rods using super glue. The samples were first cut using a Leica Ultracut ultramicrotome with glass knives to obtain planar surfaces. The cut pieces were then polished with a DIATOME diamond knife by stepwise removal of material in a series of 20 sections with successively decreasing thickness (90, 70, 40, 20, 10, and 5 nm, and each step was repeated 15 times) as reported in Fabritius et al. (2005). The polished samples were etched for 180 s using 0.1 M HEPES at a pH of 6.5 containing 2.5 % glutaraldehyde as a fixation solution. The etching procedure was followed by dehydration in 100 % isopropyl three times for 10 min each, before specimens were critical point-dried. The dried samples were rotary coated with 3 nm platinum and imaged using a Hitachi S5200 field-emission scanning electron microscope (FE-SEM) operating at 4 kV.

Microstructure and texture

For FE-SEM and electron backscatter diffraction (EBSD) analyses, 5 × 5 mm thick pieces were cut out of the shells and embedded in epoxy resin. The surface of the embedded samples was subjected to several sequential mechanical grinding and polishing steps down to a grain size of 1 μm. The final step consisted of etch-polishing with colloidal alumina (particle size ~ 0.06 μm) in a vibratory polisher. Samples were coated with 4-

6 nm of carbon for EBSD analysis, and with 5 nm Pt/Pd for SEM visualisation. EBSD measurements were carried out on a Hitachi SU5000 field emission SEM, equipped with an Oxford EBSD detector. The SEM was operated at 20 kV and measurements were indexed with CHANNEL 5 HKL software (Schmidt and Olesen, 1989; Randle and Engler, 2000). Information obtained from EBSD measurements is presented as band contrast images, and colour-coded crystal orientation maps with corresponding pole figures.

The EBSD band contrast represents the signal strength of the EBSD-Kikuchi diffraction pattern and is displayed as a greyscale component of EBSD scanning maps. The strength of the EBSD signal is high when a crystal is detected (bright), whereas it is weak or absent when a polymer such as organic matter is scanned (dark/black). Co-orientation statistics are derived from pole figures obtained by EBSD scans and is given by the MUD (multiple of uniform (random) distribution) value. The MUD value measures crystal co-orientation (texture sharpness) in the scanned area, where a high MUD value indicates high and a low MUD value reflects a low to random co-orientation, respectively.

Grain area evaluation

Individual grains can be identified and various grain related parameters, e.g. grain area, can be measured with EBSD. A grain is defined as a region completely surrounded by boundaries across which the misorientation angle relative to the neighbouring grains is larger than a critical value, i.e. the critical misorientation value. Griesshaber et al. (2013) empirically determined that a critical misorientation value of 2 ° best suits the microstructure of modern carbonate biological hard tissues. By using this value, individual mineral units (e.g., fibres, tablets, prisms, columns), also called grains, can be addressed and evaluated. For the relative frequency to grainarea statistics, we use the critical misorientation value of 2 °, grain clusters with a class width of 0.2 μm, and corrected values for absolute distribution function and probability density (F x(x)) to relative values. Care was taken that the quality of EBSD maps used in this study is very similar; hence all measurements were conducted with very small (200 to 300 nm) step sizes. Measurements with a hit rate below 90 % for calcite and below 70 % for aragonite were not used for statistical evaluation.

Alteration experiments

Laboratory-based hydrothermal alteration experiments mimicked burial diagenetic conditions in terms of fluid composition. The latter is based on previously conducted hydrothermal experiments with a defined concentration of Mg that is comparable to Mg contents found in natural diagenetic environments. However, pressure conditions could

not be adjusted to those of natural burial diagenesis due to the experimental design (closed system), and thus, corresponded to vapour pressure of water at the given temperature. In all experiments, pieces of shells or skeletons up to 2 cm × 1 cm of modern *A. islandica*, modern *M. edulis*, modern *Porites* sp., and modern *H. ovina* were placed inside a polytetrafluoroethylene (PTFE) vessel together with 10 mL of simulated burial fluid (100 mM NaCl + 10m MMgCl$_2$ aqueous solution) and sealed with a PTFE lid. Each PTFE vessel was placed in a stainless steel autoclave, sealed and kept in the oven at a temperature of 175 °C for different periods of time ranging between 1 and 35 days. After the selected time period, the autoclave was removed from the oven, cooled down to room temperature and opened. Recovered solid material was dried at room temperature and prepared for XRD, EBSD, and EDX measurements.

X-ray diffraction analysis

X-ray diffraction analysis of pristine and hydrothermally altered samples was performed with Cu-Kα_1-radiation in reflection geometry on a General Electric Inspection Technologies XRD3003 X-ray diffractometer with an incident-beam Ge111 focussing monochromator and a Meteor positionsensitive detector (GE Inspection Technology GmbH). The diffractograms underwent Rietveld analysis with the software package FULLPROF (Rodríguez-Carvajal, 2001) using the aragonite structure data of Jarosch and Heger (1986) and calcite structure data of Markgraf and Reeder (1985).

Thermal gravimetric analysis (TGA)

Determination of organic matter content occurred via TGA measurements conducted in a TA Instruments Q500 TGA. The samples were heated from ambient temperature to 1000 °C at a rate of 5 °C per minute in a flowing-air atmosphere. The initial weight of samples used for TGA measurements was 20 mg for *A. islandica*, 24 mg for *Porites* sp., 26 mg for *H. ovina*, 20 mg for *M. edulis* nacre, and 22 mg for *M. edulis* calcite.

2.4.4 Results

Microstructural characteristics of modern bivalve, gastropod and coral skeletons

FE-SEM images shown in Figs. 2.64, 2.76, and 2.77 highlight characteristic mineral units and their assembly within the skeletons of the investigated species: the modern bivalves *Arctica islandica* and *Mytilus edulis*, the modern coral *Porites* sp., and the modern

gastropod *Haliotis ovina*. Skeletons of *A. islandica*, *H. ovina*, and *Porites* sp. consist entirely of aragonite, whereas *M. edulis* contains both carbonate phases, calcite and aragonite.

The shell of *A. islandica* comprises an assemblage of irregularly shaped, micrometre-sized aragonitic mineral units (white stars in Fig. 2.64A) that are interconnected by an irregular network of thin biopolymer fibrils (this study and Casella et al., 2017). Mineral unit size, porosity, and density of aragonite crystal packing is unevenly distributed within the shell, such that, relative to inner shell portions, mineral unit and pore sizes along the shell rim pointing to seawater are increased. Mineral unit organisation in the shell of *A. islandica* is mainly unstructured, especially in shell portions along the seawater pointing shell rim. Despite this, aragonite that constitutes the inner shell layers, i.e., shell parts that are next to the soft tissue of the animal, is mainly present in a crossedlamellar microstructural arrangement. Growth lines in *A. islandica* shells are frequent and are easily observed, as in this species biopolymer contents and mineral unit sizes are increased (Casella et al., 2017; Greiner et al., 2018). Even though the shell of *A. islandica* can be addressed as consisting of densely packed aragonite, it contains primary porosity. The latter is unevenly distributed: along the seaward pointing shell portion, pores are abundant and large, while in shell parts that are closer to the soft tissue of the animal, pores are small and significantly less frequent (Greiner et al., 2018).

TGA measurements demonstrate that organic contents within the shell of pristine *A. islandica* are 2.2 wt% in the outer and 1.8 wt% in the inner shell portion, respectively. After 14 days of hydrothermal alteration we find 1.8 wt% in the outer and 1.7 wt% in the inner shell part, respectively. The skeleton of the modern stony coral *Porites* sp. consists of an assemblage of spherulitic units, the latter containing aragonitic needles and fibrils (white star in Fig. 2.64B). These grow radially outward from an organic template present at aragonite nucleation sites: the centres of calcification (white dots in Fig. 2.64B; Griesshaber et al., 2017). As skeletal growth proceeds, aragonite crystallites increase in size, and form thin fibres that are bundled into loosely co-oriented mineral units (framed in white and yellow in Fig. 2.76A; Griesshaber et al., 2017). When sectioned in two dimensions, spherical, irregularly shaped entities are obtained (yellow stars in Figs. 2.76B, C), which are cut-off from each other by cavities.

TGA measurements give 2.10 wt% organic matter for the skeleton of modern stony coral *Porites* sp. When altered for 14 days the coral skeleton still contained 1.98 wt% of organic material. Hence, we find only a minor decrease in organic content with alteration for 14 days, at an alteration temperature of 175 °C and in Mg-rich burial fluid.

The shell of the modern gastropod *H. ovina* consists of aragonite. The latter is present in two microstructural arrangements (Figs. 2.64C, D, 2.77A): aragonite prisms and nacre tablets. Aragonite prisms (yellow stars in Figs. 2.77A, 2.64C) form the outer

shell layer, while nacreous tablets (white stars in Figs. 2.77A, 2.64D) constitute inner shell portions. The prismatic mineral units in *H. ovina* show a gradation in size that decreases towards the rim of the outer shell. Accordingly, large aragonitic prisms are within the central part of the shell, next to nacreous aragonite. Nacreous tablets in *H. ovina* are stacked and form columns (white star in Fig. 2.77A).

TGA measurements give an organic content of 3.1 wt% for the shell of *H. ovina*. This value comprises both shell layers. The observed organic content agrees well with the overall microstructural design of the shell of *H. ovina*. Most of the shell consists of dense nacreous aragonite, the latter being composed of thin (200 to 300 nm thick) tablets fully encased by a biopolymer sheath. The slightly porous prismatic aragonite shell layer forms only about 20 % of the shell. At hydrothermal alteration for 21 days, the content of organics that is present in the shell of *H. ovina* decreased to 1.7 wt%.

The shell of the modern bivalve *M. edulis* contains arrays of highly co-oriented calcite fibres (yellow stars in Figs. 2.64E, 2.77B; Griesshaber et al., 2013; Checa et al., 2014) along the outward part of the shell. Inner shell layers consist of nacreous aragonite (white star in Figs. 2.64F, 2.77B). Aragonitic tablets in *M. edulis* are about 500 nm thick, are encased by an organic sheath, and are grouped in a sheeted, "brick-wall" arrangement (Fig. 2.64F; Griessshaber et al., 2013).

Organic contents are slightly different for the two shell layers, 2.7 wt% for the aragonitic and 2.0 wt% for the calcitic shell portion. Hydrothermal alteration for 21 days reduced the amount of organic material within the shell of *M. edulis* drastically to 0.7 wt% in the aragonitic and 0.6 wt% in the calcitic shell part, respectively.

Microstructure and texture of hydrothermally altered bivalve, gastropod and coral skeletons

The shells and skeletal elements of modern *Arctica islandica*, *Porites* sp., *Haliotis ovina* and *Mytilus edulis* were subjected to laboratory-based hydrothermal alteration. Experiments were carried out at 175 °C in the presence of a Mg-rich fluid simulating burial water. Experiment lasted between 1 and 35 days (Fig. 2.78).

The amount of newly formed calcite was determined by Rietveld analysis of XRD data (Fig. 2.79). Diagrams of calcite content vs. experimentation time (Fig. 2.65) demonstrate the difference in replacement kinetics between biogenic calcium carbonates and inorganic calcite, and highlight the profound influence of the biogenic microstructure on the replacement reactions. In hydrothermally altered *A. islandica* shells, new calcite formation starts after 4 days of alteration and progresses constantly. After 7 days of alteration, most shell aragonite is replaced by calcite (Figs. 2.65a, 2.79a; Casella et al., 2017). In contrast, the hard tissue of *Porites* sp. and of *H. ovina* respond
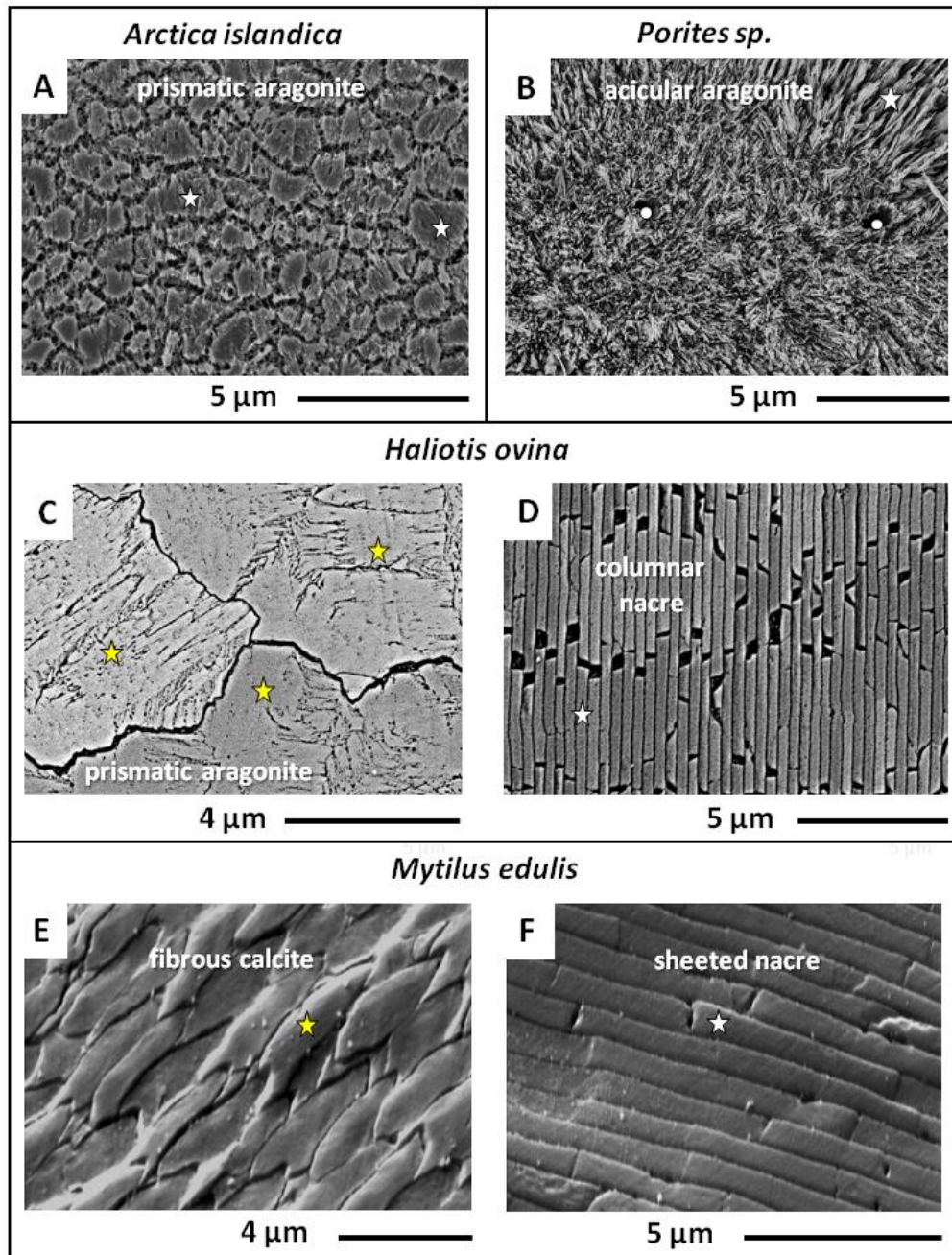
Figure 2.64: SEM micrographs showing the characteristic microstructures of skeletons of the modern specimens of (A) bivalve *Arctica islandica*, (B) scleractinian coral *Porites* sp., (C, D) gastropod *Haliotis ovina*, and (E, F) bivalve *Mytilus edulis*. The shell of *A. islandica* consists of an assemblage of irregularly shaped and sized aragonitic mineral units (white stars in A) which are embedded in a network of biopolymer fibrils (this study and Casella et al., 2017). The acicular aragonitic skeleton of the modern coral *Porites* sp. (white star in B) is composed of differently sized spherulites consisting of fibrils and needles. These grow outward from an organic template which lines the mineral nucleation sites, i.e, centres of calcification (white dots in B). Shells of the gastropod *H. ovina* and the bivalve *M. edulis* comprise two distinct carbonate layers. The shell of *H. ovina* consists of irregularly shaped and sized prisms (yellow stars in C) next to a nacreous shell layer with nacre tablets assembled as columns (white star in D). The outer shell layer in *M. edulis* is formed by stacks of calcite fibres (yellow star in E), while the inner shell layer is nacreous with nacre tablets arranged in a "brick wall fashion" (white star in F).
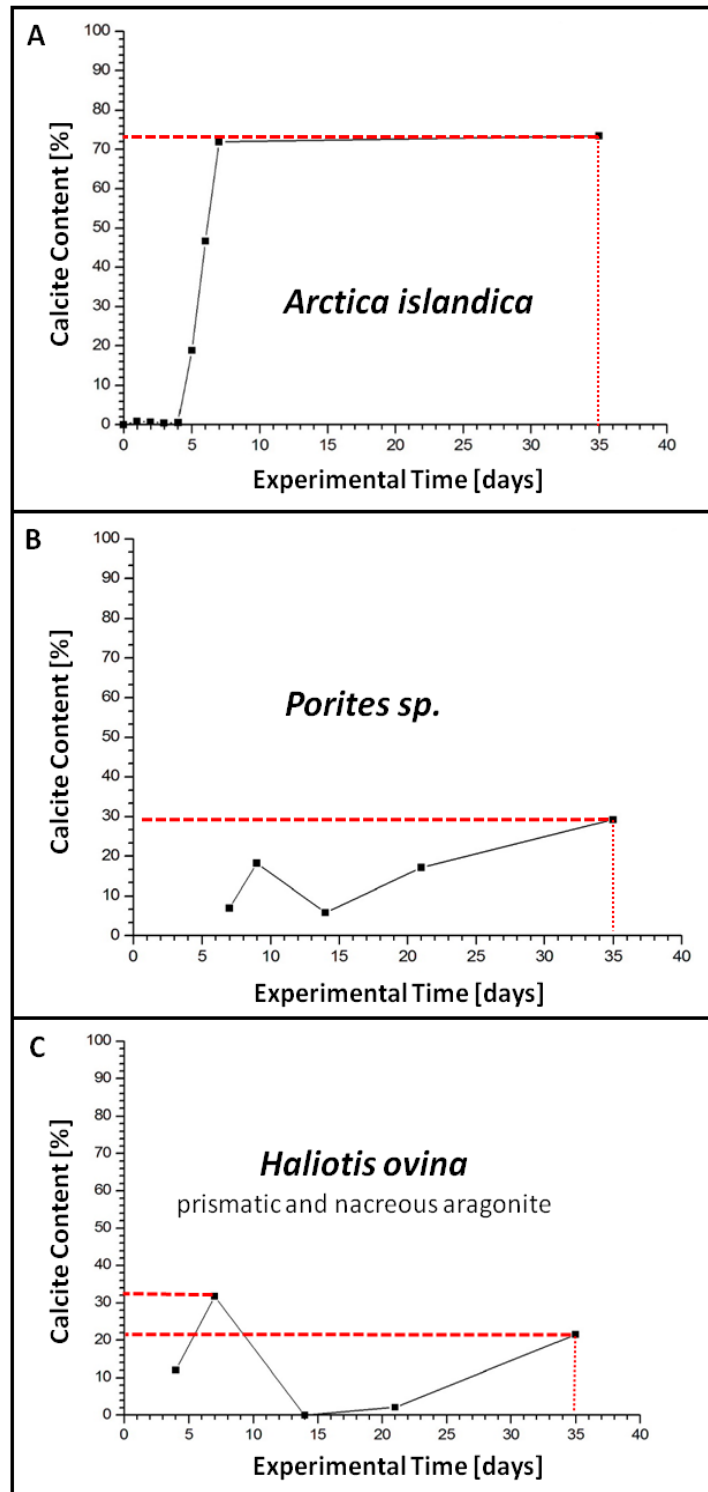
Figure 2.65: Newly formed inorganic calcite content versus alteration time plots calculated from Rietveld analyses of the XRD data obtained for hard tissues of (A) *Arctica islandica*, (B) *Porites* sp., and (C) *Haliotis ovina*. Red dashed lines indicate the percentage of newly formed calcite after 35 days of alteration as well as maximum contents of inorganic calcite for each investigated species. Differences in newly formed calcite contents among the four species clearly highlight the influence of the different microstructures on the replacement kinetics of biogenic carbonate by inorganic calcite.

differently to alteration. Replacement of biogenic aragonite by newly formed calcite is significantly slower compared to that occurring in the shell of *A. islandica*, such that after 35 days of alteration only 20 % to 30 % of biogenic aragonite is replaced by inorganic calcite (Figs. 2.65B, C, 2.79B, D). For all five investigated types of microstructures, the amount of newly formed calcite is not a continuous function of time.

Microstructure and phase characterisation was carried out with EBSD. The results are presented as EBSD band contrast (Figs. 2.80 to 2.83A), colour-coded orientation maps (Figs. 2.66 to 2.68, 2.83B), and corresponding pole figures (Figs. 2.66 to 2.68). EBSD band contrast is shown as a greyscale component that illustrates the strength of the diffracted signal for each measurement. Thus, when mineral material is hit by the electron beam, the backscattered signal is high and light grey colours form the image. When an organic component is scanned, the backscattered diffraction signal is absent, and the band contrast measurement image is black. Carbonate mineral co-orientation strength is given with MUD values (e.g., Casella et al., 2017, 2018a, 2018b). These are derived from pole density distributions and are quoted for each EBSD scan.

Figures 2.66 to 2.68, and 2.80 to 2.83 show the difference in microstructure and texture between pristine samples and the most advanced stage of alteration (35 days, at 175 °C in a Mg-rich fluid). At these conditions aragonitic mineral units in the shell of modern *A. islandica* (Fig. 2.80A) are quickly and almost completely replaced by inorganic calcite (Fig. 2.80B). In the modern shell these mineral units are surrounded by a thin network of organic fibrils. The latter are easily destroyed at hydrothermal alteration and space is created for fluid percolation. Hence, a pervasive and quickly progressing replacement of biogenic aragonite by inorganic calcite takes place. Calcite nucleation and growth in *A. islandica* shells starts after a dormant period of about 4 days (Fig. 2.79A; Casella et al., 2017). Once started, the replacement progresses readily to completion. In the outer shell layer the replacement of aragonite is completed with the development of large and randomly oriented calcite grains, while, in denser shell areas, patches of biogenic aragonite are still preserved, containing features of the original biogenic microstructure and texture (see also Casella et al., 2017).

In contrast, acicular aragonite in *Porites sp.* displays a different behaviour during alteration. Even after alteration of 35 days only minor parts of the coral skeleton are replaced by calcite (Figs. 2.65B, 2.66B to E, 2.80C, D). Our results show that the alteration fluid enters the coral skeleton predominantly at centres of calcification (Figs. 2.66B, D, 2.80D). New calcite formation starts mainly at these sites and proceeds from there into the skeleton. As Fig. 2.66D demonstrates, even after alteration for 35 days, at 175 °C and in the presence of a Mgrich fluid, some regions of the acicular microstructure are still preserved. However, we see a decrease in MUD value from 41 in the pristine (Fig. 2.66A) to an MUD of 13 (Fig. 2.66E) in the altered shell. This is the only sign of alteration: the decrease in MUD indicates growth of new aragonite with a lower degree of

crystallographic co-orientation of the newly formed mineral. With progressively longer alteration times, up to 35 days, large and randomly oriented calcite crystals grow within the coral skeleton (Figs. 2.66B, C, D, 2.80D). This calcite has high MUD values (Fig. 2.66D) similar to single crystalline calcite precipitated from solution (Nindiyasari et al., 2015; Casella et al., 2017).
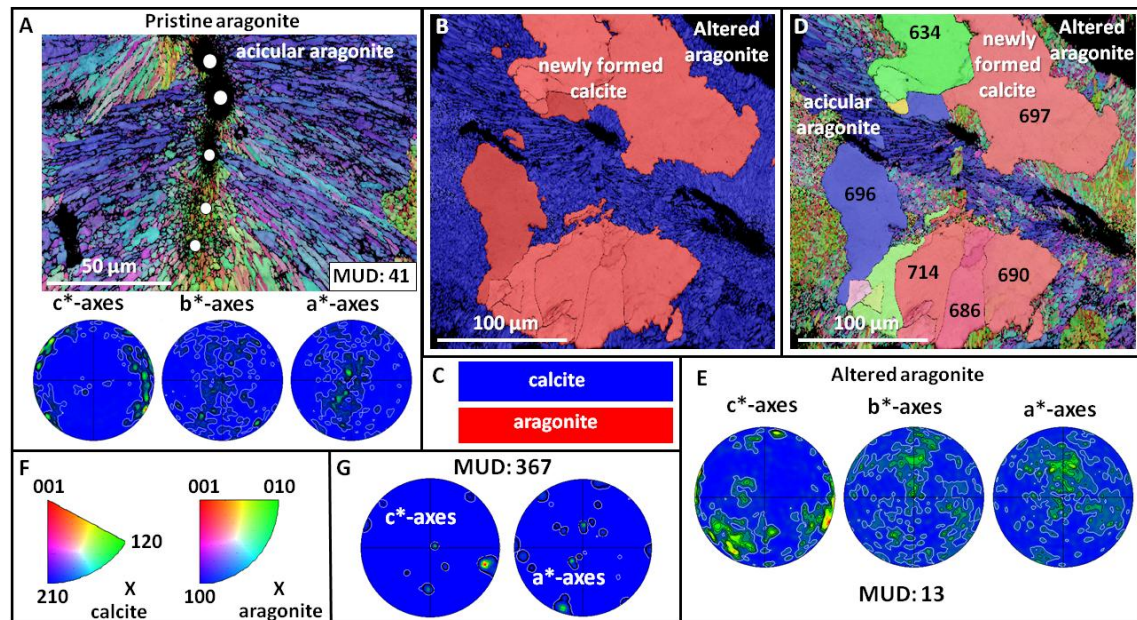
Figure 2.66: EBSD colour-coded orientation and phase maps with corresponding pole figures which depict the microstructure, texture and pattern of biogenic and inorganic carbonate phase distribution in pristine (A) and hydrothermally altered (B, C, D, E) skeletal elements of the scleractinian coral *Porites* sp. Alteration lasted for 35 days and was carried out at 175 °C in a Mg-rich fluid simulating burial water (100 mM NaCl + 10m MMgCl$_2$ aqueous solution). EBSD colour codes are given in (F). The strength of crystal co-orientation is expressed with MUD values and is given at each EBSD measurement. MUD values for newly formed calcites (D) are written into the EBSD map and are given for most newly formed calcite crystals. Even though crystal co-orientation strength is moderate in the modern coral specimen (MUD: 41 in A), it decreases significantly in the altered coral skeleton (MUD: 13 in D). Co-orientation strength in newly formed calcite is exceedingly high, as high as that of calcite grown from solution (D).

Aragonite prisms in the pristine shell of *H. ovina* (Fig. 2.67A) are within a network of biopolymer fibrils which are readily destroyed by hydrothermal alteration. A significant amount of space becomes available for fluid infiltration, which results in extensive overprint and a rapidly progressing replacement of the biogenic aragonite by inorganic calcite. Figures 2.67B and 2.81B show that after 35 days of alteration, in the presence of a Mg-rich fluid at 175 °C the highly porous prismatic aragonite shell layer of modern *H. ovina* (Figs. 2.67A, 2.81A) is completely replaced by inorganic calcite. In contrast, the nacreous shell layer of *H. ovina* is little affected. There is no major change between
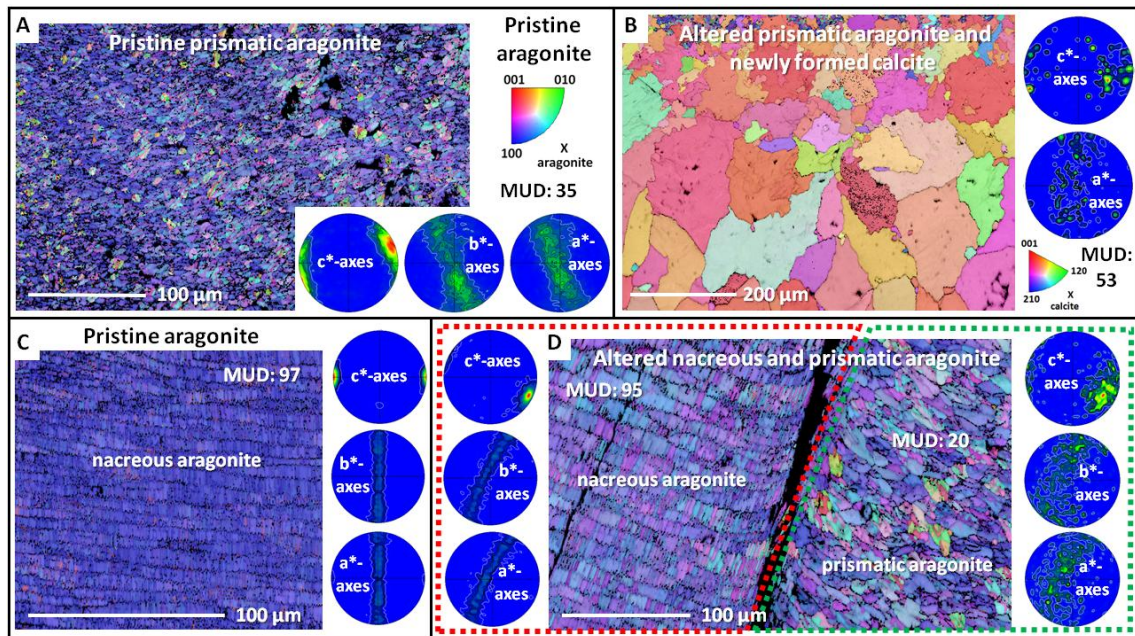
Figure 2.67: EBSD colour-coded orientation and phase maps with corresponding pole figures show the microstructure, texture, and pattern of biogenic and inorganic carbonate phase distribution in pristine (A, C) and hydrothermally altered (B, D) *Haliotis ovina* shells. Alteration lasted for 35 days and was carried out at 175 °C in a Mg-rich solution. Crystal co-orientation strengths, expressed with MUD values, are given at each EBSD map. Alteration for 35 days induces the replacement of large parts of prismatic biogenic aragonite (A) by inorganic calcite (B). However, in shell layers where replacement has not yet taken place, aragonitic prisms amalgamate and MUD values decrease (right-hand side of EBSD map shown in (D) framed with a green dashed line; compare to EBSD map, pole figures, and MUD value shown in A). The nacreous part of the shell is little affected by alteration. Even when altered for 35 days the columnar microstructure is still well preserved (D). The MUD value of altered nacre (left-hand side of EBSD map shown in (D), framed in red) is very similar to that obtained for pristine nacre (C).

pristine and altered *H. ovina* nacre, neither in carbonate phase, nor in microstructure or in MUD value (Figs. 2.67C, D and 2.81C, D).

Even though there is some correspondence in mineral unit morphology and size, and the extent of primary porosity and fabric of occluded biopolymers between prismatic aragonite in *H. ovina* and that in *A. islandica*, the kinetics of carbonate phase replacement is distinct for the two microstructures (Figs. 2.65A, C). In *A. islandica*, where small, irregularly shaped aragonite mineral units comprise the shell; replacement between carbonate phases is rapid and extensive, while replacement in the outer shell layer of *H. ovina*, where the shell consists of larger aragonite prisms, is slow and patchy. In addition, the difference between pristine and altered prismatic aragonite in *H. ovina* (compare pole figures and MUD values of Fig. 2.67A and D) is such that in the altered shell the size of aragonitic prisms increases while the strength of aragonite co-orientation decreases. This can be seen in the pole figures and the decreased MUD value (compare Fig. 2.67A with right hand part of Fig. 2.67A, the part framed in green).

In the pristine shell of *M. edulis* each calcite fibre is wrapped in an organic sheath. These decompose during alteration and leave space for fluid permeation and inorganic calcite reprecipitation. The comparison of Figs. 2.68A to C and Figs. 2.82A to B and 2.83 demonstrates that alteration of *M. edulis* calcite fibres at 175 °C, in the presence of a Mgrich fluid, results in severe distortion of the fibres. Crystal coorientation strength for fibrous calcite decreases markedly, from an MUD value of 381 in pristine to 79 in altered shell (Figs. 2.68A, C). In contrast to the calcitic fibrous microstructure, and similar to *H. ovina* nacre, after 35 days of alteration (175 °C, in the presence of a Mg-rich fluid), there is no significant change between pristine and altered *M. edulis* aragonite nacre (Figs. 2.68B, D, 2.82C, D). In altered *M. edulis* amalgamation of nacre tablets can be observed (yellow stars in Fig. 2.82D), and a slight decrease in aragonite crystal co-orientation strength (pristine nacre: MUD 129; altered nacre: MUD 105).
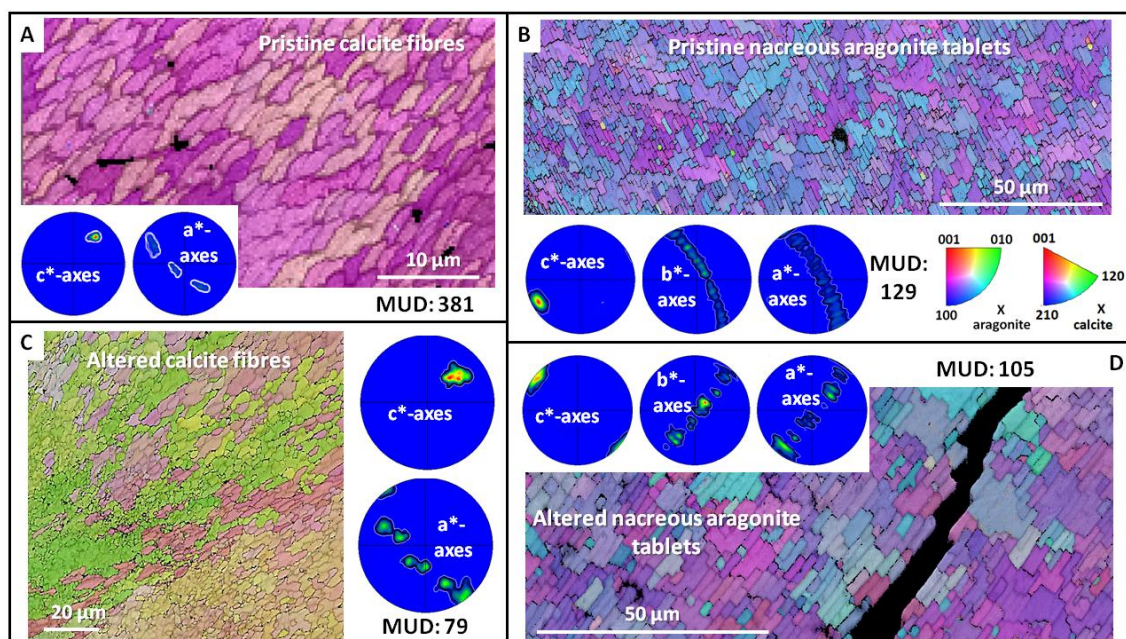
Figure 2.68: Colour-coded EBSD orientation maps with corresponding pole figures depict differences in microstructure and texture between pristine (A, B) and hydrothermally altered (C, D) *Mytilus edulis* shells. Alteration lasted for 35 days and was carried out at 175 °C in a Mgrich fluid. The EBSD colour code used is shown in (B); crystal co-orientation strengths, expressed with MUD values, are given on each EBSD map. Hydrothermal alteration induces a significant change in pristine *M. edulis* calcite fibres (compare panels A and C). The strength of calcite co-orientation decreases from an MUD of 381 in the pristine (A) to a MUD of 79 in the altered shell (C), respectively. In the overprinted sample (C), morphology of calcite fibres is highly distorted due to profound fibre amalgamation. In contrast, nacre in *M. edulis* was little affected by the applied hydrothermal alteration conditions (D); a slight decrease in MUD and sporadic tablet amalgamation can be observed. Otherwise, tablet morphology is not distorted.

Alteration pathways

Major changes in microstructure which develop during different alteration times are depicted in Figs. 2.84 to 2.86. Subsequent to decomposition of organic material, for all investigated skeletons, we find that one of the first steps in the alteration process is an increase in mineral unit dimension relative to that in the pristine skeleton. In the *Porites* sp. coral skeleton, individual spherulites grow together (white stars in Fig. 2.84B, C) and form large and compact entities. Even though the alteration fluid accessed the skeleton from all sides, calcite formation in *Porites* sp. starts within the skeleton and proceeds outward toward the outer perimeter of the hard tissue (Fig. 2.84D). An increase in mineral grain size with progressive alteration can also be observed for both microstructures that constitute the shells of *H. ovina* (Fig. 2.85) and *M. edulis* (Fig. 2.86). As the organic sheaths around the mineral units decompose, space becomes available for new mineral formation. Aragonite prisms, calcite fibres, and nacreous tablets increase in size until they abut each other. In particular, the nacreous microstructure, irrespective of its specific arrangement into columns or sheets, and the calcite fibres form compact entities in response to alteration. In addition to an increase in fibre dimension, *M. edulis* calcite fibre morphology becomes highly distorted with progressive and long alteration duration. Even though the prisms of the prismatic shell layer in *H. ovina* also amalgamate, due to their slightly rounded and irregular morphology, voids become entrapped in this layer of the shell.

A further characteristic caused by hydrothermal alteration is the significant rise in porosity within individual mineral units (Fig. 2.69). Even though the latter grow together at their perimeters (Fig. 2.70) a multitude of nanopores develop within the mineral units due to decomposition of biopolymer fibrils that is present in mineral units of the pristine skeletons (e.g., Griesshaber et al., 2013; Casella et al., 2018a, 2018b). However, as Fig. 2.71 shows, the inorganic calcite that forms from the altered biogenic aragonite is devoid of pores. The patches of pores that are visible within the newly formed calcite (white arrows in Fig. 2.71) are all residues of the incorporated altered biogenic prismatic aragonite. Our results indicate that major features of the mesoscale original microstructure are retained even at advanced stages of alteration (Fig. 2.87). In the shell of *H. ovina*, for instance, where prismatic aragonite is almost entirely replaced by calcite (Fig. 2.87), the original gradation in mineral unit size towards the rim of the outer shell layer is retained. Large newly formed calcite crystals (white stars in Fig. 2.87B) are within the central part of the shell next to nacreous aragonite and decrease in size towards outer shell portions (Fig. 2.87B) – as it is the case in the unaltered prismatic aragonitic shell.
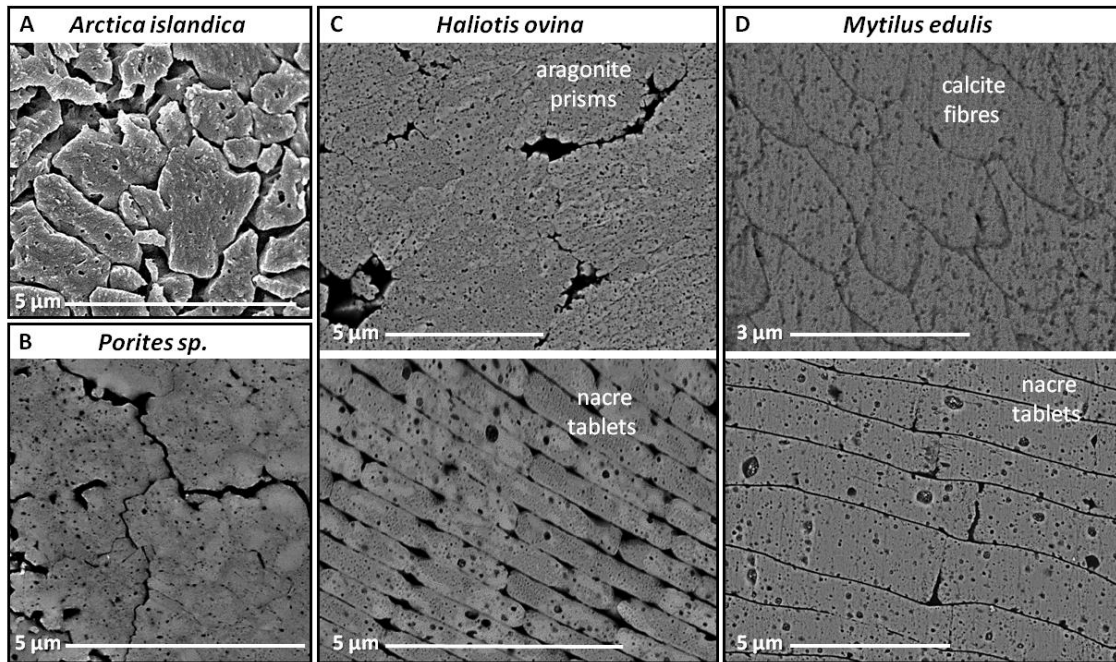
Figure 2.69: Distortion of basic mineral unit morphologies, basic mineral unit amalgamation, and development of porosity in hydrothermally altered shells and skeletons. (A) *Arctica islandica*, (B) *Porites* sp., (C) *Haliotis ovina*, and (D) *Mytilus edulis*. Hard tissue material was altered for 35 days, at 175 °C in the presence of a Mg-enriched fluid.
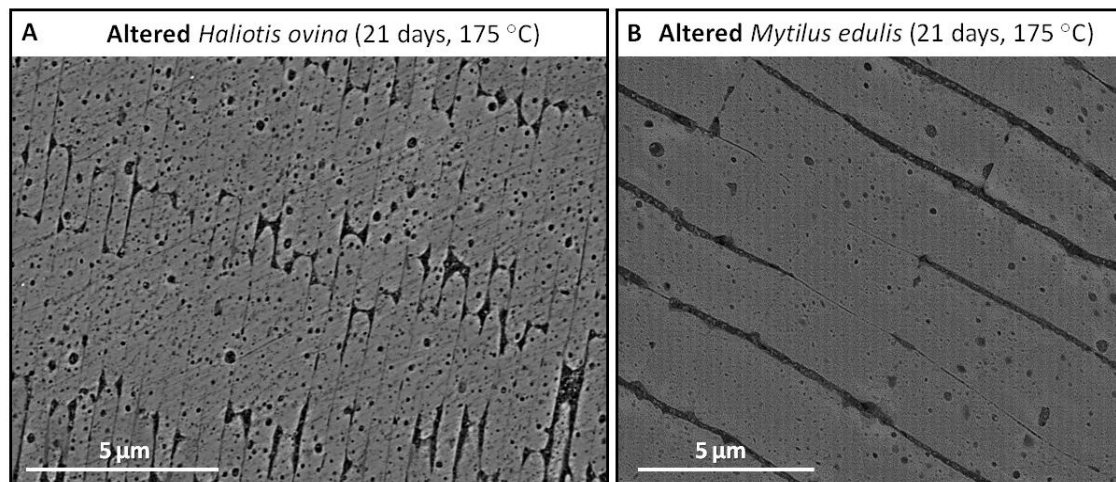
Figure 2.70: Nacre tablet amalgamation in hydrothermally altered *Haliotis ovina* (A) and in *Mytilus edulis* (B) shells. Hard tissue material was altered for 21 days, at 175 °C in the presence of an alteration fluid enriched in Mg.

Our results highlight that among all investigated microstructures, the nacreous microstructures are most resistant to hydrothermal alteration, irrespective of tablet thickness or their mode of organisation (columns or sheets). We observed that replacement of biogenic nacreous aragonite by inorganic calcite takes place with the

151
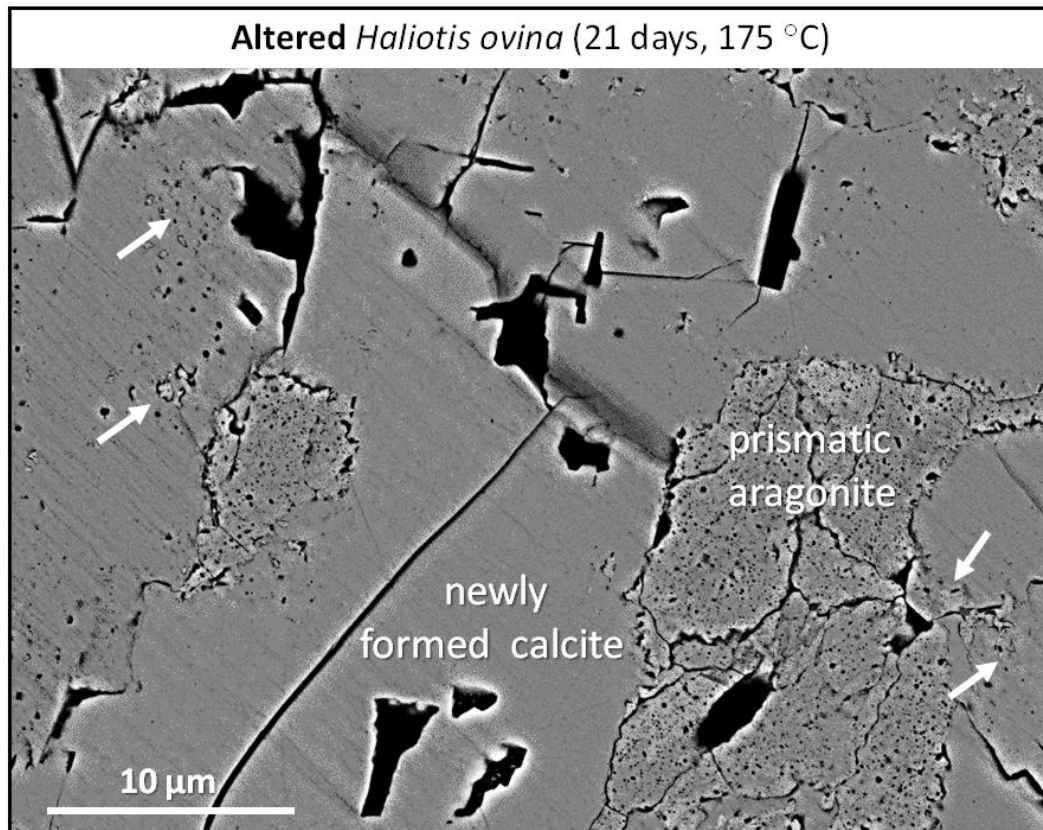
Figure 2.71: Distinctness in porosity between hydrothermally-altered biogenic prismatic aragonite and newly formed inorganic calcite. White arrows point to the aragonite interspersed with calcite; the aragonite is not yet fully consumed and replaced by calcite.

formation of various microstructural and chemical intermediate stages. These are described in detail for *H. ovina* nacre and are illustrated in Figs. 2.72 to 2.74 and 2.88 to 2.90. Alteration of bivalve and gastropod nacre starts (i) with the decomposition of organic biopolymers between and within the tablets. This is followed by (ii) overgrowth with the original phase (aragonite) onto tablet rims and results in tablet amalgamation. Ongoing alteration (iii) destroys tablet assembly (blue stars in Fig. 2.72A, B) up to the complete obliteration of the nacreous microstructure (yellow stars in Figs. 2.72A, B, 2.73A, B). However, as the phase map in Fig. 2.72E shows, a phase replacement of biogenic aragonite by inorganic calcite does not take place at this stage of overprint. Our results show that the microstructure is destroyed first; replacement of one carbonate phase by another occurs subsequently (Fig. 2.72). During alteration in a Mg-rich fluid, a Mg-rich seam of calcite is always present at the phase replacement front, between the newly formed calcite and the highly overprinted nacreous aragonite (white arrows in Figs. 2.72A, D, 2.89, white arrows in Fig. 2.90A). Based on differences in Mg-contents, we find different metastable Mg-rich carbonates with a calcite-type structure and compositions from dolomitic to ca. 80 mole% magnesite (Figs. 2.73, 2.74, 2.90). These segregate between the "final" low-Mg calcite and the overprinted (reworked) aragonite

(Figs. 2.74, 2.90). The last step in the replacement of biogenic nacreous aragonite by inorganic calcite is (iv) the formation of low-Mg calcite (the final calcite), which in the final stage of alteration constitutes the overprinted hard tissue. We could often observe that despite the change from one carbonate phase into another, the newly formed calcite retains much of the original mesoscale morphology of the mineral units inherited from the pristine biogenic skeleton.
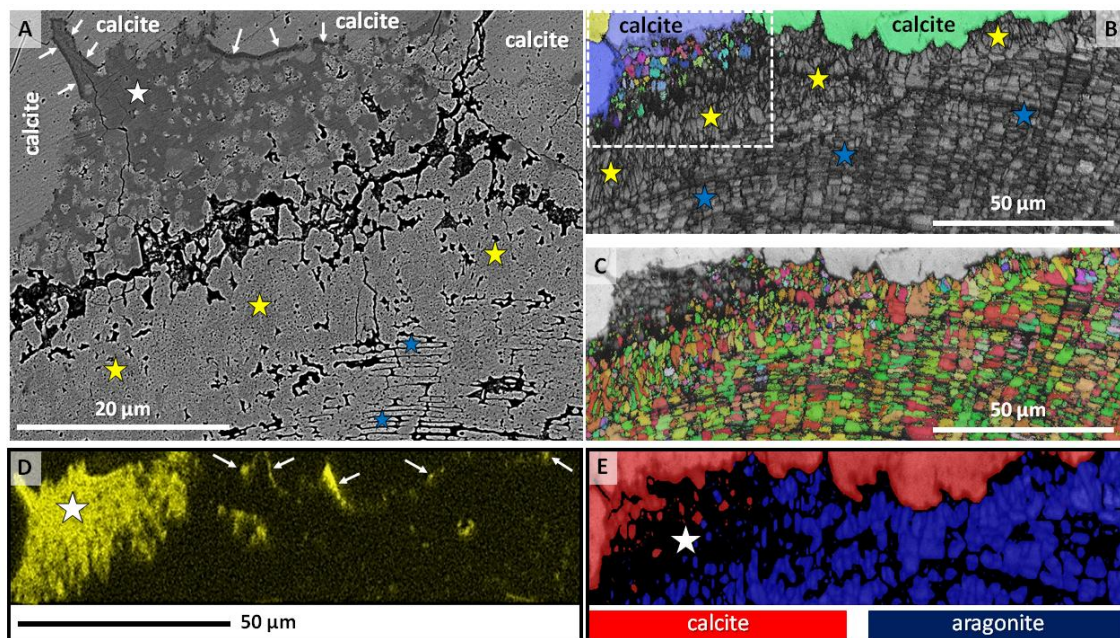
Figure 2.72: Microstructural and chemical stages in the replacement process of biogenic nacreous aragonite by inorganic calcite. *Haliotis ovina* shell material was subjected to hydrothermal alteration for 35 days at 175 °C in a Mg-enriched hydrothermal fluid. (A) SEM image depicting the replacement front between nacreous aragonite and newly formed calcite. Blue stars in (A): nacre tablets forming columns; some traces of the original microstructure can be still observed. Yellow stars in (A): a formerly nacreous shell layer, but, at this stage of alteration, the nacreous microstructure is completely erased. White arrows, white star in (A): high-Mg intercalation between the newly formed calcite and the overprinted, formerly biogenic, aragonite (yellow stars in A). (E) Phase map derived from EBSD showing the newly formed calcite (red) and biogenic aragonite (blue). Note that even though the tablet microstructure cannot be discerned any more, the original mineralogical phase (aragonite) is still preserved. The white star in (E) marks the region where high-Mg calcite intercalation is located, which, in the presence of a Mg-rich fluid, is always present at the replacement front between inorganic calcite and biogenic aragonite. (D) EDX map showing the enrichment in Mg at the transition front in yellow. (B, C) EBSD band contrast shown in grey, and colour-coded orientation maps, respectively depicting traces of columnar aragonite (blue stars in B) and overprinted aragonite (yellow stars in B). Coloured in (B): newly formed calcite. Shell layer which is marked with a white dashed rectangle in (B) is shown enlarged in (A). (C) Colour-coded EBSD map of aragonite; in light grey: newly formed calcite, in dark grey: rim containing high-Mg calcite.
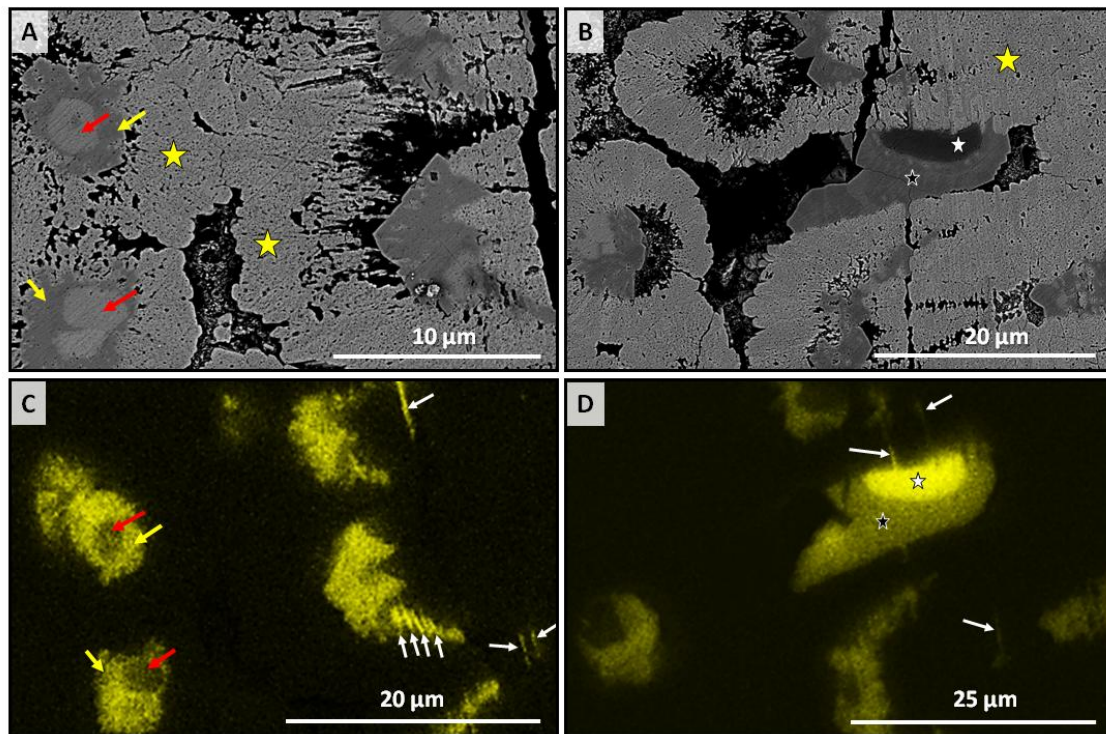
Figure 2.73: Replacement of biogenic aragonitic nacre by inorganic calcite. (A): SEM image showing the nucleation and growth of inorganic calcite within shell aragonite. Note the residual aragonite (red arrows in A and C) replacing the calcite crystals (yellow arrows in A and C). Yellow stars in (A): faint traces of nacre columns. (B) SEM image depicting the formation of high-Mg calcite crystals (black and white star) within overprinted, originally nacreous shell layer (yellow star in B). Tablet assemblages of columns (yellow star in B) are still perceivable. (C, D) EDX map showing in yellow the presence of calcite crystals with high-Mg content (white and yellow arrows in (C), black and white star and white arrows in (D). Red arrows in (C): traces of occluded aragonite distinguished by a low Mg content. White arrows in (C, D): high-Mg streaks that form in cavities between nacreous tablets subsequent to the decomposition of biopolymer membranes around the tablets.

2.4.5 Discussion

Biomineralised tissue provides the bulk of fossil material that is used for geochemical analysis. As all fossil archives are overprinted to some degree, it is of major importance to identify those that are subject to minor and moderate degrees of overprint, as (i) these are the materials that contain most primary information, and (ii) identification of extensive overprint is not challenging, as a severely overprinted microstructure is either highly distorted or is completely destroyed. The latter two characteristics are easily identified, while microstructures with a low to moderate degree of overprint are difficult to recognise and to detect.
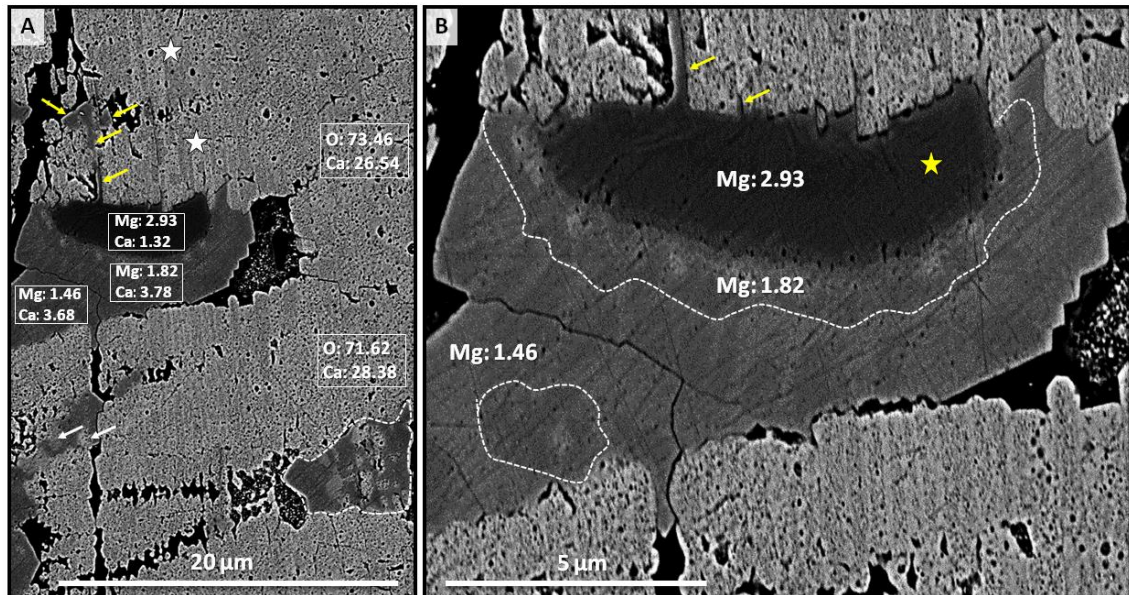
Figure 2.74: Enlargement of image shown in Fig. 2.73B and D. Mg contents of newly formed metastable Mg-rich carbonates with a calcite-type structure and compositions from dolomitic to about 80 mole% magnesite. The columnar assembly of tablets around the calcite is still perceivable (white stars in A, B). Yellow arrows in (A, B) point to the deposition of high-Mg calcite which fills voids and cavities between former nacreous tablets.

Accordingly, important questions that arise in this context are as follows: what are the intermediate steps of diagenetic alteration? What is modified first, easily destroyed and/or keeps for a short time only? The original skeletal microstructure, the original mineralogical phase, the geochemical information? What happens to the original geochemical information that is stored within the biogenic archive? On a broader scale, can we identify major pathways of diagenetic overprint? What determines the preservation potential of a fossil archive?

The process of overprint

Diagenetic overprinting of biogenic carbonates encompasses morphological and chemical changes that take place during post-mortem alteration. Fluids act as catalysts for the alteration reactions at fluid-rock contacts and allow the overprint reactions to proceed at a rapid rate (Brand, 1994). This response is in contrast to solid-state alteration in dry systems, where overprint kinetics is much slower. Brown et al. (1962) have shown that replacement of aragonite by calcite at Earth surface pressure and temperature conditions is 10 orders of magnitude faster in the presence of water compared to dry conditions. Accordingly, with the death of the organism and burial in sediments, biomineralised hard tissues become subject to diagenetic overprint, to solvent-mediated

phase replacement (Cardew and Davey, 1985), or the coupled dissolution of the original material and the reprecipitation of the new product(s) (Putnis, 2002, 2009).

It has been shown for inorganic systems that coupled dissolution–reprecipitation is highly influenced by the availability of interfaces, the reactivity of surfaces, and the extent and topological characteristics of the original and newly formed porosity (Putnis, 2002, 2009; Arvidson and Morse, 2014; Ruíz-Agudo et al., 2014). It is demonstrated that coupling of the two (sub)reactions takes place when the rate of dissolution of the original phase and the rate of crystallisation of the product is almost equal. This has the effect that coupled dissolution-reprecipitation of mineral replacement proceeds with preservation of the external shape of the primary mineral, and leads to formation of pseudomorphs (Xia et al., 2009a; Qian et al., 2010). Is the coupling between dissolution and recrystallisation well balanced, delicate microtextural features are well preserved, e.g. twin boundaries (Xia et al., 2009b) or even small features such as exsolution lamellae (Altree-Williams et al., 2015).

In inorganic materials microstructural elements such as grain boundaries are of key importance for the progress of the overprint process as at the first stages of alteration, these provide the pathways for fluid infiltration and percolation through the material (Etschmann et al., 2014; Jonas et al., 2014). In inorganic systems, mass transfer along grain boundaries is an order of magnitude faster than through the porosity which forms as a result of the mineral replacement reaction (Etschmann et al., 2014; Jonas et al., 2015). However, with progressive alteration an interconnected pore system develops in inorganic materials (Putnis, 2002, 2009; Pollok et al., 2011; Ruíz-Agudo et al., 2014; Altree-Williams et al., 2015) and allows (in ideal cases) for continuous communication between the bulk aqueous phase and the primary and secondary phases at the reaction front (Putnis, 2002, 2009; Etschmann et al., 2014). Besides, pore formation also develops as a direct consequence of the mineral replacement process, in those cases where the molar volume change involved in the reaction is negative. A further source of porosity development during mineral replacement relates to the difference in solubility between the primary and secondary phases (Pollok et al., 2011). Porosity is generated when the primary phase is more soluble than the secondary phase, as a small amount of the latter precipitates after dissolution of the former. In the case of the investigated biogenic carbonates, even though the solubility of biogenic aragonite is higher than the solubility of inorganic calcite, the solubility difference is not large enough to compensate the positive volume change in the dissolution-reprecipitation reaction. A positive molar volume change of only 8.12 % is associated with the replacement of aragonite by calcite (Perdikouri et al., 2011, 2013).

Perdikouri et al. (2011) investigated the replacement of inorganic aragonite by inorganic calcite. The authors immersed inorganic aragonite in pure water and in solutions which contained calcium and carbonate, with the solutions being saturated

with respect to calcite but undersaturated with respect to aragonite. In experiments which were carried out in the presence of water, a replacement was not observable, even after an entire month, unless the solution temperature was equal or higher than 180 °C. However, even at elevated temperatures there was only a narrow rim of aragonite replaced by some calcite overgrowth. The newly formed calcite was devoid of pores; hence, there was no communication between the bulk aqueous phase and the phases at the reaction front. It sealed the aragonite and prevented further progressive replacement.

By using aqueous solutions containing calcium and carbonate Perdikouri et al. (2011) obtained different results. When the composition of the solution was stoichiometric, comparable results were obtained to the experiment with water: little replacement of the original material and the formation of a non-porous calcite overgrowth. In contrast, at alteration in a non-stoichiometric solution, the amount of calcite overgrowth was still small; however, a high degree of replacement was achieved. This effect was increased even more by the absence of calcium in the solution.

The experiments of Perdikouri et al. (2011) demonstrate the importance of porosity and porosity generation for the progress of dissolution–reprecipitation reactions and allude to at least one fundamental difference between biologic and inorganic carbonate hard materials. The absence of primary porosity in inorganic carbonates as well as the (almost complete) drop out of secondary porosity formation. The latter should have been generated at early stages of alteration due to the positive molar volume change that is involved in the aragonite by calcite replacement. However, the only porosity that might have been generated in inorganic carbonate systems arises from the minor difference in solubility between aragonite and calcite. As the solubility products of the two main carbonate phases are similar, very little porosity formation can take place, and consequently, (i) the replacement of inorganic aragonite by inorganic calcite occurs at a very slow rate and (ii) is significantly less pervasive as it is the case when biogenic aragonite is altered into inorganic calcite.

Biological hard tissues are hierarchically organised composite materials where at all scale levels we find an interlinkage of biopolymers with minerals (Levi-Kalismann et al., 2001; Marin and Luquet, 2004; Mayer, 2005; Li et al., 2006; Metzler et al., 2007; Checa et al., 2009). The degradation of biopolymers, being occluded within and between the mineral units of the hard tissue, provides the necessary network of interconnected porosity (Figs. 2.69, 2.70, 2.71, 2.84, 2.85, 2.92). The porosity network not only facilitates alteration, it drives and accelerates it. Our results show that, for biological carbonate tissues, the presence of primary (inherent) and secondary (induced) porosity, together with the characteristics of the porosity network, determines the kinetics and extent of the alteration. Furthermore, the transient character of porosity additionally influences mineral replacement reactions: apart from porosity generation, porosity coarsening and porosity closure are widespread phenomena. These modify the geometry of the porosity

network, increase its tortuosity, and reduce its permeability, thereby affecting mass transfer at the interface between the bulk solution and the original mineral phase and hinder physicochemical re-equilibration.

Porosity characteristics are different for the different microstructures investigated in this study (Fig. 2.64). Primary porosities are present in the shell of *A. islandica* and in the prismatic shell layer of *H. ovina*. Although the skeleton of the coral *Porites* sp. is compact, the coral skeleton has a particularly high surface area, as the skeleton consists of various combinations of vertical and transverse elements, with most of these being developed as thin lamellae. Mineral units which comprise these skeletal elements consist of irregularly organised clusters of closely packed aragonitic needles. The centres of calcification are the primary pores in the skeleton of *Porites* sp. However, these are in general not interconnected, and thus, do not facilitate transfer of solutes towards and away from the reaction front to a large extent. Stacks of calcite fibres in *M. edulis* and the nacreous tablet arrangements in *M. edulis* and *H. ovina* are the most compact microstructures investigated in this study. These materials lack primary porosities. Nonetheless, when the shells are altered, the extent of alteration-induced secondary porosity is high in nacreous shell portions, as the occluded intra-tablet membranes and inter-tablet fibrils decompose and leave space behind for extensive fluid circulation.

The effect of microstructure – intermediate stages

A still unsolved problem in palaeoenvironmental reconstruction is the assessment of the extent of diagenetic overprint that compromises the fidelity of geochemical proxies. One strategy is to use numerical approaches for the quantification of the extent of diagenetic alteration. These are based either (i) on the comparison of element to Ca ratios and associated partition coefficients or (ii) the comparison between isotope compositions of the pore fluid and that of the precipitate (Regenberg et al., 2007, and references therein). In a previous study (Casella et al., 2017), we reported experimental data for *A. islandica* shell material for the replacement reaction of biogenic aragonite by inorganic calcite. In the present study, we extend our previous work with the investigation of additional carbonate skeletons, and thus, other mineral fabrics. One of the major goals of this study is the reliable identification of the first stages of alteration and the attempt to qualitatively assess diagenetic alteration based on microstructural reorganisation.

For these targets, we apply statistical grain-area evaluation and develop this approach as a qualitative tool for the detection of incipient to moderate diagenetic overprint. Figures 2.75 and 2.91 show relative frequency to grain-area (area of mineral units in the case of biological hard tissues) diagrams for the pristine and the most altered (alteration for 35 days, at 175 °C, in Mg-rich fluid) skeleton equivalents. Grain-area data are obtained from EBSD measurements. A grain is defined as a region that is completely

bounded by boundaries that have a misorientation angle larger than a critical value, the critical misorientation value. Griesshaber et al. (2013) empirically determined that a critical misorientation value of 2 ° suits best the microstructure of modern carbonate biological hard tissues. By using this value we differentiate between individual mineral units (e.g., fibres, tablets, prisms, columns).

The compilation in Fig. 2.75 clearly demonstrates the influence of the biogenic microstructure on the ability to withstand or to yield to alteration. The relation of log (frequency) vs. log (grain area) is linear for *A. islandica*, *M. edulis* calcite and *Porites* sp. aragonite, and is a clear indication of the fractal distribution in the microstructures of these skeletons.

The least difference in grain areas between pristine and most altered states was observed for *A. islandica* aragonite (Fig. 2.75A), while the most significant difference we found for *M. edulis* fibrous calcite (Fig. 2.75E). For *Porites* sp. acicular aragonite and *H. ovina* prismatic and nacreous aragonite we find a perceivable, but small difference in grain area between the pristine and the most altered states. For *M. edulis* nacre the majority of grain-area data overlap. Even though, for this type of microstructure as well some large grains also formed in the altered shell (Fig. 2.91).

As described previously, subsequent to the destruction of organic sheaths, membranes, and fibrils, the amalgamation of mineral units is the next and a highly drastic step in the overprint process. Inorganic mineral precipitation starts in cavities between the mineral units and in voids within them (e.g., Figs. 2.70, 2.92; Casella et al., 2018a, 2018b). It is important to note that this void filling occurs prior to carbonate phase replacement, and thus, prior to inorganic calcite formation. With EBSD we not only measure patterns of crystal orientation but determine the mineralogical phase of the hard tissue as well. At this early stage of alteration the newly formed crystallites that are deposited between the mineral units retain the phase of the host crystal and often even the crystallographic information of the mineral in the pristine skeleton. Thus, in aragonitic biogenic microstructures, inorganic aragonite will precipitate, while in calcitic biogenic microstructures inorganic calcite will form. Syntactic nucleation of a secondary phase that has the same mineralogical nature as the primary phase is prompted by the reduction of the energy barrier associated with heterogeneous nucleation in contrast to homogenous nucleation from a bulk aqueous solution. This barrier is reduced even further as a result of a perfect match between the crystal lattice of the original and the secondary phase. The reduction in the energy barrier explains the preference of inorganic aragonite formation on biogenic aragonite at the first stages of the alteration process, rather than the crystallisation of the more stable inorganic calcite.
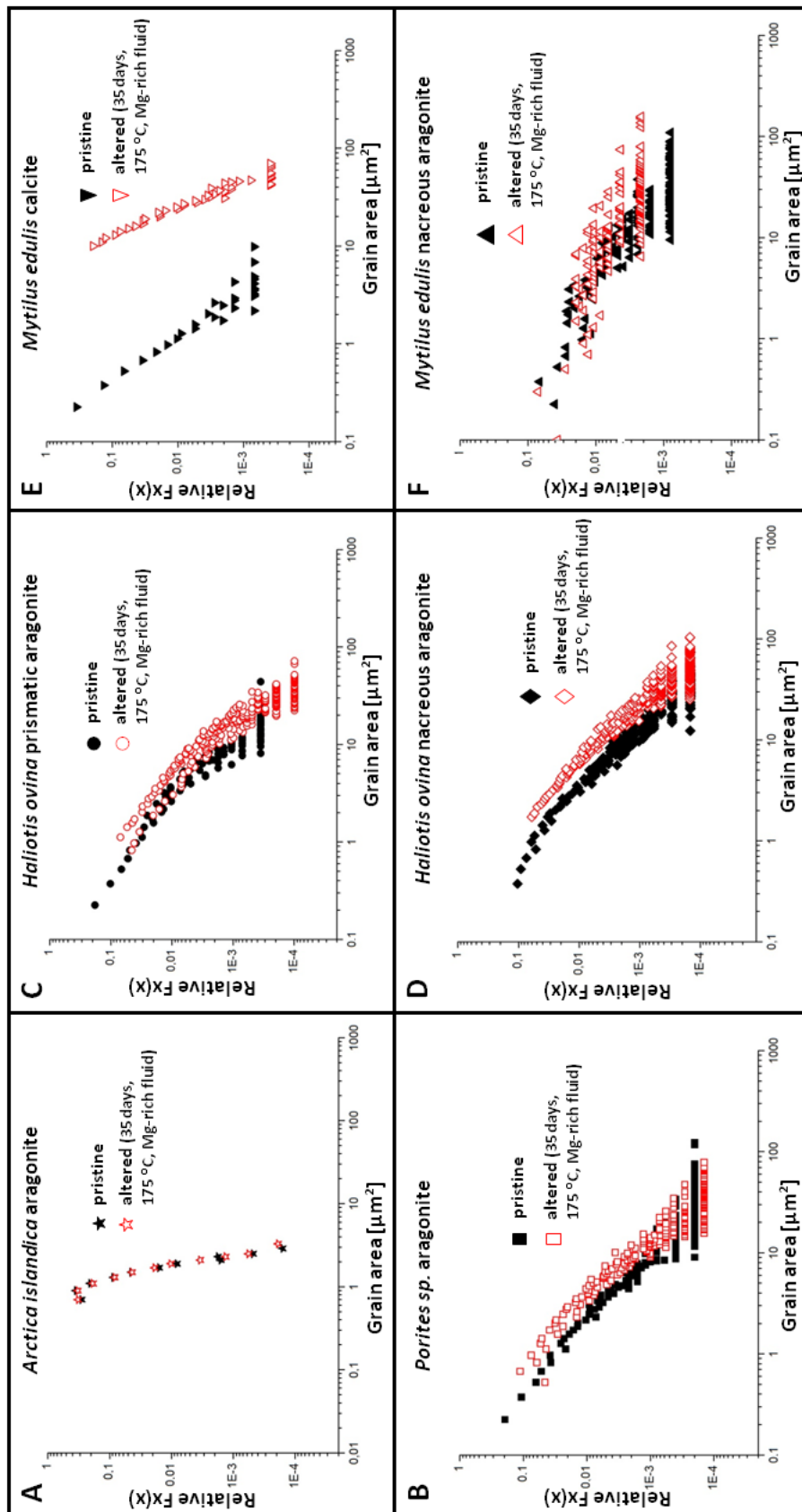
Figure 2.75: Relative frequency *vs.* grain area diagrams for pristine (black) and most altered (red: 35 days, 175 °C, Mg-rich fluid) stages. (A): *Arctica islandica*, (B): *Porites* sp., (C, D): *Haliotis ovina*, (E, F): *Mytilus edulis*. Mineral grain area increases with progressive hydrothermal alteration. The least difference in mineral grain area between pristine and the most altered stages is present for the microstructure which forms the shell of *A. islandica* (A), while the most significant difference can be observed for *M. edulis* (E) calcite. For all other investigated microstructures (B, C, D and F) mineral grain area increases with alteration prior to inorganic calcite formation.

However, due to its composite nature, biogenic aragonite is more soluble than inorganic aragonite and even more soluble than inorganic calcite. Thus, an aqueous solution in equilibrium with biogenic aragonite is supersaturated with respect to both: inorganic aragonite and inorganic calcite. As aragonite nucleation on existing biological aragonite can be epitactic, the much better match across the interface makes it more likely that inorganic aragonite is formed on the pre-existing biogenic aragonite, even though calcite is the more stable phase at Earth's surface pressure and temperature conditions. Free energies and solubilities of the two carbonate phases are close enough that the lower energy barrier associated with epitactic nucleation kinetically favours the formation of new aragonite on the surface of the pre-existing aragonite (Fernández-Díaz et al., 2009; Roncal-Herrero et al., 2017; Cuesta Mayorga et al., 2018). This feature also has been observed in nature. Hover et al. (2001) report early diagenetic overprint of foraminifera and green algae skeletal hard tissues and demonstrate that the overprint mechanism is the coupled process of dissolution and reprecipitation. The authors find thin overgrowths on the mineral units of the original hard tissues and show that the precipitated material is largely similar in composition and structure to that of the host crystallites. Accordingly, aspect ratios of the mineral units change as their original morphologies become distorted (Figs. 2.70, 2.83, 2.92), and compaction of the hard tissue is the result (e.g., nacre tablets). Hence, even though already altered, the gross microstructure of the shell or skeleton is, at this early stage of alteration, not modified to a large degree. We observe that alteration occurs in two stages: (1) related to the original carbonate phase of the hard tissue, overgrowth of inorganic aragonite or inorganic calcite in voids and pores without major destruction of the original microstructure, and (2) phase replacement, with new phase formation and distortion of the original microstructure, up to its complete destruction. These processes involve the constant rearrangement of pores, which in this case is driven by the free energy reduction associated with the increase in the volume to surface ratio of the mineral units.

We observed the above described features for all investigated microstructures (Fig. 2.75B to F) except for the aragonitic microstructure of the shell of the bivalve *A. islandica* (Fig. 2.75A). Aragonitic grains in *A. islandica* shell are small and are embedded in a network of biopolymer fibrils (Casella et al., 2017). The thin fibrils are easily destroyed when altered and leave behind a network of voids and cavities, which facilitate fluid infiltration and permeation through the shell. In addition, the large number of small mineral units gives rise to exceedingly large surface areas where the fluid can get into contact with the mineral. Carbonate phase alteration kinetics in *A. islandica* shell is sluggish at first. However, once the nucleation barrier is overcome and the alteration process is started, it proceeds instantly (Figs. 2.65A, 2.79A; Casella et al., 2017). Thus, overgrowth of inorganic aragonite in voids and mineral unit amalgamation are masked by the rapid replacement of biogenic aragonite by inorganic calcite. The high

volume of interconnected porosity and the presence of the thermodynamically less stable biogenic aragonite explain why alteration in A. islandica becomes active after such a short time when being in contact with the diagenetic fluids. The topological characteristics of porosity facilitates the coupling between the rate of aragonite dissolution and the rate of calcite reprecipitation. This, in turn, explains the minor difference in mineral unit and grain area found in the hard tissue of *A. islandica* between the pristine and the most altered states (Fig. 2.75A).

In contrast, *M. edulis* calcite shows the most significant difference in grain area between the pristine and the most overprinted states (Fig. 2.75E). When altered, the morphology of calcite fibres becomes distorted (Fig. 2.83A) and fibre amalgamation is substantial leading to the formation of large and highly irregularly shaped mineral units (Fig. 2.83B). In the pristine state, calcite co-orientation strength is high in *M. edulis*, we find a single-crystal-like distribution of c^*- and a^*-axes (Figs. 6 and 7 in Schmahl et al., 2012). Hence, many neighbouring calcite fibres are highly co-aligned, a circumstance that favours the amalgamation of similarly oriented fibres (Fig. 2.83B). The nacreous shell layer in *M. edulis* is little affected by alteration (Figs. 2.75F, 2.91A, B), even though nacre tablet amalgamation is readily perceivable. The nacreous shell part grows to a compact entity and becomes sealed and protected against fluid infiltration. This explains the observation of remnants of pieces of nacreous shell surrounded by calcite (Brand, 1994) as well as the prevalence of the nacreous shell part of *M. edulis* relative to calcitic shell pieces in seashore sediments.

Nacre in *H. ovina* behaves slightly differently when hydrothermally altered (Figs. 2.75D, 2.91A, C). In *H. ovina*, nacre tablets are assembled to columns and tablet dimensions are smaller than those present in *M. edulis*. In both shells, that of *M. edulis* and of *H. ovina*, nacre tablets are encased by organic sheaths (Addadi et al., 2006; Checa et al., 2006, 2009, 2011; Barthelat and Espinosa, 2007). Compared to *M. edulis* nacre, nacre in *H. ovina* has a larger organic-mineral interface and mineral surface area per volume fraction of shell. Nacreous tablet amalgamation and compaction occurs in the shell of *H. ovina* as well. In contrast to *M. edulis*, *H. ovina* nacre exhibits a distinct increase in grain size in the altered hard tissue. Due to the larger interface and surface area in *H. ovina* nacre alteration fluids infiltrate the shell more intensely, and dissolution-reprecipitation occurs to a higher extent. Hence, overprint is more significant and becomes more evident. The same argument holds for prismatic aragonite found in *H. ovina* (Fig. 2.75C) and acicular aragonite in *Porites* sp. (Fig. 2.75B), where, in both examples, prior to replacement of biogenic aragonite by inorganic calcite, mineral units increase in size in the altered skeleton. It is important to note that the mineral unit size increase is accompanied in *H. ovina* and *Porites* sp. by partial closure of the porosity, as the newly formed calcite is completely devoid of pores (Figs. 2.71, 2.73, 2.74, 2.80B, 2.85B). The

partial closure of pores explains the low degrees of replacement that we find in these hard tissues even after long alteration periods (Fig. 2.65).

Our study clearly shows that, of the investigated aragonitic microstructures, nacre is the most resistant to replacement with calcite, irrespective of the assembly pattern of the tablets to columns or sheets. Porosity closure and mineral unit (nacre tablet) amalgamation at first completely recasts the original microstructure – however, they preserve the original phase (Figs. 2.72A, 2.92A, B). Hence, even though nacreous aragonite is still present in the shell as aragonite, it is an overprinted aragonite that holds little of the original microstructural or geochemical signature. With an increasing degree of alteration, the "remoulded" aragonite becomes replaced by inorganic calcite. The outcome of our alteration experiments leads to the conclusion that the microstructural signature is lost first (prior to a complete loss of the original mineralogical phase) while the geochemical information is still retained in the mineral, at least to some degree. When alteration takes place in a Mg-rich fluid, metastable high-Mg carbonates are present at the original-material – newly formed product interface, in addition to the "final" inorganic, low-Mg calcite. These high-Mg carbonates have a calcite-type structure and Mg-contents ranging from dolomitic to about 80 mol% magnesite (Figs. 2.72A, 2.74). We clearly see an evolution in fluid composition at the alteration front due to an evolution in cation- anion exchange between the alteration fluid, the overprinted original, and the newly formed carbonate products.

Implications for preservation in the fossil record

Several studies have shown that in modern cold and warm water environments aragonite dissolution takes place during burial diagenesis (e.g., Cherns et al., 2008, and references therein). It has been further demonstrated that, in Palaeozoic marine fossil faunae, the taxa with calcitic skeletons prevail. This is an indication of preferential loss of aragonitic shells and skeletons due to dissolution during diagenetic overprint (e.g., Wright et al., 2003; James et al., 2005). In addition to preferential carbonate phase preservation, experimental studies document that the microstructure of the biogenic skeleton influences fossil preservation (e.g., Harper, 1998; Kidwell, 2005), leading to a possibly distorted notion of palaeoecological and evolutionary patterns. Accordingly, laboratory-based hydrothermal alteration experiments accounting for microstructural as well as mineral phase variability offer important insights into the fate of carbonate hard tissues (i) during early dissolution in shallow burial, and (ii) surviving dissolution and preservation in the fossil record.

Do we see resemblances between the microstructural and chemical outcome of our alteration results and microstructural and geochemical features of fossilised hard tissues? It is remarkable that, even though our experiments lasted for only 35 days, were

carried out at a single temperature, and were performed in the presence of only one type of alteration fluid, there is much overlap between our experimental products and carbonates which underwent diagenesis. Several decades ago Friedman (1964) and Land (1967) reported on the early diagenesis of skeletal carbonates and carbonate sediments exposed to marine waters. The biological carbonates retained their original mineralogical and textural characteristics. They found that biogenic aragonite was dissolved for the reprecipitation of low-Mg calcite, with high-Mg calcite being an intermediate phase. Mg was removed from high-Mg calcite to yield low-Mg calcite, and, on a micrometre scale, without any textural change (Friedman, 1964). Land (1967) observed that skeletal aragonite was altered much quicker relative to non-skeletal aragonite grains. Brand (1989) investigated the replacement of biogenic aragonite by calcite in fossil molluscs (Boggy Formation, Oklahoma, U.S.A.). Screening of the mineralogy, microstructure, and chemical composition indicated that primary nautiloid aragonite was gradually replaced by diagenetic low-Mg calcite. During the initial stages of alteration, nacreous tablets fused to larger units (Brand, 1989). With further alteration, amalgamated nacreous aragonite was replaced by fine- or coarse-grained, low-Mg calcite. Brand (1989) noted that the composition of the original aragonite determined the elemental and isotopic composition of the calcite in the diagenetically altered shells. Furthermore, the author reported that grain size and surface area play an important role in the process of overprinting. Diagenetically overprinted aragonitic corals were investigated by Sorauf (1980), and Tomiak et al. (2016). The authors observed that during early diagenesis, subsequent to decomposition of organic matrices, aragonitic units formed through fusion of pristine skeletal elements. Pore space became filled prior to burial, with aragonite needles growing syntaxially on existing biogenic aragonite. Subsequent submarine diagenesis led to recrystallisation of fibrous aragonite into intermediate, micritic high-Mg calcite. Tomiak et al. (2016) and Regenberg et al. (2007) observed formation of new mineral overgrowth during early diagenesis of coral aragonite and planktonic foraminifera calcite. The latter, at first, retained and corresponded to the carbonate phase of the original pristine skeleton. Wardlaw et al. (1978), Sandberg and Hudson (1983), and Martin et al. (1986) described the influence of skeletal porosity as conduits for alteration fluids during diagenesis. As the replacement of aragonite by calcite is driven by the greater solubility of aragonite relative to that of calcite, during the replacement reaction the diagenetic pore fluid is undersaturated with respect to aragonite, while it is supersaturated with respect to calcite (Maliva et al., 2000). Hendry et al. (1995) proposed, on the basis of differences in degrees of supersaturation, a "two-water diagenetic system" with a slow moving (at the dissolution-reprecipitation front) and a relatively fast moving (bulk pore water) alteration fluid.

In our experiments we detected the following major steps and pathways of alteration: (i) decomposition of biopolymers, (ii) secondary porosity formation on

nanometre and micrometre scale levels, (iii) amalgamation of mineral units, (iv) destruction of the original microstructure with subsequent carbonate phase change, and (iv) chemical evolution of the alteration fluid. These stages were also observed in nature. Our experiments, which lasted only for 35 days in comparison to geologic time scales, create the constraint that major and drastic steps of alteration take place at the very initial stages of the overprint process.

Finally, we restate our major question: what determines the preservation potential of a fossil archive? A major factor is the availability of porosity on all scale levels for fluid circulation. This enables a well balanced dissolution- reprecipitation to take place. The result is nucleation and epitactic growth of the original phase in voids and cavities at the sites of degraded biopolymers, leading to amalgamation of mineral units. The final result is the compaction of the entire hard tissue and protection from disintegration.

2.4.6 Conclusions

For an evaluation of the resistance of biogenic carbonate for withstanding diagenetic alteration, and an assessment of the ability of the biocarbonate microstructure to become preserved in the fossil record, we investigated the behaviour of six biogenic carbonate hard tissues during experimental hydrothermal alteration. Our main conclusions are as follows:

1. alteration of biogenic aragonite into inorganic calcite starts along pathways where fluids can penetrate the mineralised tissue. It is fastest in hard tissues which contain primary porosity and are composed of irregularly shaped mineral units embedded in a network of biopolymer fibrils. The latter are easily destroyed providing secondary porosity, and together with the primary pores, ample space is provided for extensive fluid infiltration into, and percolation through, the hard tissue. Moreover, porosity is created at the transition front. This mode of overprint is observed for the prismatic aragonite shell layer of the gastropod *Haliotis ovina* and for the shell of the bivalve *Arctica islandica*. Overprinting of these hard tissues is fast and is completed with the formation of irregularly shaped and randomly oriented calcite crystals.

2. The slowest alteration kinetics can be observed when biogenic nacreous aragonite is replaced by inorganic calcite, irrespective of the mode of assembly of the nacre tablets. Alteration proceeds through at least four intermediate stages: (a) decomposition of biopolymers and formation of secondary porosity; (b) lateral and longitudinal amalgamation of nacre tablets; (c) formation of a compact zone of amalgamated aragonite crystals at the alteration front, where the original nacreous

microstructure is destroyed but the original mineralogical phase is kept; and (d) complete replacement of the original microstructure and the mineralogical phase by the newly formed mineral product: inorganic calcite. This mode of overprint is observed in the nacreous shell portions of *Haliotis ovina* and *Mytilus edulis*.

3. The acicular microstructure of the stony coral *Porites* sp. is highly resistant to alteration. When altered, aragonite needles amalgamate and form a cemented compact unit; however, they retain at first some morphological aspects of the original hard tissue. Replacement of biogenic aragonite by inorganic calcite starts in *Porites* sp. at centres of calcification within the coral skeleton, and proceeds from the latter into the hard tissue.

4. For all investigated aragonitic hard tissues we first observe the destruction of the microstructure and subsequently the replacement of the original aragonitic phase by newly formed calcite.

5. Alteration in the Mg-bearing fluid results in the development of a seam of high-Mg calcite between the altered, reworked aragonite and the newly formed calcite. Metastable Mg-rich calcite phases form with Mg contents that vary between dolomitic to about 80 mole% magnesite. This high-Mg calcite seam migrates with the alteration and phase transformation front.

6. Differences in grain-area statistics in EBSD maps of pristine and altered skeletal equivalents demonstrates an increase in grain size of the originally biogenic carbonate phase within the altered hard tissues relative to that found in the pristine skeleton. Even though at early stages of alteration the original phase is retained, overprinting has already started with amalgamation of neighbouring crystals and formation of overgrowths. This is most pronounced in the calcitic shell layer of *Mytilus edulis* and is least observable for the grains which constitute the shell of *Arctica islandica*.

7. Due to formation of overgrowths, preservation of the original phase is not a reliable indicator for original elemental and isotope signals.

2.4.7 Acknowledgements

2.4.8 Author contributions

LAC, EG and WWS designed the study. VM, EMH, DJJ and AE provided sample material. LAC, VM, MG, SVV and SH performed the experiments. LAC, MG and SVV conducted the analyses and carried out the evaluation and merging of data. LAC, EG, LFD, UB and WWS drafted the manuscript. All authors contributed to discussions and the final manuscript.

2.4.9 Appendix
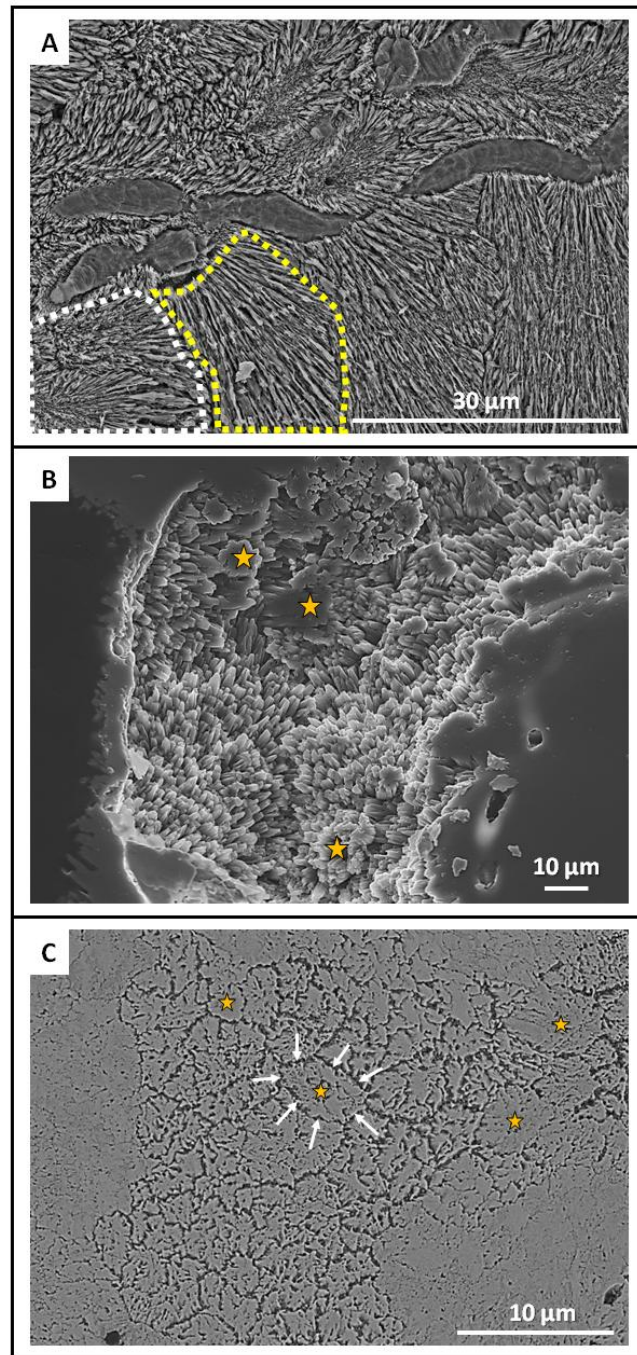
Figure 2.76: SEM micrographs showing the acicular microstructure of the modern scleractinian coral *Porites* sp. (A), differently sized and oriented spherulites constitute the skeleton of *Porites* sp. When fractured in 2-D, differently oriented individual mineral units consisting of diverging aragonite needles emerge (encircled with white and yellow dashed lines in A). (B) Fracture surface image with top view onto bundles of aragonite needles. When needles show some co-alignment, subunits with a closer packing of aragonite needles develop (yellow stars in B). On flat, 2-D surfaces (C) these co-aligned needles form irregularly shaped units with roundish morphology (yellow stars in C) that are separated from each other by a multitude of cavities (e.g., white arrows in C).
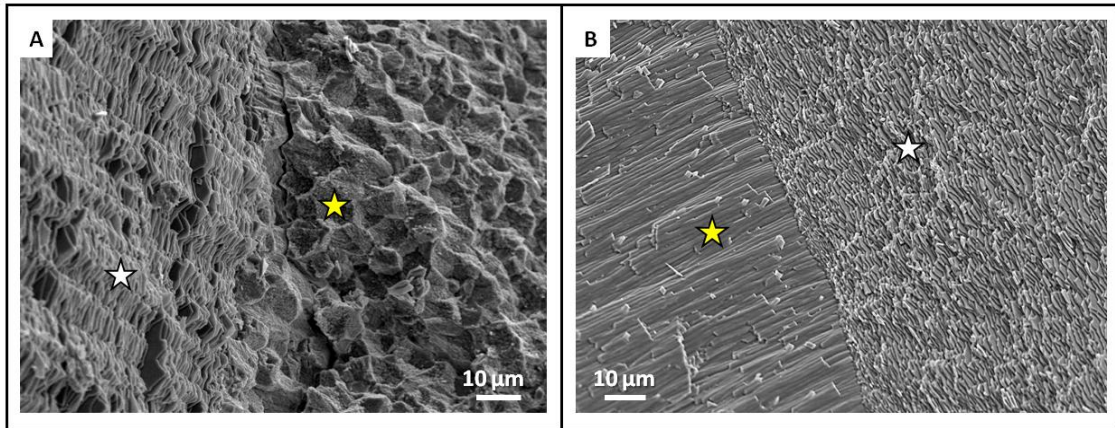
Figure 2.77: SEM micrographs of fracture surfaces showing the microstructures of modern shells of (A) the gastropod *Haliotis ovina*, and (B) the bivalve *Mytilus edulis*. White stars in (A) and (B) indicate the columnar and brick-and-mortar nacre in *H. ovina* and *M. edulis*, respectively, whereas yellow stars in (A) and (B) point to aragonitic prisms in *H. ovina* and calcite fibres in *M. edulis*, respectively.

Figure 2.78: Schematic time line illustrating hydrothermal alteration times. (A) *Arctica islandica*, (B) *Haliotis ovina*, (C) *Mytilus edulis*, and (D) *Porites* sp.. Alteration time varied between one and 35 days.
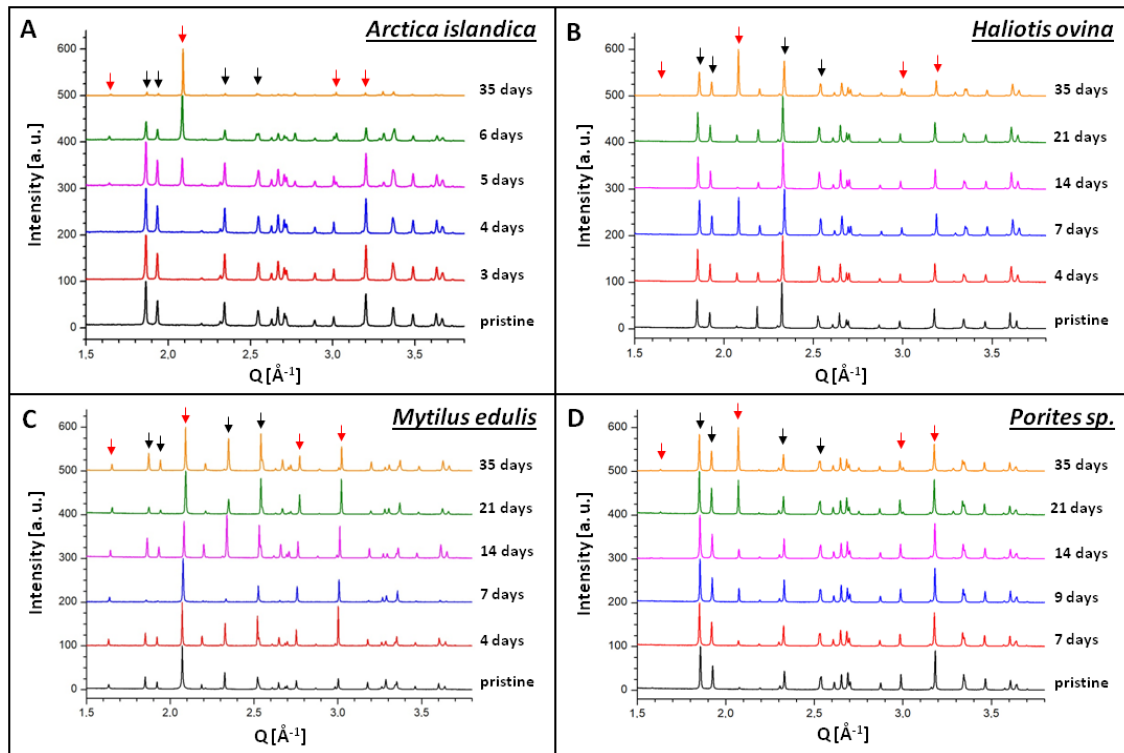
Figure 2.79: Selected X-ray diffractograms for pristine and hydrothermally altered (A) *Arctica islandica*, (B) *Haliotis ovina*, (C) *Mytilus edulis*, and (D) *Porites* sp. specimens (red arrows: calcite, black arrows: aragonite). Alteration was performed at 175 °C in a Mg-rich fluid simulating burial alteration (100 mM NaCl + 10 mM $MgCl_2$ aqueous solution) and was carried out in a time range between one and 35 days.
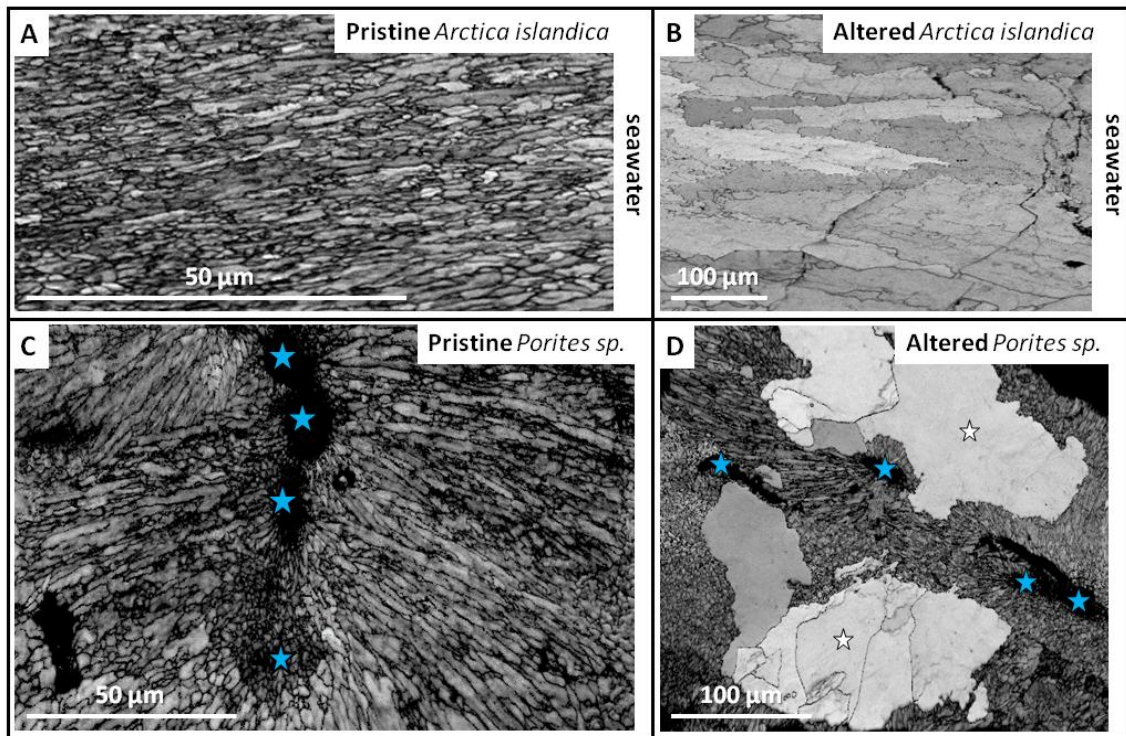
Figure 2.80: EBSD band contrast measurements illustrating the difference in microstructure between the pristine and the most altered (A, B) *Arctica islandica* shells, and (C, D) *Porites* sp. skeletons. Hydrothermal alteration lasted for 35 days and was carried out at 175 °C in a fluid simulating burial diagenesis (100 mM NaCl + 10 mM MgCl₂ aqueous solution). (A) The microstructure of the inner shell layer of pristine *A. islandica* consists of small round to elongated aragonitic mineral units. (B) Hydrothermal alteration for 35 days induces the replacement of biogenic aragonite by inorganic calcite comprising large calcite crystals. (C) Aragonite needles growing outward from centres of calcification (blue stars in C) are distinctive features of the microstructure of pristine *Porites* sp. skeletons. When altered for 35 days, large calcite crystals (white stars in D) develop and grow outward from the centres of calcification (blue stars in D). Even after 35 days of alteration, relicts of the original biogenic, acicular coral microstructure are still present and surround the newly formed calcite (D).
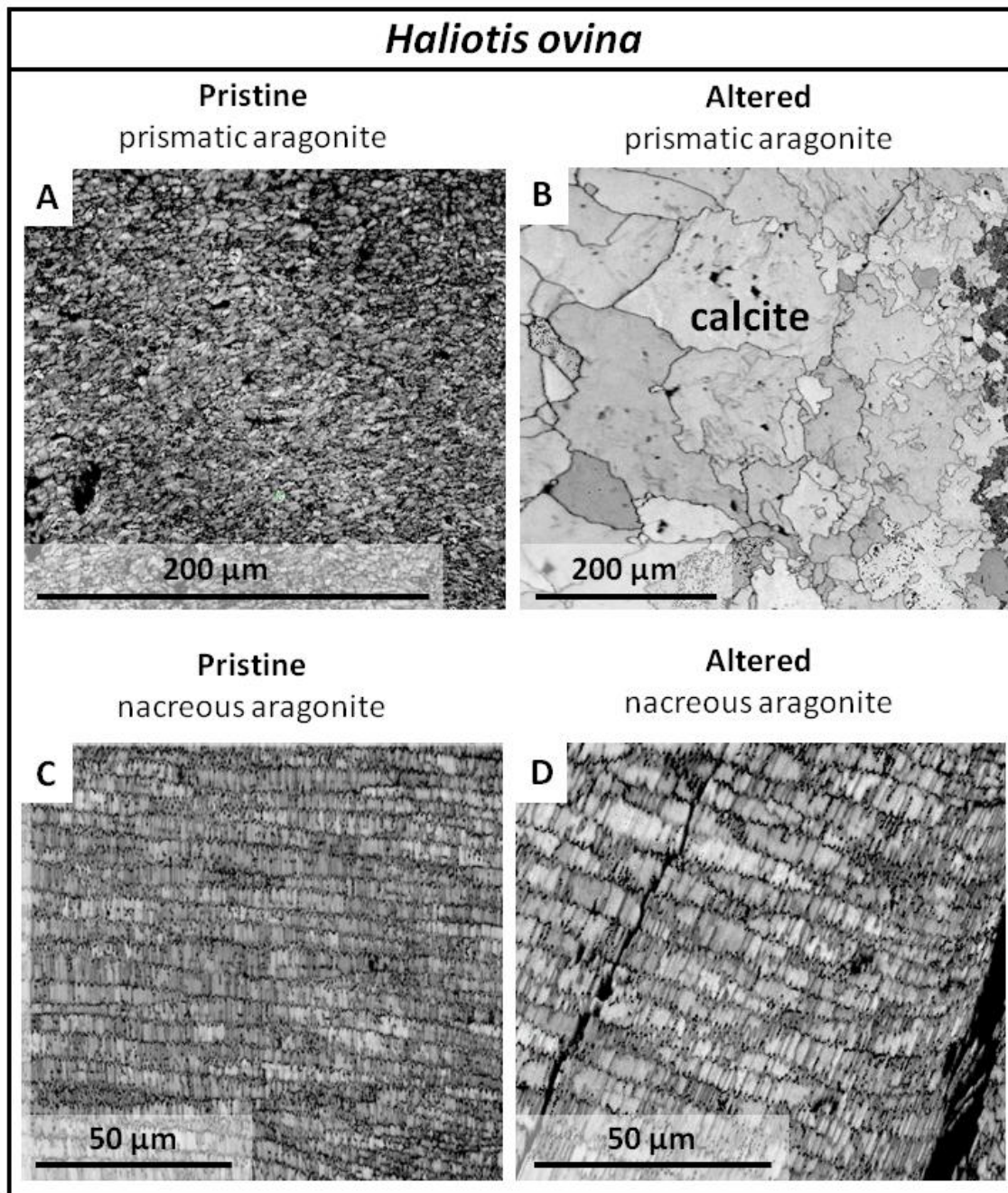
Figure 2.81: EBSD band contrast measurements illustrating the difference in microstructure between pristine and hydrothermally altered shells of the gastropod *Haliotis ovina*. Alteration occurred at 175 °C in Mg-rich fluid (100 mM NaCl + 10 mM MgCl$_2$ aqueous solution) and lasted for 35 days. (A) Prismatic aragonite comprising the pristine outer shell layer. (B) After 35 days of alteration calcite crystals which increase in size towards the centre of the hydrothermally altered shell form. (C) Columnar nacre in the pristine shell, and (D) in the hydrothermally altered specimen. Nacre is highly persistent through the alteration conditions applied in our experiments. The original microstructural features are well retained, even after 35 days of alteration.
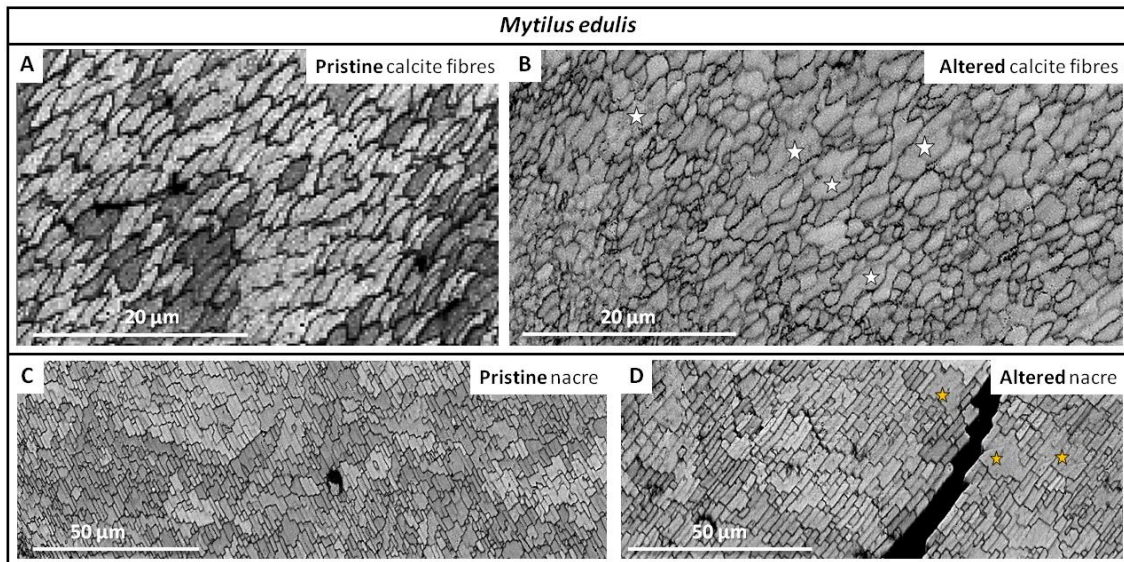
Figure 2.82: EBSD band contrast measurements illustrating the microstructures in pristine and hydrothermally altered *Mytilus edulis* shell. Alteration lasted for 35 days at 175 °C and was carried out in a fluid simulating burial diagenesis (100 mM NaCl + 10 mM MgCl$_2$ aqueous solution). (A, B) Pristine and overprinted calcite fibres. White stars in (B) point to amalgamated neighbouring calcite fibres. (C, D) Pristine and overprinted nacre tablets. The nacre is assembled in a brick-and-mortar arrangement. Even though the nacreous microstructure is very little affected by alteration, some amalgamation of nacre tablets (yellow stars in D) is perceivable in the altered sample.
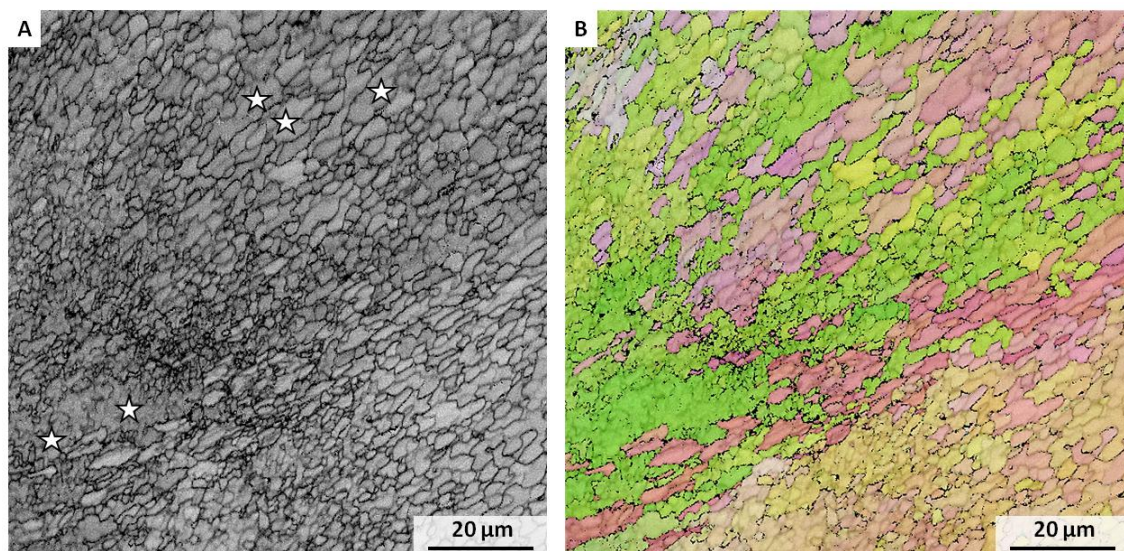
Figure 2.83: (A) EBSD band contrast and (B) colour-coded orientation maps of hydrothermally altered (35 days at 175 °C in the presence of Mg-rich burial water) *Mytilus edulis* calcite fibres. Significant distortion of fibre morphology and amalgamation into irregularly shaped and sized units can be observed (white stars in A).
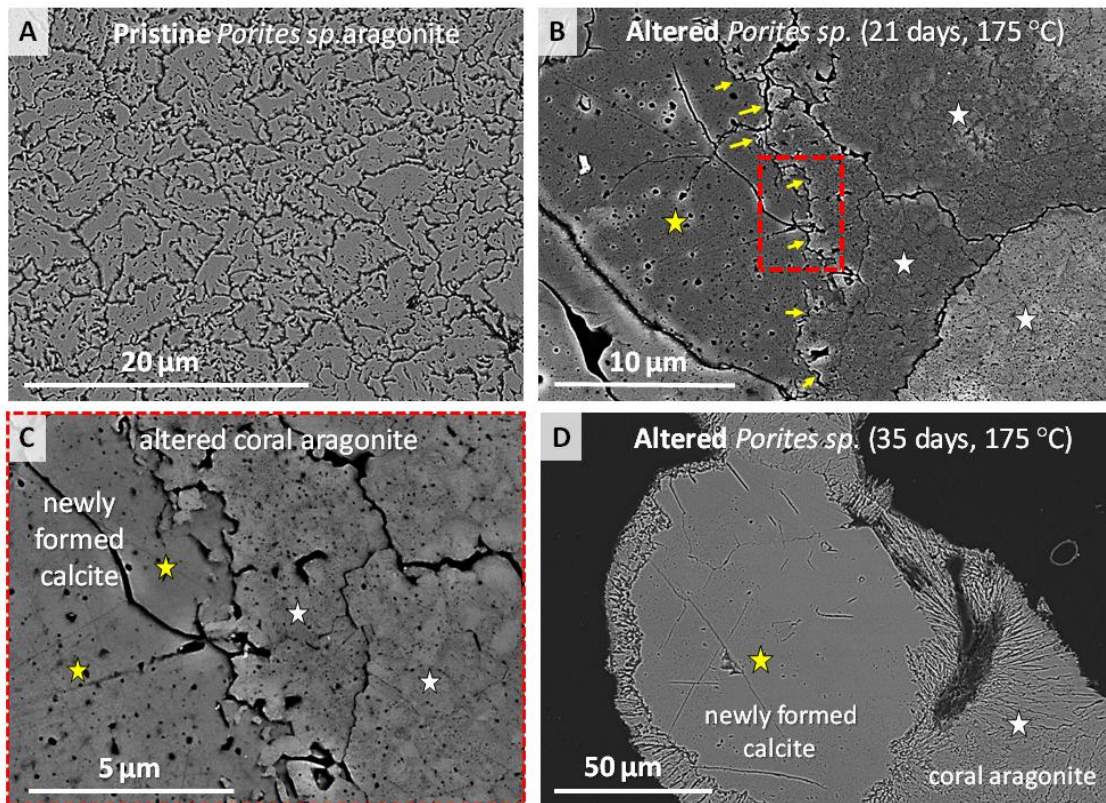
Figure 2.84: Mineral units in the pristine and altered coral skeleton. (A) SEM image of pristine *Porites* sp. showing irregularly shaped, roundish aragonite entities separated from each other by cavities. (B, C) SEM images of altered *Porites* sp.; white stars: altered aragonite; yellow stars: coral aragonite now replaced by calcite. Yellow arrows in (B) point to the aragonite-calcite border. Red dashed rectangle in (B) indicates the skeletal region which is shown with a zoom-in in (B, C). Note the amalgamation of mineral units in the overprinted, but still aragonitic skeleton. (D) *Porites* sp. skeleton altered for 35 days. Large calcite crystal (yellow star in D) extending towards the rim of the skeleton framed by coral aragonite (white star in D).
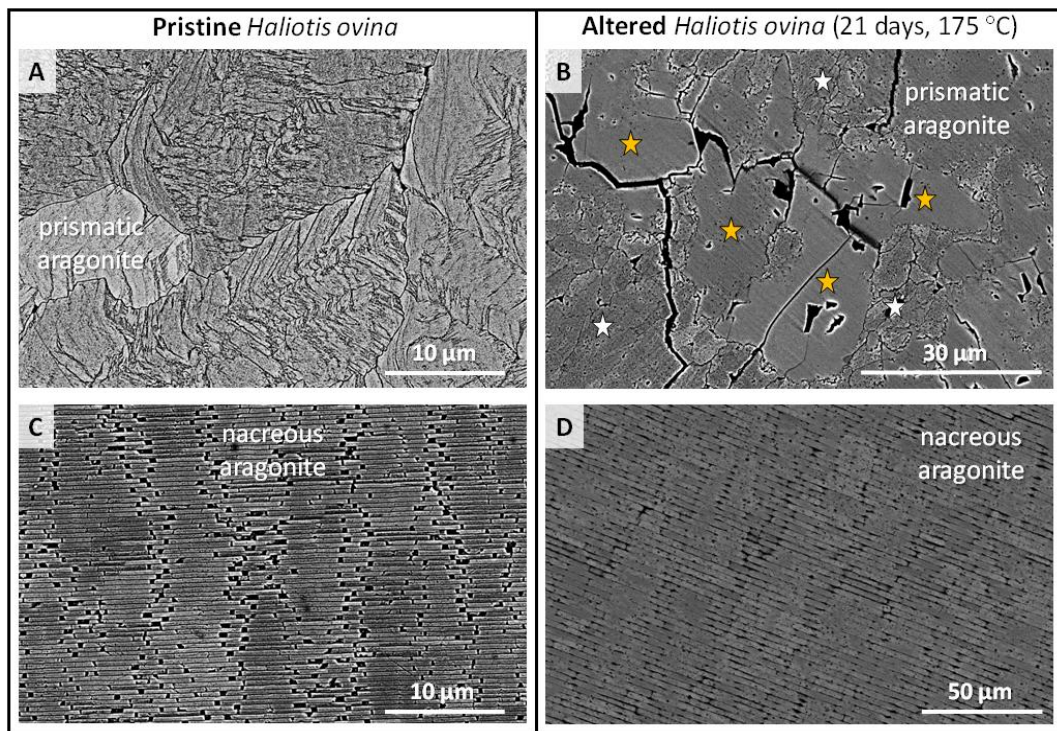
Figure 2.85: SEM images of pristine and altered *Haliotis ovina* prismatic (A, B) and nacreous (C, D) aragonite. In comparison to the pristine microstructures, amalgamation of basic mineral units is one of the major characteristics of both microstructures in the altered shell. (B) New calcite formation (yellow stars in B) is significant in the prismatic shell layer (white stars in B), while it is absent in the nacreous shell layer (D). Note the compactness of the nacreous microstructure due to tablet amalgamation in (D), as seen more clearly in Fig. 2.67D.
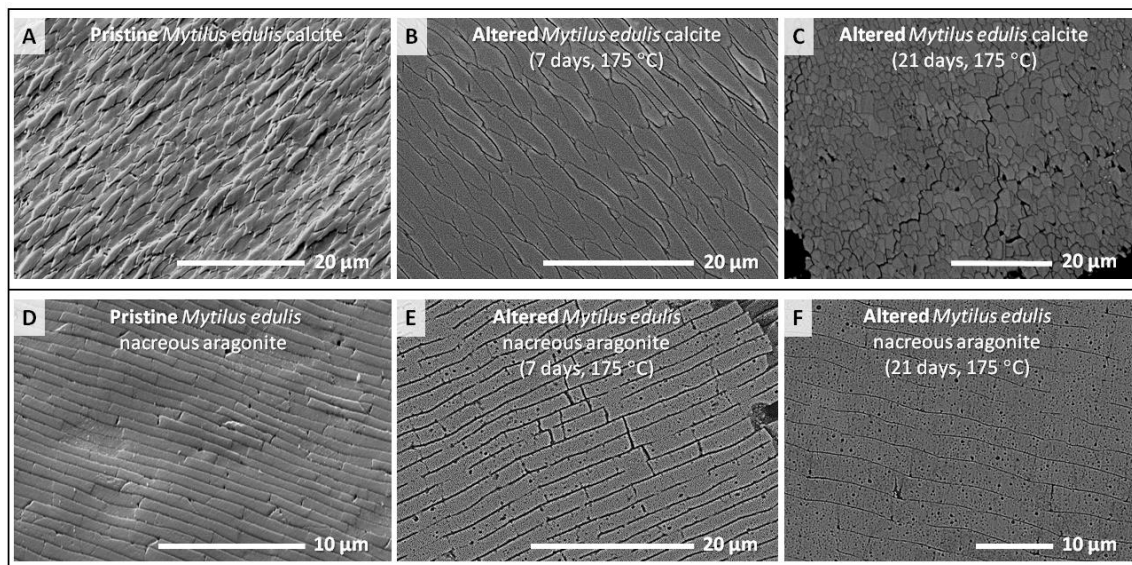
Figure 2.86: SEM images depicting microstructural characteristics of pristine and altered *Mytilus edulis* shell calcite and aragonite. (A, D) cross-sections of pristine calcite fibres (A), and nacre tablets (D). (B, C) Altered calcite fibres with the clear distortion of fibre morphology (C) after 21 days of alteration. (E, F) Nacre tablets altered for 7 and 21 days. After 7 days of alteration, the development of porosity already is evident within nacre tablets (E). This porosity increases significantly, in addition to fibre amalgamation, with progressive alteration (F).
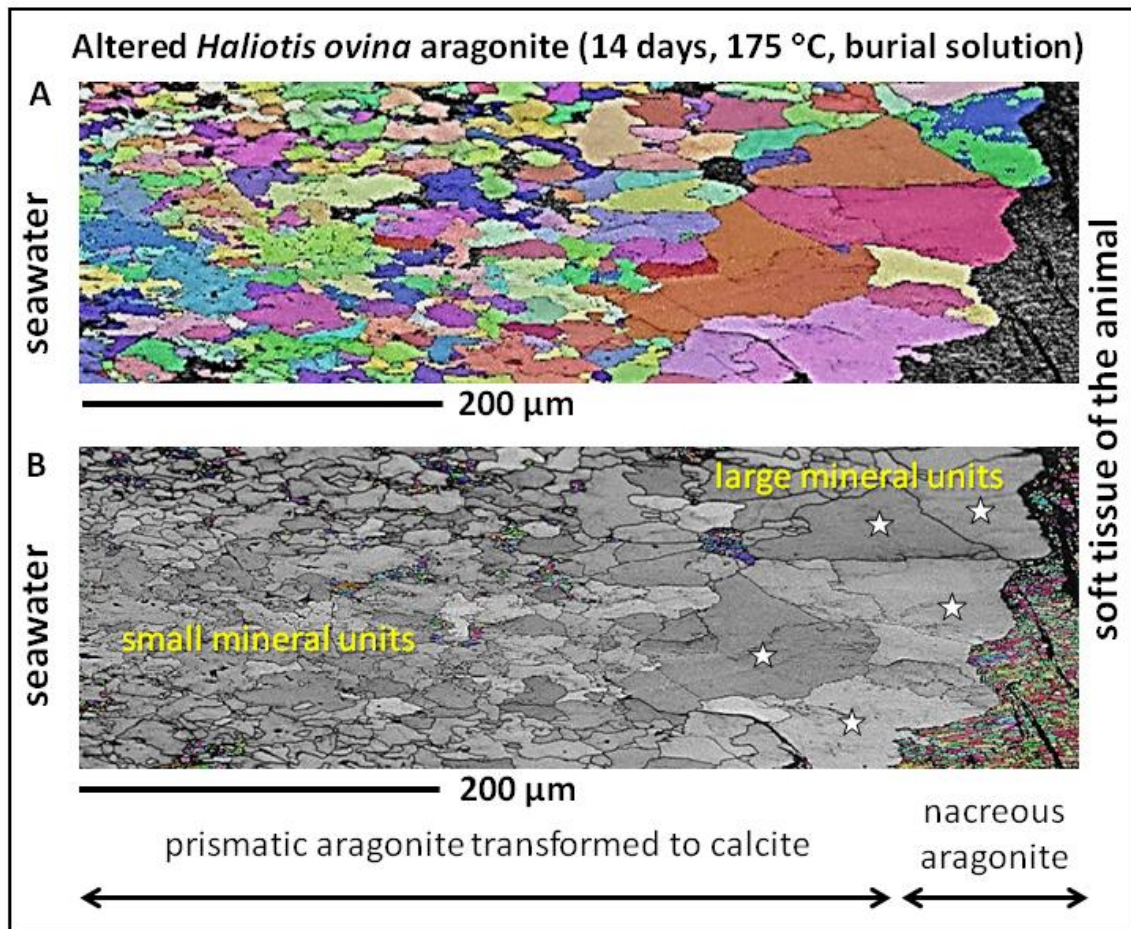
Figure 2.87: Retention of some characteristic features of the original biogenic microstructure with progressive alteration. In pristine *Haliotis ovina* there is a gradation in basic mineral unit size, such that large basic mineral units are in the central part of the shell next to the nacre (white stars in B). These decrease in size towards the outer rim of the skeleton. (A) EBSD band contrast and colour-coded orientation image showing newly formed calcite in colour and nacreous aragonite in grey. (B) EBSD band contrast and colour-coded orientation image showing newly formed calcite in grey, nacreous and prismatic aragonite in colour.
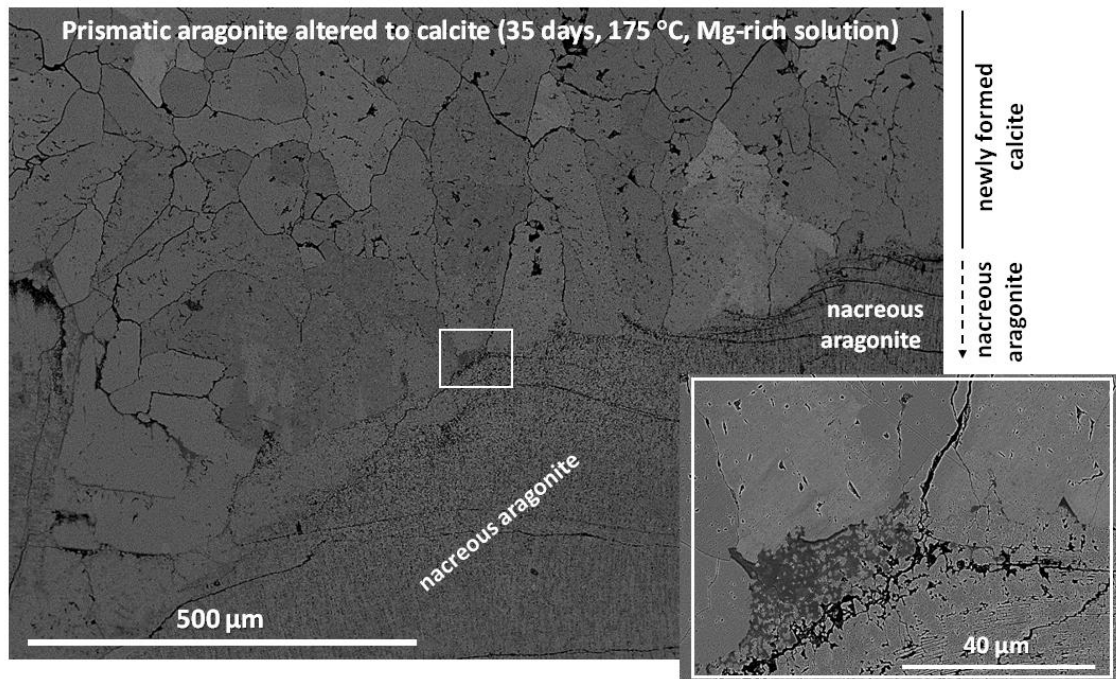
Figure 2.88: SEM image showing an overall view of a cross section through the shell of *Haliotis ovina* which was altered for 35 days at 175 °C in Mg-rich solution. The white rectangle indicates the shell area where the insert of Fig. 2.72 and Fig. 2.88 zooms into.
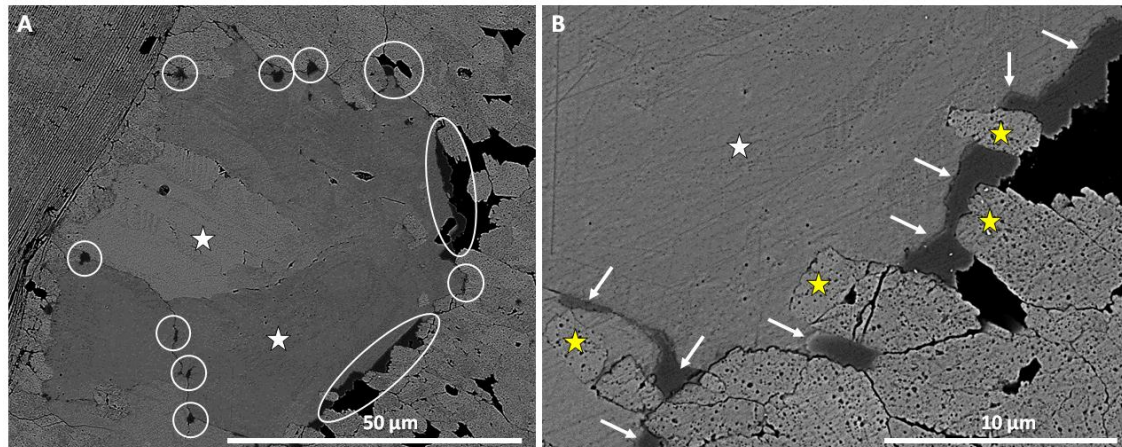
Figure 2.89: Shell segment of *Haliotis ovina* altered for 14 days at 175 °C in the presence of a Mg-rich solution. Large newly formed calcite units grow from prismatic aragonite and are present within the shell next to the nacre (white stars in A and B). These are seamed by patches of a high-Mg carbonate phase (encircled in A, indicated by white arrows in B), mainly located between the newly formed calcite and the overprinted prismatic aragonite. The newly formed calcite is framed by altered prismatic argonite, which has not yet been replaced by calcite (yellow stars in B).
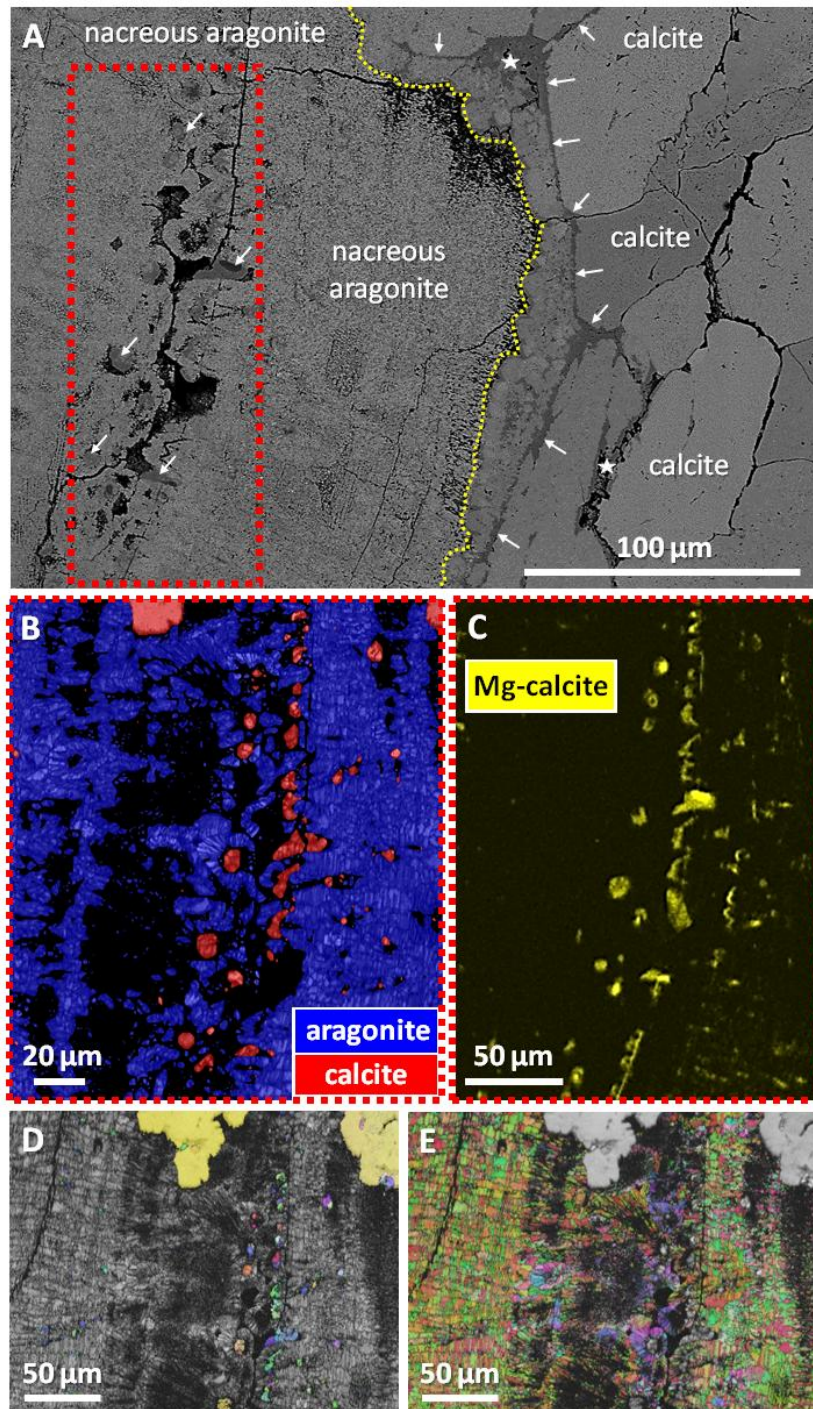
Figure 2.90: Contact between newly formed calcite and overprinted nacreous aragonite in hydrothermally altered *Haliotis ovina*. Alteration occurred for 14 days at 175 °C in the presence of a Mg-rich solution. (A) SEM image showing an overview. Accumulations of high-Mg calcite within calcite can be observed (white stars and white arrows in A) at the alteration front to nacreous aragonite (yellow dashed line in A). Red dashed rectangle in (A) indicates the shell areas shown in (B) and (C). (B) Carbonate phase determination derived from EBSD. (C) Distribution pattern of high-Mg calcite determined with EDX. (D, E) EBSD band contrast (grey scale) and orientation (in colour) maps. (D) Band contrast map giving an overview of the aragonitic microstructure (in grey) which is overlain in colour by the distribution pattern of calcite. (E) Aragonite distribution and mode of orientation in colour overlain by the distribution of calcite in grey.
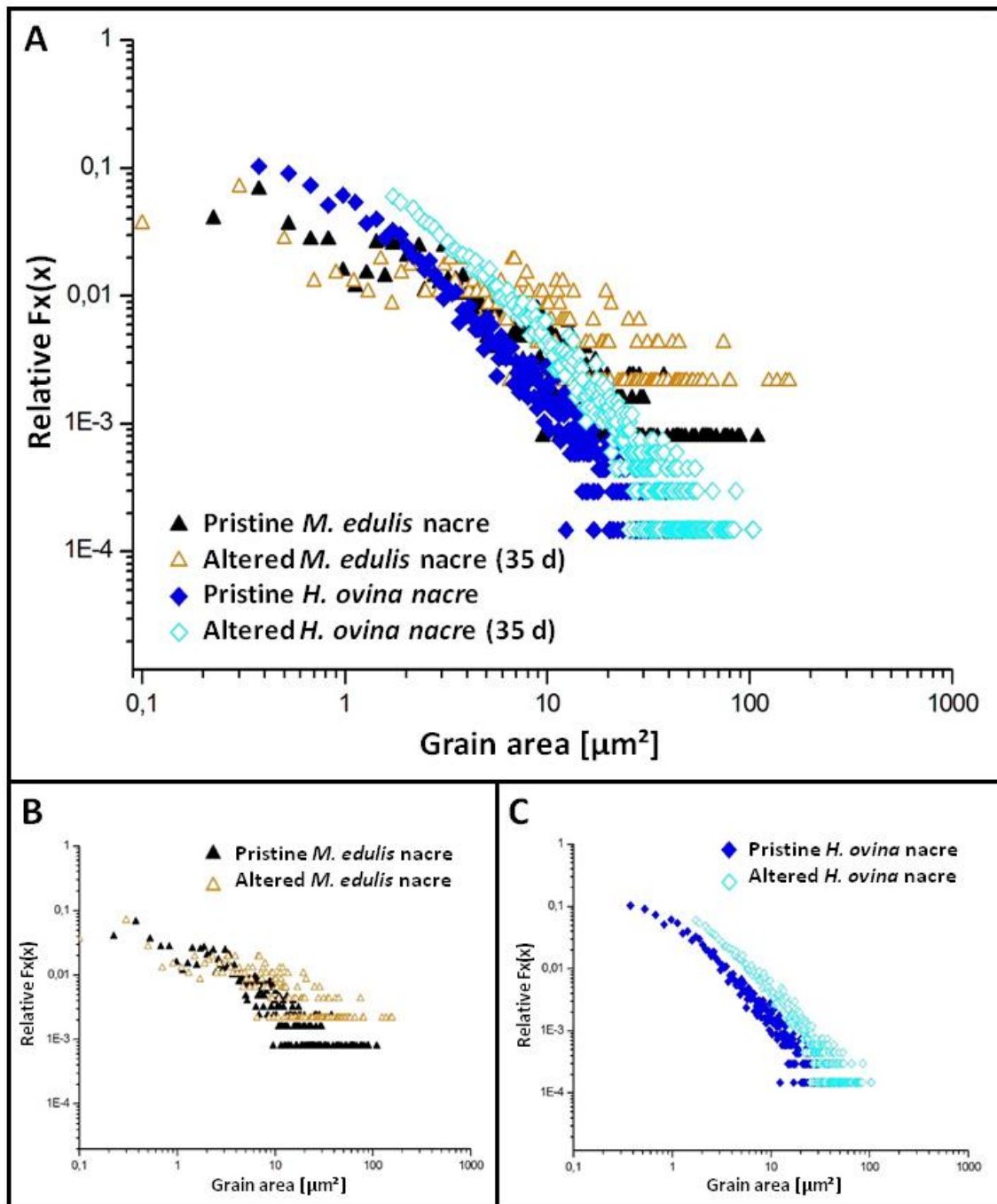
Figure 2.91: (A, B, C) Relative frequency vs. mineral grain area diagrams for pristine (filled symbols) and most altered (open symbols) *Mytilus edulis* and *Haliotis ovina* nacreous aragonite, respectively. For both nacreous structures we see basic mineral unit growth (tablet amalgamation) after performed hydrothermal alteration. This feature is most pronounced for tablet dimensions and mode of assembly in *H. ovina* nacre. Alteration occurred for 35 days in the presence of a Mg-enriched fluid at 175 °C.
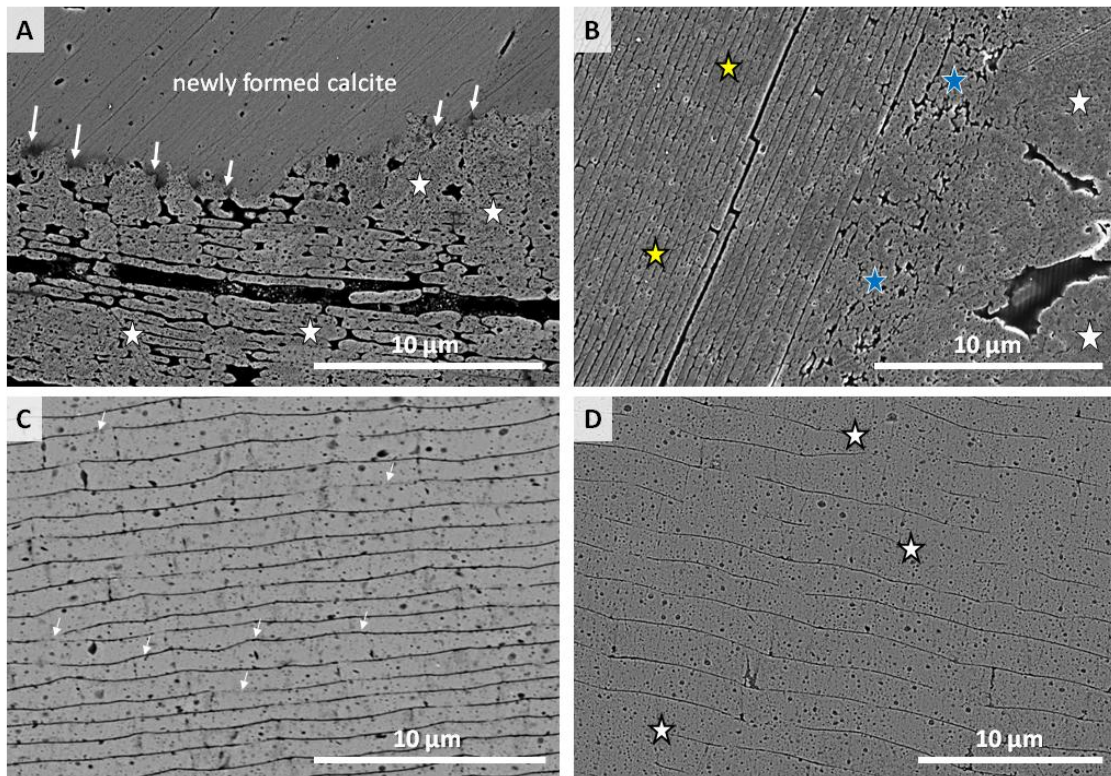
Figure 2.92: SEM images showing the distortion of the nacreous microstructure prior to phase replacement. (A, B) *Haliotis ovina* nacre, (C, D) *Mytilus edulis* nacre. White arrows in (A) point to high-Mg calcite 'spots' at the replacement front between newly formed calcite and overprinted *H. ovina* shell aragonite. White stars in (A) point to areas at the phase replacement front where traces of the original microstructure (tablets, columns) can be still observed. (B) Overprinted aragonite in three different microstructures: amalgamated nacre tablets (yellow stars), over-worked, formerly tabular aragonite (blue stars), and amalgamated aragonite prisms (white stars). (C, D) Strong tablet amalgamation in *M. edulis* (white stars in D), tablet distortion (white arrows in C), and compaction of the nacreous microstructure.

3   Concluding summary

The present dissertation covers systematic experimental studies on selected marine biocarbonate hard tissues (aragonitic and calcitic) in order to improve and extend the understanding of geochemical and physical impact of diagenetic overprint in fossil carbonate archives. Comparative studies of microstructure, texture, and mineralogy in modern pristine, hydrothermally altered, and diagenetically altered fossil materials were conducted to reach these objectives. The deployment of laboratory-based alteration experiments proved to be a useful tool to mimic diagenetic alteration processes occurring in nature and to understand diagenetic dissolution-reprecipitation reactions, as well as their impact on the preservation state of fossil material.

Investigations regarding the replacement of biogenic aragonite by inorganic calcite in mollusc shells of modern *Arctica islandica* specimens during laboratory-based hydrothermal alteration and its associated change in microstructure and texture are summarised in chapter 2.1. Results were obtained mainly from EBSD measurements. The pristine shell of *A. islandica* exhibits three zones of varying porosity, pore size, and crystallite size. Minute aragonite mineral units constituting the pristine shell are penetrated by organic fibrils and surrounded by a network of organic matter. Increased Sr contents were observed at annual growth lines in both pristine and hydrothermally altered shells. Hydrothermal treatment using simulated burial and meteoric fluids at 100 °C caused the decomposition of the majority of biopolymer matrices, as well as good preservation of the initial microstructure and mineralogy. Specimens treated hydrothermally for ≥7 days at 175 °C, however, exhibited complete decomposition of organic matter resulting in the formation of pathways for fluid penetration. In experiments carried out at 175 °C, the initially bio-aragonitic *A. islandica* shells were almost entirely replaced by inorganic calcite via dissolution-reprecipitation reactions. The usage of simulated meteoric fluid resulted in the formation of secondary calcite crystals which were much smaller in size than those observed in experiments using simulated burial fluid at identical experimental durations of 84 days. The difference in calcite grain sizes is attributed to the presence of Mg ions in the simulated burial fluid which inhibits calcite nucleation, and thus, promotes coarse grains. The presented results revealed that calcite nucleation and proceeding of replacement reactions took place at fluid-shell interfaces, i.e., at the exposed shell surfaces, in pores, and at growth lines. After a dormant time of four days newly formed calcite became detectable by powder XRD measurements, and subsequently, the replacement reaction proceeded within the following 2-3 days to almost completion. However, minor amounts of biogenic aragonite still remained after 84 days. The dormant time can be attributed to a low driving force for nucleation of inorganic calcite, albeit, future studies on the nucleation process are

necessary. The absence of bio-aragonite replacement at temperatures <175 °C contributes to explain why aragonitic or bimineralic shells and hard tissues have a good potential of preservation and therefore a complete fossil record.

Utilising a multi-analytical approach (i.e., AFM, CL, FE-SEM, and EBSD) first success regarding the visualisation and reliable assessment of diagenetic overprint, as well as disclosure of differences in the degree of alteration/diagenetic overprint was achieved. Studies summarised in chapters 2.2 and 2.3 focused on bio-calcitic brachiopod specimens (pristine – reference, thermally and hydrothermally altered – mimicked diagenetic overprint, fossil – natural diagenetic overprint). Decomposition of organic matrices was observed under simulated dry and wet alteration conditions, and in naturally overprinted (fossil) samples. Dehydration of the biopolymer membranes and their detachment from low-Mg calcite fibres was observed in experiments lasting for 3 days at 100 °C, whereas thermal degradation of biopolymers proceeded as destruction of almost the entire organic matrices was found in experiments lasting for 3 months at 100 °C. Cavities between adjacent fibres and a myriad of minute holes within single brachiopod fibres formed as a consequence of the decomposition of organic matter creating fluid pathways. Mg-rich simulated burial fluid significantly affected the degree of fibre destruction by distortion of the morphology of low-Mg calcite brachiopod fibres to a higher degree than during hydrothermal alteration experiments using Mg-free simulated meteoric fluid. Hydrothermal alteration conducted on *Terebratalia transversa* at 100 °C did not have a major impact on shell structure and morphology. Furthermore, no formation of secondary calcite was observed. However, hydrothermal experiments performed at 175 °C in simulated burial fluid caused recrystallisation of the nanomosaic structure of biogenic calcite to inorganic rhombohedral calcite. Concomitant amalgamation of fibres by lateral growth of secondary calcite into neighbouring biogenic calcite fibres, and formation of inorganic calcite between neighbouring brachiopod fibres were observed. As a consequence of locally occurring dissolution-reprecipitation reactions during hydrothermal treatment, varying degrees of alteration, partial amalgamation and distortion of fibres within the same shell were obtained. The combination of FE-SEM imaging of brachiopod fibre morphologies, and measurements of crystal orientation patterns obtained from EBSD allowed for the first qualitative (non-altered, altered/overprinted) and quantitative (low, moderate, severe) assessment of the degree of diagenetic overprint in simulated and naturally altered (fossil) marine bio-calcitic brachiopod shells. Furthermore, both analytical tools enabled the explicit identification of secondary inorganic calcite formation. Fossil samples of different geologic ages and sampling locations exhibited different degrees of diagenetic overprint as assessed by microstructural characterisation. Although the specific diagenetic conditions of the fossil specimens are unknown, it can be assumed that all samples must have experienced conditions of different diagenetic environments such as the burial

realm. The shell of naturally overprinted Ordovician *Platystrophia laticostata* showed the most severe diagenetic overprint expressed by the entire destruction of fibre morphology and substantial formation of secondary inorganic calcite. In contrast, the weakest natural diagenetic overprint was assessed in the shell of Jurassic *Lobothyris punctata* (Pliensbachian) which exhibited a good preservation state of fibre morphology and no precipitation of secondary calcite at sites of former organic matrices. Moderate natural diagenetic overprint was assessed in Jurassic *Digonella digona* and *Quadratirhynchia attenuata* shells in which overprinted shell parts were observed next to almost pristine shell morphologies. Overprinted sites were detected in the endopunctae and well-preserved fibres between single endopunctae in *D. digona*, whereas patchy amalgamation of fibres and secondary calcite formation between neighbouring fibres was observed in the impunctate specimen *Q. attenuata.* The results showed that CL imaging and EBSD measurements indicate comparable degrees of diagenetic overprint in (fossil) biogenic calcites (e.g., brachiopods). However, CL is a useful and rapid tool for the acquisition of a first impression on the existing diagenetic overprint and it should not be used as a single analytical tool for the assessment of the degree of diagenetic overprint. Thus, the first estimated degree of diagenetic overprint assessed in fossil biogenic carbonates needs to be further verified by AFM imaging of the nanostructure, and EBSD microstructure and texture analyses. The application of the presented multi-analytical tools can be fully endorsed for identification of preservation states and degrees of diagenetic overprint in fossil biogenic carbonates.

Hydrothermal alteration experiments of biogenic carbonates were expanded in order to study the influence of different microstructures on interface-coupled dissolution-reprecipitation reactions occurring in biogenic aragonites and calcites during mimicked diagenetic overprint in simulated burial fluid at 175 °C. Thus, four different specimens with overall six distinct microstructures were used for the experimental series: bivalve *A. islandica* (aragonitic mineral units), scleractinian coral *Porites* sp. (fibrous aragonite), gastropod *Haliotis ovina* (prismatic aragonite and columnar nacre), and bivalve *Mytilus edulis* (fibrous calcite and 'brick-and-mortar' nacre). Implications for fossil, overprinted carbonate materials and additional knowledge on their preservation potential, which is a crucial factor to allow for precise and correct reconstructions of palaeoclimate dynamics, may be deduced from the study summarised in chapter 2.4. As delicate biopolymer fibrils were easily decomposed at elevated temperature conditions, hard tissues comprised of small and irregularly shaped biogenic carbonate minerals surrounded or penetrated by organic matrices were more rapidly replaced by randomly oriented inorganic calcite crystallites during simulated burial diagenetic alteration. The interface-coupled dissolution-reprecipitation reaction was further promoted by the presence of primary porosity within pristine biocarbonate microstructures such as in the shell of bivalve *A. islandica*. Newly generated pore spaces found at sites of former

organic matter (secondary porosity) and initial primary porosity enabled extensive fluid infiltration as well as percolation through the biocarbonate skeletons. This allowed for rapid alteration kinetics as observed in the aragonitic shell of bivalve *A. islandica* and the prismatic shell layer of gastropod *H. ovina*. However, dissolution-reprecipitation reactions were slowest in nacreous biogenic aragonites of the bivalve *M. edulis* and gastropod *H. ovina*, and thus, independent of the mode of nacre tablet assembly. The alteration process of nacreous layers can be described by four stages and begins with (1) decomposition of biopolymers, and subsequently formed secondary porosity. (2) Neighbouring nacre tablets dissolve at their boundaries and laterally as well as longitudinally amalgamate due to recrystallisation processes. (3) Severe distortion of the initial microstructure, and thus, formation of a compact mineral area with preserved aragonitic mineralogy occurs at the fluid-solid interface, and is followed by (4) precipitation of secondary calcite. Among the investigated microstructures, acicular biogenic aragonite of the scleractinian coral *Porites* sp. exhibited the strongest resistance against simulated diagenetic alteration processes. However, slight replacement of biogenic aragonite by inorganic calcite was observed to start at organic-rich centres of calcification. The alteration process with concomitant fusion of neighbouring aragonite fibres and formation of a compact fabric proceeded towards the outer rim of the coral skeleton. Despite the occurrence of slight dissolution-reprecipitation reactions some morphological features of the initial microstructure were preserved. Generally, simulated diagenetic alteration of biogenic carbonate hard tissues started with distortion of the initial microstructure and was characterised by subsequent replacement by inorganic calcite. This process was valid for all aragonitic and calcitic microstructures utilised in this study. At contact zones between altered, compact aragonite and secondary calcite, a seam enriched in Mg was detected. This seam may be related to Mg present in the used simulated burial alteration fluid. A progressive decrease in Mg away from the aragonite-calcite interface allowed for tracing the chemical evolution of the utilised fluid. Statistical evaluation of grain sizes revealed differences in pristine and altered biogenic carbonate hard tissues towards grain coarsening caused by applied hydrothermal alteration. Even if the initial mineralogy was retained during early reaction stages, simulated diagenetic overprint caused the formation of mineral overgrowths as was detected, most severely, in the fibrous calcite layer of the *M. edulis* shell. However, the least difference in grain size distributions between pristine and altered aragonite was obtained for the shell of *A. islandica*. Thus, remnants of aragonitic hard tissues found in overprinted materials are fallacious, and more importantly, not suitable to be used as distinct indicators for initial elemental and isotope signals collected for palaeoclimate reconstruction studies.

Alteration features caused by hydrothermal experiments (e.g., dissolution, secondary calcite precipitation, alteration of organic matter) resembled features observed

in diagenetically altered fossil specimens. Observed alteration features were independent of the initial mineralogy, and microstructure of the biogenic carbonates used in the present dissertation. In naturally altered fossils, however, changes caused by diagenetic overprint were more distinct. In contrast to natural diagenetic processes, the used experimental setup was restricted to a closed system. Experimental pressures corresponded to the vapour pressure of water at the given temperatures. Thus, pressure conditions of natural diagenetic environments were not reached.

Application of sophisticated preparation methods (e.g., selective biochemical etching, microtome polishing), statistical evaluation of grain size distributions, and a broad set of state of the art analytical tools (e.g., EBSD, EPMA, FE-SEM, AFM) allowed to deepen the current knowledge on diagenetic processes taking place in (fossil) biogenic carbonates. Further, it was demonstrated that deployment of specific tools such as CL, and statistical analysis of grain sizes allow for rapid assessments of the degree of diagenetic overprint of fossil carbonates prior to the application of slower but more precise tools. The presented results give new insights into preservation states of fossil biogenic carbonates on the micro- and nanoscales and, consequently, have a deep impact on the interpretation of fossil-based palaeoclimate research as they allow for the reliable identification of areas in fossil material which have not changed by the influence of diagenetic processes and, therefore, are most suitable for sensitive isotope analyses.

4   Outlook

In order to obtain more profound insights into diagenetic alteration of fossil biogenic carbonates, and to decipher kinetic processes which occur during diagenesis, additional studies are required. Aspects of interest might cover following research topics:

The present thesis showed extensive studies regarding hydrothermal alteration experiments of carefully selected biogenic carbonates carried out in order to mimic diagenetic alteration in the laboratory. Investigations of numerous biogenic carbonate hard tissues hydrothermally treated in mainly simulated burial, and partly simulated meteoric fluid emphasised their significance for gaining fundamental knowledge on versatile, yet complex diagenetic processes. To expand the existing experimental series performed in the framework of this dissertation, additional studies focussing on hydrothermal experiments with simulated meteoric fluid using identical biogenic hard tissues, experimental temperatures and durations should be carried out. Additional experiments utilising seawater in order to cover the third diagenetic regime (i.e., marine realm) and to complement the presented study are necessary not only for the purpose of comparison, but also to set a baseline for this diagenetic environment. The use of the same sample materials and experimental parameters might be helpful in order to compare results obtained for seawater with those presented in this thesis.

Experimental hydrothermal alteration studies should be performed for longer periods of time (e.g., 4-24 months) on one specific bio-aragonite (fibrous and nacreous), and bio-calcite. These studies will be helpful to investigate if the process of aragonite replacement by calcite might be induced by longer experimental times even at low temperatures (<100 °C). Aragonitic bivalves are an appropriate sample material for hydrothermal alteration experiments carried out at low temperatures. The same experimental settings might shed light on the amalgamation of biogenic calcite, especially in fibrous calcites which are commonly found in brachiopods and bivalves, at temperatures which do not exceed 100 °C. Low temperature experiments performed for longer periods of time should cover the range between 50-100 °C with a step width of 10 °C.

All hydrothermal experiments mimicking burial and partly meteoric diagenesis presented in this thesis were carried out in a closed system and under vapour pressure at the given temperature due the experimental design. However, in nature biogenic (carbonate) minerals are exposed to the open system of their surrounding diagenetic environment. Thus, percolation of fluids with differing compositions and presumably increasing pressure conditions over the geologic time may have a greater effect on the degree of overprint in biogenic hard tissues. Future studies should consider a new experimental setup allowing for the simulation of diagenetic alteration as open system.

Apart from the temperature, pressure should be adjustable and permanent flow of experimental fluids through the reaction vessel should be enabled.

Particular focus should not only be placed on hydrothermal experiments as diagenesis may also occur in dry systems. Thus, the same specimens which were carefully selected for hydrothermal alteration experiments should be subjected to dry thermal treatments in order to (1) assess the reorganisation processes of nano- and microstructures found in the utilised biogenic carbonate specimens, and (2) obtain deeper insight into degradation processes of biopolymer matrices found in biogenic carbonates. First thermal experiments on pristine brachiopods (see Casella et al., 2018a, 2018b) at 100 °C and 400 °C for up to 3 months and 2 days, respectively, did show formation of porosity and degradation of organic matrices occurring in a manner different to hydrothermally altered specimens. Results obtained from thermal and hydrothermal alteration experiments simulating diagenetic alteration should be compared to findings obtained from diagenetically altered fossil specimens in order to better understand the natural overprint processes.

Notwithstanding hydrothermal experiments mimicking diagenetic alteration processes have showed to be a method to gain fundamental knowledge on diagenetic processes, material scientific studies utilising fossils are still indispensable. Despite the difficulty of collecting intact fossil specimens of different animals which were subjected to diagenesis, it still remains necessary to investigate fossil materials and to carry out comparative studies using their hydrothermally altered counterparts. It is of high importance that samples used in future studies should be collected from all three diagenetic regimes with known diagenetic history in order to obtain more profound knowledge on diagenetic processes occurring in burial, meteoric, and marine realms. Especially in the case of the burial environment, fossil specimens should be collected from basins with known stratigraphy, diagenetic pressure and temperature conditions, as well as the involvement of fluid phases. The latter is an important factor for the acceleration of dissolution-reprecipitation reactions. Thus, it can be assumed that kinetics differ from dry environments, and consequently, result in a different preservation state. As diagenetic overprint may be comprised of a sequence of thermal, pressure, and hydrous events, fossil specimens utilised for comparative studies have to be carefully selected. Hence, fossil biogenic carbonates of the same animal class sampled from basins or strata with known diagenetic history, e.g., realm, temperature, pressure, influence of fluid phases, should be compared to a pristine reference, but especially to biogenic hard tissues, which were subjected to (hydro-) thermal alteration experiments. Ideally, the sampling site should exhibit different diagenetic conditions, e.g., varying from a low to a high degree of overprint.

As porosity formation is a major microstructural feature of dissolution-reprecipitation reactions, and more importantly, greatly influences the kinetics of

replacement reactions by creation of additional fluid-solid contacts, porosity measurements should be carried out in future studies. These may be conducted on pristine (reference), hydrothermally (independent of applied temperatures, pressures and experimental time), and natural diagenetically altered biogenic carbonates in order to quantitatively assess the amount of porosity prior and after alteration. Obtained data could provide additional information on the assessment of the degree of (mimicked) diagenetic alteration in hard tissues comprised of calcium carbonates.

5 References

Abele D., Strahl J., Brey T., and Philipp E. E. R. (2008) Imperceptible senescence: ageing in the ocean quahog *Arctica islandica*, Free Radical Res., 42(5), 474-480.

Addadi L. and Weiner S. (1997) Biomineralization: a pavement of pearl, Nature, 389, 912-915.

Addadi L., Raz S., and Weiner S. (2003) Taking advantage of disorder: amorphous calcium carbonate and its roles in biomineralization, Adv. Mater., 15(12), 959-970.

Aharon P. (1991) Recorders of reef environment histories: stable isotopes in corals, giant clams, and calcareous algae, Coral Reefs, 10(2), 71-90.

Aissaoui D. M. and Purser B. H. (1985) Reef diagenesis: cementation at Mururoa Atoll, French Polynesia, Proc. 5th Int. Coral Reef Congr. Tahiti 3.

Aissaoui D. M., Buigues D., and Purser B. H. (1986) Model of reef diagenesis: Mururoa Atoll, French Polynesia, in: Schroeder J. H. and Purser B. H. (eds.), Reef diagenesis, Springer, Berlin, 27-52.

Aizenberg J., Addadi L., Weiner S., and Lambert G. (1996) Stabilization of amorphous calcium carbonate by specialized macromolecules in biological and synthetic precipitates, Adv. Mater., 8(3), 222-226.

Aizenberg J., Lambert G., Weiner S., and Addadi L. (2002) Factors involved in the formation of amorphous and crystalline calcium carbonate: a study of an ascidian skeleton, J. Am. Chem. Soc., 124(1), 32-39.

Akiva-Tal A., Kababya S. Balazs Y. S., Glazer L., Berman A., Sagi A., and Schmidt A. (2011) In situ molecular NMR picture of bioavailable calcium stabilized as amorphous $CaCO_3$ biomineral in crayfish gastroliths, Proc. Natl. Acad. Sci. U.S.A., 108(36), 14763-14768.

Al-Aasm I. S. and Veizer J. (1982) Chemical stabilization of low-Mg calcite: an example of brachiopods, J. Sediment. Petrol., 52, 1101-1109.

Alberts B., Johnson A., Lewis J., Morgan D., Raff M., Roberts K., and Walter P. (2014) Molecular biologogy of the cell, Norton & Company, New York.

Alexander R. R. (2001) Functional morphology and biomechanics of articulate brachiopod shells, Paleontological Society Papers, 7, 145-169.

Alexandersson E. T. (1978) Destructive diagenesis of carbonate sediments in the eastern Skagerrak, North Sea, Geology, 6(6), 324.

Ali C. A. and Mohamed K. R. (2013) Microfacies and diagenesis in the Setul Limestone in Langkawi and Perlis, Bull. Geol. Soc. Malaysia, 59, 59-66.

Ali S. A., Clark W. J., Moore W. R., and Dribus J. R. (2010) Diagenesis and reservoir quality, Oilfield Rev., 22(2), 14-27.

Altree-Williams A., Pring A., Ngothai Y., and Brugger J. (2015) Textural and compositional complexities resulting from coupled dissolution–repreciptation reactions in geomaterials, Earth-Sci. Rev., 150, 628-651.

Álvarez F. and Curry G. B. (2010) Evolution and development of the brachiopod shell, Spec. Pap. Palaeontol., 84.

References

Álvarez-Lloret P., Rodríguez-Navarro A. B., Falini G., Fermani S., and Ortega-Huertas M. (2010) Crystallographic control of the hydrothermal conversion of calcitic sea urchin spine (*Paracentrotus lividus*) into apatite, Cryst. Growth Des., 10, 5227–5232.

Amieux P., Bernier P., Dalongville R., and Medwecki V. (1989) Cathodoluminescence of carbonate-cemented Holocene beachrock from the Togo coastline (West Africa): an approach to early diagenesis, Sediment. Geol., 65, 261-272.

Anderson T. F., Bender M. L., and Broecker W. S. (1973) Surface areas of biogenic carbonates and their relation to fossil ultrastructure and diagenesis, J. Sediment. Petrol., 43, 471-477.

Andrews I. J. (2013) The carboniferous Bowland shale gas study: geology and resource estimation, British Geological Survey for Department of Energy and Climate Changes London, U. K..

Angiolini L. (1993) Ultrastructure of some Permian and Triassic Spiriferida and Arthyridida (Brachiopoda), Riv. Ital. Paleontol. Stratigr., 9, 283-306.

Angiolini L. (1995): Permian Brachiopods from Karakorum (Pakistan) Pt. 1, Riv. Ital. Paleont. Strat., 101, 165-214.

Angiolini L. (1996): Permian brachiopods from Karakorum (Pakistan) Pt. 2, Riv. Ital. Paleontol. Strat., 102(1), 3-26.

Angiolini L. (2001): Permian brachiopods from Karakorum (Pakistan) Pt. 3, Riv. Ital. Paleontol. Strat., 107(3), 307-344.

Angiolini L., Brunton H., and Zanchi A. (1999): Late carboniferous brachiopods from Karakorum, Pakistan, Riv. Ital. Paleontol. Strat., 105(1), 3-22.

Angiolini L., Jadoul F., Leng, M. J., Stephenson M. H., Rushton J., Chenery S., and Crippa G. (2009) How cold were the Early Permian glacial tropics? Testing sea-surface temperature using the oxygen isotope composition of rigorously screened brachiopod shells, J. Geol. Soc. London, 166(5), 933-945.

Angiolini L., Stephenson M., Leng M. J., Jadoul F., Millward D., Aldridge A., Andrews J. E., Chenery S. R., and Williams G. (2012) Heterogeneity, cyclicity and diagenesis in a Mississippian brachiopod shell of palaeoequatorial Britain, Terra Nova, 24(1), 16-26.

Armenteros I. (2010) Diagenesis of carbonates in continental settings, Dev. Sedimentol., 62, 61-151.

Arvidson R. S. and Morse J. W. (2014) Formation and diagenesis of carbonate sediments, in: Holland H. D. and Turekian K. K. (eds.) Treatise on geochemistry, 9, Elsevier, Oxford, 61-101.

Auclair A.-C., Joachimski M. M., and Lécuyer C. (2003) Deciphering kinetic, metabolic and environmental controls on stable isotope fractionations between seawater and the shell of *Terebratalia transversa* (Brachiopoda), Chem. Geol., 202(1-2), 59-78.

Back W., Hanshaw B. B., Pyle T. E., Plummer L. N., and Weidie A. E. (1979) Geochemical significance of groundwater discharge and carbonate solution to the formation of Caleta Xel Ha, Quintana Roo, Mexico, Water Resour. Res., 15(6), 1521-1535.

Back W., Hanshaw B. B., and van Driel J. N. (1984) Role of groundwater in shaping the eastern coastline of the Yucatan Peninsula, Mexico, in: LaFleur R. G. (ed.) Groundwater as a geomorphic agent, Allen & Unwin, London.

Balthasar U. and Cusack M. (2015) Aragonite-calcite seas – Quantifying the gray area, Geology, 43, 99-102.

Barbin V., Ramseyer K., Debenay J. P., Schein E., Roux M., and Decrouez D. (1991) Cathodoluminescence of recent biogenic carbonates - An environmental and ontogenetic fingerprint, Geol. Mag., 128, 19-26.

Barnes D. J. (1985) The effect of photosynthetic and respiratory inhibitors upon calcification in the staghorn coral *Acropora formosa*, Proc. 5th Int. Coral Reef Congr., 6, 161-165.

Bates N. R. and Brand U. (1991) Environmental and physiological influences on isotopic and elemental compositions of brachiopod shell calcite: implications for the isotopic evolution of Paleozoic oceans, Chem. Geol., 94(1), 67-78.

Bathurst R. G. C. (1975) Carbonate sediments and their diagenesis, Developments in sedimentology, 12, Elsevier, Amsterdam.

Bathurst R. G. C. (1994) Neomorphic processes in diagenesis, in: Bathurst R. G. C. (ed.) Carbonate sediments and their diagenesis, Elsevier, Amsterdam, 475-516.

Bayne B. L. (1976) Marine mussels, their ecology and physiology, Cambridge University Press, Cambridge.

Beaufort L., Couapel M., Buchet N., Claustre H., and Goyet C. (2008) Calcite production by coccolithophores in the south east Pacific Ocean, Biogeosciences, 5(4), 1101-1117.

Becker A., Bismayer U., Epple M., Fabritius H., Hasse B., Shi J., and Ziegler A. (2003) Structural characterisation of X-ray amorphous calcium carbonate (ACC) in sternal deposits of the crustacea *Porcellio scaber*, Dalton Trans., 4, 551-555.

Beniash E., Aizenberg J., Addadi L., and Weiner S. (1997) Amorphous calcium carbonate transforms into calcite during sea urchin larval spicule growth, Proc. Roy. Soc. London, Ser. B – Biol. Sci., 264, 461-465.

Ben-Nissan B. (2003) Natural bioceramics: from coral to bone and beyond, Curr. Opin. Solid St. M., 7(4-5), 283-288.

Benton M. J. and Harper D. A. T. (1997) Basic palaeontology, Prentice Hall, Upper Saddle River, NJ.

Berner R. A. (1964) Distribution and diagenesis of sulphur in some sediments from the Gulf of California, Mar. Geol., 1, 117-140.

Berner R. A. (1966) Chemical diagenesis of some modern carbonate sediments, Am. J. Sci., 264, 1-36.

Berner R. A. (1975) The role of magnesium in the crystal growth of calcite and aragonite from sea water, Geochim. Cosmochim. Acta, 39, 489-504.

Bevelander G. and Nakahara H. (1969) An electron microscope study of the formation of the nacreous layer in the shell of certain bivalve molluscs, Calc. Tis. Res., 3(1), 84-92.

Bischoff J. L. (1969) Temperature controls on aragonite-calcite transformation in aqueous solution, Am. Mineral., 54, 149-155.

Bischoff J. L. and Fyfe W. S. (1968) Catalysis, inhibition, and the calcite-aragonite problem, Part 1, The aragonite-calcite transformation, Am. J. Sci., 266, 65-79.

Bischoff W. D., Mackenzie F. T., and Bishop F.C. (1987) Stabilities of synthetic magnesian calcites in aqueous solution: comparison with biogenic materials, Geochim. Cosmochim. Acta, 51, 1413-1423.

References

Bischoff W. D., Bertram M. A., Mackenzie F. T., and Bishop F. C. (1993) Diagenetic stabilization pathways of magnesian calcites, Carbonate. Evaporite., 8, 82-89.

Blanchon P., Eisenhauer A., Fietzke J., and Liebetrau V. (2009) Rapid sea-level rise and reef back-stepping at the close of the last interglacial highstand, Nature, 458, 881-884.

Bodine M. W., Holland H. D., and Borcsik M. (1965) Coprecipitation of manganese and strontium with calcite, in: Symposium on problems of postmagmatic ore deposition, 2, Prague.

Boggs S. (2010) Petrology of sedimentary rocks, Cambridge University Press, Cambridge.

Boggs S. and Krinsley D. (1991) Application of cathodoluminescence imaging to the study of sedimentary rocks, Cambridge University Press, Cambridge.

Böhm F., Gussone N., Eisenhauer A., Dullo W.-C., Reynaud S., and Paytan A. (2006) Calcium isotope fractionation in modern scleractinian corals, Geochim. Cosmochim. Acta, 70, 4452-4462.

Bouchet P., Rocroi J. P., Fryda J., Hausdorf B., Ponder W., Valdes A., and Warén A. (2005) Classification and nomenclator of Gastropod families, Malacologia, 47(1-2), 1-368.

Bragg W. L. (1914) The analysis of crystals by the X-ray spectrometer, Proc. Roy. Soc. London, Ser. A – Math. Phys., 89, 468-489.

Bragg W. L. (1924) The structure of aragonite, Proc. Roy. Soc. London, Ser. A – Math. Phys., 105(729), 16-39.

Brahmi C., Kopp C., Domart-Coulon I., Stolarski J., and Meibom A. (2012) Skeletal growth dynamics linked to trace-element composition in the scleractinian coral *Pocillopora damicornis*, Geochim. Cosmochim. Acta, 99, 146-158.

Brand U. (1981) Mineralogy and chemistry of the Lower Pennsylvanian Kendrick Fauna, eastern Kentucky, U.S.A. – 1. Trace elements, Chem. Geol., 32, 1-16.

Brand U. (1987) Biogeochemistry of nautiloids and paleoenvironmental aspects of buckhorn seawater (Pennsylvanian), Southern Oklahoma, Palaeogeogr. Palaeoclimat. Palaeoecol., 61, 255-264.

Brand U. (1989a) Aragonite-calcite transformation based on Pennsylvanian molluscs, Geol. Soc. Am. Bull., 101, 377-390.

Brand U. (1989b) Biogeochemistry of late Paleozoic American brachiopods and secular variation of seawater composition, Biogeochemistry, 7, 159-193.

Brand U. (1991) Strontium isotope diagenesis of biogenic aragonite and low-Mg-calcite, Geochim. Cosmochim. Acta, 55, 505-513.

Brand U. (1994) Morphochemical and replacement diagenesis of biogenic carbonates, Dev. Sedimentol., 51, 217-282.

Brand U. (2004) Carbon, oxygen and strontium isotopes in Paleozoic carbonate components: an evaluation of original seawater-chemistry proxies, Chem. Geol., 204(1-2), 23-44.

Brand U. and Brenckle P. (2001) Chemostratigraphy of the Mid-Carboniferous boundary global stratotype section and point (GSSP), Bird Spring Formation, Arrow Canyon, Nevada, U.S.A., Palaeogeogr. Palaeoclimatol. Palaeoecol., 165(3-4), 321-347.

Brand U. and Logan A. (1991) Brachiopod geochemistry: a tracer tool of present and past ocean circulation, chemistry and cycles, Geol. Assoc. Can. Prog. Abstr., 16, A14.

Brand U. and Morrison J. O. (1987) Diagenesis and pyritization of crinoid ossicles, Can. J. Earth Sci., 24, 2486-2498.

Brand U. and Veizer J. (1980) Chemical diagenesis of a multicomponent carbonate system - 1: trace elements, J. Sediment. Res., 50(4), 1219-1236.

Brand U. and Veizer J. (1981) Chemical diagenesis of a multicomponent carbonate system - 2: stable isotopes, J. Sed. Res., 51(3), 987-997.

Brand U., Logan A., Hiller N., and Richardson J. (2003) Geochemistry of modern brachiopods: applications and implications for oceanography and paleoceanography, Chem. Geol., 198(3-4), 305-334.

Brand U., Azmy K., Tazawa J.-I., Sano H., and Buhl D. (2010) Hydrothermal diagenesis of Paleozoic seamount carbonate components, Chem. Geol., 278, 173-185.

Brand U., Logan A., Bitner M. A., Griesshaber E., Azmy K., and Buhl D. (2011) What is the ideal proxy of Palaeozoic seawater chemistry?, Memoirs of the Association of Australasian Palaeontologists, 41, 9-24.

Branson O., Redfern S. A.T., Tyliszczak T., Sadekov A., Langer G., Kimoto K., and Elderfield H. (2013) The coordination of Mg in foraminiferal calcite, Earth Planet. Sc. Lett., 383, 134-141.

Brigaud B., Durlet C., Deconinck J.-F., Vincent B., Pucéat E., Thierry J., and Trouiller A. (2009) Facies and climate/environmental changes recorded on a carbonate ramp: a sedimentological and geochemical approach on Middle Jurassic carbonates (Paris Basin, France), Sediment. Geol., 222, 181-206.

Brocas W. M., Reynolds D. J., Butler P. G., Richardson C. A., Scourse J. D., Ridgway I. D., and Ramsay K. (2013) The dog cockle, *Glycymeris glycymeris* (L.), a new annually-resolved sclerochronological archive for the Irish Sea, Palaeogeogr. Palaeoclimatol. Palaeoecol., 373, 133-140.

Bromley R. G. (1978) Bioerosion of Bermuda Reefs, Palaeogeogr. Palaeoclimat. Palaeoecol., 23, 169-197.

Brooks R., Clark L. M., and Thurston E. F. (1950) Calcium carbonate and its hydrates, Philos. Trans. R. Soc. Lond. Ser. A, 243, 145-167.

Brown W. H., Fyfe W. S., and Turner F. J. (1962) Aragonite in California glaucophane schists, and the kinetics of the aragonite-calcite transformation, J. Petrol., 3, 566-582.

Brugger J., Mcfadden A., Lenehan C. E., Etschmann B., Xia F., Zhao J., and Pring A. (2010) A novel route for the synthesis of mesoporous and low-thermal stability materials by coupled dissolution-reprecipitation reactions: mimicking hydrothermal mineral formation, Chimia, 64(10), 693-698.

Burdett H. L., Aloisio E., Calosi P., Findlay H. S., Widdicombe S., Hatton A. D., and Kamenos N. A. (2012) The effect of chronic and acute low pH on the intracellular DMSP production and epithelial cell morphology of red coralline algae, Mar. Biol. Res., 8(8), 756-763.

Burdige D. J., Hu X., and Zimmerman R. C. (2010) The widespread occurrence of coupled carbonate dissolution/reprecipitation in surface sediments on the Bahamas Bank, Am. J. Sci., 310(6), 492-521.

Burke W. H., Denison R. E., Heatherington E. A., Koepnick R. B., Nelson H. F., and Otto J. B. (1982) Variation of seawater $^{87}Sr/^{86}Sr$ throughout Phanerozoic time, Geology, 10, 516-519.

Burley S. D. and Kantorowicz J. D. (1986) Thin section and SEM. textural criteria for the recognition of cement-dissolution porosity in sandstones, Sedimentology, 33(4), 587-604.

References

Burley S. D., Kantorowicz J. D., and Waugh B. (1985) Clastic diagenesis, in: Brenchley P., and Williams B. P. B. (eds.) Sedimentology: recent and applied aspects, Spec. Publ. Geol. Soc. London, 18, Blackwell Scientific Publications, Oxford.

Busenberg E. and Plummer L. N. (1986) A comparative study of the dissolution and crystal growth kinetics of calcite and aragonite, U.S. Geol. Surv. Bull., 1578, 139–169.

Butler P. G., Richardson C. A., Scourse J. D., Witbaard R., Schöne B. R., Fraser N. M., Wanamaker A. D. Jr., Bryant C. L., Harris I., and Robertson I. (2009) Accurate increment identification and the spatial extent of the common signal in five *Arctica islandica* chronologies from the Fladen Ground, northern North Sea, Paleoceanography, 24, PA2210.

Butler P. G., Wanamaker A. D., Scourse J. D., Richardson C. A., and Reynolds D. J. (2013) Variability of marine climate on the North Icelandic Shelf in a 1357-year proxy archive based on growth increments in the bivalve *Arctica islandica*, Palaeogeogr. Palaeoclimat. Palaeoecol., 373, 141-151.

Butler S., Bailey T. R., Lear C. H., Curry G. B., Cherns L., and McDonald I. (2015) The Mg/Ca–temperature relationship in brachiopod shells: calibrating a potential palaeoseasonality proxy, Chem. Geol., 397, 106-117.

Cabrol P. (1978) Contribution à l'étude du concrétionnement carbonaté des grottes du sud de la France: morphologie, genèse, diagenèse, Centre d´Etudes et de Recherches Géologiques et Hydrogéologiques, Memoires, Montpellier, France, 12.

Cabrol P. and Coudray J. (1982) Climatic fluctuations influence in the genesis and diagenesis of carbonate speleotherms in southwestern France, National Speleological Society, Huntsville, Alabama, Bulletin, 44, 112-117.

Cardew P. T. and Davey R. J. (1985) The kinetics of solvent-mediated phase transformations, Proc. Roy. Soc. London, Ser. A Math. Phys. Eng. Sci., 398, 415-428.

Carlson W. D. (1983) The polymorphs of $CaCO_3$ and the aragonite-calcite transformation, in: Reeder R. J. (ed.) Carbonates: mineralogy and chemistry, Mineral. Soc. Am., Bookcrafters Inc., Chelsea, Mich., 191-225.

Carpenter W. (1848) Report on the microscopic structure of shells, Part II, Rep. Br. Assoc. Adv. Sci., 17th Meeting, 93-134.

Carpenter S. J. and Lohmann K. C. (1995) $\delta^{18}O$ and $\delta^{13}C$ values of modern brachiopod shells, Geochim. Cosmochim. Acta, 59, 3749-3764.

Cartwright J. H. E. and Checa A. G. (2007) The dynamics of nacre self-assembly, J. R. Soc. Interface, 4(14), 491-504.

Cartwright J. H. E., Checa A. G., Gale J. D., Gebauer D., and Sainz-Diaz C. I. (2012) Calcium carbonate polyamorphism and its role in biomineralization: how many amorphous calcium carbonates are there?, Angew. Chem. Int. Edit., 51(48), 11960-11970.

Casella L. A., Griesshaber E., Yin X., Ziegler A., Mavromatis V., Müller D., Ritter A.-C., Hippler D., Harper E. M., Dietzel M., Immenhauser A., Schöne B. R., Angiolini L., and Schmahl W. W. (2017) Experimental diagenesis: insights into aragonite to calcite transformation of *Arctica islandica* shells by hydrothermal treatment, Biogeosciences, 14, 1461-1492.

Casella L. A., Griesshaber E., Simonet Roda M. d. M., Ziegler A., Mavromatis V., Henkel D., Laudien J., Häussermann V., Neuser R. D., Angiolini L., Dietzel M., Eisenhauer A., Immenhauser A., Brand U., and Schmahl W. W. (2018a) Micro- and nanostructures reflect

the degree of diagenetic alteration in modern and fossil brachiopod shell calcite: a multi-analytical screening approach (CL, FE-SEM, AFM, EBSD), Palaeogeogr. Palaeoclimat. Palaeoecol., 502, 13-30.

Casella L. A, Simonet Roda M. d. M., Angiolini L., Ziegler A., Schmahl W. W., Brand U., and Griesshaber E. (2018b) Archival biogenic micro- and nanostructure data analysis: signatures of diagenetic systems, Data in Brief, 19, 299-311.

Casella L. A, He S., Griesshaber E., Fernández-Díaz L., Greiner M., Harper E. M., Jackson D., Ziegler A., Mavromatis V., Dietzel M., Eisenhauer A., Veintemillas-Verdaguer S., Brand U., and Schmahl W. W. (2018c) Hydrothermal alteration of aragonitic biocarbonates: assessment of micro- and nanostructural dissolution-reprecipitation and constraints of diagenetic overprint from quantitative statistical grain-area analysis, Biogeosciences, 15, 7451-7484.

Casey F. G. S. (1952) Some genera and subgenera, mainly new, of Mesozoic heterodont lamellibranchs, Proc. Malacol. Soc. Lond., 29, 121-176.

Cerrato R. M. (2000) What fish biologists should know about bivalve shells, Fish. Res., 46(1-3), 39-49.

Chakoumakos B. C., Pracheil B. M., Koenigs R. P., Bruch R. M., and Feygenson M. (2016) Empirically testing vaterite structural models using neutron diffraction and thermal analysis, Scientific Reports, 6, 36799.

Chalker B. E., Carr K., and Gill E. (1985) Measurement of primary production and calcification in situ on coral reefs using electrode techniques, Proc. 5th Int. Coral Reef Congr., (6), 167-172.

Chave K. E. (1954) Aspects of the biogeochemistry of magnesium - 1: calcareous marine organisms, J. Geol., 62(3), 266-283.

Checa A. G., Okamoto T., and Ramirez J. (2006) Organization pattern of nacre in Pteriidae (Bivalvia: Mollusca) explained by crystal competition, Proc. Roy. Soc. London, Ser. B. Biol. Sci., 273, 1329-1337.

Checa A. G., Cartwright J. H. E., and Willinger M.-G. (2009) The key role of the surface membrane in why gastropod nacre grows in towers, Proc. Natl. Acad. Sci. U.S.A., 106(1), 38-43.

Checa A. G., Bonarski J. T., Willinger M. G., Faryna M., Berent K., Kania B., Gonzalez-Segura A., Pina C. M., Pospiech J., and Morawiec A. (2013) Crystallographic orientation inhomogeneity and crystal splitting in biogenic calcite, J. R. Soc. Interface, 10, 20130425.

Checa A. G., Macias-Sanchez E., and Ramirez-Rico J. (2016) Biological strategy for the fabrication of highly ordered aragonite helices: the microstructure of the cavolinioidean gastropods, Sci. Rep. U. K., 6, 25989.

Cherns L. and Wright V. P. (2000) Missing molluscs as evidence of largescale, early skeletal aragonite dissolution in a Silurian sea, Geology, 28, 791-794.

Cherns L., Wheeley J. R., and Wright V. P. (2008) Taphonomic windows and molluscan preservation, Palaeogeogr. Palaeoclimatol. Palaeoecol., 270, 220-229.

Chessin H., Hamilton W. C., and Post B. (1965) Position and thermal parameters of oxygen atoms in calcite, Acta Cryst., 18(4), 689-693.

Chester J. S., Lenz S. C., Chester F. M., and Lang R. A. (2004) Mechanisms of compaction of quartz sand at diagenetic conditions, Earth Planet. Sc. Lett., 220, 435-451.

References

Choquette P. W. (1955) A petrographic study of the "State College" siliceous oolite, J. Geol., 63, 337-347.

Choudens-Sánchez V. and Gonzáles L. A. (2009) Calcite and aragonite precipitation under controlled instantaneous supersaturation: elucidating the role of $CaCO_3$ saturation state and Mg/Ca ratio on calcium carbonate polymorphism, J. Sediment. Res., 79, 363-376.

Cohen A. L. and McConnaughey T. A. (2003) Geochemical perspectives on coral mineralization, Rev. Mineral. Geochem., 54(1), 151-187.

Cohen A. L., Layne G. D., and Hart S. R. (2001) Kinetic control of skeletal Sr/Ca in a symbiotic coral: implications for the paleotemperature proxy, Paleoceanography, 16(1), 20-26.

Cölfen H. and Antonietti M. (2008) Mesocrystals and nonclassical crystallization, John Wiley & Sons Inc., Hoboken, NJ, U. S. A..

Constantz B. R. (1986) Coral skeleton construction: a physiochemically dominated process, Palaios, 1(2), 152-157.

Constantz B. R. (1989) Skeletal organization in Caribbean *Acropora spp.*, in: Crick R. E. (ed.) Origin, evolution and modern aspects of biomineralization in plants and animals, Plenum Press, New York, 175-199.

Constantz B. and Weiner S. (1988) Acidic macromolecules associated with the mineral phase of scleractinian coral skeletons, J. Exp. Zool., 248(3), 253-258.

Copper P. (1996) Brachiopods: proceedings of the third International brachiopod congress, Sudbury, Ontario, Canada, 2 - 5 September 1995, Balkema, Rotterdam.

Cox K. W. (1962) California abalones, family Haliotidae, Fish Bull., 118, 123-128.

Crippa G. (2013) The shell ultrastructure of the genus Glycymeris da Costa, 1778: a comparison between fossil and recent, Riv. Ital. Paleontol. Stratigr., 119(3), 387-399.

Crippa G. and Raineri G. (2015) The genera Glycymeris, Aequipecten and Arctica, and associated mollusk fauna of the Lower Pleistocene Arda River section (Northern Italy), Riv. Ital. Paleontol. Stratigr., 121, 61-101.

Crippa G., Angiolini L., Bottini C., Erba E., Felletti F. Frigerio C., Hennissen J. A., Leng M. J., Petrizzo M. R., Raffi I., Raineri G., and Stephenson M. H. (2016) Seasonality fluctuations recorded in fossil bivalves during the early Pleistocene: implications for climate change, Palaeogeogr. Palaeoclimatol. Palaeoecol., 446, 234-251.

Cubillas P., Köhler S., Prieto M., Chaïrat C., and Oelkers E. H. (2005) Experimental determination of the dissolution rates of calcite, aragonite, and bivalves, Chem. Geol., 216(1-2), 59–77.

Cuesta Mayorga I., Astilleros J. M., Fernández-Díaz L., Morales J., Prieto M., Roncal-Herrero T., and Benning L. G. (2018) Epitactic overgrowths of calcite ($CaCO_3$) on anhydrite ($CaSO_4$) cleavage surfaces, Cryst. Growth Des., 18, 1666-1675.

Cuif J.-P., and Dauphin Y. (1998) Microstructural and physico-chemical characterization of 'centers of calcification' in septa of some recent scleractinian corals, Paläontol. Z., 72(3-4), 257-269.

Cuif J.-P. and Dauphin Y. (2005a) The environment recording unit in coral skeletons – a synthesis of structural and chemical evidences for a biochemically driven, stepping-growth process in fibres, Biogeosciences, (2), 61-73.

Cuif J.-P., and Dauphin Y. (2005b) The two-step mode of growth in the scleractinian coral skeletons from the micrometre to the overall scale, J. Struct. Biol., 150(3), 319-331.

Cuif J.-P., Dauphin Y., Doucet J., Salome M., and Susini J. (2003) XANES mapping of organic sulfate in three scleractinian coral skeletons, Geochim. Cosmochim. Acta, 67(1), 75-83.

Cuif J.-P., Dauphin Y., Howard L., Nouet J., Rouzière S., and Salomé M. (2011a). Is the pearl layer a reversed shell? A re-examination of the theory of pearl formation through physical characterisations of pearl and shell developmental stages in *Pinctada margaritifera*, Aquat. Living Resour., 24(4), 411-424.

Cuif J.-P., Dauphin Y., and Sorauf J. E. (2011b) Biominerals and fossils through time, Cambridge Univ. Press, Cambridge.

Curry G. B. and Brunton C. H. C. (2007) Stratigraphic distribution of brachiopods, in: Selden P. A. (ed.) Treatise on invertebrate paleontology (Part H, Brachiopoda Revised), Supplement, 6, Geological Society of America, University of Kansas Press, Boulder, CO, 2901-2964.

Curtis C. D., Burns R. G., and Smith J. V. (1977) Sedimentary geochemistry: environments and processes dominated by involvement of an aqueous phase, Philos. Trans. R. Soc. Lond. Ser. A, 286, 353-372.

Cusack M. (2015) Biomineral electron backscatter diffraction for palaeontology, Palaeontology, 59, 171-179.

Cusack M. and Williams A. (2001) Evolutionary and diagenetic changes in the chemico-structure of the shell of cranioid brachiopods, Palaeontology, 44(5), 875-903.

Cusack M., Pérez-Huerta A., Janousch M., and Finch A. A. (2008a) Magnesium in the lattice of calcite-shelled brachiopods, Chem. Geol., 257(1-2), 59-64.

Cusack M., Dauphin Y. Chung P., Pérez-Huerta A., and Cuif J.-P. (2008b) Multiscale structure of calcite fibres of the shell of the brachiopod *Terebratulina retusa*, J. Struct. Biol., 164(1), 96-100.

Dauphin Y., Cuif J. P., Mutvei H., and Denis A. (1989) Mineralogy, chemistry and ultrastructure of the external shell-layer in ten species of Haliotis with reference to *Haliotis tuberculata* (Mollusca: Archaeogastropoda), Bull. Geol. Inst. Univ. Uppsala, N. S., (15), 7-38.

Dauphin Y., Ball A. D., Cotte M., Cuif J.-P., Meibom A., Salomé M., Susini J., and Williams C. T. (2008) Structure and composition of the nacre–prisms transition in the shell of *Pinctada margaritifera* (Mollusca, Bivalvia), Anal. Bioanal. Chem., 390(6), 1659-1669.

Davis S. N. and DeWiest R. J. M. (1966) Hydrogeology, John Wiley, London.

de Nooijer L. J., Toyofuku T., and Kitazato H. (2009) Foraminifera promote calcification by elevating their intracellular pH, Proc. Natl. Acad. Sci. U. S. A., 106(36), 15374-15378.

De Villiers, J. P. R. (1971) The crystal structures of aragonite, strontianite, and witherite, Am. Min., (56), 758-767.

De Yoreo J. J., Zepeda-Ruiz L. A., Friddle R. W., Qiu S. R., Wasylenki L. E., Chernov A. A., Gilmer G. H., and Dove P. M. (2009) Rethinking classical crystal growth models through molecular scale insights: consequences of kink-limited kinetics, Cryst. Growth Des., 9, 5135-5144.

Delanghe D., Bard E., and Hamelin B. (2002) New TIMS constraints on the uranium-238 and uranium-234 in seawaters from the main ocean basins and the Mediterranean Sea, Mar. Chem., 80, 79-93.

Demichelis R., Raiteri P., Gale J. D., Quigley D., and Gebauer D. (2011) Stable prenucleation mineral clusters are liquid-like ionic polymers, Nat. Commun., 2, 590.

References

Demichelis R., Raiteri P., Gale J. D., and Dovesi R. (2013) The multiple structures of vaterite, Cryst. Growth Des., 13(6), 2247-2251.

Dickens B. and Bowen J. S. (1971) Refinement of the crystal structure of the aragonite phase of $CaCO_3$, J. Res. Natl. Bur. Stan. Sect. A., 75A(1), 27.

Dominici S. (2001) Taphonomy and paleoecology of shallow marine macrofossil assemblages in a collisional setting (Late Pliocene-Early Pleistocene, Western Emilia, Italy), Palaios, 16(4), 336-353.

Dominici S. (2004) Quantitative taphonomy in sandstones from an ancient fan delta system (Lower Pleistocene, Western Emilia, Italy), Palaios, 19(3), 193-205.

Dove P. M. and Hochella M. F. Jr. (1993) Calcite precipitation mechanisms and inhibition by orthophosphate: in situ oberservations by scanning force microscopy, Geochim. Cosmochim. Acta, 57(3), 705-714.

Eisenhauer A., Wasserburg G. J., Chen J. H., Bonani G., Collins L. B., Zhu Z. R., and Wyrwoll K. H. (1993) Holocene sea-level determination relative to the Australian continent: U/Th (TIMS) and ^{14}C (AMS) dating of coral cores from the Abrolhos Islands, Earth Planet. Sc. Lett., 114(4), 529-547.

Eisenhauer A., Heiss G. A., Sheppard C. R. C., and Dullo W.-C. (1999) Reef and island formation and Late Holocene sea-level changes in the Chagos islands, in: Sheppard R. C. and Seaward M. R. D. (eds.) Ecology of the Chagos Archipelago, Linnean Society Occasional Publications, London, 21-33.

Elliot M., deMenocalm P. B., Linsley B. K., and Howe S. S. (2003) Environmental controls on the stable isotopic composition of *Mercenaria mercenaria*: potential application to paleoenvironmental studies, Geochem. Geophys. Geosyst., 4(7), 1056.

Emerson S., Jahnke R., Bender M., Froelich P., Klinkhammer G., Bowser C., and Setlock G. (1980) Early diagenesis in sediments from the eastern equatorial Pacific: I. Pore water nutrient and carbonate results, Earth Planet. Sci. Lett., 49, 57-80.

England J., Cusack M., and Lee M. R. (2007) Magnesium and sulphur in the calcite shells of two brachiopods, *Terebratulina retusa* and *Novocrania anomala*, Lethaia, 40(1), 2-10.

Enmar R., Stein M., Bar-Matthews M., Sass E., Katz A., and Lazar B. (2000) Diagenesis in live corals from the Gulf of Aqaba I: the effect on paleo-oceanography tracers, Geochim. Cosmochim. Acta, 64(18), 3123-3132.

Estes J. A. (2005) Evolution of large body size in abalones (Haliotis): patterns and implications, Paleobiology, 31(4), 591-606.

Etschmann B., Brugger J., Pearce M. A., Ta C., Brautigan D., Jung M., and Pring A. (2014) Grain boundaries as microreactors during reactive fluid flow: experimental dolomitization of a calcite marble, Contrib. Mineral. Petrol., 168, 1045.

Ewbank G., Manning D. A. C., and Abbott G. D. (1995) The relationship between bitumens and mineralization in the South Pennine Orefield, central England, J. Geol. Soc. London, 152(5), 751-765.

Fabritius H., Walther P., and Ziegler A. (2005) Architecture of the organic matrix in the sternal $CaCO_3$ deposits of *Porcellio scaber* (Crustacea, Isopoda), J. Struct. Biol., 150, 190-199.

Falini G., Albeck S., Weiner S., and Addadi L. (1996) Control of aragonite or calcite polymorphism by mollusk shell macromolecules, Science, 271, 67-69.

Fernández-Díaz L., Pina C. M., Astilleros J. M., and Sánchez-Pastor N. (2009) The carbonatation of gypsum: pathways and pseudomorph formation, Am. Mineral., 94, 1223-1234.

Fischer C. and Lüttge A. (2016) Beyond the conventional understanding of water-rock reactivity, Earth Planet. Sc. Lett., 457, 100-105.

Floquet N., Vielzeuf D., Ferry D., Ricolleau A., Heresanu V., Perrin J., Laporte D., and Fitch A. N. (2015) Thermally induced modifications and phase transformations of red coral Mg-calcite skeletons from infrared spectroscopy and high resolution synchrotron powder diffraction analyses, Cryst. Growth Des., 15(8), 3690-3706.

Flügel E. (2004) Microfacies of carbonate rocks, Springer, Berlin.

Ford D. (1988) Characteristics of dissolutional cave systems in carbonates, in: James N. P. and Choquette P. W. (eds.) Paleokarst, Springer, Berlin.

Foster L. C., Allison N., Finch A. A., Andersson C., and Ninnemann U. S. (2009) Controls on ^{18}O and ^{13}C profiles within the aragonite bivalve *Arctica islandica*, Holocene, 19(4), 549-558.

Fowler A. C. and Yang X.-S. (2003) Dissolution/precipitation mechanisms for diagenesis in sedimentary basins, J. Geophys. Res., 108(B10), 207.

Friedman G. M. (1964) Early diagenesis and lithification in carbonate sediments, J. Sediment. Petrol., 34(4), 777-813.

Frisia S. (1996) Petrographic evidences of diagenesis in speleotherms: some examples, Speleochronos, 7, 21-30.

Frisia S., Borsato A., Fairchild I. J., and McDermott F. (2000) Calcite fabrics, growth mechanisms, and environment of formation in speleotherms from the Italian Alps and southwestern Ireland, J. Sed. Res., 70, 1183-1196.

Frisia S., Borsato A., Fairchild I. J., McDermott F., and Selmo E. M. (2002) Aragonite-calcite relationships in speleotherms (Grotte de Clamouse, France): environment, fabrics, and carbonate geochemistry, J. Sediment. Res., 72(5), 687-699.

Fyfe W. S. and Bischoff J. L (1965) The calcite-aragonite problem, Soc. Econ. Pa., 13, 3-13.

Gaetani M. (1997) The Karakorum Block in Central Asia, from Ordovician to Cretaceous, Sediment. Geol., 109(3-4), 339-359.

Gaetani M., Angiolini L., Garzanti E., Jadoul F., Leven E. Y., Nicora A., and Sciunnach D. (1995) Permian stratigraphy in the Northern Karakorum, Pakistan, Riv. It. Paleont. Strat., 101, 112-158.

Gaetani M., Zanchi A., Angiolini L., Olivini G., Sciunnach D., Brunton H., Nicora A., and Mawson R. (2004) The Carboniferous of the Western Karakoram (Pakistan), J. Asian Earth Sci., 23(2), 275-305.

Gaetani M., Nicora A., Henderson C., Cirilli S., Gale L., Rettori R., Vuolo I., and Atudorei V. (2013) Refinements in the Upper Permian to Lower Jurassic stratigraphy of Karakorum, Pakistan, Facies, 59(4), 915-948.

Gal A., Hirsch A., Siegel S., Li C., Aichmayer B., Politi Y., Fratzl P., Weiner S., and Addadi L. (2012) Plant cystoliths: a complex functional biocomposite of four distinct silica and amorphous calcium carbonate phases, Chemistry, 18(33), 10262-10270.

Garbelli C. (2017) Shell microstructures in Lopingian brachiopods: implication for fabric evolution and calcification, Riv. Ital. Paleontol. Stratigr., 123(3), 541-560.

References

Garbelli C., Angiolini L., Jadoul F., and Brand U. (2012) Micromorphology and differential preservation of Upper Permian brachiopod low-Mg calcite, Chem. Geol., 298-299, 1-10.

Garbelli C., Angiolini L., Brand U., Shen S.-Z., Jadoul F., Posenato R., Azmy K, and Cao C.-Q. (2016) Neotethys seawater chemistry and temperature at the dawn of the end Permian mass extinction, Gondwana Res., 35, 272-285.

Gebauer D. and Cölfen H. (2011) Prenucleation clusters and nonclassical nucleation, Nano Today, 6, 564-584.

Gebauer D., Völkel A., and Cölfen H. (2008) Stable prenucleation calcium carbonate Clusters, Science, 322, 1819-1822.

Gebauer D., Kellermeier M., Gale J. D., Bergström L., and Cölfen H. (2014) Pre-nucleation clusters as solute precursors in crystallisation, Chem. Soc. Rev., 43, 2348–2371.

Geiger D. L. and Owen B. (2012) Abalone: world-wide Haliotidae, ConchBooks, Hackenheim.

Geisler T., Nagel T., Kilburn M. R., Janssen A., Icenhower J. P., Fonseca R. O. C., Grange M., and Nemchin A. A. (2015) The mechanism of borosilicate glass corrosion revisited, Geochim. Cosmochim. Acta, 158(1), 112-129.

Giacovazzo C. (1998) Fundamentals of crystallography, Oxford University Press, Oxford.

Gilbert P. U. P. A., Metzler R. A., Zhou D., Scholl A., Doran A., Young A., Kunz M., Tamura N., and Coppersmith S. N. (2008) Gradual ordering in red abalone nacre, J. Am. Chem. Soc., 130(51), 17519-17527.

Ginsburg R. N., Schroeder J. H., and Shinn E. A. (1971) Recent synsedimentary cementation in subtidal Bermuda reefs, in: Bricker O. P. (ed.) Carbonate cements, The Johns Hopkins University Press, Baltimore, 54-58.

Gladfeiter E. H. (1982) Skeletal development in *Acropora cervicornis*: I. Patterns of calcium carbonate accretion in the axial corallite, Coral Reefs, 1, 45-51.

Goetz A. J., Griesshaber E., Neuser R. D., Lüter C., Hühner M., Harper E., Schmahl W. W. (2009) Calcite morphology, texture and hardness in the distinct layers of rhynchonelliform brachiopod shells, Eur. J. Mineral., 21, 303-315.

Goetz A. J., Steinmetz D. R., Griesshaber E., Zaefferer S., Raabe D., Kelm K., Irsen S., Sehrbrock A., and Schmahl W. W. (2011) Interdigitating bio-calcite dendrites form a 3-D jigsaw structure in brachiopod shells, Acta Biomater., 7, 2237-2243.

Goetz A. J., Griesshaber E., Abel R., Fehr T., Ruthensteiner B., and Schmahl W. W. (2014) Tailored order: the mesocrystalline nature of sea urchin teeth, Acta Biomater., 10, 3885-3898.

Goldsmith J. R., Graf D. L., and Joensuu O. I. (1955) The occurrence of magnesian calcites in nature, Geochim. Cosmochim. Acta, 7(5-6), 212-230.

Goodhew P. J., Humphreys J., and Beanland R. (2001) Electron microscopy and analysis, Taylor & Francis, London.

Gosling E. (2003) Bivalve molluscs: biology, ecology and culture, Blackwell Science, Oxford.

Gothmann A. M., Stolarski J., Adkins J. F., Schöne B., Dennis K. J., Schrag D. P., Mazur M., and Bender M. L. (2015) Fossil corals as an archive of secular variations in seawater chemistry since the Mesozoic, Geochim. Cosmochim. Acta, 160(1), 188-208.

Gower L. B. (2008) Biomimetic model systems for investigating the amorphous precursor pathway and its role in biomineralization, Chem. Rev., 108(11), 4551-4627.

Grandjean J., Grégoire C., and Lutts A. (1964) On the mineral components and the remnants of organic structures in shells of fossil molluscs, Acad. R. Belg. Bull. Sci., 50, 562-595.

Grasby S. E. (2003) Naturally precipitating vaterite (μ-CaCO$_3$) spheres: unusual carbonates formed in an extreme environment, Geochim. Cosmochim. Acta, 67(9), 1659-1666.

Gratier J. P. and Guiget R. (1986) Experimental pressure solution-deposition on quartz grains: the crucial effect of the nature of the fluid, J. Struct. Geol., 8, 845-856.

Grégoire C., Duchateau G., and Florkin M. (1955) La trame protodique des nacres et des perles, Ann. Inst. Oceanogr., Paris, 31, 1-36.

Griesshaber E., Kelm K., Sehrbrock A., Schmahl W. W., Mader W., Mutterlose J., and Brand U. (2007a) Amorphous components in the shell material of the brachiopod *Megerlia truncata*, Geochim. Cosmochim. Acta, 71, Supplement S, A354-354.

Griesshaber E., Schmahl W. W., Neuser R., Pettke Th., Blüm M., Mutterlose, J., and Brand U. (2007b) Crystallographic texture and microstructure of terebratulide brachiopod shell calcite: an optimized materials design with hierarchical architecture, Am. Mineral., 92, 722-734.

Griesshaber E., Neuser R. D., Brand U., and Schmahl W. W. (2007c) Texture and microstructure of modern rhynchonellide brachiopod shells - an ontogenetic study, in: Rollett A. D. (ed.) Applications of Texture Analysis, John Wiley & Sons Inc., Hoboken, NJ, U. S. A., 605-617.

Griesshaber E., Kelm K., Sehrbrock A., Mader W., Mutterlose J., Brand U., and Schmahl W. W. (2009) Amorphous calcium carbonate in the shell material of the brachiopod *Megerlia truncata*, Eur. J. Mineral., 21(4), 715-723.

Griesshaber E., Neuser R. D., and Schmahl W. W. (2010) The application of EBSD analysis to biomaterials: microstructural and crystallographic texture variations in marine carbonate shells, Semin. Soc. Esp. Mineral., 7, 22-34.

Griesshaber E., Goetz A. J., Howard L., Ball A., Ruff S., and Schmahl W. W. (2012) Crystal architecture of the tooth and jaw bone (pyramid) of the sea urchin *Paracentrotus lividus*, Bioinspir. Biomim. Nan., 1(2), 133-139.

Griesshaber E., Schmahl W. W., Singh Ubhi H., Huber J., Nindiyasari F., Maier B., and Ziegler A. (2013) Homoepitaxial meso- and microscale crystal co-orientation and organic matrix network structure in *Mytilus edulis* nacre and calcite, Acta Biomater., 9, 9492-9502.

Griesshaber E., Yin X., Ziegler A., Kelm K., Checa A., Eisenhauer A., and Schmahl W. W. (2017) Patterns of mineral organization in carbonate biological hard materials, in: Heuss-Aßbichler S., Amthauer G., and John M. (eds.) Highlights in applied mineralogy, de Gruyter, Berlin, 245-272.

Gröcke D. R. and Gillikin D. P. (2008) Advances in mollusc sclerochronology and sclerochemistry: tools for understanding climate and environment, Geo.-Mar. Lett., 28(5-6), 265-268.

Grossman E. L., Zhang C., and Yancey T. E. (1991) Stable isotope stratigraphy of brachiopods from Pennsylvanian shales in Texas, Geol. Soc. Am. Bull., 103, 953-965.

Grossman E. L., Mii H.-S., and Yancey T. E. (1993) Stable isotopes in Late Pennsylvanian brachiopods from the United States: implications for Carboniferous paleoceanography, Geol. Soc. Am. Bull., 105, 1284-1296.

References

Grossmann E. L., Mii H.-S., Zhang C., and Yancey, T. E. (1996) Chemical variation in Pennsylvanian brachiopod shells - diagenetic, taxonomic, microstructural and seasonal effects, J. Sediment. Res., 66, 1011-1022.

Guillemet B., Faatz M., Grohn F., Wegner G., and Gnanou Y. (2006) Nanosized amorphous calcium carbonate stabilized by poly(ethylene oxide)-b-poly(acrylic acid) block copolymers, Langmuir, 22(4), 1875-1879.

Gutteridge P. (1995) Late Dinantian (Brigantian) carbonate mud-mounds of the Derbyshire Carbonate Platform, in: Monty C. L. V., Bosence D. W. J., Bridges P. H., and Pratt B. R. (eds.) Carbonate mud-mounds: their origin and evolution, Blackwell Science, Oxford, 289-307.

Hahn S., Rodolfo-Metalpa R., Griesshaber E., Schmahl W. W., Buhl D., Hall-Spencer J. M., Baggini C., Fehr K. T., and Immenhauser A. (2012) Marine bivalve shell geochemistry and ultrastructure from modern low pH environments: environmental effect versus experimental bias, Biogeosciences, 9, 1897-1914.

Hahn S., Griesshaber E., Schmahl W. W., Neuser R. D., Ritter A.-C., Hoffmann R., Buhl D., Niedermayr A., Geske A., and Immenhauser A. (2014) Exploring aberrant bivalve shell ultrastructure and geochemistry as proxies for past sea water acidification, Sedimentology, 61, 1625-1658.

Hamelin B., Bard E., Zindler A., and Fairbanks R. G. (1991) $^{234}U/^{238}U$ mass spectrometry of corals: how accurate is the U-Th age of the last interglacial period?, Earth Planet. Sc. Lett., 106, 169-180.

Han T. Y.-J. and Aizenberg J. (2008) Calcium carbonate storage in amorphous form and its template-induced crystallization, Chem. Mater., 20(3), 1064-1068.

Hanshaw B. B., Black W., and Deike R. G. (1971) A geochemical hypothesis for the dolomitization by groundwater, Econ. Geol., 66, 710-724.

Harlov D. E., Wirth R., and Hetherington C. J. (2011) Fluid-mediated partial alteration in monazite: the role of coupled dissolution–reprecipitation in element redistribution and mass transfer, Contrib. Mineral. Petrol., 162(2), 329-348.

Harper E. M. (1997) The molluscan periostracum: an important constraint in bivalve evolution, Palaeontology, 40, 71-97.

Harper E. M. (1998) The fossil record of bivalve molluscs, in: Donovan S. K. and Paul C. R. C. (eds.) The adequacy of the fossil record, John Wiley and Sons, Chichester, 243-267.

Haszeldine R. S., Macaulay C. I., Marchand A., Wilkinson M., Graham C. M., Cavanagh A., Fallick A. E., and Couples G. D. (2000) Sandstone cementation and fluids in hydrocarbon basins, J. Geo. Exp., 69, 195-200.

Hatchett C. (1799) XVIII. Experiments and observations on shell and bone, Phil. Trans. R. Soc. Lond., 89, 315-334.

Heinemann A., Fietzke J., Eisenhauer A., and Zumholz K. (2008) Modification of Ca isotope and trace metal composition of the major matrices involved in shell formation of *Mytilus edulis*, Geochem. Geophys. Geosyst., 9(1), 1-8.

Helgeson H. C., Delany J. M., Nesbitt H. W., and Byrd D. K. (1978) Summary and critique of the thermodynamic properties of rock-forming minerals, Am. J. Sci., 278A, 1-229.

Hellmann R., Penisson J.-M., Hervig R. L., Thomassin J.-H., and Abrioux M.-F. (2003) An EFTEM/HRTEM high-resolution study of the near surface of labradorite feldspar altered at acid pH: evidence for interfacial dissolution-reprecipitation, Phys. Chem. Miner., 30(4), 192-197.

Hellmann R., Wirth R., Daval D., Barnes J.-P., Penisson J.-M., Tisserand D., Epicier T., Florin B., and Hervig R. L. (2012) Unifying natural and laboratory chemical weathering with interfacial dissolution-reprecipitation: a study based on the nanometer-scale chemistry of fluid-silicate interfaces, Chem. Geol., 294-295, 203−216.

Henderson G. M., Cohen A. S., and O´Nions R. K. (1993) $^{234}U/^{238}U$ ratios and ^{230}Th ages for Hateruma Atoll corals: implications for coral diagenesis and seawater $^{234}U/^{238}U$ ratios, Earth Planet. Sc. Lett., 115, 65-73.

Hendry J. P., Dirchfield P. W., and Marshall J. D. (1995) Two-stage neomorphism of Jurassic aragonitic bivalves: implications for early diagenesis, J. Sediment. Res., A65, 214-224.

Hesse R. (1987) Selective and reversible carbonate-silica replacements in lower Cretaceous carbonate-bearing turbidites of the eastern Alps, Sedimentology, 34, 1055-1077.

Hesse R. (1990) Silica Diagenesis: origin of inorganic and replacement cherts, in: McIlreath I. A. and Morrow D. W. (eds.) Diagenesis, Geosci. Can. Ser., 4, 253-275.

Heydari E. (1997) The role of burial diagenesis in hydrocarbon destruction and H_2S accumulation, Upper Jurassic Smackover Formation, Black Creek Field, Mississippi, AAPG Bull., 81, 26-45.

Hild S., Marti O., and Ziegler A. (2008) Spatial distribution of calcite and amorphous calcium carbonate in the cuticle of the terrestrial crustaceans *Porcellio scaber* and *Armadillidium vulgare*, J. Struct. Biol., 163(1), 100-108.

Hippler D., Buhl D., Witbaard R., Richter D. K., and Immenhauser A. (2009) Towards a better understanding of magnesium-isotope ratios from marine skeletal carbonates, Geochim. Cosmochim. Acta, 73(20), 6134-6146.

Hoffmann R., Richter D. K., Neuser R. D., Jöns N., Linzmeier B. J., Lemanis R. E., Fusseis F., Xiao X., and Immenhauser A. (2016) Evidence for a composite organic–inorganic fabric of belemnite rostra: implications for palaeoceanography and palaeoecology, Sediment. Geol., 341, 203-215.

Hövelmann J., Putnis C. V., Ruiz-Agudo E., and Austrheim H. (2012) Direct nanoscale observations of CO_2 sequestration during brucite $[Mg(OH)_2]$ dissolution, Environ. Sci. Technol., 46, 5253–5260.

Hover V. C., Walter L. M., and Peacor D. R. (2001) Early marine diagenesis of biogenic aragonite and Mg-calcite: new constraints from high-resolution STEM and AEM analyses of modern platform carbonates, Chem. Geol., 175, 221–248.

Howarth R. W. (1979) Pyrite – its rapid formation in a salt marsh and its importance in ecosystem metabolism, Science, 203, 49-51.

Hu X. and Burdige D. J. (2007) Enriched stable carbon isotopes in the pore waters of carbonate sediments dominated by seagrasses: evidence for coupled carbonate dissolution and reprecipitation, Geochim. Cosmochim. Acta, 71(1), 129–144.

References

Huang S.-C., Naka K., and Chujo Y. (2007) A carbonate controlled-addition method for amorphous calcium carbonate spheres stabilized by poly(acrylic acid)s, Langmuir, 23(24), 12086-12095.

Huber J., Griesshaber E., Nindiyasari F., Schmahl W. W., and Ziegler A. (2015) Functionalization of biomineral reinforcement in crustacean cuticle: calcite orientation in the partes incisivae of the mandibles of *Porcellio scaber* and the supralittoral species *Tylos europaeus* (Oniscidea, Isopoda), J. Struct. Biol., 190(2), 173-191.

Immenhauser A., Nägler T. F., Steuber T., and Hippler D. (2005) A critical assessment of mollusk $^{18}O/^{16}O$, Mg/Ca, and $^{44}Ca/^{40}Ca$ ratios as proxies for Cretaceous seawater temperature seasonality, Palaeogeogr. Palaeoclimat. Palaeoecol., 215(3-4), 221-237.

Immenhauser A., Schöne B. R., Hoffmann R., and Niedermayr A. (2015) Mollusc and brachiopod skeletal hard parts: intricate archives of their marine environment, Sedimentology, 63(1), 1-59.

Jacka A. D. (1974) Replacement of fossils by length-slow chalcedony and associated dolomitization, J. Sediment. Petrol., 44, 421-427.

Jackson D. J., McDougall C., Woodcroft B., Moase P., Rose R. A., Kube M., Reinhardt R., Rokhsar D. S., Montagnani C., Joubert C., Piquemal D., and Degnan B. M. (2010) Parallel evolution of nacre building gene sets in molluscs, Mol. Biol. Evol., 27(3), 591-608.

Jacob D. E., Soldati A. L., Wirth R., Huth J., Wehrmeister U., and Hofmeister W. (2008) Nanostructure, composition and mechanisms of bivalve shell growth, Geochim. Cosmochim. Acta, 72(22), 5401-5415.

Jacques T. G. and Pilson M. E. Q. (1980) Experimental ecology of the temperate scleractinian coral *Astrangia danae* I: partition of respiration, photosynthesis and calcification between host and symbionts, Mar. Biol., 60(2-3), 167-178.

Jacques T. G., Marshall N., and Pilson M. E. Q. (1983) Experimental ecology of the temperate scleractinian coral *Astrangia danae*, Mar. Biol., 76(2), 135-148.

James N. P. and Choquette P. W. (1988) Paleokarst, Springer, Berlin.

James N. P. and Ginsburg R. N (1979) The seaward margin of Belize barrier and atoll reefs, Spec. Publ. Int. Assoc. Sedimento., 3, 191.

James N. P. and Jones B. (2016) Origin of carbonate sedimentary rocks, John Wiley & Sons, Chichester, West Sussex, U. K..

James N. P. and Ginsburg R. N., Marszalek D. S., and Choquette P. W. (1976) Facies and fabric specificity of early subsea cements in shallow Belize (British Honduras) reefs, J. Sediment. Res., 46(3), 523-544.

James N. P., Bone Y., and Kyser K. T. (2005) Where has all the aragonite gone? Mineralogy of Holocene neritic cool-water carbonates, Southern Australia, J. Sediment. Res., 75(3), 454-463.

Jamtveit B., Putnis C. V., and Malthe-Sørenssen A. (2009) Reaction induced fracturing during replacement processes, Contrib. Mineral. Petrol., 157(1), 127–133.

Jamtveit B., Kobchenko M., Austrheim H., Malthe-Sørenssen A., Røyne A.,and Svensen H. (2011) Porosity evolution and crystallization-driven fragmentation during weathering of andesite, J. Geophys. Res., 116, B12204.

Janssen A., Putnis A., Geisler T., and Putnis C. V. (2010) The experimental replacement of ilmenite by rutile in HCl solutions, Mineral. Mag., 74(4), 633–644.

Jarosch D. and Heger G. (1986) Neutron diffraction refinement of the crystal structure of aragonite, Tscher. Miner. Petrog., 35, 127-131.

Jonas L., John T., and Putnis, A. (2013) Influence of temperature and Cl on the hydrothermal replacement of calcite by apatite and the development of porous microstructures, Am. Mineral., 98, 1516–1525.

Jonas L., John T., King H. E., Geisler T., and Putnis A. (2014) The role of grain boundaries and transient porosity in rocks as fluid pathways for reaction front propagation, Earth Planet. Sci. Lett., 386, 64–74.

Jonas L., Müller T., Dohmen R., Baumgartner L., and Putlitz B. (2015) Transport-controlled hydrothermal replacement of calcite by Mg-carbonates, Geology, 43(9), 779-782.

Jope H. M. (1965) Composition of brachiopod shell, in: Moore R. C. (ed.) Treatise on invertebrate paleontology (Part H), 1, Geological Society of America, University of Kansas Press, Boulder, CO.

Karney G. B., Butler P. G., Speller S., Scourse J. D., Richardson C. A., Schröder M., Hughes G. M., Czernuszka J. T., and Grovenor C. R. M. (2012) Characterizing the microstructure of *Arctica islandica* shells using NanoSIMS and EBSD, Geochem. Geophys. Geosyst., 13(4), 1-14.

Kasioptas A., Perdikouri C., Putnis C. V., and Putnis A. (2008) Pseudomorphic replacement of single calcium carbonate crystals by polycrystalline apatite, Mineral. Mag., 72(1), 77-80.

Katz A. (1973) The interaction of magnesium with calcite during crystal growth at 25-90 °C and one atmosphere, Geochim. Cosmochim. Acta, 37(6), 1563-1586.

Kemp R. A. and Trueman C. N. (2003) Rare earth elements in Solnhofen biogenic apatite: geochemical clues to the palaeoenvironment, Sediment. Geol., 155, 109-127.

Kerans C., Hurley, N. F., Playford P. E. (1986) Marine diagenesis in Devonian reef complexes of the Canning Basin, Western Australia, in: Schroeder J. H. and Purser B. H. (eds.) Reef diagenesis, Springer, Berlin, 357-380.

Khim B.-K., Woo K. S., and Yoon S. H. (2000a) Comparison of oxygen isotope profile of a fossil bivale with the modern hydrographic condition: case study of the Seoguipo Formation (Korea), Geosci. J., 4(1), 15-24.

Khim B.-K., Woo K. S., and Je J.-G. (2000b) Stable isotope profiles of bivalve shells: seasonal temperature variations, latitudinal temperature gradients and biological carbon cycling along the east coast of Korea, Cont. Shelf Res., 20, 843-861.

Kidwell S. M. (2005) Shell composition has no net impact on large-scale evolutionary patterns in mollusks, Science, 307, 914-917.

King H. E., Plümper O., and Putnis A. (2010) Effect of secondary phase formation on the carbonation of olivine, Environ. Sci. Technol., 44, 6503–6509.

Kinsman D. J. J. (1969) Interpretation of Sr^{2+} concentrations in carbonate minerals and rocks, J. Sed. Petrol., 39, 486-508.

Kitano Y., Park K., and Hood D. W. (1962) Pure aragonite synthesis, J. Geophys. Res., 67, 4873-4874.

References

Kitano Y., Yoshioka S., and Kanamori N. (1972) The transformation of aragonite to calcite in aqueous solutions, Kaseki, 23/24, 15-25. (in Japanese)

Knoll A. H. (2003) Biomineralization and evolutionary history, Rev. Mineral. Geochem., 54(1), 329-356.

Korte C., Kozur H. W., and Veizer J. (2005) $\delta^{13}C$ and $\delta^{18}O$ values of Triassic brachiopods and carbonate rocks as proxies for coeval seawater and palaeotemperature, Palaeogeogr. Palaeoclimat. Palaeoecol., 226(3-4), 287-306.

Krief S., Hendy E. J., Fine M., Yam R., Meibom A., Foster G. L., and Shemesh A. (2010) Physiological and isotopic responses of scleractinian corals to ocean acidification, Geochim. Cosmochim. Acta, 74(17), 4988-5001.

Ku T. C. W., Walter L. M., Coleman M. L., Blake R. E., and Martini A. M. (1999) Coupling between sulfur recycling and syndepositional carbonate dissolution: evidence from oxygen and sulfur isotope composition of pore water sulfate, South Florida Platform, U. S. A., Geochim. Cosmochim. Acta, 63(17), 2529-2546.

Lackner K. S. (2002) Carbonate chemistry for sequestering fossil carbon, Annu. Rev. Energ. Env., 27, 193-232.

Lahann R. W. (1978) A chemical model for calcite crystal growth and morphology control, J. Sediment. Petrol., 48, 337-344.

Lam R. S. K., Charnock J. M., Lennie A., and Meldrum F. C. (2007) Synthesis-dependant structural variations in amorphous calcium carbonate, Cryst. Eng. Comm., 9(12), 1226-1236.

Land L. S. (1967) Diagenesis of skeletal carbonates, J. Sediment. Res., 37(3), 914-930.

Land L. S. and Goreau T. F. (1970) Submarine lithification of Jamaican reefs, J. Sediment. Res., 40(1), 457-462.

Lavoie D. and Bourque P.-A. (1993) Marine, burial, and meteoric diagenesis of Early Silurian carbonate ramps, Quebec Appalachians, Canada, J. Sediment. Petrol., 63, 233-247.

Le Bail A., Ouhenia S., and Chateigner D. (2011) Microtwinning hypothesis for a more ordered vaterite model, Powder Diffraction, 26(1), 16-21.

Le Chatelier H. (1893) Sur la chaleur de formation de l'arragonite, Compt. Rend., 116, 390-392. (in French)

Le Tissier M. D'A. A. (1988) Diurnal patterns of skeleton formation in *Pocillopora damicornis* (Linnaeus), Coral Reefs, 7(2), 81-88.

Leadbeater B. S. C. and Riding R. (1987) Biomineralization in lower plants and animals, Nord. J. Bot., 7(5), 608.

Lebron I. and Suárez D. L. (1996) Calcite nucleation and precipitation kinetics as affected by dissolved organic matter at 25 °C and pH >7.5, Geochim. Cosmochim. Acta, 60(15), 2765-2776.

Leclercq N., Gattuso J.-P., and Jaubert J. (2000) CO_2 partial pressure controls the calcification rate of a coral community, Glob. Change Biol., 6(3), 329-334.

Leitner W. (2000) Green chemistry: designed to dissolve, Nature, 405, 129-130.

Levi-Kalisman Y., Falini G., Addadi L., and Weiner S. (2001) Structure of the nacreous organic matrix of a bivalve mollusk shell examined in the hydrated state using cryo-TEM, J. Struct. Biol., 135(1), 8-17.

Levi-Kalisman Y., Raz S., Weiner S., Addadi L., and Sagi I. (2002) Structural differences between biogenic amorphous calcium carbonate phases using X-ray absorption spectroscopy, Adv. Funct. Mater., 12(1), 43-48.

Lin A. and Meyers M. A. (2005) Growth and structure in abalone shell, Mater. Sci. Eng. A, 390(1-2), 27-41.

Lippmann F. (1973) Sedimentary carbonate minerals, Springer, Berlin.

Logan A. (2007) Geographic distribution of extant articulated brachiopods, in: Selden P. A. (ed.) Treatise on invertebrate paleontology (Part H, Brachiopoda Revised), Geological Society of America, Supplement, 6, University of Kansas Press, Boulder, CO, 3082-3115.

Loste E., Wilson R. M., Seshadri R., and Meldrum F. C. (2003) The role of magnesium in stabilising amorphous calcium carbonate and controlling calcite morphologies, J. Cryst. Growth, 254(1-2), 206-218.

Lowenstam H. A. (1961) Mineralogy, $^{18}O/^{16}O$ ratios, and strontium and magnesium contents of recent and fossil brachiopods and their bearing on the history of the oceans, J. Geol., 69, 241-260.

Lowenstam H. A. (1981) Minerals formed by organisms, Science, 211, 1126-1131.

Lowenstam H. A. and Abbott D. (1975) Vaterite: a mineralization product of the hard tissues of a marine organism (Ascidiacea), Science, 188, 363-365.

Lowenstam H. A. and Weiner S. (1989) On biomineralisation, Oxford University Press, Oxford.

Lüttge A. and Arvidson R. S. (2010) Reactions at surfaces: a new approach integrating inferometry and kinetic simulations, J. Am. Ceram. Soc., 93, 3519-3530.

Lüttge A. and Conrad P. G. (2004) Direct observation of microbial inhibition of calcite dissolution, Appl. Environ. Microb., 70(3), 1627-1632.

MacDonald J., Johna C., and Girard J.-P. (2015) Dolomitization processes in hydrocarbon reservoirs: insight from geothermometry using clumped isotopes, Earth Planet. Sci. Lett., 13, 265-268.

Machel H.-G. and Mountjoy E. W. (1986) Chemistry and environments of dolomitization — a reappraisal, Earth-Sci. Rev., 23, 175-222.

Machel H.-G., Mason R. A., Mariano A. N., and Mucci A. (1991) Causes and emission of luminescence in calcite and dolomite, in: Barker C. E., Burruss R. C., Kopp O. C., Machel H.-G., Marshall D. J., Wright P., and Colbum H. Y. (eds.) Luminescence microscopy and spectroscopy: qualitative and quantitative applications, Short Course Notes, 25, SEPM Society for Sedimentary Geology, Tulsa, Oklahoma, 9-25.

Macintyre I. G. and Mountjoy E. W. (1968) An occurrence of submarine cementation of carbonate sediments off the west coast of Barbados, W. I, J. Sediment. Res., 38(2), 660-664.

Mackenzie C. L., Ormondroyd G. A., Curling S. F., Ball R. J., Whiteley N. M., and Malham S. K. (2014) Ocean warming, more than acidification, reduces shell strength in a commercial shellfish species during food limitation, Plos One, 9(1), e86764.

Maier B. J., Griesshaber E., Alexa P., Ziegler A., Ubhi H. S., and Schmahl W. W. (2014) Biological control of crystallographic architecture: hierarchy and co-alignment parameters, Acta Biomater., 10(9), 3866-3874.

References

Maliva R. G. (1995) Recurrent neomorphic and cement microtextures from different diagenetic environments, Quaternary to late Neogene carbonates, Great Bahama Bank, Sediment. Geol., 97, 1-7.

Maliva R. G. (1998) Skeletal neomorphism – quantitative modeling of a two water diagenetic system, Sediment. Geol., 121, 179-190.

Maliva R. G. and Siever R. (1988a) Mechanism and controls of silification of fossils in limestones, J. Geol., 96, 387-398.

Maliva R. G. and Siever R. (1988b) Diagenetic replacement controlled by force of crystallization, Geology, 16, 688-691.

Maliva R. G., Missimer T. M., and Dickson J. A. D. (2000) Skeletal aragonite neomorphism in Plio-Pleistocene sandy limestones and sandstones, Holloywood, Florida, U.S.A., Sediment. Geol., 136, 147-154.

Mann S. (2001) Biomineralization: principles and concepts in bioinorganic materials chemistry, Oxford University Press, Oxford.

Marchitto T. M., Jones G. A., Goodfriend G. A., and Weidman C. R. (2000) Precise temporal correlation of Holocene mollusk shells using sclerochronology, Quat. Res., 53(2), 236-246.

Marin F. and Luquet G. (2004) Molluscan shell proteins, C. R. Palevol., 3(6-7), 469-492.

Marin F., Luquet G., Marie B., and Medakovic D. (2008) Molluscan shell proteins: primary structure, origin, and evolution, Curr. Top. Dev. Biol., (80), 209-276.

Markgraf S. A. and Reeder R. J. (1985) High-temperature structure refinements of calcite and magnesite, Am. Mineral., 70, 590-600.

Marshall J. F. (1983) Submarine cementation in a high-energy platform reef: One Tree Reef, southern Great Barrier Reef, J. Sediment. Res., 53(4), 1133-1149.

Marshall J. F. (1986) Regional distribution of submarine cements within an epicontinental reef system: Central Great Barrier Reef, Australia in: Schroeder J. H. and Purser B. H. (eds.) Reef diagenesis, Springer, Berlin.

Marshall J. F. and Davies P. J. (1981) Submarine lithification on windward reef slopes: Capricorn-Bunker Group, Southern Great Barrier Reef, J. Sediment. Res., 51(3), 953-960.

Martin G. D., Wilkinson B. H., and Lohmann K. C. (1986) The role of skeletal porosity in aragonite neomorphism - Strombus and Montastrea from the Pleistocene Key Largo Limestone, Florida, J. Sediment. Petrol., 56, 194-203.

Mavromatis V. (2015) Personal communication.

Mavromatis V., Gautier Q., Bosc O., and Schott J. (2013) Kinetics of Mg partition and Mg stable isotope fractionation during its incorporation in calcite, Geochim. Cosmochim. Acta, 114(1), 188-203.

McAllister J. E. and Brand U. (1989) Geochemistry of some Ordovician and Devonian trilobite cuticles from North America, Chem. Geol., 78, 51-63.

McClintock J. B., Amsler M. O., Angus R. A., Challener R. C., Schram J. B., Amsler C. D., Mah C. L., Cuce J., and Baker B. J. (2011) The Mg-calcite composition of Antarctic echinoderms: important implications for predicting the impacts of ocean acidification, J. Geol., 119(5), 457-466.

McCoy, V., Soriano C., and Gabbott S. (2018) A review of preservational variation of fossil inclusions in amber of different chemical groups, Earth Env. Sci.T. R. So., 107(2-3), 203-2011.

McGregor H. V. and Gagan M. K. (2003) Diagenesis and geochemistry of porites corals from Papua New Guinea, Geochim. Cosmochim. Acta, 67(12), 2147-2156.

Meibom A., Cuif J.-P., Hillion F., Constantz B. R., Juillet-Leclerc A., Dauphin Y., Watanabe T., and Dunbar R. B. (2004) Distribution of magnesium in coral skeleton, Geophys. Res. Lett., 31(23), L23306.

Meibom A., Yurimoto H., Cuif J.-P., Domart-Coulon I., Houlbreque F., Constantz B., Dauphin Y., Tambutté E., Tambutté S., Allemand D., Wooden J., and Dunbar R. (2006) Vital effects in coral skeletal composition display strict three-dimensional control, Geophys. Res. Lett., 33(11), L11608.

Meibom A., Mostefaoui S., Cuif J.-P., Dauphin Y., Houlbreque F., Dunbar R., and Constantz B. (2007) Biological forcing controls the chemistry of reef-building coral skeleton, Geophys. Res. Lett., 34(2), L02601.

Melim L. A., Westphal H., Swart P. K., Eberli G. P., and Munnecke A. (2002) Questioning carbonate diagenetic paradigms: evidence from the Neogene of the Bahamas, Mar. Geol., 185, 27–53.

Metzger C. A., Terry D. O., and Grandstaff D. E. (2004) Effect of paleosol formation on rare earth element signatures in fossil bone, Geology, 32, 467-500.

Metzger W. J. and Barnard W. M. (1968) Transformation of aragonite to calcite under hydrothermal conditions, Am. Mineral., 53, 295-300.

Metzler R. A., Abrecht M., Olabisi R. M., Ariosa D., Johnson C. J., Frazer B. H., Coppersmith S. N., and Gilbert P. U. P. A. (2007) Architecture of columnar nacre, and implications for its formation mechanism, Phys. Rev. Lett., 98, 268102.

Meyers M. A., Lin A. Y.-M., Chen P.-Y., and Muyco J. (2008) Mechanical strength of abalone nacre: role of the soft organic layer, J. Mech. Behav. Biomed., 1(1), 76-85.

Milke R., Neusser G., Kolzer K., and Wunder B. (2013) Very little water is necessary to make a dry solid silicate system wet, Geology, 41(2), 247–250.

Miller W. L. and Zepp R. G. (1995) Photochemical production of dissolved inorganic carbon from terrestrial organic matter: significance to the oceanic organic carbon cycle, Geophys. Res. Lett., 22(4), 417-420.

Milliman J. D. (1974) Marine Carbonates, Springer, Berlin.

Mitsuguchi T., Matsumoto E., Abe O., Uchida T., and Isdale P. J. (1996) Mg/Ca Thermometry in coral skeletons, Science, 274, 961-963.

Möller P. and Kubanek F. (1976) Role of magnesium in nucleation process of calcite, aragonite and dolomite, Neues Jahrb. Miner. Abh., (126), 199-220.

Moore C. H. (1997) Carbonate diagenesis and porosity, Elsevier, Amsterdam.

Morse J. W. (1983) The kinetics of calcium carbonate dissolution and precipitation, in: Reeder R. J. (ed.) Carbonates: mineralogy and chemistry, Mineral. Soc. Am., Bookcrafters Inc., Chelsea, Mich., 227-264.

References

Morse J. W. (2003) Formation and diagenesis of carbonate sediments, in: Mackenzie F. T., Holland H. D., and Turekian K. K. (eds.) Sediments, diagenesis, and sedimentary rocks: treatise on Geochemistry, 7, Elsevier, Amsterdam, 67-85.

Morse J. W. and Casey W. H. (1988) Ostwald processes and mineral paragenesis in sediments, Am. J. Sci., 288, 537–560.

Morse J. W. and Mackenzie F. T. (1990) Geochemistry of Sedimentary Carbonates, Developments in Sedimentology, 48, Elsevier, Amsterdam.

Morse J. W., Mucci A., and Millero F. J. (1980) The solubility of calcite and aragonite in seawater of 35 % salinity at 25 °C and atmospheric pressure, Geochim. Cosmochim. Acta, 44(1), 85-94.

Morse J. W., Wang Q., and Tsio M. Y. (1997) Influences of temperature and Mg:Ca ratio on $CaCO_3$ precipitates from seawater, Geology, 25, 85-87.

Morse J. W., Andersson A. J., and Mackenzie F. T. (2006) Initial responses of carbonate-rich shelf sediments to rising atmospheric pCO_2 and "ocean acidification": role of high Mg-calcites, Geochim. Cosmochim. Acta, 70(23), 5814-5830.

Morse J. W., Arvidson R. S., and Lüttge A. (2007) Calcium carbonate formation and dissolution, Chem.Rev., 107(2), 342-381.

Mortimer C. E. and Müller U. (2007) Chemie, Thieme, Stuttgart.

Morton B. (2011) The biology and functional morphology of *Arctica islandica* (Bivalvia: Arcticidae): a gerontophilic living fossil, Mar. Biol. Res., 7, 540-553.

Mucci A. and Morse, J. W. (1990) The chemistry of low temperature abiotic calcites: experimental studies on coprecipitation, stability and fractionation, Rev. Aquat. Sci., 3, 217-254.

Mucci A., Canuel R., and Zhong S. (1989) The solubility of calcite and aragonite in sulfate-free seawater and the seeded growth kinetics and composition of the precipitates at 25 °C, Chem. Geol., 74, 309-320.

Mugnaioli E., Andrusenko I., Schüler T., Loges N., Dinnebier R. E., Panthöfer M., Tremel W., and Kolb U. (2012) Ab initio structure determination of vaterite by automated electron diffraction, Angew. Chem. Int. Ed., 51, 7041-7045.

Munnecke A., Westphal H., and Kölbl-Ebert M. (2008) Diagenesis of plattenkalk: examples from the Solnhofen area (Upper Jurassic, southern Germany), Sedimentology, 55(6), 1931-1946.

Mutvei H. (1978) Ultrastructural characteristics of the nacre of some gastropods, Zool. Scr., 7, 287-296.

Mutvei H. (1980) The nacreous layer in molluscan shells, in: Omori M. and Watabe N. (eds.) The mechanisms of biomineralisation in animals and plants, Tokai University Press, 49-56.

Naganuma T., Hoshino W., Shikanai Y., Sato R., Liu K., Sato S., Muramoto K., Osada M., Yoshimi K., and Ogawa T. (2014) Novel matrix proteins of Pteria penguin pearl oyster shell nacre homologous to the jacalin-related beta-prism fold lectins, Plos One, 9(11), e112326.

Nahon D. and Merino E. (1997) Pseudomorphical replacement in tropical weathering: evidence, geochemical consequences, and kinetic-rheological origin, Am. J. Sci., 297, 393-417.

Nakahara H. (1983) Calcification of gastropod nacre, in: Westbroek P., and de Jong E. W. (eds.), Biomineralization and biological metal accumulation, Springer, Berlin, 225-230.

Nakahara H. (1991) Nacre formation in bivalve and gastropod mollusks, in: Suga S. and Nakahara H. (eds.) Mechanisms and phylogeny of mineralization in biological systems, Springer, Tokyo, 343-350.

Nakamura M. and Watson E. B. (2001) Experimental study of aqueous fluid infiltration into quartzite: implications for the kinetics of fluid redistribution and grain growth driven by interfacial energy reduction, Geofluids, 1(2), 73–89.

Nakayama S., Suzuki M., Endo H., Iimura K., Kinoshita S., Watabe S., Kogure T., and Nagasawa H. (2013) Identification and characterization of a matrix protein (PPP-10) in the periostracum of the pearl oyster, *Pinctada fucata*, FEBS Open Bio, 3, 421-427.

Navrotsky A. (2004) Energetic clues to pathways to biomineralization: precursors, clusters, and nanoparticles, Proc. Natl. Acad. Sci. U. S. A., 101, 12096-12101.

Neuser R. D., Bruhn F., Götze J., Habermann D., and Richter D. K. (1995) Kathodolumineszenz: Methodik und Anwendung, Zentralbl. Geol. Palaeontol., Teil 1, H 1/2, 287-306.

Nielsen J. K., Błażejowski B., and Gieszcz P. (2013) Carbon and oxygen isotope records of Permian brachiopods from relatively low and high palaeolatitudes: climatic seasonality and evaporation. Geol. Soc. London Spec. Publ., 376(1), 387-406.

Nindiyasari F., Fernández-Díaz L., Griesshaber E., Astilleros J. M., Sánchez-Pastor N., and Schmahl W. W. (2014) Influence of gelatin hydrogel porosity on the crystallization of $CaCO_3$, Cryst. Growth Des., 14(4), 1531-1542.

Nindiyasari F., Ziegler A., Griesshaber E., Fernández-Díaz L., Huber J., Walther P., and Schmahl W. W. (2015) Effect of hydrogel matrices on calcite crystal growth morphology, aggregate formation, and co-orientation in biomimetic experiments and biomineralization environments, Cryst. Growth Des., 15(6), 2667-2685.

Norberg N., Neusser G., Wirth R., and Harlov D. (2011) Microstructural evolution during experimental albitization of K-rich alkali feldspar, Contrib. Mineral. Petrol., 162, 531–546.

Novoa J. J., Braga D., and Addadi L. (2008) Engineering of crystalline materials properties, Springer, Berlin.

Oberthür T., Weiser T. W., Melcher F., Gast L., and Wöhrl C. (2013) Detrital platinum-group minerals in rivers draining the Great Dyke, Zimbabwe, Can. Mineral., 51, 197-222.

Oeschger R. and Storey K. B. (1993) Impact of anoxia and hydrogen sulphide on the metabolism of *Arctica islandica* L. (Bivalvia), J. Exp. Mar. Biol. Ecol., 170, 213-226.

Ogilvie M. M. (1896) Systematic study of Madreporan corals, Phil. Trans. Roy. Soc. London, 187, 83-345.

Ogino T., Suzuki T., and Sawada K. (1987) The formation and transformation mechanism of calcium carbonate in water, Geochim. Cosmochim. Acta, 51, 2757–2767.

Oliver N. H. S., Cleverley J. S., Mark G., Pollard P. J., Fu B., Marshall L. J., Rubenach M. J., Williams P. J., and Baker T. (2004) Modeling the role of sodic alteration in the genesis of iron oxide-copper-gold deposits, Eastern Mount Isa Block, Australia, Econ. Geol., 99(6), 1145-1176.

Olson I. C., Kozdon R., Valley J. W., and Gilbert P. U. P. A. (2012) Mollusk shell nacre ultrastructure correlates with environmental temperature and pressure, J. Am. Chem. Soc., 134(17), 7351-7358.

References

Oomori T., Kaneshima H., Maezato Y., and Kitano Y. (1987) Distribution coefficient of Mg^{2+} ions between calcite and solution at 10-50 °C, Mar. Chem., 20, 327-336.

Otálora F. and García-Ruiz J. (2014) Nucleation and growth of the Naica giant gypsum crystals, Chem. Soc. Rev., 43(7), 2013–2026.

Pagel M., Barbin V., Blanc P., and Ohnenstetter D. (2000) Cathodoluminescence in geosciences, Springer, Berlin.

Palmer A. R. (1983) Relative cost of producing skeletal organic matrix versus calcification: evidence from marine gastropods, Mar. Biol., 75(2-3), 287-292.

Palmer A. R. (1992) Calcification in marine molluscs: how costly is it?, Proc. Natl. Acad. Sci. U. S. A., 89(4), 1379-1382.

Parkinson D., Curry G. B., Cusack M., and Fallick A. E. (2005) Shell structure, patterns and trends of oxygen and carbon stable isotopes in modern brachiopod shells, Chem. Geol., 219, 193-235.

Patterson W. P. and Walter L. M. (1994) Sydepositional diagenesis of modern platform carbonates: evidence from isotopic and minor element data, Geology, 22, 127-130.

Pecharsky V. and Zavalij P. (2009) Fundamentals of powder diffraction and structural characterization of materials, Springer, Berlin.

Pedrosa E. T., Putnis C. V., and Putnis A. (2016) The pseudomorphic replacement of marble by apatite: the role of fluid composition, Chem. Geol., 425, 1-11.

Pelosio G. and Raffi S. (1977) Preliminary remarks on mollusc assemblages of the Stirone river Pleistocene series (Parma Province, Northern Italy), X INQUA Congress, Birmingham, 1-19.

Perdikouri C., Kasioptas A., Putnis C. V., and Putnis A. (2008) The effect of fluid composition on the mechanism of the aragonite to calcite transition, Mineral. Mag., 72(1), 111-114.

Perdikouri C., Kasioptas A., Geisler Schmidt B. C., and Putnis A. (2011) Experimental study of the aragonite to calcite transition in aqueous solution, Geochim. Cosmochim. Acta, 75(20), 6211-6224.

Perdikouri C., Piazolo S., Kasioptas A., Schmidt B. C., and Putnis A. (2013) Hydrothermal replacement of aragonite by calcite: interplay between replacement, fracturing and growth, Eur. J. Mineral., 25(2), 123–136.

Pérez-Huerta A., Cusack M., and England J. (2007) Crystallography and diagenesis in fossil Craniid brachiopods, Palaeontology, 50(4), 757-763.

Pérez-Huerta A., Cusack M., and Zhu W. (2008) Assessment of crystallographic influence on material properties of calcite brachiopods, Mineral. Mag., 72(2), 563-568.

Pérez-Huerta A., Cusack M., McDonald S., Marone F., Stampanoni M., and MacKay S. (2009) Brachiopod punctae: a complexity in shell biomineralisation, J. Struct. Biol., 167(1), 62-67.

Pérez-Huerta A., Dauphin Y., Cuif J. P., and Cusack M. (2011) High resolution electron backscatter diffraction (EBSD) data in recent biogenic carbonates: implications for detecting the effects of diagenesis, Micron, 42, 246-251.

Pérez-Huerta A., Dauphin Y., and Cusack M. (2013) Biogenic calcite granules - Are brachiopods different?, Micron, 44, 395-403.

Peterman Z. E., Hedge C. E., and Tourtelot H. A.(1970) Isotopic composition in seawater throughout the Phanerozoic time, J. Geochem. Meteorol. Soc., 34, 105-120.

Petzow G. (2006) Metallographisches, keramographisches und plastographisches Ätzen, Gebrüder Borntraeger, Berlin/Stuttgart.

Pina C. M., Becker U., Risthaus P., Bosbach D., and Putnis A. (1998) Molecular-scale mechanisms of crystal growth in barite, Nature, 395, 483-486.

Pingitore N. E. Jr. (1976) Vadose and phreatic diagenesis processes, products, and their recognition in corals, J. Sediment. Petrol., 46, 985-1006.

Plummer L. and Busenberg E. (1982) The solubilities of calcite, aragonite and vaterite in CO_2-H_2O solutions between 0 and 90 °C, and an evaluation of the aqueous model for the system $CaCO_3$-CO_2-H_2O, Geochim. Cosmochim. Acta, 46(6), 1011-1040.

Plummer L. N. and Mackenzie F. T. (1974) Predicting mineral solubility from rate data: application to the dissolution of magnesian calcites, Am. J. Sci., 274, 61-83.

Pokrovsky O. S. and Schott J. (2001) Kinetics and mechanism of dolomite dissolution in neutral to alkaline solutions revisited, Am. J. Sci., 301, 597–626.

Pokroy B., Demensky V., and Zolotoyabko E. (2009) Nacre in mollusk shells as a multilayered structure with strain gradient, Adv. Funct. Mater., 19(7), 1054-1059.

Pokroy B., Kabalah-Amitai L., Polishchuk I., DeVol R. T., Blonsky A. Z., Sun C.-Y., Marcus M. A., Scholl A., and Gilbert P. U. P. A. (2015) Narrowly distributed crystal orientation in biomineral vaterite, Chem. Mater., 27(19), 6516-6523.

Politi Y., Levi-Kalisman Y., Raz S., Wilt F., Addadi L., Weiner S., and Sagi I. (2006) Structural characterization of the transient amorphous calcium carbonate precursor phase in sea urchin embryos, Adv. Funct. Mater., 16(10), 1289-1298.

Pollok K., Putnis C. V., and Putnis A. (2011) Mineral replacement reactions in solid solution-aqueous solution systems: volume changes, reactions paths and end-points using the example of model salt systems, Am. J. Sci., 311(3), 211–236.

Popp B. N., Podosek F. A., Brannon J. C., Anderson T. F., and Pier J. (1986) [87]Sr/[86]Sr ratios in Permo-Carboniferous seawater from the analyses of well-preserved brachiopod shells, Geochim. Cosmochim. Acta, 50(7), 1321-1328.

Pouchou J. L. and Pichoir F. (1984) A new model for quantitative X-ray microanalysis part I: application to the analysis of homogeneous samples, Rech. Aérosp., 3, 13-38.

Pouget E. M., Bomans P. H. H., Goos J. A. C. M., Frederik P. M., de With G., and Sommerdijk N. A. J. M. (2009) The initial stages of template-controlled $CaCO_3$ formation revealed by cryo-TEM, Science, 323, 1455–1458.

Press F., Siever R., and Grotzinger J. (2011) Allgemeine Geologie, Spektrum Akademischer Verlag, Berlin.

Prieto M., Putnis A., and Fernández-Díaz L. (1993) Crystallization of solid solutions from aqueous solutions in a porous medium: zoning in (Ba, Sr)SO_4, Geol. Mag., 130(3), 289-299.

Prior D. J., Boyle A. P., Brenker F., Cheadle M. C., Day A., Lopez G., Peruzzo L., Potts G J., Reddy S., Spiess R., Timms N. E., Trimby P., Wheeler J., and Zetterström L. (1999) The application of electron backscatter diffraction and orientation contrast imaging in the SEM to textural problems in rocks, Am. Mineral., 84, 1741-1759.

Przeniosło R., Stolarski J., Mazur M., and Brunelli M. (2008) Hierarchically structured scleractinian coral biocrystals, J. Struct. Biol., 161(1), 74-82.

References

Putnis A. (2002) Mineral replacement reactions: from macroscopic observations to microscopic mechanisms, Mineral. Mag., 66(5), 689-708.

Putnis A. (2009) Mineral replacement reactions, Rev. Mineral. Geochem., 70, 87-124.

Putnis A. and Austrheim H. (2010) Fluid-induced processes: metasomatism and metamorphism, Geofluids, 10, 254–269.

Putnis A. and Austrheim H. (2013) Mechanisms of metasomatism and metamorphism on the local mineral scale: the role of dissolution-reprecipitation during mineral reequilibration, in: Harlov D. E. and Austrheim H. (eds.), Metasomatism and the chemical transformation of rock, Springer, Berlin, 141-170.

Putnis A. and John T. (2010) Replacement processes in the Earth´s crust, Elements, 6, 159-164.

Putnis A. and Mauthe G. (2001) The effect of pore size on cementation in porous rocks, Geofluids, 1(1), 37–41.

Putnis A. and Putnis C. V. (2007) The mechanism of reequilibration of solids in the presence of a fluid phase, J. Solid State Chem., 180, 1783-1786.

Putnis A., Prieto M., and Fernández-Díaz L. (1995) Fluid supersaturation and crystallization in porous media, Geol. Mag., 132(1), 1-13.

Putnis C. V. and Fernández-Díaz L. (2010) Ion partitioning and element mobilization during mineral replacement reactions in natural and experimental systems, EMU Notes Mineralog., 10(1), 189-226.

Putnis C. V. and Mezger K. (2004) A mechanism of mineral replacement: isotope tracing in the model system KCl-KBr-H_2O, Geochim. Cosmochim. Acta, 68(13), 2839–2848.

Putnis C. V. and Ruíz-Agudo E. (2013) The mineral-water-interface: where minerals react with the environment, Elements, 9, 177-182.

Putnis C. V., Tsukamoto K., and Nishimura Y. (2005) Direct observations of pseudomorphism: compositional and textural evolution at a fluid–solid interface, Am. Mineral. 90(11-12), 1909-1912.

Putnis C. V., Geisler T., Schmid-Beurmann P., Stephan T., and Giampaolo C. (2007) An experimental study of the replacement of leucite by analcime, Am. Mineral., 92(1), 19–26.

Qian G., Brugger J., Skinner W. M., Chen G., and Pring A. (2010) An experimental study of the mechanism of the replacement of magnetite by pyrite up to 300 °C, Geochim. Cosmochim. Acta, 74(19), 5610-5630.

Qiao L., Feng Q.-L., and Li Z. (2007) Special vaterite found in freshwater lackluster pearls, Cryst. Growth Des., 7(2), 275-279.

Rachlin A. L., Henderson G. S., and Goh M. C. (1992) An atomic force microscope (AFM) study of the calcite cleavage plane: image averaging in Fourier space, Am. Min., (77), 904-910.

Radha A. V. and Navrotsky A. (2013) Thermodynamics of carbonates, Rev. Mineral. Geochem., 77(1), 73-121.

Radha A. V., Forbes T. Z., Killian C. E., Gilbert P. U. P. A., and Navrotsky A. (2010) Transformation and crystallization energetic of synthetic and biogenic amorphous calcium carbonate, Proc. Natl. Acad. Sci. U. S. A., 107, 16438-16443.

Raffi S. (1986) The significance of marine boreal molluscs in the Early Pleistocene faunas of the Mediterranean area, Palaeogeogr. Palaeoclimat. Palaeoecol., 52(3-4), 267-289.

Raiswell R. and Berner R. A. (1985) Pyrite formation in euxinic and semieuxinic sediments, Am. J. Sci., 285, 710-724.

Randle V. and Engler O. (2000) Introduction to texture analysis, CRC Press, Amsterdam.

Rashid R., Eisenhauer A., Stocchi P., Liebetrau V., Fietzke J., Rüggeberg A., and Dullo W.-C. (2014) Constraining mid to late Holocene relative sea level change in the southern equatorial Pacific Ocean relative to the Society Islands, French Polynesia, Geochem. Geophys. Geosyst., 15(6), 2601-2615.

Raufaste C., Jamtveit B., John T., Meakin P., and Dysthe D. K. (2011) The mechanism of porosity formation during solvent-mediated phase transformations, Proc. Roy. Soc. London, Ser. A Math. Phys. Eng. Sci., 467, 1408–1426.

Raz S., Testeniere O., Hecker A., Weiner S., and Luquet G. (2002) Stable amorphous calcium carbonate is the main component of the calcium storage structures of the crustacean *Orchestia cavimana*, Biol. Bull., 203(3), 269-274.

Raz S., Hamilton P. C., Wilt F. H., Weiner S., and Addadi L. (2003) The transient phase of amorphous calcium carbonate in sea urchin larval spicules: the involvement of proteins and magnesium ions in its formation and stabilization, Adv. Funct. Mater., 13(6), 480-486.

Reddy M. M. and Wang K. K. (1980) Crystallization of calcium carbonate in the presence of metal ions – I. Inhibition of magnesium ion at pH 8.8 and 25 °C, J. Cryst. Growth, 50, 470-480.

Redfern S. A. T., Salje E., and Navrotsky A. (1989) High-temperature enthalpy at the orientational order-disorder transition in calcite: implications for the calcite/aragonite phase equilibrium, Contrib. Mineral. Petr., 101, 479-484.

Reeder R. J. (1990) Carbonates: mineralogy and chemistry, Mineralogical Soc. of America, Washington, D.C..

Regenberg M., Nürnberg D., Schönfeld J., and Reichart G. J. (2007) Early diagenetic overprint in Caribbean sediment cores and its effect on the geochemical composition of planktonic foraminifera, Biogeosciences, 4, 957-973.

Reid R. P. and Macintyre I. G. (1998) Carbonate recrystallization in shallow marine environments: a widespread diagenetic process forming micritized grains, J. Sed. Res., 68, 928–946.

Renard F., Brosse É., and Gratier J. P. (2000) The different processes involved in the mechanism of pressure solution in quartz rich rocks and their interactions, in: Worden R. H. and Morad S. (eds.) Quartz cement in oil field sandstones, Int. As. Sed., 29, 67-78.

Revil A. (2001) Pervasive pressure solution transfer in a quartz sand, J. Geophys. Res., 106(B5), 8665-8686.

Rexfort A. and Mutterlose J. (2009) The role of biogeography and ecology on the isotope signature of cuttlefishes (Cephalopoda, Sepiidae) and the impact on belemnite studies, Palaeogeogr. Palaeoclimat. Palaeoecol., 284(3-4), 153-163.

Richardson C. A. (2001) Molluscs as archives of environmental change, Oceanogr. Mar. Biol., 39, 103-164.

Richardson J. R. (1997) Ecology of articulated brachiopods, in: Kaesler R. L. (ed.) Treatise on invertebrate paleontology (Part H, Brachiopoda Revised), 1, Geological Society of America, University of Kansas Press, Boulder, CO, 441-462.

References

Richter D. K. (1974) Zur subaerischen Diagenese von Echinidenskeletten und das relative Alter pleistozäner Karbonatterrassen bei Korinth (Griechenland), Neues Jahrb. Geol. Paläontol., Abh., 146, 51-77.

Richter D. K., Götte T., Götze J., and Neuser R. D. (2003) Progress in application of cathodoluminescence (CL) in sedimentary petrology, Miner. Petrol., 79(3-4), 127-166.

Riechelmann S., Mavromatis V., Buhl D., Dietzel M., Eisenhauer A., and Immenhauser A. (2016) Impact of diagenetic alteration on brachiopod shell magnesium isotope (δ^{26}Mg) signatures: experimental versus field data, Chem. Geol., 440, 191–206.

Ritter A.-C., Mavromatis V., Dietzel M., Wiethoff F., Griesshaber E., Casella L. A., Schmahl W. W., Koelen J., Neuser R. D., Leis A., Buhl D., Niedermayr A., Bernasconi S. M., and Immenhauser A. (2017) Exploring the impact of diagenesis on (isotope)geochemical and microstructural alteration features in biogenic aragonite, Sedimentology, 64(5), 1354-1380.

Roark A., Grossman E. L., and Lebold J. (2015) Low seasonality in central equatorial Pangea during a late Carboniferous highstand based on high-resolution isotopic records of brachiopod shells, Geol. Soc. Am. Bull., 128(3-4), 597-608.

Rodriguez-Blanco J. D., Shaw S., and Benning L. G. (2011) The kinetics and mechanisms of amorphous calcium carbonate (ACC) crystallization to calcite, via vaterite, Nanoscale, 3(1), 265-271.

Rodríguez-Carvajal J. (2001) Recent developments of the program FULLPROF, Commission on Powder Diffraction (IUCr), Newsletter, 26, 12-19.

Rodriguez-Navarro C., Kudłacz K., Cizer Ö., and Ruiz-Agudo E. (2015) Formation of amorphous calcium carbonate and its transformation into mesostructured calcite, Cryst. Eng. Comm., 17, 58–72.

Rollins H. B., Eldredge N., and Spiller J. (1971) Gastropoda and monoplacophora of the Solsville members (Middle Devonian, Marcellus Formation) in the Chennango Valley, New York State, Am. Mus. Nat. Hist., 144, 131-170.

Roncal-Herrero T., Astilleros J. M., Bots P., Diego J., Blanco R., Prieto M., Benning L. G., and Fernández-Díaz L. (2017) Reaction pathways and textural aspects of the replacement of anhydrite by calcite at 25 °C, Am. Mineral., 120, 1270-1278.

Rousseau M., Lopez E., Stempflé P., Brendlé M., Franke L., Guette A. Naslain R., and Bourrat X. (2005) Multiscale structure of sheet nacre, Biomaterials, 26, 6254-6262.

Rude P. D. and Aller R. C. (1991) Fluorine mobility during early diagenesis of carbonate sediments: an indicator of mineral transformations, Geochim. Cosmochim. Acta, 55(9), 2491–2509.

Ruggiero E. T. (2001) Brachiopods of the Isca submarine cave: observations during ten years, in: Brunton H., Robin L., Cocks M., and Long S. M. (eds.) Brachiopods, past and present, Taylor and Francis, New York, NY.

Ruíz-Agudo E. and Putnis C. V. (2012) Direct observations of mineral-fluid reactions using atomic force microscopy: the specific example of calcite, Mineral. Mag., 76, 227-253.

Ruíz-Agudo E., Putnis C. V., Rodriguez-Navarro C., and Putnis A. (2012) Mechanism of leached layer formation during chemical weathering of silicate minerals, Geology, 40, 947-950.

Ruíz-Agudo E., Álvarez-Lloret P., Putnis C. V., Rodriguez-Navarro A. B., and Putnis A. (2013) Influence of chemical and structural factors on the calcite-calcium oxalate transformation, Cryst. Eng. Comm., 15(46), 9968.

Ruíz-Agudo E., Putnis C. V., and Putnis A. (2014) Coupled dissolution and precipitation at mineral-fluid interfaces, Chem. Geol., 383, 132-146.

Runnegar B. (1985) Shell microstructures of Cambrian molluscs replicated by phosphate, Alcheringa, 9, 245-257.

Runnegar B. and Bengtson S. (1990) Origin of hard parts – early skeletal fossils, in: Briggs D. E. G. and Crowther P. R. (eds.) Palaeobiology: a synthesis, Blackwell Scientific Publications, Oxford, 24-29.

Ruppert E. E., Fox R. S., and Barnes R. D. (2004) Invertebrate zoology: a functional evolutionary approach, Cengage Learning Services, Australia, Brazil, Japan, Korea.

Rush P. F. and Chafetz H. S. (1990) Fabric-retentive, non-luminescent brachiopods as indicators of original ^{13}C and [18]O compositions: a test, J. Sediment. Petrol., 60, 968-981.

Rutter E. H. (1983) Pressure solution in nature, theory and experiment, J. Geol. Soc. London, 140, 725-740.

Saldi G. D., Jordan G., Schott J., and Oelkers E. H. (2009) Magnesite growth rates as a function of temperature and saturation state, Geochim. Cosmochim. Acta, 73(19), 5646-5657.

Saldi G. D., Schott J., Pokrovsky O. S., Gautier Q., and Oelkers E. H. (2012) An experimental study of magnesite precipitation rates at neutral to alkaline conditions and 100-200 °C as a function of pH, aqueous solution composition and chemical affinity, Geochim. Cosmochim. Acta, 83, 93-109.

Saller A. H. (1984) Petrologic and geochemical constraints on the origin of subsurface dolomite, Enewetak Atoll: an example of dolomitization by normal seawater, Geology, 12(4), 217-220.

Samtleben C., Munnecke A., and Bickert T. (2001) Shell succession, assemblage and species dependent effects on the C/O-isotopic composition of brachiopods - examples from the Silurian of Gotland, Chem. Geol., 175, 61-107.

Sandberg P. A. and Hudson J. D. (1983) Aragonite relic preservation in Jurassic calcite-replaced bivalves, Sedimentology, 30, 879-892.

Saruwatari K., Matsui T., Mukai H., Nagasawa H., and Kogure T. (2009) Nucleation and growth of aragonite crystals at the growth front of nacres in pearl oyster, *Pinctada fucata*, Biomaterials, 30(16), 3028-3034.

Sass E., Morse J. W., and Millero F. J. (1983) Dependence of the values of calcite and aragonite thermodynamic solubility products on ionic models, Am. J. Sci., 283, 218-229.

Sassoni E., Naidu S., and Scherer G. W. (2011) The use of hydroxyapatite as a new inorganic consolidant for damaged carbonate stones, J. Cult. Herit., 12(4), 346-355.

Sato A., Nagasaka S., Furihata K., Nagata S., Arai I., Saruwatari K., Kogure T., Sakuda S., and Nagasawa H. (2011) Glycolytic intermediates induce amorphous calcium carbonate formation in crustaceans, Nat. Chem. Biol., 7(4), 197-199.

Sawada K. (1997) The mechanisms of crystallization and transformation of calcium carbonates, Pure Appl. Chem., 69(5), 921-928.

References

Sayani H. R., Cobb K. M., Cohen A. L., Elliott W. C., Nurhati I. S., Dunbar R. B., Rose K. A., and Zaunbrecher L. K. (2011) Effects of diagenesis on paleoclimate reconstructions from modern and young fossil corals, Geochim. Cosmochim. Acta, 75(21), 6361-6373.

Sayles F. L. (1980) The solubility of $CaCO_3$ in seawater at 2 °C based upon in situ sampled pore water composition, Mar. Chem., 9, 223-235.

Schenk A. S., Albarracin E. J., Kim Y.-Y., Ihli J., and Meldrum F. C. (2014) Confinement stabilises single crystal vaterite rods, Chem. Commun., 50, 4729-4732.

Scherer G. W. (1999) Crystallization in pores, Cement Concrete Res., 29(8), 1347–1358.

Schlanger S. O. (1964) Petrology of the limestones of Guam, U. S. Geol. Surv. Prof. Papers, 403-D, 1-52.

Schmahl W. W., Griesshaber E., Neuser R., Lenze A., Job R., and Brand U. (2004) The microstructure of the fibrous layer of terebratulide brachiopod shell calcite, Eur. J. Mineral., 16(4), 693-697.

Schmahl W. W., Griesshaber E., Kelm K., Goetz A., Jordan G., Ball A., Xu D., Merkel C., and Brand U. (2012) Hierarchical structure of marine shell biomaterials: biomechanical functionalization of calcite by brachiopods, Z. Kristallogr., 227(11), 793-804.

Schmidt N. H. and Olesen N. O. (1989) Computer-aided determination of crystal-lattice orientation from electron channeling patterns in the SEM, Can. Mineral., 27, 15-22.

Schmidt V. and Mcdonald D. A. (1979) The role of secondary porosity in the course of sandstone diagenesis, Soc. Econ. Pa., 26, 175-207.

Schöne B. R. (2013) *Arctica islandica* (Bivalvia): a unique paleoenvironmental archive of the northern North Atlantic Ocean, Global Planet. Change, 111, 199-225.

Schöne B. R. and Fiebig J. (2009) Seasonality in the North Sea during the Allerød and Late Medieval Climate Optimum using bivalve sclerochronology, Int. J. Earth Sci. (Geol. Rundsch.), 98(1), 83-98.

Schöne B. R. and Surge D. M. (2012) Bivalve sclerochronology and geochemistry, in: Selden P. A. (ed.) Treatise on invertebrate paleontology (Part N Revised), Treatise Online, 46(1), University of Kansas Press, Lawrence, KS, 1-24.

Schöne B. R., Freyre Castro A. D., Fiebig J., Houk S. D., Oschmann W., and Kröncke I. (2004) Sea surface water temperatures over the period 1884-1983 reconstructed from oxygen isotope ratios of a bivalve mollusk shell (*Arctica islandica*, southern North Sea), Palaeogeogr. Palaeoclimat. Palaeoecol., 212(3-4), 215-232.

Schöne B. R., Fiebig J., Pfeiffer M., Gleβ R., Hickson J., Johnson A. L., Dreyer W., and Oschmann W. (2005a) Climate records from a bivalved Methuselah (*Arctica islandica*, Mollusca; Iceland), Palaeogeogr. Palaeoclimat. Palaeoecol., 228(1-2), 130-148.

Schöne B. R., Pfeiffer M., Pohlmann T., and Siegismund F. (2005b) A seasonally resolved bottom-water temperature record for the period AD 1866-2002 based on shells of *Arctica islandica* (Mollusca, North Sea), Int. J. Climatol., 25(7), 947-962.

Schöne B. R., Houk S. D., Freyre Castro A. D., Fiebig J., Oschmann W., Kröncke I., Dreyer W., and Gosselck F. (2005c) Daily growth rates in shells of *Arctica islandica*: assessing sub-seasonal environmental controls on a long-lived bivalve mollusk, Palaois, 20(1), 78-92.

Schroeder J. H. (1969) Experimental dissolution of calcium, magnesium, and strontium from recent biogenic carbonates: a model of diagenesis, J. Sediment. Res., 39(3), 1057-1073.

Schroeder J. H. (1972) Fabrics and sequences of submarine carbonate cements in Holocene Bermuda cup reefs, Geol. Rundsch., 61(2), 708-730.

Schumann D. (1970) Inäquivalver Schalenbau bei *Crania anomala*, Lethaia, 3, 413-421.

Schwartz A. J. (2009) Electron backscatter diffraction in materials science, Springer Science+Business Media, New York, NY.

Scourse J., Richardson C., Forsythe G., Harris I., Heinemeier J., Fraser N., Briffa K., and Jones P. (2006) First cross-matched floating chronology from the marine fossil record: data from growth lines of the long-lived bivalve mollusc *Arctica islandica*, Holocene, 16(7), 967-974.

Seidl B. H. M. and Ziegler A. (2012) Electron microscopic and preparative methods for the analysis of isopod cuticle, Zookeys, 176, 73-85.

Seto J., Ma Y., Davis S. A., Meldrum F., Gourrier A., Kim Y.-Y., Schilde U., Sztucki M., Burghammer M., Maltsev S., Jäger C., and Cölfen H. (2012) Structure-property relationships of a biological mesocrystal in the adult sea urchin spine, Proc. Natl. Acad. Sci. U.S.A., 109(10), 3699-3704.

Shirai K., Schöne B. R., Miyaji T., Radarmacher P., Krause Jr. R. A., and Tanabe K. (2014) Assessment of the mechanism of elemental incorporation into bivalve shells (*Arctica islandica*) based on elemental distribution at the microstructural scale, Geochim. Cosmochim. Acta, 126, 307-320.

Sjöberg E. L. (1978) Kinetics and mechanism of calcite dissolution in aqueous solutions at low temperatures, Acta Univ. Stockholm, Contrib. Geol., 332, 1-92.

Sjöberg E. L. and Rickard D. T. (1985) The effect of added dissolved calcium on calcite dissolution kinetics in aqueous solutions at 25 °C, Chem. Geol., 49, 405-413.

Schmidt W. J. (1924) Die Bausteine des Tierkörpers in polarisiertem Licht, Friedrich Cohen Verlag, Bonn.

Smirnova T. N. and Zhegallo E. A. (2016) Shell microstructure and variability of cell imprints of the mantle outer epithelium in the genus *Suiaella* Moisseev (Brachiopoda, Rhynchonellida) from the Lower Cretaceous of Crimea, Paleontolog. J., 50, 239-244.

Smit M. A., Bröcker M., and Scherer E. E. (2008) Aragonite and magnesite in eclogites from the Jæren nappe, SW Norway: disequilibrium in the system $CaCO_3$–$MgCO_3$ and petrological implications, J. Metamorph. Geol., 26(9), 959-979.

Smith S. V., Buddemeier R. W., Redalje R. C., and Houck J. E. (1979) Strontium-calcium thermometry in coral skeletons, Science, 204, 404-407.

Smyth J. R. and Ahrens T. J. (1997) The crystal structure of calcite III, Geophys. Res. Lett., 24(13), 1595-1598.

Sorauf J. E. (1980) Biomineralization, structure and diagenesis of the coelenterate skeleton, Acta Palaeont. Polonica, 25 (3/4), 237-343.

Spann N., Harper E. M., and Aldridge D. C. (2010) The unusual mineral vaterite in shells of the freshwater bivalve *Corbicula fluminea* from the U.K., Naturwissenschaften, 97(8), 743-751.

Stack A. G., Fernandez-Martinez A., Allard L. F., Bañuelos J. L., Rother G., Anovitz L. M., Cole D. R., and Waychunas G. A. (2014) Pore-size-dependent calcium carbonate precipitation controlled by surface chemistry, Environ. Sci. Technol., 48(11), 6177-6183.

References

Stanley S. M., Ries J. B., and Hardie L. A. (2002) Low-magnesium calcite produced by coralline algae in seawater of Late Cretaceous composition, Proc. Natl. Acad. Sci. U. S. A., 99(24), 15323-15326.

Steefel C. I. and Van Cappellen P. (1990) A new kinetic approach to modeling water-rock interaction: the role of nucleation, precursors, and Ostwald ripening, Geochim. Cosmochim. Acta, 54(10), 2657–2677.

Stehli F. J. (1956) Shell mineralogy in Paleozoic invertebrates, Science, 123, 1031-1032.

Steuber T. (1999) Isotopic and chemical intra-shell variations in low-Mg calcite of rudist bivalves (Mollusca-Hippuritacea): disequilibrium fractionations and late Cretaceous seasonality, Int. J. Earth Sci., 88(3), 551-570.

Stevens K., Iba Y., Suzuki A., and Mutterlose J. (2015) Biological and environmental signals recorded in shells of *Argonauta argo* (Cephalopoda, Octobrachia) from the Sea of Japan, Mar. Biol., 162(11), 2203-2215.

Stevens K., Griesshaber E., Schmahl W. W., Casella L. A., Iba Y., and Mutterlose J. (2017) Belemnite biomineralization, development, and geochemistry: the complex rostrum of *Neohibolites minimus*, Palaeogeogr. Palaeoclimat. Palaeoecol., 468, 388-402.

Stirling C. H., Esat T. M., McCulloch M. T., and Lambeck K. (1995) High-precision U-series of corals from Western Australia and implications for the timing and duration of the Last Interglacial, Earth Planet. Sc. Lett., 135, 115-130.

Stolarski J. (2003) Three-dimensional micro- and nanostructural characteristics of the scleractinian coral skeleton: a biocalcification proxy, Acta Palaeontol. Pol., 48(4), 497-530.

Strahl J., Dringen R., Schmidt M. M., Hardenberg S., and Abele D. (2011) Metabolic and physiological responses in tissues of the longlived bivalve *Arctica islandica* to oxygen deficiency, Comp. Biochem. Physiol. A, 158, 513-519.

Sud D., Poncet J.-M., Saihi A., Lebel J.-M., Doumenc D., and Boucaud-Camou E. (2002) A cytological study of the mantle edge of *Haliotis tuberculata* L. (Mollusca, Gastropoda) in relation to shell structure, J. Shellfish Res., 21, 201-210.

Sugawara A., Nishimura T., Yamamoto Y., Inoue H., Nagasawa H., and Kato T. (2006) Self-organization of oriented calcium carbonate/polymer composites: effects of a matrix peptide isolated from the exoskeleton of a crayfish, Angew. Chem. Int. Edit., 45(18), 2876-2879.

Sujkowski Z. L. (1958) Diagenesis, Bull. Am. Assoc. Pet. Geol., 42(11), 2692-2717.

Sun W., Jayaramana S., Chen W., Persson K. A., and Cedera G. (2015) Nucleation of metastable aragonite $CaCO_3$ in seawater, Proc. Natl. Acad. Sci. U. S. A., 112, 3199-3204.

Sunagawa I. (1981), Characteristics of crystal growth in nature as seen from the morphology of mineral crystals, Bull. Mineral., 104, 81-87.

Swart P. K. (2015) The geochemistry of carbonate diagenesis: the past, present and future, Sedimentology, 62(5), 1233-1304.

Swart P. K. and Leder J. J. (1996) The utility of isotopic signatures in coral skeletons, Paleontol. Soc. Pap., 1, 249-291.

Taborosi D. and Stafford K. (2003) Littoral dripstone and flowstone - non-spelean carbonate secondary deposits, Int. J. Speleol., 32(1/4), 85-106.

Taft W. H. (1967) Physical chemistry of formation of carbonates, Dev. Sediment., 9, 151-167.

Takahashi T. and Broecker W. S. (1977) Mechanisms for calcite dissolution on the seafloor, in: Anderson N. R. and Malahoff A. (eds.) The fate of fossil fuel CO_2 in the oceans, Plenum, New York, 455-477.

Takayanagi H., Asami R., Abe O., Miyajima T., Kitagawa H., Sasaki K., and Iryu Y. (2013) Intraspecific variations in carbon-isotope and oxygen-isotope compositions of a brachiopod *Basiliola lucida* collected off Okinawa-jima, southwestern Japan, Geochim. Cosmochim. Acta, 115, 115-136.

Tang C. C., Thompson S. P., Parker J. E., Lennie A. R., Azough F., and Kato K. (2009) The ikaite-to-vaterite transformation: new evidence from diffraction and imaging, J. Appl. Crystallogr., 42(2), 225-233.

Taylor A. C. (1976) Burrowing behavior and anaerobiosis in the bivalve *Arctica islandica* (L.), J. Mar. Biol. Assoc. U. K., 56, 95-109.

Taylor T. R. and Sibley D. F. (1986) Petrographic and geochemical characteristics of dolomite types and the origin of ferroan dolomite in the Trenton Group, Ordovician, Michigan Basin, U.S.A., Sedimentology, 33, 61-86.

Teng H. H., Dove P. M., and De Yoreo J. J. (2000) Kinetics of calcite growth: surface processes and relationships to macroscopic rate laws, Geochim. Cosmochim. Acta, 64(13), 2255-2266.

Threlfall T. (2003) Structure and thermodynamic explanations of Ostwald's rule, Org. Process. Res. Dev., 7, 1017–1027.

Titschak J., Radtke U., and Freiwald A. (2009) Dating and characterization of polymorphic transformation of aragonite to calcite in pleistocene bivalves from Rodes (Greece) by combined shell microstructure, stable isotope, and electron spin resonance, J. Sediment. Res., 79, 332-346.

Todd D. K. (1980) Groundwater hydrology, John Wiley & Sons, London.

Tomiak P. J., Andersen M. B., Hendy E. J., Potter E. K., Johnson K. G., and Penkman K. E. H. (2016) The role of skeletal micro-architecture in diagenesis and dating of *Acropora palmata*, Geochim. Cosmochim. Acta, 183, 153-175.

Towe K. M. and Lowenstam H. A. (1967) Ultrastructure and development of iron mineralization in the radular teeth of *Cryptochiton stelleri* (Mollusca), J. Ultrastruct. Res., 17(1), 1-13.

Trueman C. N. (1999) Rare earth element geochemistry and taphonomy of terrestrial vertebrate assemblages, Palaios, 14, 555-568.

Trueman C. N. (2013) Chemical taphonomy of biomineralized tissues, Palaeontology, 56(3), 475-486.

Tucker M. E. (1990a) Diagenetic processes, products and environments, in: Tucker M. E. and Wright V. P. (eds.) Carbonate Sedimentology, Blackwell Scientific Publications, Oxford, 314-364.

Tucker M. E. (1990b) Diagenesis, in: Briggs D. E. G. and Crowther P. R. (eds.) Palaeobiology: a synthesis, Blackwell Scientific Publications, Oxford, 247-250.

Tucker M. E. and Wright V. P. (1990) Carbonate sedimentology, Blackwell Science, Oxford.

Turekian K. K. (1972) Chemistry of the Earth. Holt, Rinehart and Winston, New York.

Turner B. D., Binning P., and Stipp S. L. S. (2005) Fluoride removal by calcite: evidence for fluorite precipitation and surface adsorption, Environ. Sci. Technol., 39(24), 9561-9568.

References

Ullmann C. V. and Korte C. (2015) Diagenetic alteration in low-Mg calcite from macrofossils: a review, Geol. Quart., 59(1), 3-20.

Ullmann C. V., Frei R., Korte C., and Hesselbo S. P. (2015) Chemical and isotopic architecture of the belemnite rostrum, Geochim. Cosmochim. Acta, 159, 231-243.

Veizer J. (1983) Trace elements and isotopes in sedimentary carbonates, in: Reeder R. J. (ed.) Carbonates: mineralogy and chemistry, Mineral. Soc. Am., Bookcrafters Inc., Chelsea, Mich., 265-300.

Veizer J., Fritz P., and Jones B. (1986) Geochemistry of brachiopods: oxygen and carbon isotopic records of Paleozoic oceans, Geochim. Cosmochim. Acta, 50(8), 1679-1696.

Veizer J., Ala D., Azmy K., Bruckschen P., Buhl D., Bruhn F., Carden G. A., Diener A., Ebneth S., Godderis Y., Jasper T., Korte C., Pawellek F., Podlaha O. G., and Strauss H. (1999) $^{87}Sr/^{86}Sr$, $\delta^{13}C$ and $\delta^{18}O$ evolution of Phanerozoic seawater, Chem. Geol., 161(1-3), 59-88.

Verruijt A.(1968) A note on the Ghyben-Herzberg formula, Hydrolog. Sci. J., 13, 43-46.

Vielzeuf D., Garrabou J., Gagnon A., Ricolleau A., Adkins J., Günther D., Hametner K., Devidal J.-L., Reusser E., Perrin J., and Floquet N. (2013) Distribution of sulphur and magnesium in the red coral, Chem. Geol., 355, 13-27.

Voldman G. G., Bustos-Marún R. A., and Albanesi G. L. (2010) Calculation of the conodont color alteration index (CAI) for complex thermal histories, Int. J. Coal Geol., 82(1-2), 45-50.

Vörös A. (1986) Brachiopod palaeoecology on a Tethyan Jurassic Seamount (Pliensbachian, Bakony Mountains, Hungary), Palaeogeogr. Palaeoclimatol. Palaeoecol., 57, 241-271.

Wada K. (1972) Nucleation and growth of aragonite crystals in the nacre of some bivalve molluscs, Biomineralisation, 4, 141-159.

Wadleigh M. A. and Veizer J. (1992) $^{18}O/^{16}O$ and $^{13}C/^{12}C$ in lower Paleozoic articulate brachiopods: implications for the isotopic composition of seawater, Geochim. Cosmochim. Acta, 56(1), 431-443.

Wählisch F. C., Peter N. J., Abad O. T., Oliveira M. V. G., Schneider A. S., Schmahl W., Griesshaber E., and Bennewitz R. (2014) Surviving the surf: the tribomechanical properties of the periostracum of *Mytilus* sp., Acta Biomater., 10(9), 3978-3985.

Wainwright S. A. (1964) Studies of the mineral phase of coral skeleton, Exp. Cell Res., 34(2), 213-230.

Walker G. and Burley S. (1991) Luminescence petrography and spectroscopic studies of diagenetic minerals, in: Barker C. E. and Kopp O. C. (eds.) Luminescence microscopy and spectroscopy: qualitative and quantitative applications, Short Course Notes, 25, SEPM Society for Sedimentary Geology, Tulsa, Oklahoma, 83-180.

Wall M. and Nehrke G. (2012) Reconstructing skeletal fiber arrangement and growth mode in the coral *Porites lutea* (Cnidaria, Scleractinia): a confocal Raman microscopy study, Biogeosciences, 9(11), 4885-4895.

Walls R. A. (1983) Golden Spike Reef Complex, Alberta, in: Scholle P. A., Bebout D. G., and Moore C. H. (eds.) Carbonate depositional environments, Mem. Am. Ass. Petrol. Geol., 33, 445-453.

Walls R. A. and Burrowes G. (1985) The role of cementation in the diagenetic history of Devonian reefs, Western Canada, in: Schneidermann N. and Harris P. M. (eds.) Carbonate cements, Soc. Econ. Paleont. Miner. Spec. Publ., 36, 185-220.

Walter L. M. (1986) Relative efficiency of carbonate dissolution and precipitation during diagenesis: a progress report on the role of solution chemistry, in: Gautier D. L. (ed.) Roles of organic matter in sediment diagenesis, SEPM Spec. P., 28, 1-11.

Walter L. M. and Morse J. W. (1984a) Reactive surface area of skeletal carbonates during dissolution: effect of grain size, J. Sediment. Petrol., 54, 1081-1090.

Walter L. M. and Morse J. W. (1984b) Magnesian calcite stabilities: a reevaluation, Geochim. Cosmochim. Acta, 48(5), 1059-1069.

Walter L. M., Ku T. C. W., Muehlenbachs K., Patterson W. P., and Bonnell L. (2007) Controls on the $\delta^{13}C$ of dissolved inorganic carbon in marine pore waters: an integrated case study of isotope exchange during syndepositional recrystallization of biogenic carbonate sediments (South Florida Platform, USA), Deep-Sea Res. Pt. II, 54, 1163-1200.

Wanamaker Jr. A. D., Kreutz K. J., Borns H. W., Introne D. S., Feindel S., Funder S., Rawson P. D., and Barber B. J. (2007) Experimental determination of salinity, temperature, growth, and metabolic effects on shell isotope chemistry of *Mytilus edulis* collected from Maine and Greenland, Paleoceanography, 22, PA2217.

Wanamaker Jr. A. D., Kreutz K. J., Schöne B. R., Pettigrew N., Borns H. W., Introne D. S., Belknap D., Maasch K. A., and Feindel S. (2008) Coupled North Atlantic slope water forcing on Gulf of Maine temperatures over the past millennium, Clim. Dyn., 31(2-3), 183-194.

Wanamaker Jr. A. D., Kreutz K. J., Schöne B. R., and Introne D. S. (2011) Gulf of Main shells reveal changes in seawater temperature seasonality during the Medieval Climate Anomaly and the Little Ice Age, Palaeogeogr. Palaeoclimatol. Palaeoecol., 302(1-2), 43-51.

Wang J. and Becker U. (2009) Structure and carbonate orientation of vaterite ($CaCO_3$), Am. Mineral., 94(2-3), 380-386.

Wang L., Ruíz-Agudo E., Putnis C. V., Menneken M., and Putnis A. (2012) Kinetics of calcium phosphate nucleation and growth on calcite: implications for predicting the fate of dissolved phosphate species in alkaline soils, Environ. Sci. Technol., 46(2), 834-842.

Wardlaw N., Oldershaw A., and Stout M. (1978) Transformation of aragonite to calcite in a marine gastropod, Can. J. Earth Sci., 15, 1861-1866.

Watabe N. (1965) Studies on the shell formation: XI. Crystal-matrix relationships in the inner layers of mollusk shells, J. Ultrastruct. Res., 12(3), 351-370.

Weiner S. and Dove P. M. (2003) An overview of biomineralization processes and the problem of the vital effect, Rev. Mineral. Geochem., 54(1), 1-29.

Weiner S., Traub W., and Parker S. B. (1984) Macromolecules in mollusc shells and their functions in biomineralization, Philos. Trans. R. Soc. B, 304(1121), 425-434.

Weiss I. M., Tuross N., Addadi L., and Weiner S. (2002) Mollusc larval shell formation: amorphous calcium carbonate is a precursor phase for aragonite, J. Exp. Zool., 293(5), 478-491.

Wenk H.-R. and Van Houtte P. (2004) Texture and anisotropy, Rep. Prog. Phys., 67, 1367-1428.

Wenzel B. and Joachimski M. M. (1996) Carbon and oxygen isotopic composition of Silurian brachiopods (Gotland/Sweden): palaeoceanographic implications, Palaeogeogr. Palaeoclimatol. Palaeoecol., 122, 143-166.

References

Wenzel B., Lécuyer C., and Joachimski M. M. (2000) Comparing oxygen isotope records of Silurian calcite and phosphate-δ^{18}O compositions of brachiopods and conodonts, Geochim. Cosmochim. Acta, 64(11), 1859-1872.

White W. B. (1967) Cave minerals and speleothems, in: Ford D. T. and Cullingford C. H. D. (eds.) The science of speleology, Academic Press, London.

Williams A. (1968) Evolution of the shell structure of articulate brachiopods, Spec. Pap. Palaeontol., 2, 1-55.

Williams A. and Cusack M. (2007) Chemicostructural diversity of the brachiopod shell, in: Selden P. A. (ed.) Treatise on invertebrate paleontology (Part H, Brachiopoda Revised), 6, Geological Society of America, University of Kansas Press, Boulder, CO, 2397-2521.

Williams A. and Wright A. D. (1970) Shell structure of the Craniacea and other calcareous inarticulate brachiopods, Spec. Pap. Palaeontol., 7, 1-51.

Williams A., Carlson S. J., Brunton C. H. C., Holmer L. E., and Popov L. (1996) A supra-ordinal classification of the brachiopoda, Philos. Trans. R. Soc. B, 351, 1171-1193.

Williams A., Hardesty J., and Moore R. C. (1997) Treatise on invertebrate paleontology (Part H Revised), Geological Society of America, 6, University of Kansas Press, Boulder, CO.

Williams C. T. (1988) Alteration of chemical composition of fossil bones by soil processes and groundwater, in: Grupe G. and Herrmann B. (eds.) Trace elements in environmental history, Springer, Berlin, 27-40.

Wilmsen M. and Neuweiler F. (2008) Biosedimentology of the Early Jurassic post-extinction carbonate depositional system, Central High Atlas rift basin, Morocco, Sedimentology, 55, 773-807.

Wilson L. and Pollard A. M. (2002) Here Today, Gone Tomorrow? Integrated experimentation and geochemical modeling in studies of archaeological diagenetic change, Acc. Chem. Res., 35(8), 644-651.

Winland H. D. (1969) Stability of calcium carbonate polymorphs in warm, shallow seawater, J. Sediment. Res., 39, 1579-1587.

Wischnitzer S. (1970) Introduction to electron microscopy, Pergamon Press, New York, NY.

Wise S. W. (1970) Microarchitecture and mode of formation of nacre (mother of pearl) in pelecypods, gastropods and cephalopods, Eclogae Geol. Helv., 63, 775–797.

Witbaard R. and Bergman M. (2003) The distribution and population structure of the bivalve *Arctica islandica* L. in the North Sea: what possible factors are involved?, J. Sea Res., 50(1), 11-25.

Wolfe K., Smith A. M., Trimby P., and Byrne M. (2013) Microstructure of the paper nautilus (*Argonauta nodosa*) shell and the novel application of electron backscatter diffraction (EBSD) to address effects of ocean acidification, Mar. Biol., 160(8), 2271-2278.

Wombacher F., Eisenhauer A., Böhm F., Gussone N., Regenberg M., Dullo W.-C., and Rüggeberg A. (2011) Magnesium stable isotope fractionation in marine biogenic calcite and aragonite, Geochim. Cosmochim. Acta, 75(19), 5797-5818.

Wood R. (2005) Reef evolution, Oxford University Press, New York.

Wooldridge S. (2013) A new conceptual model of coral biomineralisation: hypoxia as the physiological driver of skeletal extension, Biogeosciences, 10(5), 2867-2884.

Worden R. H. and Burley S. D. (2009) Sandstone diagenesis: recent and ancient, Blackwell Publishing, Malden, MA.

Wordon R. H., Smalley P. C., and Cross M. M. (2000) The influence of rock fabric and mineralogy on thermochemical sulfate reduction: Khuff Formation, Abu Dhabi, J. Sed. Res., 70(5), 1210-1221.

Wright V. P. and Cherns L. (2004) Are there "black holes" in carbonate deposystems?, Geol. Acta, 2, 285-290.

Wright V. P., Cherns L., and Hodges P. (2003) Missing molluscs: field testing taphonomic loss in the Mesozoic through early largescale aragonite dissolution, Geology, 31, 211-214.

Wyckoff R. W. G. (1925) Orthorhombic space group criteria and their application to aragonite, Am. J. Sci., 9(5), 145-175.

Xia F., Zhou J., Brugger J., Ngothai Y., O´Neill B., Chen G., and Pring A. (2008) Novel route to synthesize complex metal sulfides: hydrothermal coupled dissolution-reprecipitation replacement reactions, Chem. Mater., 20(8), 2809-2817.

Xia F., Brugger J. I., Chen G., Ngothai Y., O'Neill B., Putnis A., and Pring A. (2009a) Mechanism and kinetics of pseudomorphic mineral replacement reactions: a case study of the replacement of pentlandite by violarite, Geochim. Cosmochim. Acta 73(7), 1945-1969.

Xia F., Brugger J. l., Ngothai Y., O'Neill B., Chen G., and Pring A. (2009b) Three-dimensional ordered arrays of zeolite nanocrystals with uniform size and orientation by a pseudomorphic coupled dissolution-reprecipitation replacement route, Cryst. Growth Des., 9, 4902-4906.

Xiang L., Kong W., Su J.-T., Liang J., Zhang G.-Y., Xie L.-P., and Zhang R.-Q. (2014) Amorphous calcium carbonate precipitation by cellular biomineralization in mantle cell cultures of *Pinctada fucata*, Plos One, 9(11), e113150.

Xu A.-W., Yu Q., Dong W.-F., Antonietti M., and Cölfen H. (2005) Stable amorphous $CaCO_3$ microparticles with hollow spherical superstructures stabilized by phytic acid, Adv. Mater., 17(18), 2217-2221.

Yamamoto K., Asami R., and Iryu Y. (2013) Correlative relationships between carbon- and oxygen-isotope records of two cool-temperature brachiopod species off Otsuchi Bay, northeastern Japan, Paleontol. Res., 17, 12-26.

Yang M., Hashimoto T., Hoshi N., and Myoga H. (1999) Fluoride removal in a fixed bed packed with granular calcite, Water Res., 33(16), 3395-3402.

Ye F., Crippa G., Angiolini L., Brand U., Capitani G.-C., Cusack M., Garbelli C., Griesshaber E., Harper E., and Schmahl W. W. (2018a) Mapping of recent brachiopod microstructure: a tool for environmental studies, J. Struct. Biol., 201(3), 221-236.

Ye F., Crippa G., Garbelli C., and Griesshaber E. (2018b) Microstructural data of six recent brachiopod species: SEM, EBSD, morphometric and statistical analyes, Data in Brief, 18, 300-318.

Yin X., Ziegler A., Kelm K., Hofmann R., Watermeyer P., Alexa P., Villinger C., Rupp U., Schlüter L., Reusch T., Griesshaber E., Walther P., and Schmahl W. W. (2018) Formation and mosaicity of coccolith segment calcite of the marine algae *Emiliania huxleyi*, J. Phycol., 54(1), 85-104.

References

Yoshioka S., Ohde S., Kitano Y., and Kanamori N. (1986) Behaviour of magnesium and strontium during the transformation of coral aragonite to calcite in aquatic environments, Mar. Chem., 18, 35-48.

Zaefferer S. And Habler G. (2017) Scanning electron microscopy and electron backscatter diffraction, in: Heinrich W. and Abart R. (eds.) Mineral reaction kinetics: microstructures, textures, chemical and isotopic signatures, EMU Notes Mineralog., 16, 37-95.

Zanchi A. and Gaetani M. (2011) The geology of the Karakoram range, Pakistan: the new 1:100,000 geological map of Central-Western Karakoram, Ital. J. Geosci., 130(2), 161-262.

Zazzo A., Lécuyer C., Sheppard S. M., Grandjean P., and Mariotti A. (2004) Diagenesis and the reconstruction of paleoenvironments: a method to restore original $\delta^{18}O$ values of carbonate and phosphate from fossil tooth enamel, Geochim. Cosmochim. Acta, 68(10), 2245-2258.

Zeppenfeld K. (2003) Experimentelle Untersuchungen über den Einfluss einiger zwei- und dreiwertiger Metallkationen auf die Bildung und das Wachstum von $CaCO_3$: experimental study of the influence of some divalent and trivalent metal cations on nucleation and growth of $CaCO_3$, Chem. Erde-Geochem., 63, 264-280.

Zhang R., Hu S., Zhang X., and Yu W. (2007) Dissolution kinetics of dolomite in water at elevated temperatures, Aquat. Geochem., 13, 309-338.

Zhang Y. (2010) Diffusion in minerals and melts: theoretical background, Rev. Mineral. Geochem., 72, 5-59.

Zhang Y. and Evans J. R. (2012) Approaches to the manufacture of layered nanocomposites, Appl. Surf. Sci., 258(6), 2098-2102.

Zhou W. and Wang Z. L. (2007) Scanning microscopy for nanotechnology: techniques and applications, Springer, Berlin.

Ziegler B. (1992) Allgemeine Paläontologie, Schweizerbart, Stuttgart.

Zuykov M., Pelletier E., Belzile C., and Demers S. (2011) Alteration of shell nacre micromorphology in blue mussel *Mytilus edulis* after exposure to free-ionic silver and silver nanoparticles, Chemosphere, 84(5), 701-706.

Appendix

A I General information on investigated organisms

The following subchapters provide information on all marine animal species investigated in the framework of the present dissertation. All animals differ not only in class and but also in mineralogy and microstructure of their biomineralised carbonate hard tissues. The latter is comprised of either bio-calcite or bio-aragonite. However, these mono-mineralic hard tissues can be complemented by an additional nacreous aragonite layer.

A I.1 Calcite-forming marine organisms

Brachiopods

Brachiopods (see Fig. A1) are ubiquitous marine invertebrates providing an immense fossil record dating back to the Proterozoic, i.e., 2.5 Ga-540 Ma ago (Copper, 1996; Schmahl et al., 2004). During the Phanerozoic (540 Ma until the present day), brachiopods were of high significance for benthic marine faunas and became a prevalent organism from the Permian/Triassic border (Wood, 2005). It is known that approx. 120 genera are still living at the present day (Williams et al., 1997; Griesshaber et al., 2007b). However, brachiopods decreased in importance in the recent oceans (Cuif et al., 2011b).
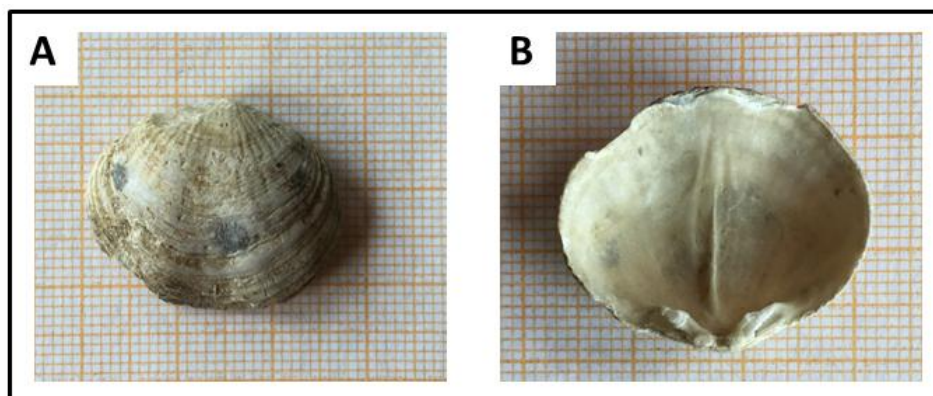
Figure A1: Photographs showing the shell of the modern brachiopod *Terebratalia transversa* in front (A) and bottom view (B).
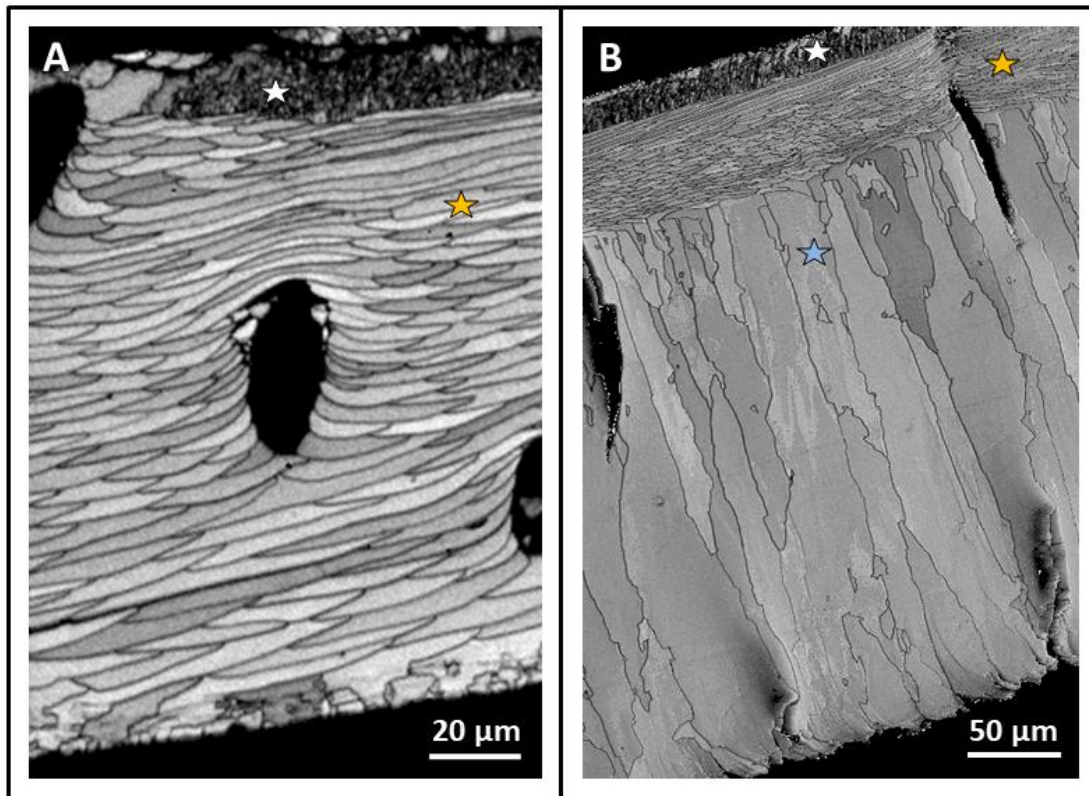
Figure A2: EBSD band contrast illustrating the microstructure of the shell of modern brachiopods (A) *Terebratalia transversa* which is comprised of a primary layer (white star) and the fibrous secondary layer (yellow star; modified after Casella et al., 2018a), and (B) *Gryphus vitreus* which is comprised of a primary layer (white star), secondary fibrous layer (yellow star) as well as of a third columnar layer (blue star; modified courtesy of Dr. Erika Griesshaber).

The phylum of brachiopods is divided into three subphyla which are mainly based on the mineralogy and structure of the shells (Williams et al., 1996).

[1] *Rhynchonelliformea* brachiopods form shells consisting of low-Mg calcite fibres (Cusack and Williams, 2001; Cusack et al., 2008b; Pérez-Huerta et al., 2009). They comprise the orders *Rhynchonellida* and *Terebratulida* which cover the majority of present day brachiopod species.

[2] The subphylum of *Craniiformea* is characterised by high Mg-calcitic semi-nacre shells and is less abundant (Jope, 1965; Williams and Wright, 1970; England et al., 2007; Cusack et al., 2008b; Pérez-Huerta et al., 2008; Immenhauser et al., 2015).

[3] *Linguliformea* constitute the exception as they mineralise a calcium phosphate shell. Aragonitic brachiopod species (Trimerellacea) have been declared extinct since the Late Silurian (Williams, 1968; Lowenstam and Weiner, 1989; Álvarez and Curry, 2010; Immenhauser et al., 2015).

In 1970, Williams and Wright as well as Schumann described the organo-calcitic shell ultrastructure of cranioid brachiopods for the first time. According to their report, the mineral components of the brachiopod shell are covered with an organic layer (i.e.,

periostracum) and a subjacent secreting epithelium (i.e., the mantle) with its corresponding papillose outgrowths (i.e., caeca). The latter permeate the succession of the brachiopod skeleton. As the majority of brachiopods exhibits a physical linkage between their valves by a variety of forms of articulations, they are referred to as Articulata, whilst a simple linkage of the two valves by muscles refers to as Inarticulata (Williams, 1968; Immenhauser et al., 2015). The life span of Articulata and Inarticulata reaches up to 30 years and ten years, respectively, and is dependent on several factors, such as temperature of the ocean water, food supply, parasitism, and predators (Ruggiero, 2001).

Shells of articulated brachiopods are assembled by two or three calcitic layers dependent on the author cited: (1) the primary layer beneath the periostracum (see Fig. A2A), (2) the fibrous secondary layer (see Fig. A2A), and (3) the columnar third layer (e.g., found in *Gryphus vitreus*, Born, 1778; see Fig. A2B). While the protective primary layer consists of needle-like low-Mg calcite embedded within an organic matrix, the low-Mg calcite fibres of the thick secondary layer are made of an mineral-biopolymer composite material. Single calcite fibres are surrounded by an organic sheath (Griesshaber et al., 2007b; Pérez-Huerta et al., 2013; Casella et al., 2018a, 2018b).

Except for Rhynchonellids, all living and partly fossil brachiopods exhibit so called 'punctae'. These perforations or discontinuities represent one of the most characteristic shell features which perforate both the primary as well as secondary calcitic shell layers. The detailed purpose of punctae is still under debate. Speculations suggest that they act as storage departments, aides in respiration, or sensory devices (Pérez-Huerta et al., 2009).

In the past decades, the phylum of brachiopods has been extensively investigated due to their use as proxies for, e.g., reconstruction of palaeotemperature, physiological conditions, composition of ancient seawater, reconstruction studies of secular variations in $\delta^{18}O$ and $\delta^{13}C$, and for studies of the palaeoenvironment in the Palaeozoic (Veizer et al., 1986; Bates and Brand, 1991; Wadleigh and Veizer, 1992; Veizer et al., 1999; Brand and Brenckle, 2001; Auclair et al., 2003; Brand et al., 2003).

A I.2   Aragonite-forming marine organisms

Bivalve *Arctica islandica*

The mussel *Arctica islandica* (see Fig. A3; Linnaeus, 1767), also referred to as ocean quahog, belongs to the phylum Mollusca and the order Bivalvia. Its evolutionary line dates back to the Jurassic (Casey, 1952; Schöne, 2013) and subfossil shells were described by Witbaard and Bergman (2003) and by Scourse et al. (2006).
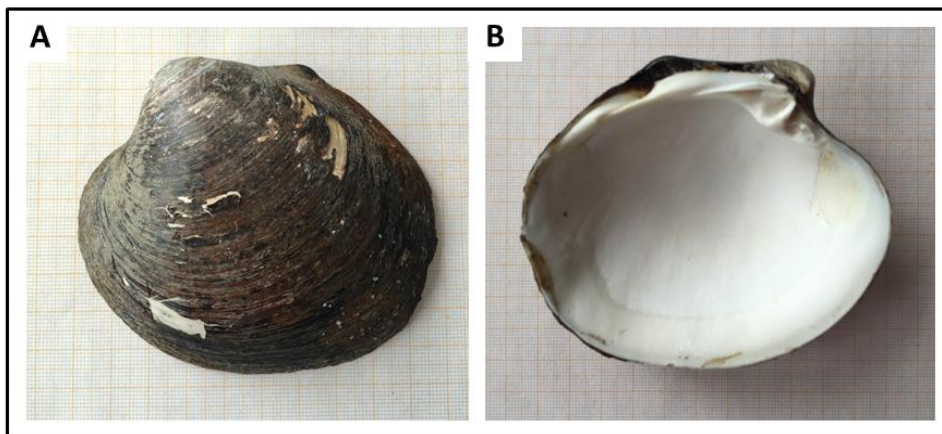
Figure A3: Photographs of a modern specimen of the bivalve *Arctica islandica* showing the (A) exterior of the shell which is coated with the organic periostracum, and (B) the interior of the shell. The sample was collected by Prof. Dr. Elizabeth Harper at Loch Etive, Scotland.
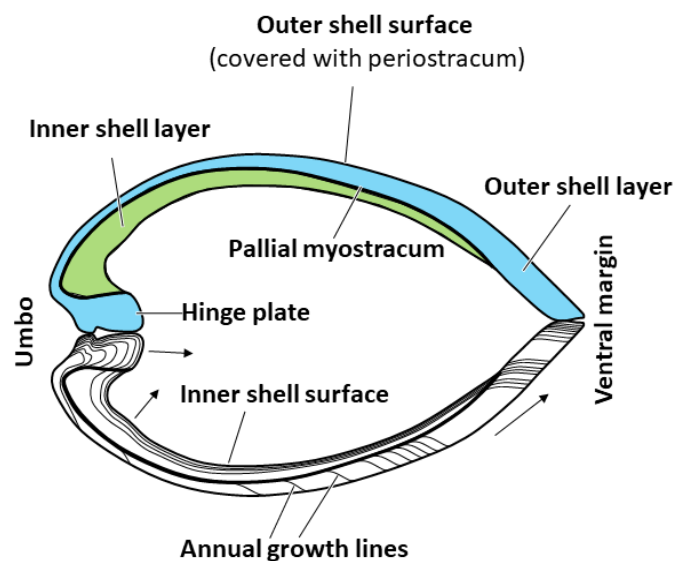
Figure A4: Schematic drawing illustrating the major morphological characteristics of the shell of the bivalve *Arctica islandica*: outer shell layer (blue), inner shell layer (green), outer and inner shell surface, pallial myostracum, hinge plate, as well as annual growth lines (modified after Casella et al., 2017). Detailed descriptions are published by Schöne (2013).
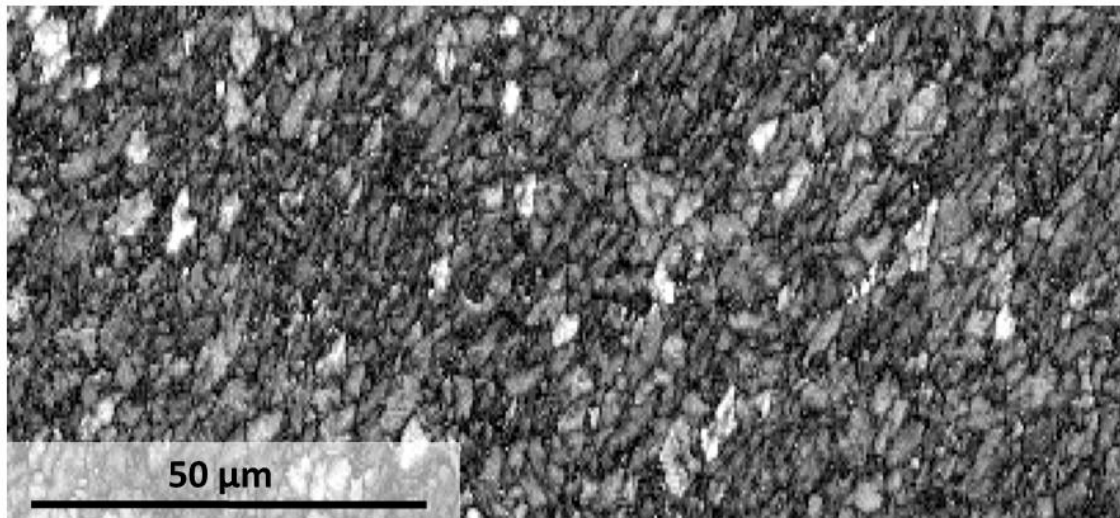
Figure A5: EBSD band contrast measurement (grey scale) showing the fine grained aragonitic microstructure of the bivalve *Arctica islandica* (taken from Casella et al., 2017).

Arctica islandica are by far the most intensively studied species in marine bivalve archives of the recent to sub-recent past (Schöne, 2013). Not only is their wide distribution throughout the shelf seas of the North Atlantic Ocean but also the remarkable lifespan of the mussel responsible for the keen interest. With ages which can exceed 500 years it is the longest-lived species among all bivalves and molluscs on Earth (Abele et al., 2008; Karney et al., 2012; Butler et al., 2013; Casella et al., 2017; Ritter et al., 2017).

Typical morphological characteristics of the *A. islandica* shell are presented in Figure A4. The aragonitic shell features three parts, (1) the inner shell layer, which is adjacent to the soft tissue of the animal, (2) the pallial myostracum, which is the shell area formed at the attachment of the adductor muscles, and (3) the outer shell layer, which is in contact to seawater. Moreover, the microstructure found in modern specimens of *A. islandica* can be described as fine-grained mineral units comprised of bio-aragonite (Casella et al., 2017; Fig. A5). According to Schöne and co-workers (2005a), the shell growth period of *A. islandica* appears to stay the same throughout the living period of the animal. Further, the authors state that the shell remains unchanged for at least the first 39 years of shell growth. During the fourth year of living, the bivalve forms circadian growth increments of 31.5 µm in size per day on the average (Schöne et al., 2005c). Resulting annual growth lines begin to become visible on the microstructural level. Irregularly-shaped aragonite crystal units, which are surrounded and also penetrated by organic fibrils, assemble the microstructure of modern *A. islandica* specimens (Casella et al., 2017).

As annually banded aragonitic shells are produced by living *A. islandica* mussels, they became potential research objects for studies regarding, e.g., climate variability (Foster et al., 2009), and reconstruction studies of marine water temperatures (Schöne et

al., 2005b). Furthermore, *Arctica islandica* has gained profound attention as suitable specimen for application of oxygen isotopes proxy data (Schöne et al., 2004, 2005a; 2005b) of Holocene shells (Schöne et al., 2005b; Wanamaker et al., 2008, 2011; Schöne and Fiebig, 2009; Karney et al., 2012) in a sclerochronological[3] (Marchitto et al., 2000) and stratigraphic (Butler et al., 2009, 2013) context.

Scleractinian corals

Scleractinian corals (here, mainly *Porites* sp.; see Fig. A6), also known as stony corals, belong to the phylum Cnidaria and the order Scleractinia. Due to their accretion of aragonitic hard exoskeletons, they can be distinguished from soft corals like Antipatheria and Octocorallia (Cohen and McConnaughey, 2003; Przeniosło et al., 2008). The existence of scleractinian marine calcifying organisms dates back to the Triassic and lasts until the present day. Scleractinian corals can be either found as solitary individuals, ahermatypic corals (Benton and Harper, 1997), or as massive reef-building, hermatypic corals which occur in colonies (Wainwright, 1964; Meibom et al., 2004). Due to their symbiotic association with zooxanthellae or algae in their polyp tissues, hermatypic scleractinian corals are able to grow rapidly which leads to a high calcification rate for the creation of reefs (Cohen and McConnaughey, 2003; Wooldridge, 2013). The accretion of coral exoskeletons occurs at day and night, called "dark calcification", and takes place either with or without symbionts (Jacques and Pilson, 1980; Jacques et al., 1983; Barnes, 1985; Chalker et al., 1985).
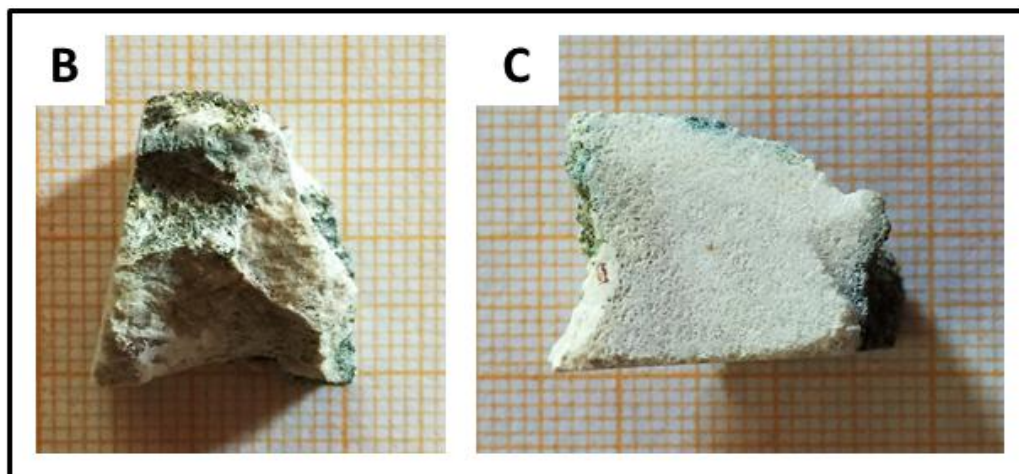
Figure A6: Images of fragments of a pristine scleractinian coral *Porites* sp. sampled in Moorea, French Polynesia (Rashid et al., 2014). (A) Top view, (B) bottom view showing the porous structure of the *Porites* sp. skeleton.

---

[3] The term 'sclerochronology' refers to studies of chemical and physical variations found in accretionary hard tissues formed by organisms, and includes the temporal context in which they were secreted (Gröcke und Gillikin 2008).
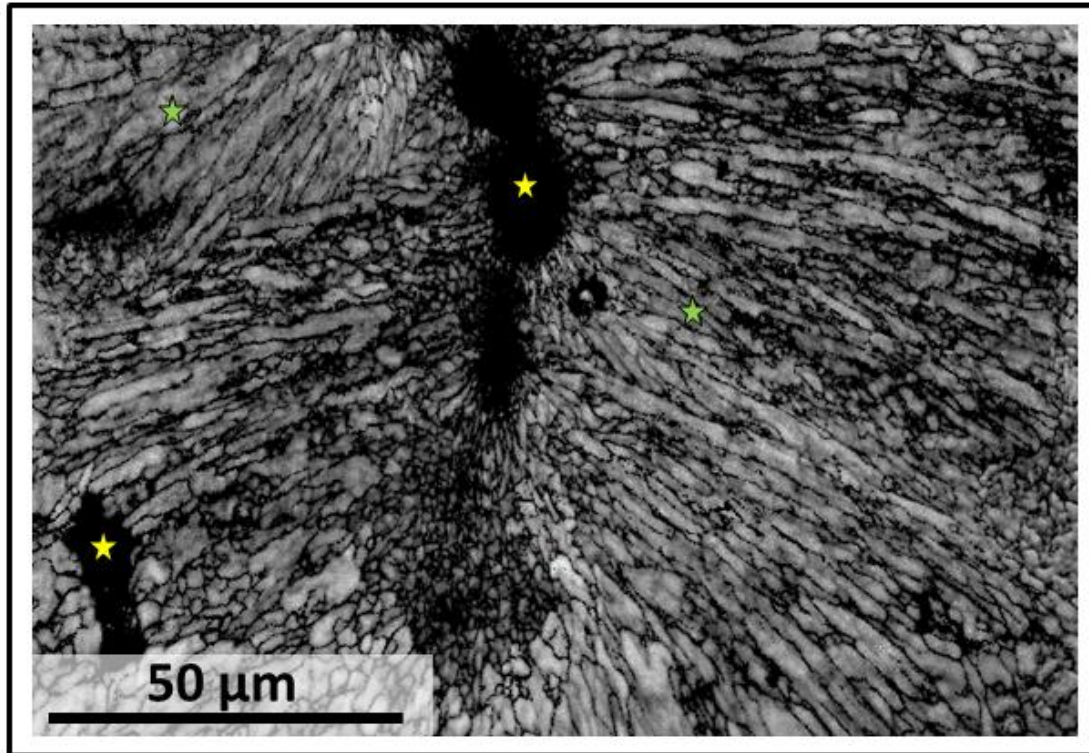
Figure A7: EBSD band contrast measurement (grey scale) showing the microstructure of the pristine scleractinian coral Porites sp. with characteristic bunches of aragonitic needles (green stars) which are radially arranged around organic-rich centres of calcification (yellow stars; modified after Casella et al., 2018c).

The animal part of the coral which is responsible for the formation of the exoskeleton is called polyp. The corallite[4] resembles a tube-like structure (theca), which is intercepted by septa (i.e., radiating vertical partitions) and their accompanying structures. Dissepiments are thin horizontal sheets on which the base of the polyps is located. Sclerodermites constitute the basic building units of all coral skeletal hard tissues. These building blocks consist of fibres, which are between 0.05-4 µm in diameter and show a preferential elongation in c-axis direction or fine crystals of aragonite. The arrangement of the latter resembles three dimensional fans located around centres of calcification (COC) or early mineralisation zone and rapid accretion deposits – depending on the author cited (see Stolarski, 2003; Cuif and Dauphin, 2005a; Brahmi et al., 2012; Fig. A7). COC are assembled by randomly oriented, nm-sized $CaCO_3$ crystals, which are embedded in organic matrices consisting of acidic proteins and polysaccharides, forming micrometre-sized, rounded aggregates (Gladfeiter, 1982; Constantz and Weiner, 1988; Cuif and Dauphin, 1998; Cuif et al., 2003; Meibom et al., 2004). Aragonitic spherulites are grouped into fascicles (or fasciculi), which represent fish scale shaped bundles (Ogilvie, 1896; Constantz, 1989; Cohen and McConnaughey, 2003). When numerous

---

[4] The corallite constitutes the skeleton of a coral individual (Ziegler, 1992).

sclerodermites are simultaneously growing upwards in the plane of the up-folded matter, a vertical spine known as trabecula is created. United groups of trabeculae, with or without the presence of intervening spaces or pores, assemble septa which are the primary structures of coral skeletal hard parts. Each trabecula ends up in a dentation, which corresponds to an assembly of a delicate array of thin spikes, at the expanding tip of the septum.

Despite the large dimensions of massive coral colonies, biomineralisation occurs exclusively in the wall tissue layer. This layer exists only at the top few millimetres of the coral skeleton and is occupied by living matter (Cohen and McConnaughey, 2003). However, the process of biomineralisation in corals is still under debate as many models, such as physicochemical or fully biologically controlled processes, are postulated (Cuif and Dauphin, 2005a, 2005b; Meibom et al., 2007). COCs are assumed to play a fundamental role in any model as they are considered to act as nucleation sites for the growth of aragonitic fibres (e.g., Constantz, 1986, 1989; Le Tissier, 1988; Cohen et al., 2001).

Neighbouring corals either share their cell walls or form a so called coenosteum by linking their skeletons (Wall and Nehrke, 2012). In the majority of coral colonies, the exoskeleton underneath the tissue layer forms the greatest amount of coral hard tissue, which is continuously surrounded by seawater. Thus, the growth of aragonite crystals continues at a very slow rate within porous spaces which were once occupied by living tissue. Aragonitic fibres in fascicles grow out at low angles from each of the COCs until they converge with crystals growing out from neighbouring COCs up to the point of mutual interference, and prevents any further growth of the fibres (Cohen and McConnaughey, 2003). According to Enmar and co-workers (2000), the chemical composition, growth rates, as well as the morphology differ in abiotic and biotic aragonite crystals. Thus, it is possible to distinguish between these two types of aragonitic crystals present in the corals.

Many palaeoclimate reconstruction studies are empirically based on observations of isotopic compositions of skeletal oxygen or selected trace element abundances of scleractinian corals which vary in reaction to seawater temperature changes (Smith et al., 1979; Mitsuguchi et al., 1996; Swart and Leder, 1996; Meibom et al., 2006, 2007). Furthermore, past seawater levels are determined based on data obtained from stratigraphic observations, Ur/Th dating, and [230]Th ages (Eisenhauer et al., 1993, 1999; Blanchon et al., 2009; Rashid et al., 2014).

A I.3 Marine organisms forming mixed calcitic/aragonitic and nacreous shells

Bivalve *Mytilus edulis*

Mytilus edulis (Linneaus, 1758; see Fig. A8), also known as the common blue mussel, is categorised into the phylum Mollusca and the class Bivalvia. The evolutionary origin of the *Mytilus* genus dates back to the Pliocene, and thus, is a relatively modern genus compared to the first appearance of Mytilidae, which is reported to date back to the Jurassic or perchance to the Devonian (Bayne, 1976).

Three distinct layers characterise the microstructure of *M. edulis* shells (see Fig. A9A): (1) the outermost, protective organic layer called periostracum (e.g., Lowenstam and Weiner, 1989; Harper, 1997; Gosling, 2003; Wählisch et al., 2014), (2) followed by a layer comprised of 'prismatic' fibrous calcite (see Fig. A9B) in which each fibre is surrounded by an organic sheath (e.g., Marin and Luquet, 2004; Griesshaber et al., 2013; Casella et al., 2018c). (3) The innermost part of the shell is comprised of an aragonitic nacreous layer in a 'brick-and-mortar'-arrangement (see Fig. A9C). Isolated nacre tablets expose a (pseudo-)hexagonal shape and are separated by a network of an intra-tablet organic matrix (e.g., Checa et al., 2006; Cartwright and Checa, 2007; Jacob et al., 2008; Zuykov et al., 2011; Zhang and Evans, 2012; Griesshaber et al., 2013; Casella et al., 2018c). Each nacre tablet shows a thickness of approx. 200 nm and a width of approx. 300 nm (e.g., Checa et al., 2006; Pokroy et al., 2009; Griesshaber et al., 2013).
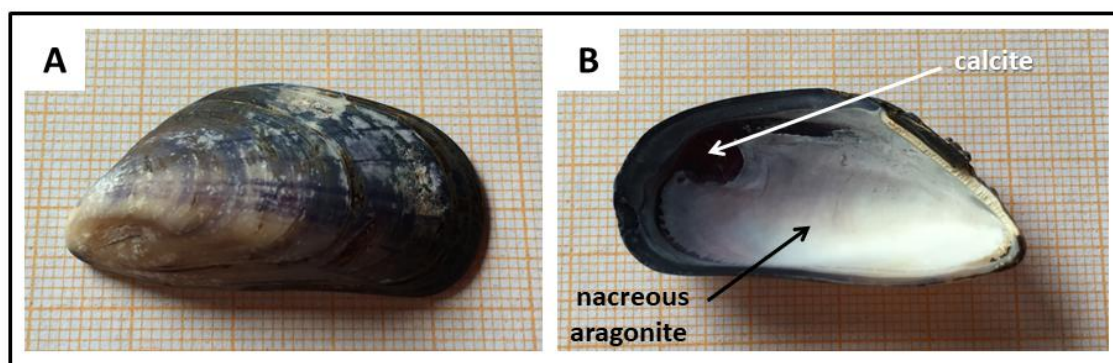
Figure A8: Photographs of a modern specimen of the bivalve *Mytilus edulis* showing the (A) exterior of the shell which is coated with the organic periostracum, and (B) the interior of the shell with indication of the calcitic layer (white arrow) and the nacre layer (black arrow). The sample was collected from 5-7 m depth in the subtidal of Menai Strait Wales, U. K. (see Casella et al., 2018c).
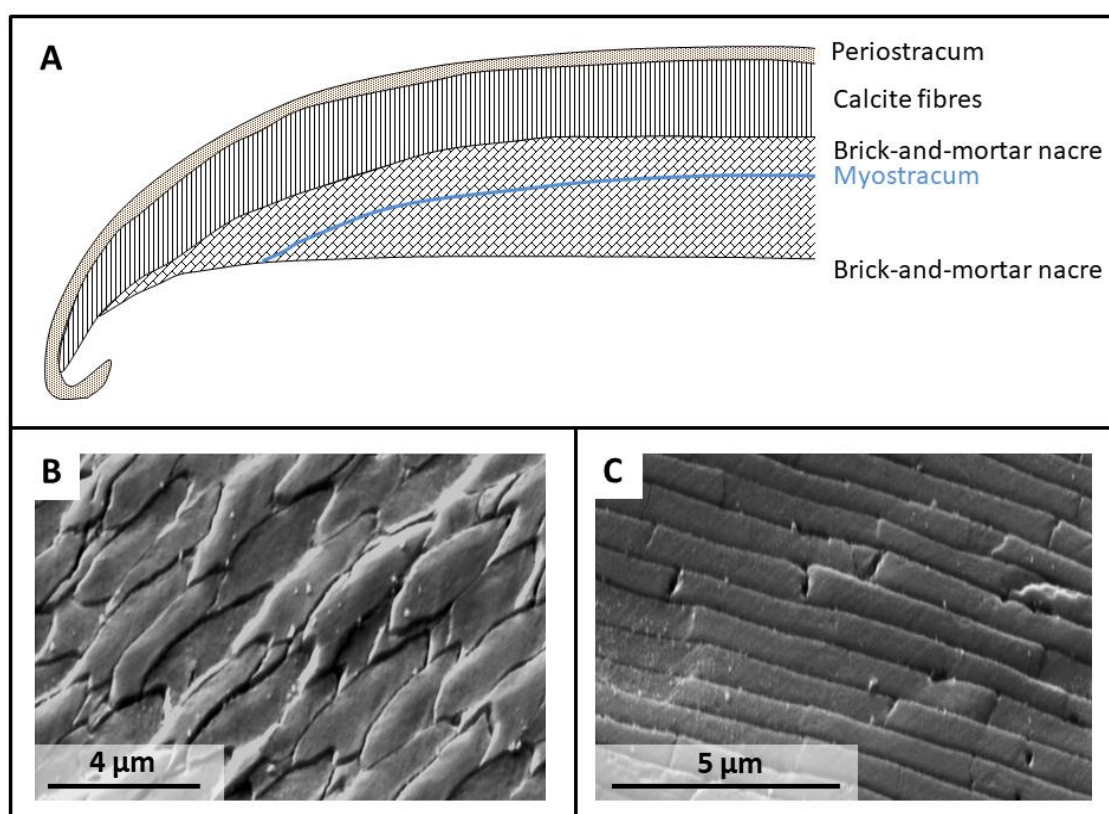
Figure A9: (A) Schematic drawing illustrating the different layers comprising the shell of the bivalve *Mytilus edulis* (modified after Lowenstam and Weiner, 1989). (B-C) SE micrographs showing the microstructures of calcite fibres and brick-and-mortar nacre, respectively (from Casella et al., 2018c).

Maier and co-workers (2014) have shown that aragonitic nacre tablets in the mollusc *M. edulis* are comprised of spherical nanocrystals. Molluscan shell material is precipitated from the extrapallial fluid, which is physically isolated from external solutions by the mantle membrane, old shell, and periostracum (e.g., Bevelander and Nakahara, 1969; Heinemann et al., 2008; Griesshaber et al., 2013).

Environmental changes are recorded in the nacreous aragonitic and calcitic shells due to the sessile lifestyle of *M. edulis* bivalves (e.g., Elliot et al., 2003; Immenhauser et al., 2005; Hippler et al., 2009; Hahn et al., 2014). Hence, *M. edulis* is an useful proxy for the study of palaeoenvironmental changes, especially for the acidification of seawater (Hahn et al., 2014). However, profiles of $\delta^{13}C$ data obtained from *M. edulis* appear to be not suitable for the reconstruction of palaeo-DIC[5] or palaeo-pCO$_2$[6] (Wanamaker et al., 2007).

---

[5] DIC corresponds to dissolved inorganic carbon (Miller and Zepp, 1995).

[6] Partial pressure of CO_2 is commonly abbreviated by pCO$_2$ (Leclercq et al., 2000).

Gastropod *Haliotis ovina*

Haliotis ovina (Gmelin, 1791; see Fig. A10), also known as the sheep´s ear abalone, is a wide-spread marine biomineraliser belonging to the phylum Mollusca and the class Gastropoda, which comprises over 50.000 living species (Ruppert et al., 2004). The number of identified Haliotidae varies between 30 and 130 species (e.g., Cox, 1962; Dauphin et al., 1989). The most prevalent Haliotis taxa are *Haliotis asinina*, *Haliotis clathrata*, *Haliotis ovina*, as well as *Haliotis planata* (Geiger and Owen, 2012). Depending on the author, the fossil record of gastropods dates back either to the late Cretaceous (Estes, 2005) or to the Cambrian (Bouchet et al., 2005).
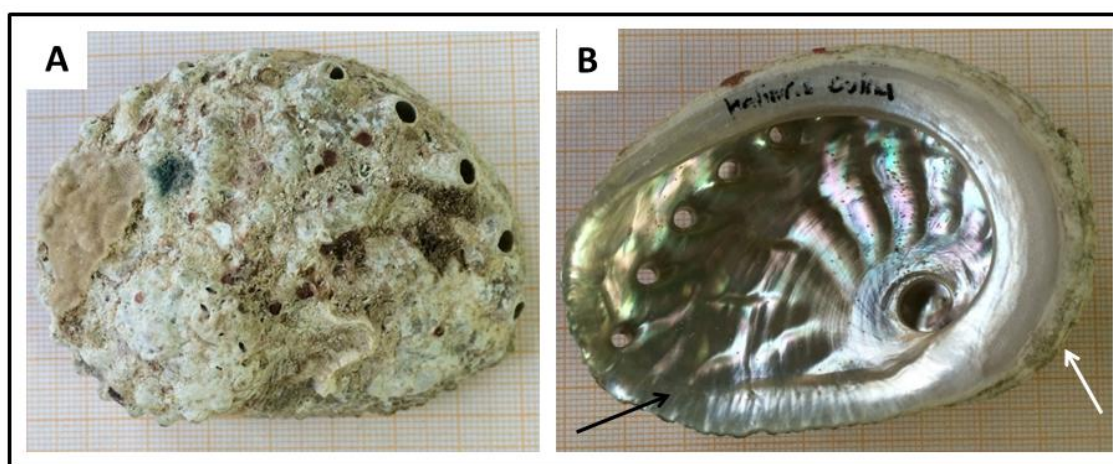
Figure A10: Photographs of a modern specimen of the gastropod *Haliotis ovina* showing the (A) exterior of the shell which is coated with the organic periostracum, and (B) the interior of the shell with indication of the prismatic aragonitic layer (white arrow) and the nacre layer (black arrow). The sample was collected from the reef flat of Heron Island, Queensland, Australia (see Casella et al., 2018c).

Abalone shells are mineral-biopolymer composite materials (Palmer, 1983, 1992) and their formation, mineralogy, as well as morphologies are assumed to be genetically controlled by physiology (e.g., Weiner et al., 1984; Jackson et al., 2010). The $CaCO_3$ shell of Haliotidae (see Fig. A10 for the shell of a pristine *H. ovina* shell) is formed by the mantle tissue (Sud et al., 2002). Furthermore, the microstructure of *H. ovina* and *Haliotis* sp. is comprised of three layers: (1) the outermost part consists of a thin protein-rich, organic layer called periostracum which acts as protective cover and prevents the decalcification of the shell (e.g., Marin et al., 2008; Nakayama et al., 2013). Depending on the species, (2) the secondary layer is comprised of a mixture of prismatic aragonite and calcite (e.g., *H. asinina*) or aragonitic prisms only (e.g., *H. ovina* (see Fig. A11A)**,** and *H. rufescens*; Dauphin et al., 1989; Casella et al., 2018c). (3) A thick layer consisting of iridescent, columnar nacre of approx. 0.5 µm thick stacked tablets (Fig. A11B**)** is located
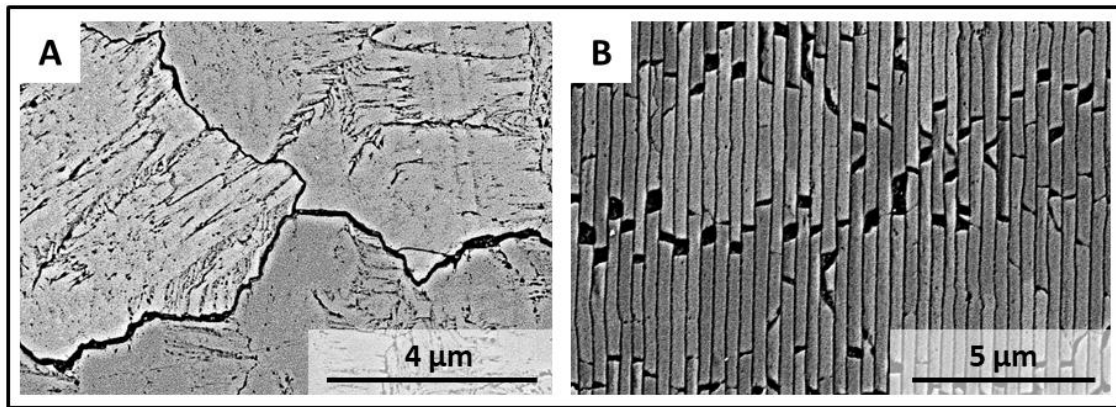
Figure A11: SE micrographs showing the microstructure of the pristine shell of *Haliotis ovina* comprised of (A) prismatic aragonite, and (B) columnar nacre (taken from Casella et al., 2018c).

beneath the prismatic secondary layer (e.g., Addadi and Weiner, 1997; Levi-Kalisman et al., 2001; Metzler et al., 2007; Checa et al., 2009; Olson et al., 2012; Casella et al., 2018c). Each nacre tablet is surrounded by an organic proteinaceous matrix with a thickness of 20-50 nm. The organic matter defines and controls the growth and size during the crystal formation of aragonitic nacre tablets (e.g., Gilbert et al., 2008; Meyers et al., 2008; Casella et al., 2018c).

Due to the outstanding toughness of nacreous aragonite, shells of abalones are of high interest in terms of developing new, bio-inspired ceramic materials (e.g., Lin and Meyers, 2005; Gilbert et al., 2008; Olson et al., 2012).

A II   Experimental hydrothermal alteration

A II.1   Experimental setup

Hydrothermal alteration of inorganic and biogenic calcium carbonate samples was conducted in order to mimic meteoric and burial diagenetic alteration. One part of the samples used in this thesis was prepared in collaboration by colleagues at Graz University of Technology, Austria. Artificial burial solution contained 100 mM NaCl and 10 mM $MgCl_2$ and artificial meteoric solution was prepared using 10 mM NaCl. The solutions prepared in Graz were additionally spiked with ^{16}O-rich water in order to trace fluid-solid exchange reactions. Sample fragments of 20 x 10 x 5 mm in dimension were placed in a PTFE (polytetrafluoroethylene) liner (2.5 cm in diameter and 14 cm in height) filled with 25 mL of either simulated burial or meteoric fluid and sealed with a PTFE lid. Each of the PTFE liners was inserted into a stainless steel autoclave, sealed and kept in a preheated oven at 100, 125, 150 or 175 °C, respectively. The duration of single experiments ranged from 1 day to 84 days. After the experimental time, the autoclaves were removed from the oven, cooled down to room temperature and opened.

Alteration experiments carried out in Munich were conducted with sample fragments of approximately 5-20 x 5-20 x 5 mm in size, and aragonitic powder material. Compositions of simulated burial and meteoric fluids were identical to those described above, however, not additionally spiked with ^{16}O-rich water. Figure A12 illustrates the experimental setup used at LMU Munich. The samples were placed in a PTFE liner (4.5 cm in diameter and 5.8 cm in height) filled with 10 mL of either simulated burial or meteoric fluid and sealed with a PTFE lid. Each of the PTFE liners was inserted into a stainless steel autoclave (PARR INSTRUMENT COMPANY, 276AC T304 031310), sealed and kept in a preheated oven at temperatures between 100 °C and 175 °C for a time range of 1 day to 42 days. The estimated pressure within the autoclave during the hydrothermal alteration experiments conducted in Graz and Munich was 1 and 9 bar for 100 and 175 °C, respectively, and corresponded to the vapour pressure at the given temperature. After the experiment, the autoclaves were removed from the oven, cooled down to room temperature in a laboratory hood before being opened.

Powdered samples were recovered by using a membrane filter (Merck Millipore polycarbonate membranes, pore size 0.22 μm, type GTTP) placed inside a vacuum-filtration unit. Subsequently, the powder was placed inside a sample beaker and dried at 40 °C for at least 12 hours.

Further details on the experimental methods are given in Casella et al. (2017, 2018a, 2018b, 2018c) and Ritter et al. (2017).
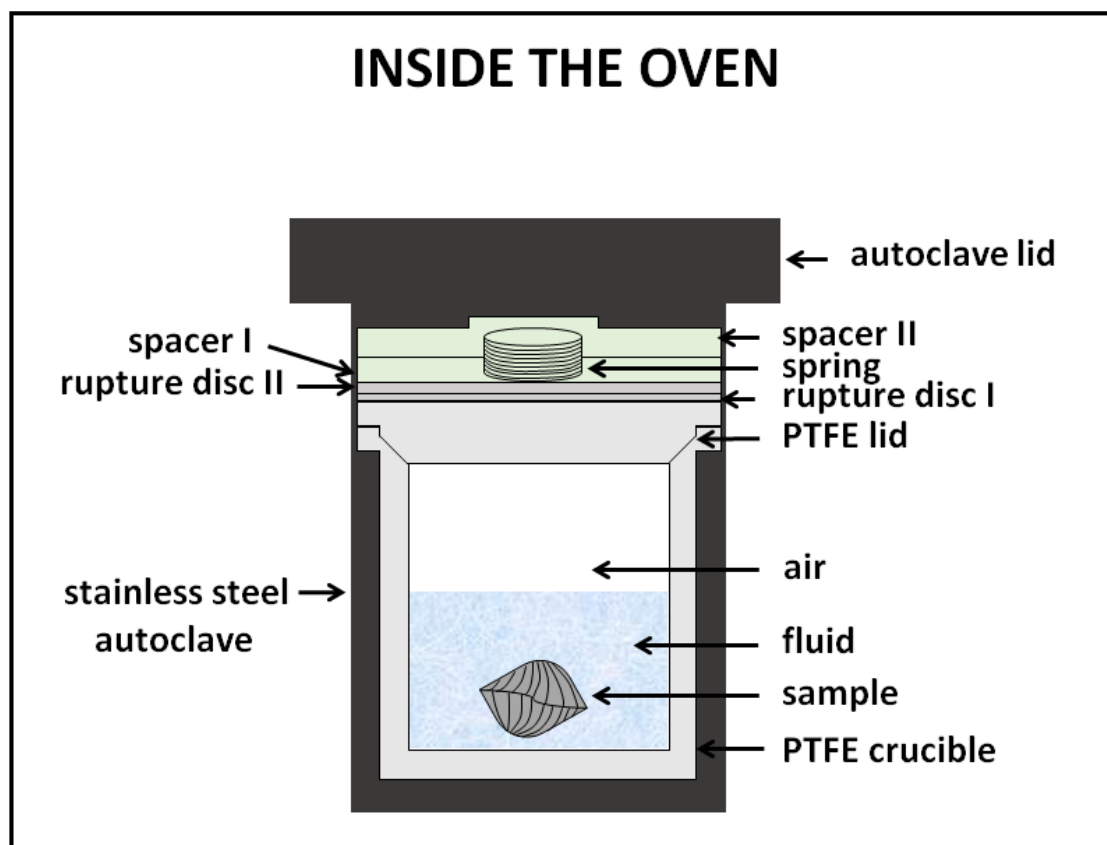
Figure A12: Schematic drawing of conducted hydrothermal alteration experiments of biogenic carbonates inside a PTFE crucible which is encapsulated by a stainless steel autoclave and placed inside a preheated oven.

A II.2   Overview on hydrothermally altered samples

This subchapter compiles all experimental information on altered biogenic and inorganic carbonate samples. It should be noted that experiment names beginning with "Exp. SH" were conducted by Sixin He in the framework of her master thesis which was a project associated with the scientific study presented in this thesis. Furthermore, experiment names beginning with 'CHA-' were prepared in collaboration by colleagues from Graz University of Technology, Austria.

Biogenic carbonates

Biogenic carbonate specimens which were subject to laboratory-based hydrothermal alteration in Munich and Graz are given in Tables A1-A8 and Tables A9-A10, respectively. Experiments were partially conducted in the framework of the project-internal CHARON collaboration by the working group of TP 1 (Dr. Vasileios

Mavromatis, PI: Prof. Dr. Martin Dietzel). The analytical investigation was carried out by the author at *Ludwig-Maximilians-Universität München* in the context of the presented thesis.

Seven different animal species consisting of either biogenic aragonite (*Arctica islandica*, *Porites* sp., *Acropora palmata*), biogenic low-Mg calcite (*Terebratalia transversa*), or a mixture of calcitic/aragonitic layers with nacreous aragonite (*Mytilus edulis*, *Haliotis ovina*, *Gryphus vitrius*) were experimentally altered.

Table A1: Experimental conditions used in mimicked diagenetic alteration of biogenic aragonite of modern *A. islandica* bivalve shells.

Experiment	Temperature [°C]	Time [d]	Solution
Exp. 1	175	1	meteoric
Exp. 2	175	1	burial
Exp. 3	125	1	meteoric
Exp. 4	125	1	burial
Exp. 5	150	2	meteoric
Exp. 6	150	2	burial
Exp. 7	125	14	meteoric
Exp. 8	125	14	burial
Exp. 11a	175	3	burial
Exp. 11b	175	4	burial
Exp. 11c	175	5	burial
Exp. 11d	175	6	burial
Exp. 16a	175	4 ¼	burial
Exp. 16b	175	4 ½	burial
Exp. 16c	175	4 ¾	burial
Exp. 17	100	1	burial
Exp. 20	175	7	meteoric
Exp. 21	175	7	burial
Exp. 22	175	10	burial
Exp. 23	150	14	burial
Exp. 24	150	7	burial
Exp. 25	175	2	burial
Exp. 26	175	7	burial
Exp. 27	175	10	burial
Exp. 37	175	35	burial

Table A2: Experimental conditions used in mimicked diagenetic alteration of biogenic aragonite of modern, 70-years old *Porites* sp. (RP4II) corals.

Experiment	Temperature [°C]	Time [d]	Solution
Exp. 29a	175	35	burial
Exp. SH 6e	175	2	burial
Exp. SH 3e	175	4	burial
Exp. SH 2e	175	5	burial
Exp. SH 5e	175	6	burial
Exp. SH 1d	175	7	burial
Exp. SH 1d_2	175	7	burial
Exp. SH 9e	175	8	burial
Exp. SH 10e	175	9	burial
Exp. SH 7e	175	10	burial
Exp. SH 7e_2	175	10	burial
Exp. SH 8e	175	14	burial
Exp. SH 11e	175	21	burial

Table A3: Experimental conditions used in mimicked diagenetic alteration of biogenic aragonite of 3000 years old *Porites* sp. (H-tai 2) corals.

Experiment	Temperature [°C]	Time [d]	Solution
Exp. SH 3c	175	4	burial
Exp. SH 2c	175	5	burial
Exp. SH 5c	175	6	burial
Exp. SH 1b	175	7	burial

Table A4: Experimental conditions used in mimicked diagenetic alteration of biogenic aragonite of 117 ka old *A. palmata* (XD4-2) corals.

Experiment	Temperature [°C]	Time [d]	Solution
Exp. SH 3d	175	4	burial
Exp. SH 2d	175	5	burial
Exp. SH 5d	175	6	burial
Exp. SH 1c	175	7	burial

Table A5: Experimental conditions used in mimicked diagenetic alteration of biogenic aragonite (nacre) and calcite of modern *G. vitreus* shells (brachiopod).

Experiment	Temperature [°C]	Time [d]	Solution
Exp. 32	175	14	meteoric
Exp. 33	175	14	burial

Table A6: Experimental conditions used in mimicked diagenetic alteration of biogenic aragonite and nacre of modern *H. ovina* shells (gastropod).

Experiment	Temperature [°C]	Time [d]	Solution
Exp. 28d	175	2	burial
Exp. 28e	175	10	burial
Exp. 29b	175	35	burial
Exp. SH 3b	175	4	burial
Exp. SH 2b	175	5	burial
Exp. SH 5b	175	6	burial
Exp. SH 1e	175	7	burial
Exp. SH 4b	175	14	burial
Exp. SH 11b	175	21	burial

Table A7: Experimental conditions used in mimicked diagenetic alteration of biogenic aragonite (nacre) and calcite of modern shells of the common blue mussel *M. edulis* (bivalve).

Experiment	Temperature [°C]	Time [d]	Solution
Exp. 9	100	14	meteoric
Exp. 10	100	14	burial
Exp. 29c	175	35	burial
Exp. 39	175	42	burial
Exp. SH 3a	175	4	burial
Exp. SH 2a	175	5	burial
Exp. SH 5a	175	6	burial
Exp. SH 1f	175	7	burial
Exp. SH 11a	175	21	burial

Table A8: Experimental conditions used in mimicked diagenetic alteration of biogenic calcite of modern *T. transversa* brachiopod shells.

Experiment	Temperature [°C]	Time [d]	Solution
Exp. 12	100	28	meteoric
Exp. 13	100	28	burial
Exp. 14	100	21	meteoric
Exp. 15	100	21	burial
Exp. 35	175	28	burial
Exp. 38	175	28	meteoric

Table A9: Experimental conditions applied to modern biogenic aragonite of *A. islandica* bivalve shells in hydrothermal treatments conducted by project collaborators (TP1, working group of Prof. Dr. M. Dietzel) at Graz University of Technology.

Sample Name	Temperature [°C]	Time [d]	Solution
CHA-M-018 AI16 B2	0	0	---
CHA-M-040 AI 21 B2	100	28	meteoric
CHA-M-041 AI22 B2	175	7	burial
CHA-M-042 AI23 B2	175	7	meteoric
CHA-M-043 AI24 B2	100	28	burial
CHA-M-044 AI25 B3	175	14	modified seawater[7]
CHA-M-046 AI27 B1	175	84	meteoric
CHA-M-046 AI27 B2	175	84	burial

Table A10: Experimental conditions applied to modern biogenic calcite of *Terebratalia transversa* brachiopod shells in hydrothermal treatments conducted by project collaborators (TP1, working group of Prof. Dr. M. Dietzel) at Graz University of Technology.

Sample Name	Temperature [°C]	Time [d]	Solution
CHA-B-029-1	100	28	meteoric
CHA-B-029-9	100	28	burial
CHA-B-030-5	100	28	modified seawater
CHA-B-031-1	175	7	meteoric
CHA-B-031-3	175	14	meteoric
CHA-B-032-5	175	7	modified seawater

---

[7] Seawater which was depleted in SO_4 by the addition of $BaCl_2$ in order to prevent the formation of anhydrite (Mavromatis, 2015).

Inorganic carbonates

In order to compare hydrothermally altered biogenic carbonates with an inorganic reference, alteration experiments were conducted using aragonite single crystals. Single crystals from Molina de Aragon, Spain, were either used as crystal pieces cut perpendicular to the c-axis or as ground powder. All experiments were conducted with artificial burial solution (100 mM NaCl + 10 mM $MgCl_2$ aqueous solution). Applied experimental conditions for inorganic aragonite samples are given in Tables A11-A12.

Table A11: Overview on experimental conditions applied to powdered inorganic aragonite single crystals sampled at Molina de Aragon, Spain.

Experiment	Temperature [°C]	Time [d]	Solution
Exp. 18a	100	1	burial
Exp. 18b	100	3	burial
Exp. 31a	175	1	burial
Exp. 31b	175	3	burial
Exp. 31b	175	7	burial

Table A12: Overview on experimental conditions applied to inorganic aragonite single crystals (Molina de Aragon, Spain) cut perpendicular to the c-axis.

Experiment	Temperature [°C]	Time [d]	Solution
Exp. 19a	100	1	burial
Exp. 19b	100	3	burial
Exp. 30a	175	1	burial
Exp. 30b	175	3	burial

A III Sample preparation

A III.1 Microtome cutting and polishing for selective chemical etching procedure

Selected specimens were cut into small cubes of maximum 3 x 3 x 2 mm in dimension using a razor blade or diamond pad saw. Obtained samples were subsequently glued on top of aluminium rods using cyanoacrylate adhesive. In order to obtain a plane surface, the samples were trimmed using a microtome (Reichert-Jung ULTRACUT) equipped with a glass knife. Material from the sample surface was trimmed in 100 nm steps. Each step was repeated for 10 times. Subsequent polishing was carried out using a diamond knife (DiATOME). Sample material was gradually removed in a series of sections with successively decreasing thicknesses (90, 70, 40, 20, and 10 nm). Each step was repeated 15 times following standard procedures (Fabritius et al., 2005).

A III.2 Selective chemical etching procedure for visualisation of organic matrices by SEM

Selective chemical etching procedure was carried out in order to expose the organic matrices by dissolving the mineral component of biogenic carbonate samples. Selected biocarbonate specimens were prepared as described in appendix III.1 prior to selective chemical etching.

The etching solution was prepared by mixing 27 mL of 0.1 M HEPES buffer (4-(2-hydroxyethyl)-1-piperazineethanesulfonic acid) with a pH of 6.5 with 3 mL of 2.5 % glutaraldehyde fixation solution (Seidl and Ziegler, 2012). Subsequently, the etching procedure was conducted by holding the specimen which was glued on an aluminium rod with a gripper into the etching solution for 180 seconds. In order to remove all remnants of the etching solution, the specimen was dipped into pure isopropyl (p. a.) three times for 10 minutes each. In order to stabilise the exposed organic matrix, the sample was then subjected to critical point drying in a Liechtenstein BAL-TEC CPD 030 apparatus (see appendix IV.1). The sample preparation process was completed by applying a 3 nm thick rotary platinum coating prior to SEM imaging.

A III.3 Surface polishing procedure for SEM imaging and EBSD measurements

High-quality EBSD measurements require highly polished and plane sample surfaces. For this purpose, specimens of marine biocarbonates were embedded into resin prior to grinding and polishing steps. The utilised resin was prepared by vigorous stirring a mixture of 30 mL of EpoFix Resin and 4 mL of EpoFix Hardener (Buehler) for 2 minutes in the laboratory hood. In order to guarantee easy removal of the embedded sample after hardening, walls of the sample holders were lubricated with petroleum jelly. To assist the hardening process of the resin, the embedded samples were placed into a desiccator for a minimum of 12 hours. The usage of a desiccator is necessary during the hardening process in order to remove any bubbles which are present in the liquid resin. This step is essential as air bubbles are known to cause problems during the subsequent sample preparation and lower the quality of obtained EBSD measurements. After the hardening process, the samples were trimmed in order to remove remnants of petroleum jelly.

In order to obtain plane and highly polished surfaces, sample material was ground in three steps with decreasing grain sizes of SiC (silicon carbide) grinding paper (P 320, P 600, and P 1200; grain sizes: approximately 46, 26, and 15 μm, respectively) under water flow and a rotation of 150 rpm (rounds per minute) using a Buehler MetaServ 250 GrinderPolisher. Each grinding step removed scratches created by the previous, coarser SiC grinding paper and caused new, thinner scratches on the surface of the samples.

Ground samples with a thickness exceeding 3 mm were cut by using a diamond blade saw from HI-TECH DIAMOND and shortened to a height of maximum 3 mm using P 320 SiC grinding paper on the Buehler MetaServ 250 GrinderPolisher under water flow.

Polishing of ground specimens was carried out in two steps. Firstly, polishing was conducted by using an artificial silk cloth and MetaDi Supreme Polycrystalline Diamond Suspension 3 Fμm (grain size: 3 μm; Buehler). Best results of shininess were achieved by using a rotation of 150 rpm for 10 min on a Buehler MetaServ 250 GrinderPolisher. Subsequently, the polished sample was fixed on a metal punch using wax. This step is essential in order to keep a constant low pressure on the samples during the final polishing step. The latter was conducted on a Buehler VibroMet2 Vibratory Polisher with a thin layer of Buehler MasterPrep Polishing Suspension with a grain size of 0.05 μm for 3 hours and vibration amplitude of 40 %. Due to the rotary movement and vibration of the samples inside the apparatus, approximately the top 40 nm were being carefully removed. By using a synthetic fibre cloth and a water-detergent mixture, the remaining polishing suspension was removed from the highly

polished sample surface before rinsing it with high-purity deionised water. Drying after the cleansing step was carried out using a hairdryer at low temperature in order to avoid water spotting.

Samples were coated with 3-4 nm of carbon prior to SEM imaging and EBSD measurements.

A III.4   Fluid preparation for laboratory-based hydrothermal alteration experiments

Artificial meteoric and burial fluids utilised in hydrothermal alteration experiments were defined as aqueous solutions with a NaCl concentration of 10 mM, and 100 mM NaCl and 10 mM $MgCl_2$, respectively. In order to prepare the simulated meteoric and burial fluids, 0.5844 g of NaCl for meteoric, and 5.844 g of NaCl and 2.033 g of $MgCl_2 \cdot 6H_2O$ for burial were weighed and dissolved inside lockable plastic containers with 1 litre of high-purity deionised water. After preparation, the simulated diagenetic fluids were stored inside a refrigerator.

A III.5   Sample preparation for XRD measurements

All samples used for XRD measurements were prepared in one of three different ways depending on the available sample amount, utilised X-ray radiation wavelength, and diffractometer geometry. Independent of the subsequent preparation method, all sample pieces were ground to a fine powder with an agate mortar.

Measurements conducted with molybdenum $K_{\alpha 1}$-radiation in Debye-Scherrer geometry (transmission mode) required a sample preparation using glass capillaries with a diameter of 0.3 mm in which powder of the selected sample material was homogeneously distributed. Subsequently, the funnel of each glass capillary was removed and the opening sealed by either using a droplet of clear nail polish or a lighter in order to melt the top of the thin glass walls. Single glass capillaries were mounted on brass holders using clear nail polish and centred prior to XRD measurements.

The instrumental parameters were set to: 2θ range: 5-50 ° with 0.013 ° step width and an exposure time of 1000 seconds with enabled sample rotation.

Measurements using copper $K_{\alpha 1}$-radiation in Bragg-Brentano geometry (reflection mode) were performed with a sample holder consisting of a plastic ring which was placed around a brass holder creating a thin cavity at the centre. This central cavity was filled with sample powder. The latter was carefully compacted using a square-shaped

glass slide in order to create an even sample surface. To avoid measurement artefacts, the height of the sample material should be equal to that of the used XRD sample holder.

In case of extremely low quantities of available sample powder, the powder was mixed with 2-3 drops of ethanol inside an agate mortar. The suspension was taken using a disposable pipette and carefully dripped on top of a sample holder equipped with a single crystalline quartz platelet which was prepared in such a way that no background signal was detected during the measurement. The sample suspension was air-dried prior to XRD measurements in order to obtain a thin and smooth layer on top of the sample holder.

All data obtained for measurements with copper $K_{\alpha 1}$-radiation were collected with enabled sample rotation on a GE XRD 3003 TT diffractometer equipped with a position-sensitive, semiconductor-based 1D-detector (Meteor). Applied instrumental parameters were a 2θ range of 20-90 ° with a step width of 0.013 ° and exposure time of 1000 seconds.

A III.6   Sample preparation for EPMA element mapping

Elemental mappings measured by EPMA require highly polished sample surfaces in order to obtain precise values and best results. The sample preparation procedure for EPMA is equal to the sample preparation described for SEM imaging and EBSD measurements (see appendix III.3).

Selected brachiopod specimens for EPMA element mapping were prepared as thin sections at *Ruhr-Universität Bochum*, Germany. All EPMA samples were coated with a 15 nm thick carbon layer prior to carried out mappings.

A III.7   Sample preparation for CL imaging

In order to enable luminescence in a transmitted-light microscope and to obtain highly polished sample surfaces, selected sample materials were prepared as thin sections at *Ruhr-Universität Bochum*, Germany. The samples were coated with a 15 nm thick layer of carbon prior to CL imaging.

A IV   Methods

A IV.1   Critical point drying

The procedure of critical point drying (CPD) is commonly used in biosciences to dry biological samples. Water present in biological sample materials evaporates under low pressure conditions, and thus, disturbs imaging of the samples conducted with (FE-) SEM.

By using a conventional drying method (e.g., air drying), water would be compelled to change its liquid to a gaseous state resulting in high surface tension. This leads to collapse or damage of the delicate structures and surfaces of biological samples. In order to preserve the specimen morphology, CPD is applied as the state of the art method. As the physical characteristics of the liquid and gaseous state are not distinguishable at the critical point, compounds can be transformed from one to the other state without crossing interfaces, thus, avoiding any damaging effects. Due to the very high temperature and pressure conditions at the critical point of water (T_c = 374 °C, p_c = 221 bar), this liquid is not feasible for dehydration processes as it would cause severe damage to the samples. Hence, water is replaced by liquid carbon dioxide (CO_2) as the transitional fluid (T_c = 31.1 °C, p_c = 73.8 bar; see Fig. A13). However, CO_2 is not miscible with water, and therefore, has to be replaced by another fluid (in this case isopropyl) which acts as an intermediate fluid/exchange fluid. After the replacement of water by the intermediate fluid, an exchange of the intermediate fluid and liquid CO_2 is compelled (Leitner, 2000; Mortimer and Müller, 2007).
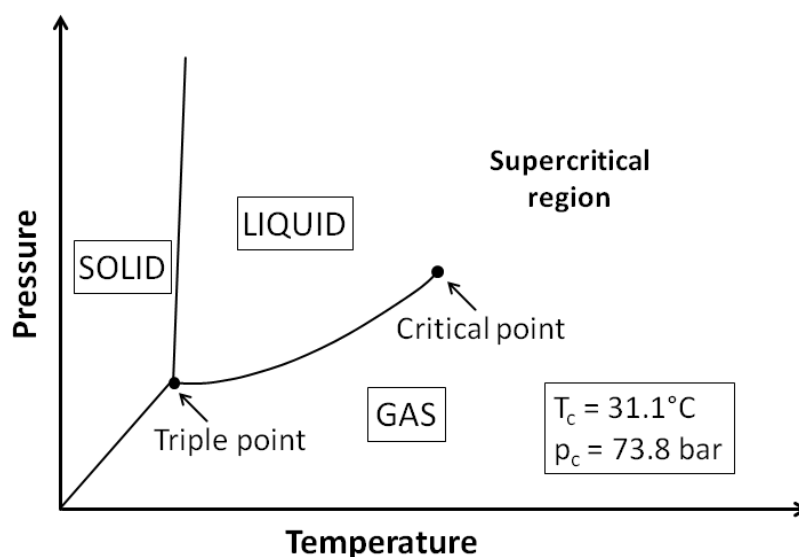
Figure A13: Phase diagram of carbon dioxide illustrating all present states, modified after Leitner (2000). At and above the critical point, CO_2 obtains the features of a gas and a liquid.

A IV.2   Cathodoluminescence

Cathodoluminescence (CL) is a method prevalent in geosciences to characterise, e.g., internal structures of fossils, minerals and rocks, origin of mineral grains which constitute sedimentary rocks, and for the recognition of diagenetic processes in siliciclastic as well as sedimentary carbonate rocks. Sample preparation is simple; measurements are relatively fast and allow for conclusions on fundamental geological processes (e.g., deformation and crystal growth; Richter et al., 2003). First CL studies were carried out with a petrographic microscope attached to a cathode gun. Nowadays, electron probe microanalysers and scanning electron microscopes are utilised to produce CL emission images with high-resolution and high-magnification.

It should be noted here, that the emergence and fundamental causes of the emission of CL are moderately understood until the present day.

The phenomenon of CL occurs as emission of photons (visible and UV range) by a material which is bombarded by a stream of high-energy electrons originating from a cathode (Pagel et al., 2000).

By bombardment of a specimen with high-energy electrons, electrons of the valence band (i.e., ground state) are removed and promoted into the conduction band (i.e., excited state), thus, leaving a hole in the valence band. Excited electrons reside in the conduction band for a very short time before falling back to the ground state via a loss in energy (photons). Due to the presence of defects in crystals (e.g., ion impurities, lattice defects), discrete energy levels of the band gap prevent de-excitation by capturing energised electrons inside electron traps. After the occupation of excited electrons for a few microseconds, they return to the ground state with simultaneous emission of photons. The electron traps inside band gaps, which are referred to as centres of luminescence, can be divided into extrinsic and intrinsic centres. Extrinsic centres (i.e., impurity centres) are incorporated into the crystals due to some characteristic features of the melt or fluid from which the mineral phase crystallised, whereas intrinsic centres (defect centres) are the result of crystal lattice imperfections (Walker and Burley, 1991). The number of CL emissions in the range of visible light increases with an increasing number of electron traps existing in the band gaps of the investigated crystals (Boggs and Krinsley, 2010).

A IV.3 X-ray diffraction

X-ray diffraction is a method conventionally applied for structure determination and analysis, as well as phase determination and quantification of crystalline materials. Its main fields of application are found in chemistry, biochemistry, pharmaceutical studies, material physics and crystallography.

Atoms of crystalline materials are characterised by their periodic arrangement within the crystal lattice. As typical unit cell parameters of crystalline materials range in the order of a few to tenths of nanometres, electromagnetic radiation with similar dimensions in wavelengths (X-rays) is diffracted at lattice planes of the investigated specimens.

X-rays are generated when a beam of electrons accelerated by the application of high voltage hits a metal target. Consequently, the deceleration of the electron beam is caused by a collision with atoms of the target and the majority of electrons lose their energy gradually due to multiple collision events. This results in the creation of a so called continuous X-ray spectrum or white radiation. If the energy of the electrons hitting the metal target is higher than a particular threshold value, a second spectrum type is created, the so called characteristic spectrum. The latter is characterised by discrete wavelengths which are dependent on the target material. If the energy of electrons exceeds the energy of the threshold potential, ionisation of target atoms may occur due to the ejection of an inner shell electron. The created vacancy can be occupied by an electron of a higher energetic level. Thus, the new occupied energy level is lower compared to the initial one and the difference in energy is emitted as characteristic X-ray photons by the electron of the higher energetic level. The wavelength of the emitted X-ray photon is dependent on the difference between the two involved energy levels. Characteristic lines of the second spectrum type are known as K, L, and M and correspond to transitions from the K, L, and M orbitals. When the transition involves two adjacent orbitals, the resulting line is termed as α. In the case of two orbitals which are separated by another shell, the line is termed as β. Due to the small difference between the two energy levels, both line types are divided into multiple lines which are fairly close to another.

X-rays are produced by using a sealed-tube generator which consists of a cathode filament emitting accelerated electrons under vacuum when high voltage is applied. These electrons collide with a fixed anode made of a specific metal target material. The wavelength of the anode material must have a characteristic K_α line which is suitable for the planned diffraction experiments. As the presence of gas molecules in the tube leads to a decrease in efficiency of the X-ray generating process caused by collisions with electrons in the beam, it is essential that a high vacuum is applied (Giacovazzo, 1998). In order to select a characteristic X-ray radiation, and to reduce the background caused by

white radiation a monochromator is applied. Furthermore, the utilisation of a collimator leads to a reduction of angular divergence.

When the X-ray beam hits the sample, it gets diffracted on the crystal lattice planes. This results in interferences, and thus, to the appearance of a diffraction pattern with sharp peaks. Using the Bragg´s law, it is possible to calculate the angles at which the sharp peaks appear (see Fig. A14).
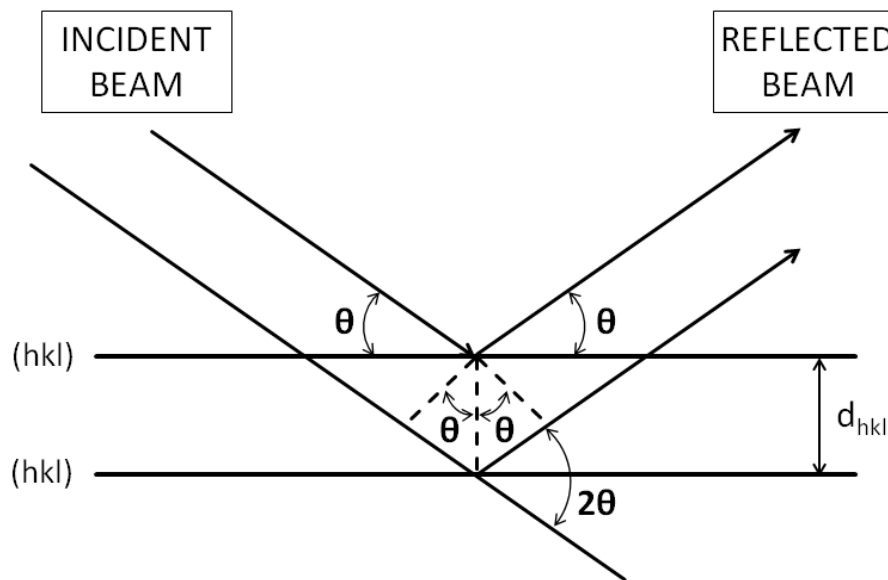
Figure A14: Illustration of the Bragg´s law geometry, modified after Pecharsky and Zavalij (2009). Diffraction angle (θ), lattice plane (hkl), and lattice plane distance (d_{hkl}).

Bragg´s law is a formula derived from geometry and is written as

$$n\,\lambda = 2d_{hkl}\sin\theta, \tag{eq. 5}$$

where n is the non-negative integer giving the order of diffraction, λ is the wavelength of the incident X-ray beam, d_{hkl} is the lattice spacing of the (hkl) plane and θ is the scattering angle. The square modulus of the structure factor F_{hkl} is proportional to the intensity I of Bragg reflexions and is written as

$$|F_{hkl}|^2 \propto I \tag{eq. 6}$$

with

$$F_{hkl} = \sum f_j \exp\left[2\pi i\,(hx_j + ky_j + lz_j)\right], \tag{eq. 7}$$

i.e., the summation over all atoms j comprised in the unit cell, the scattering factor f of the atom j with the coordinates x_j, y_j, and z_j and the Miller indices h, k, and l.

A IV.4 Scanning electron microscopy

Scanning electron microscopy (SEM) is a widely-spread tool used for the assessment and imaging of sample morphologies and microstructures. Its application can be found in various scientific fields such as in biology, metallurgy, materials science and geosciences. A common SEM setup is shown in Fig. A15.

Accelerated electrons are created in an electron gun which is located at the top of the SEM apparatus column. By passing through a combination of apertures and lenses, a focussed beam of accelerated electrons bombards and simultaneously scans a defined surface area of the specimen placed in a vacuum chamber. Due to the strong interaction behaviour of electrons with any kind of matter, the evacuation of the electron beam column needs to be well-conducted (Wischnitzer, 1970, Zaefferer and Habler, 2017). Three different types of electron guns are commonly used: the most basic version comprises a tungsten filament cathode. Electrons are then either emitted by the filament
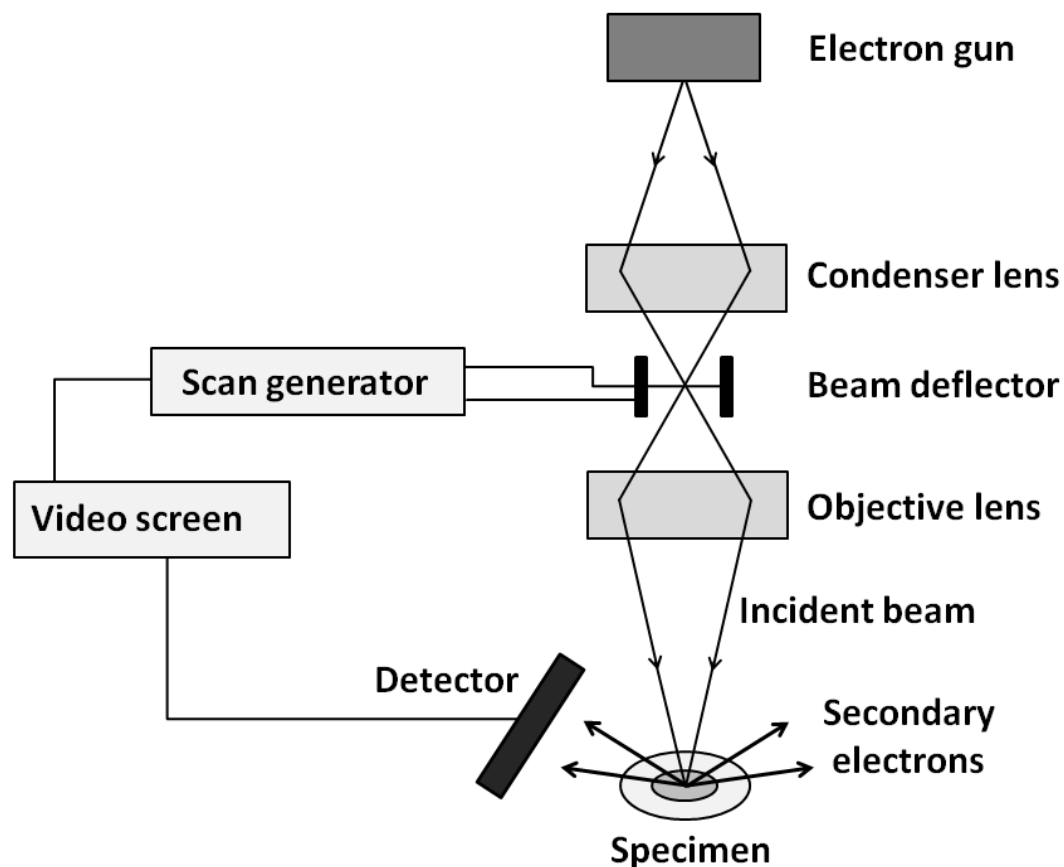
Figure A15: Schematic drawing of the SEM setup (modified after Alberts et al., 2014). Electromagnetic coils function as lenses, and thus, focus the electron beam on the specimen for scanning. The detector measures the incoming secondary electrons scattered or emitted from each successively scanned specimen point, which leads to the creation of an image on the video screen.

or the cathode. Electron acceleration is caused by the anode and kinetic energies range between 1 to 40 keV. The second type of electron gun consists of a lanthanum hexaboride cathode which is most common for its high brightness due to a high emission current and its long lifetime. Satisfactory results can be obtained by using the lanthanum hexaboride cathode for several hours of operating time. Even higher brightness can be obtained by the last type of electron guns, i.e., the field emission gun. As its name implies, the emission of electrons is produced by using field emission, i.e., electrons are tunnelling through the potential barrier (Wischnitzer, 1970, Zaefferer and Habler, 2017).

SEM images are generated by the collection of secondary electrons which are emitted from a distinctive sample area. The secondary electrons are amplified in order to produce a signal voltage passing through a cathode-ray tube. The beam of the cathode-ray tube is modulated and results in the creation of a SEM image.

Scanning of the specimen surface and recording of the measured signal for each single scan point allows for the reconstruction of a bitmap image of the scanned sample surface. A computer-controlled scan generator controls a set of crossed deflection coils which enable the scanning of the sample material.

The spatial resolution of the SEM technique is determined by the size of the interaction volume of the primary electron beam with the investigated specimen for a particular chosen observation signal. The interaction volume of the electron probe itself is dependent on the properties of the beam (e.g., acceleration voltage, diameter of the probe), studied material (e.g., density) as well as the measured type of signal (Zaefferer and Habler, 2017).

A IV.5 Electron backscatter diffraction

Electron backscatter diffraction (EBSD), also known as backscatter Kikuchi diffraction (BKD) or electron backscatter pattern technique (EBSP), is a common method found in geosciences and materials science. This method is commonly used for the investigation of microstructures and textures of crystalline specimens. However, it is also applied for phase determination and strain measurements (Schwartz, 2009). Additionally, EBSD measurements reveal the size, orientation and boundaries of crystal grains. Crystallographic information of a large variety of inorganic crystalline materials, e.g., metals, semiconductors, ceramics and minerals, can be obtained from EBSD measurements (Zhou and Wang, 2007). This technique can either be used in SEM systems or a TEM as first EBSD patterns of mica were observed in the latter by Kikuchi.
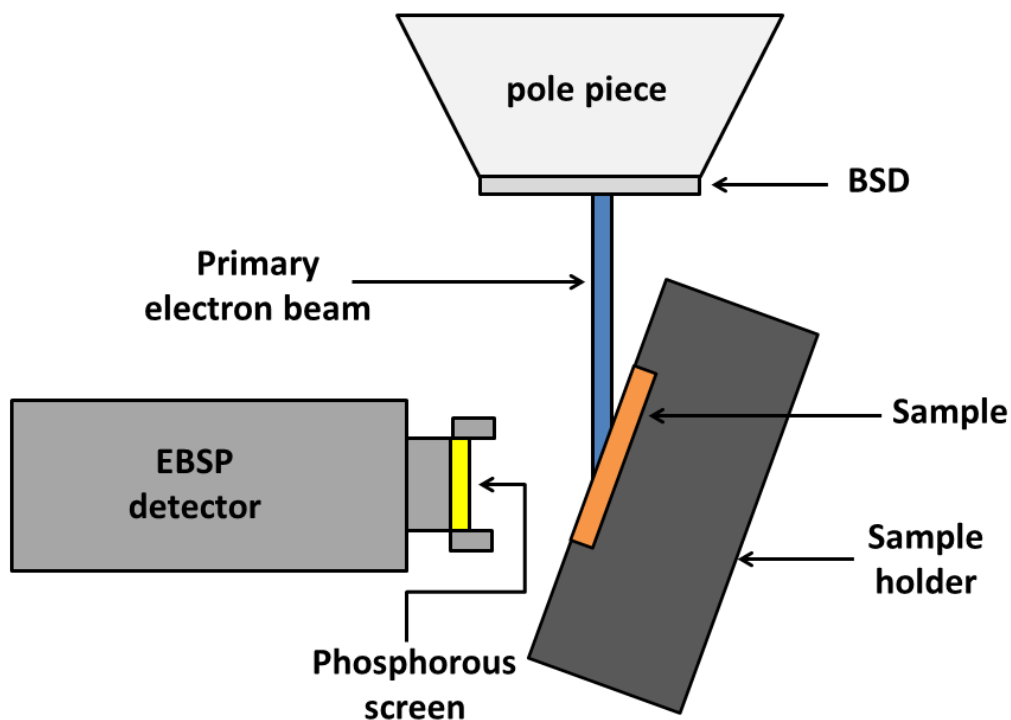
Figure A16: Schematic setup of an EBSD indicating the orientation of the sample, modified after Zhou and Wang (2007).

When an electron beam in a SEM or TEM system hits the sample surface, different energy conversion events are taking place. These result in a variety of signals (e.g., secondary electrons, Auger electrons, backscattered electrons (BSE)). In the case of EBSD, the diffraction of backscattered electrons is used for imaging, phase identification, and determination of crystallographic orientations. EBSD measurements are usually conducted on either highly polished sample surfaces or as-deposited thin films. In order to obtain a high intensity for EBSD patterns, it is required to position the specimens in such a way that a shallow angle of usually 20 ° with the incident beam is set. Due to the fact that SEM stages are commonly used for tilting the samples, the stage tilt value is reported as 70 °. Typical instrument parameters for EBSD measurements range from 10-30 kV for the accelerating voltage and 1-50 nA for the beam current (Schwartz, 2009).

Backscattered electrons are created by a diffusive inelastic scattering event; thus, BSE have a lower energy value compared to the incident electron beam. When the Bragg´s equation is fulfilled, constructive and destructive interference of the BSE results from the interaction between the primary beam and the crystal lattice of the investigated specimen. This leads to the formation of two cones with diffracted electrons in the 3D space on each lattice plane (Zhou and Wang, 2007). According to Prior et al. (1999), the intensity of these cones is dependent on the atomic species. Incoming signals are detected by a phosphorous screen of the EBSD camera which is positioned in such a way that both cones are intercepted (see Fig. A17). This setup leads to a pair of nearly straight
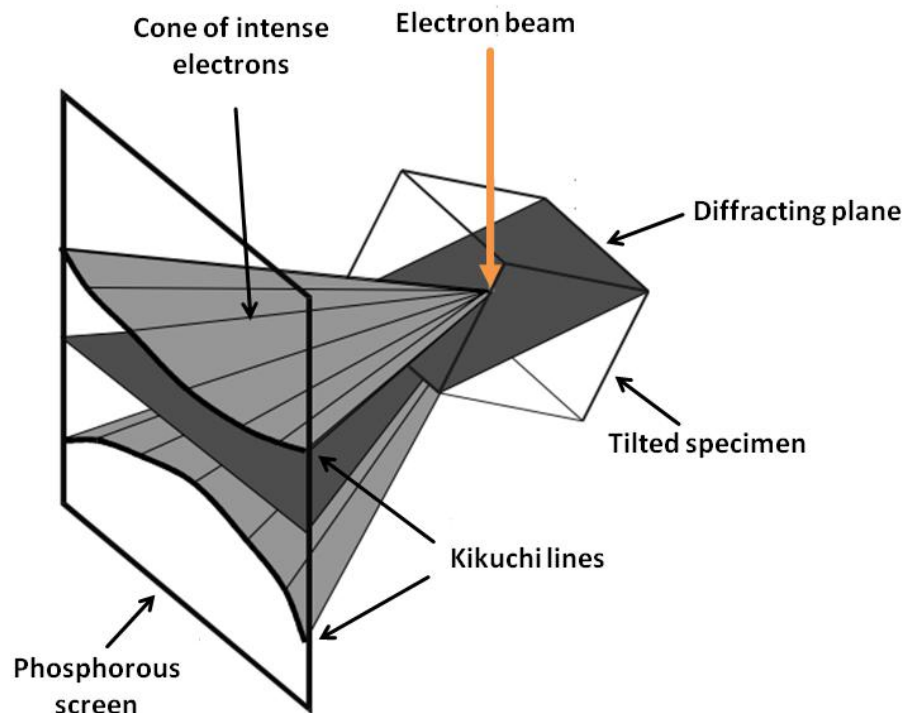
Figure A17: Illustration of the Kikuchi band formation in an oriented sample bombarded by an electron beam (orange arrow). Modified after Prior et al. (1999).

conic sections which appear as parallel lines. Both lines are referred to as Kikuchi lines which form the so called Kikuchi band (see Fig. A17).

All measured EBSD patterns consist of a multitude of Kikuchi bands. Each single Kikuchi band has a particular width and corresponds to a particular crystallographic orientation. The intersection of Kikuchi bands in the obtained EBSD pattern illustrates the zone axis. Major zone axes are recognised by the intersection of several Kikuchi bands, thus, the Kikuchi pattern expresses all angular relationships in the crystalline specimen and contains the symmetry and orientation of the investigated crystals/crystallites.

The indexing of measured EBSD patterns is automated by software which identifies poles and patterns. Relationships between these patterns and some chosen reference axes are calculated (Zhou and Wang, 2007). It is inevitable to know the present mineral phases of the specimen beforehand in order to set up the reference patterns as otherwise no match can be found by the software.

A IV.6   Electron probe microanalysis

Electron probe microanalysis (EPMA) is a common technique which provides in situ morphological (shape and roughness), qualitative and quantitative chemical data of small sample volumes (several μm^3) by a non-destructive measurement. This method is mainly established in materials science for ceramics and glass, as well as in geoscientific fields including geochemistry and mineralogy.

This technique is based on the same principles as a SEM as the experimental setup only differs by an additional X-ray detector (Goodhew et al., 2001). High temperatures of a tungsten filament placed inside the gun lead to the production of electrons, which are then accelerated due to their charged particle characteristics. Microvolumes of highly flat and polished sample surfaces are bombarded with an electron beam focussed by electrostatic lenses. Interactions between the electron beam and the electrons of the atoms in the sample lead to the emission of X-rays. The wavelength of the emitted X-rays is characteristic and element-specific. The composition of a specimen can be identified by the acquisition of WDS (wavelength-dispersive spectroscopy) spectra. Furthermore, the interaction between the focussed electron beam and the sample surface can lead to the generation of other secondary particles (e.g., BSE, SE, CL). These may provide more information on the composition of the analysed specimen.

Most of the machines are equipped with built-in microscopy tools which allow for the collection of simultaneous X-rays as WDS and EDS spectra as well as BSE and high resolution SEM imaging.

Danksagung

Der Weg zum Erfolg ist kein gerader Weg, sondern eher ein langer, kurvenreicher Pfad mit vielen Abzweigungen. Auch wenn es nicht immer einfach war, habe ich auf jedem der Pfade, die ich während meiner Promotion genommen habe, wertvolle Erfahrungen für meine Zukunft gesammelt. Diese hätte ich nicht missen wollen.

Ich möchte mich bei allen Personen, die mich während meiner Zeit als Promovendin begleitet haben, herzlich bedanken.

Zu allererst gilt meine tiefe Dankbarkeit meinem Doktorvater Herrn Prof. Dr. Wolfgang W. Schmahl für das Ermöglichen meines Promotionswunsches und meiner Teilnahme an vielen lehrreichen Konferenzen – vor allem in Japan, seine große Unterstützung, Beratung, brillanten Ideen, ergebnisreichen Diskussionen, spannenden Geschichten und seine humorvolle Art, durch die jede schwierige Zeit angenehmer wurde.

Ich bedanke mich bei Frau Dr. Erika Griesshaber für ihre tatkräftige Unterstützung während unserer Zusammenarbeit.

Desweitern möchte ich Dr. Kevin Steven, Dr. Andreas Ziegler, Dr. Vasileios Mavromatis, Prof. Dr. Lurdes Fernández-Díaz, Prof. Dr. Elizabeth M. Harper, Prof. Dr. Uwe Brand, Prof. Dr. Jörg Mutterlose, Prof. Dr. Martin Dietzel, Prof. Dr. Anton Eisenhauer und Prof. Dr. Adrian Immenhauser meinen Dank für die superbe Zusammenarbeit und fruchtbaren Diskussionen aussprechen.

Ich danke den Masterstudentinnen Kornelia Taubert und Sixin He, die ihre Abschlussarbeiten auf meinem Forschungsgebiet geschrieben haben und teils mit sehr interessanten Ergebnissen zu dieser Dissertation beigetragen haben.

Ich schätze sehr die Bemühungen von Anna und Justin Pearson und Julia Pipo, die mich beim Korrekturlesen meiner Doktorarbeit sehr unterstützt haben.

Ich danke der Deutschen Forschungsgesellschaft (DFG) für die finanzielle Unterstützung dieser Dissertation im Rahmen des DFG SPP 1644 "CHARON"-Projektes.

Ich möchte mich auch bei allen Teilnehmerinnen und Teilnehmern des „CHARON"-Projektes für die großartige Zeit bedanken. Besonders danke ich den anderen

Publications

Casella L. A., Griesshaber E., Simonet Roda M., Ziegler A., Mavromatis V., Henkel D., Laudien J., Häussermann V., Neuser R. D., Angiolini L., Dietzel M., Eisenhauer A., Immenhauser A., Brand U., and Schmahl W. W. (2018a):
Micro- and nanostructures reflect the degree of diagenetic alteration in modern and fossil brachiopod shell calcite: a multi-analytical screening approach (CL, FE-SEM, AFM, EBSD);
Palaeogeography, Palaeoclimatology, Palaeoecology, 502, 13-30.
DOI: 10.1016/j.palaeo.2018.03.11

Casella L. A., Simonet Roda M. d. M., Angiolini L., Ziegler A., Schmahl W. W, Brand U., and Griesshaber E. (2018b):
Archival biogenic micro- and nanostructure data analysis: signatures of diagenetic systems;
Data in brief, 19, 299-311.
DOI: 10.1016/j.dib.2018.05.041

Casella L. A., He S., Griesshaber E., Fernández-Días L., Greiner M., Harper E. M., Jackson D., Ziegler A., Mavromatis V., Dietzel M., Eisenhauer A., Veintemillas-Verdaguer S., Brand U., and Schmahl W. W. (2018c):
Hydrothermal alteration of aragonitic biocarbonates: assessment of micro- and nanostructural dissolution-reprecipitation and constraints of diagenetic overprint from quantitative statistical grain-area analysis;
Biogeosciences, 15, 7451-7484.
DOI: 10.5194/bg-15-7451-2018

Casella L. A., Griesshaber E., Yin X., Ziegler A., Mavromatis V., Müller D., Ritter A.-C., Hippler D., Harper E. M., Dietzel M., Immenhauser A., Schöne B. R., Angiolini L., and Schmahl W. W. (2017):
Experimental diagenesis: insights into aragonite to calcite transformation of *Arctica islandica* shells by hydrothermal treatment;
Biogeosciences, 14, 1464-1492.
DOI: 10.5194/bg-14-1461-2017

Publications

Ritter A.-C., Mavromatis V., Dietzel M., Kwiecien O., Wiethoff F., Griesshaber E., <u>Casella L. A.</u>, Schmahl W. W., Koelen J., Neuser R. D., Leis A., Buhl D., Niedermayr A., Breitenbach S. F. M., Bernasconi S. M., and Immenhauser A. (2017):
Exploring the impact of diagenesis on (isotope) geochemical and microstructural alteration features in biogenic aragonite;
Sedimentology, 64(5), 1354-1380.
DOI: 10.1111/sed.12356

Stevens K., Griesshaber E., Schmahl W. W., <u>Casella L. A.</u>, Iba Y., and Mutterlose J. (2017):
Belemnite biomineralization, development, and geochemistry: the complex rostrum of *Neohibolites minimus;*
Palaeogeography, Palaeoclimatology, Palaeoecology, 468, 388-402.
DOI: 10.1016/j.palaeo.2016.12.022

Conference contributions

<u>14th International symposium on biomineralization (BIOMIN XIV)</u>
Tsukuba, Japan, October 9th-13th, 2017.

<u>Casella L. A.*</u>, He S., Griesshaber E., Harper E. M., Ziegler A., Fernández-Díaz L., Eisenhauer A., and Schmahl W. W. (2017):
The effect of microstructure on the degree of diagenetic overprint of proxy archives: a qualitative assessment of alteration deduced from biocarbonate phase, orientation and grain size analysis. (Oral)

<u>Casella L. A.*</u>, He S., Griesshaber E., Harper E. M., Ziegler A., Fernández-Díaz L., Eisenhauer A., and Schmahl W. W. (2017):
The effect of microstructure on proxy archives: a qualitative assessment of diagenetic alteration. (Poster)

Schmahl W. W.*, Griesshaber E., Simonat Roda M., Yin X., <u>Casella L. A.</u>, Greiner M., Kocsis B., Maier B., Ziegler A., Kelm K., and Fernández-Díaz L. (2017):
Pathways of biomineralisation by marine organisms – atom by atom growth vs. particle accretion. (Oral)

<u>26th Goldschmidt Conference</u>
Yokohama, Japan, June 26th-July 1st, 2016.

<u>Casella L. A.*</u>, Griesshaber E., Mavromatis V., Dietzel M., Ritter A.-C., Immenhauser A., and Schmahl W. W. (2016):
Mimicking diagenetic alteration in the laboratory: effects on the microstructure and mineralogy of *Arctica islandica* shells. (Oral)

<u>European Geosciences Union (EGU2016) general assembly</u>
Vienna, Austria, April 17th-22nd, 2016.

<u>Casella L. A.*</u>, Griesshaber E., Mavromatis V., Harper E. M., Dietzel M., Immenhauser A., and Schmahl W. W. (2016):
Towards the kinetics of diagenetic overprint processes deduced from laboratory-based hydrothermal alteration of modern *Arctica islandica* shell material. (Oral)

Conference contributions

Casella L. A.*, Griesshaber E., Neuser R. D., Ritter A.-Ch., Mutterlose J., Brand U., and Schmahl W. W. (2016):
Microstructural changes reflect the degree of diagenetic alteration in biogenic carbonates. (Poster)

Griesshaber E.*, Casella L. A., Mavromatis V., Simonet Roda M., Harper E. M., Ziegler A., Dietzel M., Immenhauser A., and Schmahl W. W. (2016):
Quantification of diagenetic overprint processes deduced from fossil carbonate shells and laboratory-based hydrothermal alteration processes. (Keynote lecture)

3rd Euro bio-inspired materials
Potsdam, Germany, February 22nd-25th, 2016.

Casella L. A., Stevens K., Griesshaber E.*, Mutterlose J., Iba Y., Suzuki A., Ziegler A., and Schmahl W. W. (2016):
Gland versus mantle tissue induced biomineralisation: competitive growth of calcite in *Argonauta* sp. versus fibre, tablet array formation in bivalve shells. (Poster)

13th International symposium on biomineralization (BIOMIN XIII)
Granada, Spain, September 16th-19th, 2015.

Casella L. A.*, Stevens K., Griesshaber E., Ziegler, A. Mutterlose, J. Iba, Y., Suzuki A., and Schmahl W. W. (2015):
Gland versus mantle tissue induced biomineralisation: spherulitic growth of calcite in *Argonauta argo* versus fibre and tablet array formation in bivalve shells. (Oral)

25th Goldschmidt Conference
Prague, Czech Republic, August 16th-21st, 2015.

Casella L. A.*, Griesshaber E., Neuser R. D., Stevens K., Ritter A.-Ch., Mutterlose J., Brand U., Immenhauser A., and Schmahl W. W. (2015):
The impact of diagenetic and hydrothermal alteration on brachiopod calcite. (Oral)

Griesshaber E.*, <u>Casella L. A.</u>, Purgstaller B., Hippler D., Mavromatis V., Dietzel M., Immenhauser A., and Schmahl W. W. (2015):
Microstructural and microchemical signatures derived from hydrothermal alteration of *Arctica islandica* aragonite. (Oral)

Stevens K.*, <u>Casella L. A.</u>, Griesshaber E., and Mutterlose J. (2015):
EBSD analysis of belemnite rostra: a screening tool for diagenetic alteration. (Oral)

Ritter A.-C.*, Mavromatis V., Dietzel M., Schmahl W. W., Griesshaber E., <u>Casella L. A.</u>, Koelen J., Neuser R., Niedermayr A., Buhl D., and Immenhauser A. (2015):
Experimental diagenesis: exploring the impact of differential fluid temperature and chemistry on biogenic aragonite. (Poster)

Workshops attended

<u>4th Granada-Münster discussion meeting on mineral-fluid interaction</u>

Organised by Prof. Dr. Andrew Putnis and Dr. Christine V. Putnis;

Münster, Germany, November 24th-25th, 2016.

Casella L. A.*, Griesshaber E., Yin X., Ziegler A., Mavromatis V., Müller D., Ritter A.-C., Hippler D., Harper E. M., Dietzel M., Immenhauser A., Schöne B. R., Angiolini L., and Schmahl W. W. (2016):

Experimental diagenesis: insights into aragonite to calcite transformation of *Arctica islandica* and *Porites* sp. coral skeletons by hydrothermal treatment. (Oral)

<u>MRK2016 EMU school on mineral reaction kinetics</u>

Organised by the European Mineralogical Union (EMU);

Vienna, Austria, September 19th-23rd, 2016.

Casella L. A.*, He S., Griesshaber E., Harper E. M., Jackson D. J., and Schmahl W. W. (2016):

Do different biogenic microstructures have an effect on mineral dissolution-reprecipitation processes? (Poster)

<u>4th "CHARON" workshop</u>

Organised by Prof. Dr. Martin Dietzel;

Graz, Austria, February 22nd-25th, 2016.

Casella L. A.*, Griesshaber E., Mavromatis V., Dietzel M., Ziegler A., Stevens K., Neuser R. D., Ritter A.-C., Goos M., Simonet Roda M., Taubert K., He S., Angiolini L., Mutterlose J., Liebetrau V., Eisenhauer A., Immenhauser A., and Schmahl W. W. (2016):

Understanding diagenetic overprint of biogenic carbonates: natural vs. experimental alteration. (Oral)

Biochemical controls on mineral growth: application and advances

> Organised by Dr. Karina Sand, Dr. Dominique Tobler, Dr. Shaun Hall and Dr. Maria Romero-Gonzalez;
>
> Sponsored by the UK EPSRC programme grant "Materials interface with biology";
>
> 25th Goldschmidt Conference, Prague, Czech Republic, August 15th-16th, 2015.

3rd "CHARON" workshop

> Organised by Prof. Dr. Harald Strauss;
>
> Münster, Germany, May 20th-22nd, 2015.

> Casella, L. A.* (2015):
>
> **Microstructures and textures of modern, fossil, and artificially altered calcitic and aragonitic marine skeletons.** (Oral)

"CHARON" – Shell Global workshop

> Organised by Prof. Dr. Adrian Immenhauser and M. Sc. Ann-Christine Ritter;
>
> Bochum, Germany, March 27th, 2015.

> Casella, L. A.* (2015):
>
> **EBSD – a promising tool for diagenetic overprint determination**. (Oral)

2nd "CHARON" workshop

> Organised by Prof. Dr. Wolfgang W. Schmahl and Dr. Erika Griesshaber;
>
> Munich, Germany, November 3rd-5th, 2014.

> Casella, L. A.* (2014):
>
> **Can we measure diagenetic overprint in biogenic carbonates?** (Oral)

Kolloquium für Kristallographie und technische Mineralogie

> Organised by Prof. Dr. Wolfgang W. Schmahl;
>
> Munich, Germany, October 24th, 2014.

> Casella, L. A.* (2014):
>
> **Can we measure diagenetic overprint in biogenic carbonates?** (Oral)

Arbeitsgruppentreffen der Kristallographie und Mineralogie

Organised by Prof. Dr. Wolfgang W. Schmahl;

Unterlippach, Germany, June 6th, 2014.

Casella, L. A.* (2014):

Can we measure diagenetic overprint in biogenic carbonates? (Oral)

1st "CHARON" workshop

Organised by Prof. Dr. Anton Eisenhauer;

Kiel, Germany, February 26th-28th, 2014.

Casella, L. A.* (2014):

Microstructure characterisation of modern and fossil biological hard tissues.
(Oral)

Arbeitsgruppentreffen der Kristallographie und Mineralogie